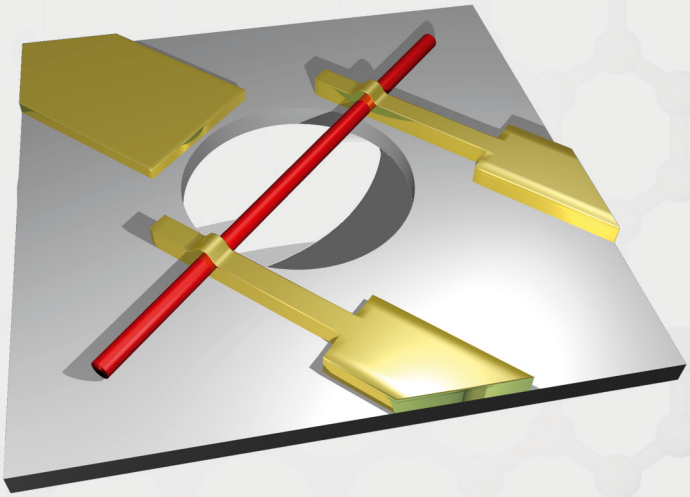

# Structural influences on electrical transport in nanostructures

Robert Dietrich Frielinghaus

Member of the Helmholtz Association

JÜLICH
FORSCHUNGSZENTRUM

Schriften des Forschungszentrums Jülich
Reihe Schlüsseltechnologien / Key Technologies Band / Volume 60

Forschungszentrum Jülich GmbH
Peter Grünberg Institute (PGI)
Electronic Properties (PGI-6)

# Structural influences on electrical transport in nanostructures

Robert Dietrich Frielinghaus

Schriften des Forschungszentrums Jülich
Reihe Schlüsseltechnologien / Key Technologies Band / Volume 60

ISSN 1866-1807 ISBN 978-3-89336-867-9

Bibliographic information published by the Deutsche Nationalbibliothek.
The Deutsche Nationalbibliothek lists this publication in the Deutsche Nationalbibliografie; detailed bibliographic data are available in the Internet at http://dnb.d-nb.de.

| | |
|---|---|
| Publisher and Distributor: | Forschungszentrum Jülich GmbH<br>Zentralbibliothek<br>52425 Jülich<br>Tel: +49 2461 61-5368<br>Fax: +49 2461 61-6103<br>Email: zb-publikation@fz-juelich.de<br>www.fz-juelich.de/zb |
| Cover Design: | Grafische Medien, Forschungszentrum Jülich GmbH |
| Printer: | Grafische Medien, Forschungszentrum Jülich GmbH |
| Copyright: | Forschungszentrum Jülich 2013 |

Schriften des Forschungszentrums Jülich
Reihe Schlüsseltechnologien / Key Technologies, Band / Volume 60

D 464 (Diss., Duisburg, Univ., 2013)

ISSN 1866-1807
ISBN 978-3-89336-867-9

The complete volume is freely available on the Internet on the Jülicher Open Access Server (JUWEL) at www.fz-juelich.de/zb/juwel

## Zusammenfassung

In dieser Arbeit wird das Zusammenspiel der molekularen Konfiguration mit den elektrischen und optischen Eigenschaften einiger einzelner Nanostrukturen untersucht. Diese sind Kohlenstoffnanoröhren (CNTs), Tetramangan-dekorierte Kohlenstoffnanoröhren und InAs Nanodrähte, die jeweils mit hochauflösender Transmissionselektronenmikroskopie und -spektroskopie (HR-TEM), Ramanstreuung sowie Tieftemperatur-Quantentransportmessungen auf dem Niveau einzelner Bauteile untersucht werden. Diese Techniken messen komplementäre Materialeigenschaften und ermöglichen, zusammen genommen, eine vollständige Charakterisierung der einzelnen Nanostruktur.

Diese Korrelation wird durch eine neuartige Probengeometrie ermöglicht, die im Rahmen der Arbeit entwickelt wurde. Hierbei werden verschiedene Lithographieschritte auf einer TEM-Membran kombiniert. Das Verfahren ist kompatibel mit vielen (selbstorganisierten) Nanostrukturen. Ferner werden Bauteil und Substrat entkoppelt, wodurch der Transport sehr ungestört abläuft.

Eine einzelne, dreiwandige Kohlenstoffnanoröhre wird mittels HR-TEM als solche identifiziert und mit Ramanstreuung und elektrischem Transport bei Raumtemperatur untersucht. Die optischen Eigenschaften und der Transportkanal können den einzelnen Wänden zugeordnet werden.

Quantentransportexperimente werden an zwei weiteren Kohlenstoffnanoröhren durchgeführt, die mittels HR-TEM als ein Zweierbündel aus einwandigen CNTs beziehungsweise als dreiwandige CNT identifiziert werden. Die entsprechenden Stabilitätsdiagramme weisen komplexe Charakteristiken wie verhinderte Kreuzungen, Fano-förmige Coulombmaxima und Sägezahnmuster auf. Der ihnen zugrunde liegende Mechanismus kann nur mit dem detaillierten Wissen der atomaren Struktur bestimmt werden. Genauer gesagt können die Charakteristika mit kapazitiven und molekularen Interaktionen zwischen den verschiedenen Elementen des Bauteils und der Umgebung modelliert werden.

Ebenfalls werden universellen Leitwertfluktuationen und die Phasenkohärenzlänge vier einzelner InAs Nanodraht-Tansportbauteile untersucht. Zwei verschiedene Temperaturabhängigkeiten können beobachtet werden. Diese stehen nicht im Zusammenhang mit der Kristallphasenmischung, da alle vier Nanodrähte diesbezüglich statistisch identisch sind, wie eine HR-TEM Messung zeigt.

Die Eigenschaften der Kohlenstoffnanoröhren können durch chemische Funktionalisierung verändert werden. In dieser Arbeit wird ein Verfahren vorgestellt, bei dem ein Carboxylat-Ligandenaustausch die Kohlenstoffnanoröhre mit einem molekularem Tetramanganantiferromagneten dekoriert. Der Grad der Funktionalisierung kann über die Oxidation der CNTs kontrolliert werden. Die Bedeckung wird mit Hell- und Dunkelfeld HR-TEM sowie energiedispersiver Röntgen- und Elektronenenergieverlustspektroskopie überwacht, die die Mn-Verteilung auf der Kohlenstoffnanoröhre abbilden. Ramanstreuung und SQUID-Messungen zeigen ebenfalls die erfolgreiche Bedeckung und die Integrität der Hybride. Transportmessungen an funktionalisierten Kohlenstoffnanoröhrennetzwerken demonstrieren die Verwendbarkeit solcher Strukturen für Einzelhybridquantentransportbauteile.

Zusammenfassend ist das entwickelte Probenformat sehr mächtig, den Einfluss spezifischer struktureller Veränderungen auf die optischen und elektrischen Eigenschaften einzelner Nanostrukturen zu untersuchen. Dies ist ein wichtiger Baustein für den Vergleich zwischen theoretischen Vorhersagen und experimentellen Ergebnissen.

## Abstract

The interplay between the molecular configuration and the electrical and optical properties of various individual nanostructures is studied in this thesis. These are carbon nanotubes (CNTs), tetramanganese-decorated carbon nanotubes, and InAs nanowires that are investigated on the single-device level with high-resolution transmission electron microscopy and spectroscopy (HR-TEM), Raman scattering, and low-temperature quantum transport measurements. These techniques probe complementary material properties and can jointly provide a comprehensive characterization of the individual nanostructure.

This correlation is achieved on a novel sample design developed in the course of this thesis. It combines various lithographic steps on a TEM membrane and is compatible with many (self-assembled) nanostructures. It decouples the device from the substrate, leading to clean transport properties.

An individual triple-walled carbon nanotube, as identified using HR-TEM, is investigated with Raman spectroscopy and room-temperature electrical transport. The optical response and the transport channel can be assigned to the individual walls.

Quantum transport experiments are performed on two additional carbon nanotube devices, identified with the HR-TEM as a two-fold bundle of single-walled CNTs and a triple-walled CNT, respectively. The stability diagrams exhibit complex features as avoided crossings, Fano-shaped coulomb peaks, and regular saw tooth patterns. Their origin is only found with the detailed knowledge of about the atomic structure. More precisely, these features can be modeled with capacitive and molecular interactions between the various elements of the devices and the environment.

Universal conductance fluctuations and the phase-coherence length of four individual InAs nanowire transport devices are likewise studied. Two different temperature dependences can be measured. They are not related to a crystal phase mixing because all four nanowires are statistically identical in these terms as determined by a HR-TEM measurement.

The properties of carbon nanotubes can be modified by chemical functionalization. The route proposed in this thesis is the decoration with a tetramanganese molecular antiferromagnet via a carboxylate ligand exchange with the carbon nanotube. The degree of functionalization can be controlled with the oxidation of the CNT. The decoration is monitored with bright- and dark field HR-TEM as well as energy-dispersive X-ray and electron energy loss spectroscopy that show the repartition of the Mn on the carbon nanotubes. Raman spectroscopy and SQUID measurements provide further evidence of a successful decoration and show the integrity of the hybrids. Transport experiments on functionalized carbon nanotube networks demonstrate the integrability of such structures into single-hybrid quantum transport devices.

In conclusion, the developed sample layout has a great potential to investigate the impact of specific structural modifications on optical and electrical properties of individual nanostructures. This is an important ingredient for the comparison of theoretical predictions and experimental results.

# Contents

CHAPTER 1

# Introduction

Nanotechnology has been a highly active field of research in the past decades for it had two driving forces, application and fundamental research with almost 30,000 publications in the past year, increasing exponentially [Sco12]. The term has found its way into everyday life, fiction, and countless products.

The birth of nanotechnology dates to 1959 when Richard P. Feynman held a lecture entitled "There's Plenty of Room at the Bottom", in which he considered various applications in the field of medicine, mechanical engineering, and electronics [Fey60]. The aim of using nanotechnology for the latter is to reduce circuit sizes and likewise increase computing power. This increased circuit density is the original formulation of the so-called Moore's law [Moo65] that states that the number of transistors crammed on a chip will double every two years. It has proven surprisingly reliable although it is purely phenomenological and was several times predicted to fail within the next decade [Moo65]. Consequently, today's microprocessors are in fact nanoprocessors and the physical barrier of the individual atom is close [Lan12]. This can hamper the development due to considerable device-to-device fluctuations – or trigger new concepts of unprecedented capabilities like spintronics and quantum computing, where computation is not performed on the electron charge but on its spin [Los98].

Apart from these application issues, nanotechnological methods enabled the exploration of many fundamental quantum phenomena in solids and the discovery of new materials. Several physics and chemistry Nobel prices have been awarded for basic research in this area like the development of the scanning tunneling microscope [Bin82], the study of the giant magnetoresistance in thin magnetic films [Bai88, Bin89] or the discovery of fullerenes [Kro85] and graphene [Nov04]. Other prominent, recent examples of scientific breakthroughs with nanotechnological methods are the splitting of Cooper pairs [Hof09, Her10] or the first signatures of the Majorana fermion [Mou12].

My thesis aims at extending both the understanding and the functionality of material systems that are of high relevance to the field of nanotechnology. Thereby, both driving forces are merged in my work in order to take this research area to a matured state. I



investigate fundamental physics in carbon nanotubes and InAs semiconductor nanowires, two materials with a high technological potential. Both are self-assembled cylindrical nanostructures with a high aspect ratio and have many possible applications ranging from optoelectronics [Li06, Avo08] to quantum computing [Ind07, Tra09, Bau10] and from biochemistry [Mar03, Du09] to solar energy [Wei09, Ham10]. They are mesoscopic systems, meaning that they are large enough to be readily manipulated with current nanotechnological methods and at the same time small enough to exhibit various quantum phenomena originating from the propagation of individual electrons [Hei07].

One goal of my thesis is to understand in depth the properties of individual carbon nanotube or InAs nanowire devices, with an emphasis on the electrical transport behaviour. Most of the experiments performed so far on these material systems lack a direct comparison of the lattice structure and the transport data because this requires an analysis with usually incompatible investigation methods. I tackle this issue with a novel sample design developed within the framework of this thesis. Low-temperature transport experiments, optical spectroscopy, and transmission electron microscopy are combined by its means to characterize the very same, freestanding nanostructure.

Each of these methods gives an information on the nanostructure that is complementary to the others. The (quantum) transport experiments probe the electronic structure and the interaction of the electrons with their environment as well as with the host lattice. These structural properties can be imaged with atomic resolution in the transmission electron microscope. Raman spectroscopy finally probes the dynamics of the lattice and its interaction with the electronic system. Their combination gives an insight on if, how and to which extent structural modifications like bundling and multiple walls in the case of the carbon nanotubes or stacking faults and polytypism in the case of the InAs nanowires determine the electrical transport and the optical response of the investigated systems. This novel sample design has the additional benefit of uncoupling the nanostructure from the substrate, leading to an increased clarity of effects in the electrical transport measurements. This is crucial since the suppression or control of detrimental environmental influences is a key issue to understand the characteristics of a system and to develop novel devices.

The second aim of my thesis is to modify the pristine carbon nanotube properties by controlled functionalization. This issue is intimately linked to the first subject because such a functionalization is a structural modification whose influence and degree has to be monitored. I choose a covalent exohedral decoration with a tetramanganese cluster, based on a ligand exchange between the carbon nanotube and the complex. This is a very versatile route because the magnetic core is interchangeable, altering the spin center close to the carbon nanotube. These experiments are part of the emerging field of molecular spintronics. It combines nanotechnology with the versatility of chemical variations, all on a mesoscopic system that can readily be controlled from our macroscopic world. The resulting hybrids are again characterized by the three methods, electrical transport, Raman scattering, and transmission electron microscopy and spectroscopy, demonstrating the successful functionalization and analyzing the changes of the carbon nanotube properties.

The thesis is divided into six chapters that discuss the material systems and experimental techniques and present the obtained results. They are structured as follows:

**Chapter II** introduces the atomic structure and the electronic properties of the investigated material systems, namely carbon nanotubes and InAs nanowires. Both properties are intimately linked and can vary substantially from one structure to the other. The theory of Raman scattering and the major phonon modes of the carbon nanotubes are likewise explained.

**Chapter III** explains the operating principles of the employed investigation methods, i.e. Raman spectroscopy, transmission electron microscopy, and low-temperature electrical transport. It gives also an overview of the quantum transport phenomena observed in the experimental chapters.

**Chapter IV** presents the sample design and the fabrication of the nanostructures. Its capabilities are exemplarily shown on an individual carbon nanotube transport device that is comprehensively characterized by Raman spectroscopy and transmission electron microscopy, demonstrating that only a combination of these methods describes the device completely.

**Chapter V** reports on low-temperature quantum transport measurements on InAs nanowires with transparent contacts, revealing universal conductance fluctuations that are sensitive to the evolution of the electron phase-coherence with temperature. These results are compared with transmission electron micrographs of the very same nanowires that expose a number of stacking faults.

**Chapter VI** analyzes the stability diagrams of quantum dots formed within different carbon nanotube device structures, namely a triple-walled carbon nanotube and a twofold single-walled carbon nanotube bundle. They show a very different transport behaviour and mutual coupling of their constituents. The structure was again measured by transmission electron microscopy.

**Chapter VII** finally introduces the tetramanganese cluster and the functionalization procedure. The resulting hybrids are analyzed with various element-sensitive operation modes of the transmission electron microscope to obtain information on the cluster repartition. These results are compared to Raman spectroscopy and transport measurements that monitor the changes imposed on the carbon nanotubes by the grafting process.

# CHAPTER II

## Basic properties of carbon nanotubes and InAs nanowires

Carbon nanotubes (CNTs) and InAs nanowires both exhibit some peculiar properties that are quite different from their macroscopic counterparts graphite and bulk InAs crystals. Their cylindrical shape, together with the extreme surface-to-volume ratio, make them highly sensitive to structural and environmental changes. The nanoscale dimensions of both material systems lead to the appearance of various quantum phenomena.

In other aspects however, the material systems differ fundamentally. Carbon nanotubes are ideal one-dimensional ballistic conductors. The InAs nanowires, on the other hand, conduct rather diffusively and three-dimensionally with certain two-dimensional contributions. Some of their properties are inherited from the respective bulk materials graphite and InAs crystals or layers. In the following, I will introduce and derive some material characteristics, focusing on the structural, electronic and optical properties. These descriptions will be rather succinct and focused on aspects relevant for this work. More details may be found in the literature cited.

## II.1 Carbon nanotubes

Carbon has three major allotropes depending on the hybridization: $sp^3$-hybridized diamond, $sp^2$-hybridized graphite with delocalized $\pi$-electrons and $sp^2$-hybridized fullerenes. All other modifications such as carbon nanotubes or graphene may be derived from these fundamental forms. Although CNTs belong to the family of fullerenes [Hen06], they inherit the major properties used in this work from graphene, which is a single sheet of graphite.

### II.1.1 The atomic and electronic structure

#### Atomic lattice of graphene and carbon nanotubes

Carbon nanotubes may be seen as a rolled-up sheet of graphene, resulting in many inherited properties [Rei04]. The hexagonal honeycomb lattice of the graphene sheet is preserved. Here, each atom has three nearest neighbours with an interatomic distance of $a_{CC} = 1.42\,\text{Å}$ [Odo00]. The carbon atoms form two triangular sublattices $A$ and $B$ as can be seen in Fig. II.1(a).

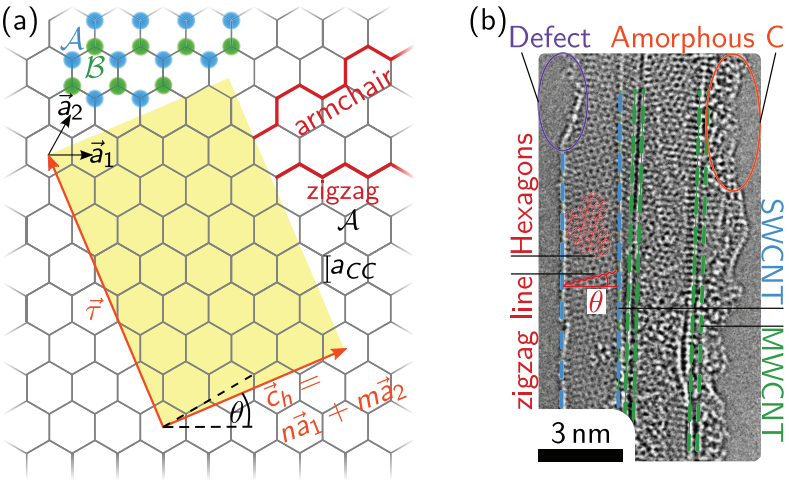


**Figure II.1:** (a) Graphene consists of two triangular sublattices $\mathcal{A}$ and $\mathcal{B}$ with base vectors $\vec{a}_1$ and $\vec{a}_2$, offset by a nearest-neighbour distance $a_{CC}$. A $(n, m)$ CNT can be obtained by seamlessly rolling up a graphene sheet along the chiral vector $\vec{c}_h := n\vec{a}_1 + m\vec{a}_2$. The resulting length of the CNT unit cell (yellow) is described by the translational vector $\vec{\tau}$. It is $\theta = \sphericalangle(\vec{a}_1, \vec{c}_h)$. The symmetric cases of a zigzag ($\theta = 0$) and an armchair ($\theta = 30$) nanotube are indicated in red. (b) Transmission electron micrograph summarizing the various carbon nanotube structures. A single- and a double-walled CNT form a bundle. Both are slightly defective and decorated with amorphous carbon. The chiral angle can be determined from the individual graphene hexagons.

Two translational vectors $\vec{a}_1$ and $\vec{a}_2$ are needed along with the two sublattices to describe the graphene unit cell. A CNT can be constructed from the graphene sheet by cutting out a rectangle defined by the chiral vector $\vec{c}_h = n\vec{a}_1 + m\vec{a}_2$ with $n, m \in \mathbb{N}_0$ and the translational vector $\vec{\tau}$. This rectangle can then be rolled up seamlessly with the chiral vector $\vec{c}_h$ describing the circumference. The resulting carbon nanotube is thus fully described by the chiral indices $(n, m)$ and its length $L$ that is a multiple of $|\vec{\tau}|$. It is $n \geq m$ by convention. All electrical and optical properties are determined by $(n, m)$ except for edge effects as will be discussed in the following [Krü07].

The chiral vector $\vec{c}_h$ defines an angle $0° \leq \theta = \sphericalangle(\vec{a}_1, \vec{c}_h) \leq 30°$. The extreme cases $\theta = 0°$ ($m = 0$) and $\theta = 30°$ ($m = n$) are called zigzag and armchair, respectively, due to the shape around their circumference (cf. Fig II.1(a)). They are symmetric and special selection rules apply for their electrical and optical properties (vide infra). All other cases are chiral with the periodic zigzag or armchair-lines winding along the tube axis. An as-grown CNT is capped with a fullerene-like structure [Cha01]. This is the reason why carbon nanotubes belong to the fullerene material class.

The chiral indices $(n, m)$, the chiral angle $\theta$, the diameter $D$ and the length of the translational vector $|\vec{\tau}|$ are related via [Dre01, Dre95]

$$\sin\theta = \frac{\sqrt{3m}}{2\sqrt{n^2 + nm + m^2}} = \frac{a_{CC}}{\pi}\frac{\sqrt{3m}}{2D} \tag{II.1a}$$

$$D = \frac{a_{CC}\sqrt{3}}{\pi}\sqrt{n^2 + nm + m^2} \tag{II.1b}$$

$$|\vec{\tau}| = \frac{a_{CC}\sqrt{3\,(n^2 + nm + m^2)}}{\gcd(2n + m, 2m + n)}\ . \tag{II.1c}$$

Here, gcd denotes the greatest common divisor. The chirality can be extracted from high-resolution transmission electron microscopy (HR-TEM) measurements (cf. Fig. II.1) using these relations.

The above description holds for single-walled carbon nanotubes (SWCNTs). My measurements are partly conducted on more complex systems, namely multi-walled CNTs (MWCNTs) or bundles of both. These cases can be observed in the measurement shown in Fig. II.1(b). MWCNTs are interstacked SWCNTs with an interlayer distance of 3.4. . . 3.9 Å depending on the wall diameter [Kia98] that I can observe in my transmission electron micrographs.

Bundles of carbon nanotubes may consist of both SWCNTs and MWCNTs. Depending on their chirality and curvature they ideally lie in mutual axial orientations of different symmetry like hexagonal or tetragonal [Dre95], tied together by van-der-Waals forces. The constituents interact electronically what has to be taken into account in order to interpret the optical and transport measurements correctly [Goß11b].

### The electronic band structure

The carbon nanotube band structure can be derived from the one of graphene. The route via the so-called zone folding approximation is analogous to the CNT construction from a graphene sheet. The tubular, one-dimensional CNT geometry modifies the graphene band structure in two aspects. First, the one-dimensionality introduces a quantization of the permitted $\vec{k}$-vectors. Second, the bent graphene lattice leads to a different overlap of the $p_z$ orbitals, i.e. a partial $sp^3$-hybridization that makes them much more reactive than flat graphene (cf. section II.1.4). Additionally, several curvature effects arise that have only a corrective impact on the electrical transport in carbon nanotubes and are not of relevance for the systems studied in this thesis [Sai00]. Nevertheless, the optical

and vibrational properties are affected more strongly and new eigenmodes appear (see section II.1.3). The carbon nanotube band structure will be derived from graphene in the following, as discussed in more detail e.g. in [Rei04].

Already in 1947, almost 60 years before the first fabrication of graphene [Nov04], its band structure was calculated using a tight-binding approximation allowing only nearest-neighbour hopping [Wal47]. This yields

$$E_{\pm}(\vec{k}) = \pm\gamma_0\sqrt{1+4\left[\cos^2\left(\frac{\pi k_y a_{CC}}{\sqrt{3}}\right)+\cos\left(\frac{\pi k_y a_{CC}}{\sqrt{3}}\right)\cos\left(\pi k_x a_{CC}\right)\right]} \qquad \text{(II.2)}$$

for the energy of the $\pi$-orbitals. The result is plotted in Figure II.2. All major features like, e.g., the semimetallic character or the linear dispersion around $K$ discussed in the following are nicely reproduced, although a complete description needs to take more neighbours into account [Rei02].[1]

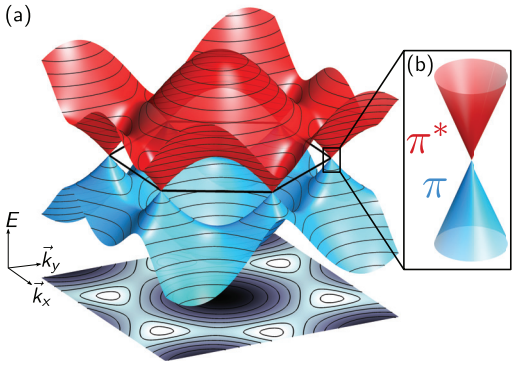


**Figure II.2:** The electronic band structure of graphene, calculated with eq. (II.2). (a) Full structure of the $\pi$-orbitals with electron- and hole-like states (red and blue, respectively). The $\Gamma$-point is in the center of the graph. The valence and conduction band touch each other at the six $K$-points. (b) Close-up of an arbitrary $K$-point. Electrons and holes follow a linear dispersion in the vicinity of the $K$-points.

The two-atomic hexagonal crystal structure is directly reflected in the dispersion of the bonding, hole-like $\pi$- and the antibonding, electron-like $\pi^*$-bands. They have a maximum band gap at the $\Gamma$-point and touch each other at six $K$-points. These $K$-points reside at two non-equivalent sites $K$ and $K'$ like the $A$- and $B$-sublattices in the crystal structure. The dispersion relation near these $K$-points is linear, leading to a vanishing effective mass $m^* \sim 1/(\partial^2 E_{\pm}/\partial\vec{k}^2)$.

Indeed, the dispersion relation expanded around $K$ can be described by the Dirac Hamiltonian for massless relativistic fermions [Dir28, Gei07]

$$\hat{H} = \hbar v_F \begin{pmatrix} 0 & \hat{\kappa}_x - i\hat{\kappa}_y \\ \hat{\kappa}_x + i\hat{\kappa}_y & 0 \end{pmatrix} = \hbar v_F \underline{\underline{\sigma}}_y \cdot \hat{\vec{\kappa}} \qquad \text{(II.3)}$$

[1] Next-nearest neighbour hopping, e.g., lifts the electron-hole symmetry and makes the hole-like $\pi$-orbital shallower [CN09].

rather than by the non-relativistic Schrödinger equation. Here, $v_F \approx 10^6\,\mathrm{m/s}$ denotes the Fermi velocity, $\underline{\underline{\sigma}}_y$ a Pauli spin matrix and $\hat{\vec{\kappa}}$ is the expansion of the wave vector $\hat{\vec{k}}$ around $K$:

$$\hat{\vec{\kappa}} := \hat{\vec{k}} - K \tag{II.4a}$$

$$\hat{\vec{\kappa}}' := \hat{\vec{k}} - K'. \tag{II.4b}$$

This expansion is a good approximation for $|E| < 1\,\mathrm{eV}$. The two $K$-points or valleys and their expansions $\vec{\kappa}$ are the reason for the ballistic conductance in carbon nanotubes and graphene which is further discussed in section III.3.1 because a charge carrier cannot simply trespass from one to the other. The affiliation to one valley is rather a quantum number, the so-called pseudospin, that can have two values and can be treated like the spin in the standard Dirac equation [Gei07]. Since the states close to $E = 0$ have contributions from $K$ and $K'$, they are four-fold (two-fold spin and two-fold valley) degenerate. $K$ and $K'$ are referred to as Dirac points and one speaks of Dirac cones due to this analogy. The suppressed backscattering and the vanishing effective mass lead to a high mobility $\mu \lesssim 2 \cdot 10^5\,\mathrm{cm}^2/(\mathrm{Vs})$ independent of the charge carrier density $n$ [Che08].

#### From graphene to carbon nanotubes

Rolling up the graphene sheet to form a carbon nanotube introduces a constraint to the wave vector. In this so-called zone folding approximation [Ham92, Lou01, Rei04, Krü07], electron waves along the circumference $\vec{c}_h$ have to obey periodic boundary conditions while wave vectors $\vec{k}_\parallel$ along the nanotube axis remain unconstrained

$$\vec{c}_h \cdot \vec{k}_\perp = 2\pi N; \qquad (N \in \mathbb{N}) \tag{II.5a}$$

$$\vec{k}_\parallel \quad \text{continuous.} \tag{II.5b}$$

The result of this discretization may be seen in Fig. II.3. The $K$-points do not necessarily belong to the set of allowed $\vec{k}$-vectors and thus CNTs come as semi-metallic and as semiconducting species. The character can be predicted as [Lou01]:

$$(n-m)/3 = 0 \;\Rightarrow\; \text{semimetallic like graphene: } E_g = 0 \tag{II.6a}$$

$$(n-m)/3 = N \;\Rightarrow\; \text{small band gap: } E_g \sim \mathcal{O}(\mathrm{meV}) \tag{II.6b}$$

$$(n-m)/3 \neq N \;\Rightarrow\; \text{semiconducting: } E_g \sim \mathcal{O}(\mathrm{eV}), \tag{II.6c}$$

with $N \in \mathbb{N}$. The tiny band gap of eq. (II.6b) originates from curvature effects and approaches the case of eq. (II.6a) for increasing diameters $D$ as $1/D^2$. It is so small that both species are metallic at room temperature. Consequently, standard growth conditions yield a ratio of 1:2 between metallic and semiconducting CNTs.

Another consequence of the reduced dimensionality is the appearance of van-Hove-singularities in the carbon nanotube density of states as can be seen in the right parts of

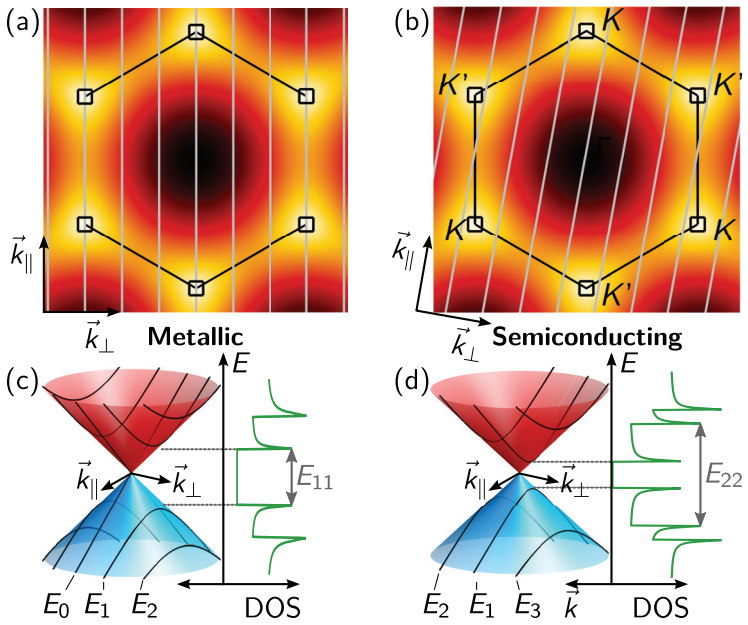


**Figure II.3:** Schematic carbon nanotube bandstructures, derived from graphene via zone-folding approximation, see also Fig. II.2. (a,b) Graphene band structure ($\pi$-orbital, colour-coded is the energetic distance to the Fermi energy). Superimposed are the allowed wave vectors of (a) a metallic and (b) a semiconducting nanotube (gray lines). Note that the allowed wave vectors (a) do include or (b) do not include the $K$-points. (c,d) Close-up of a $K$-point similar to Fig. II.2(b). The black lines denote allowed $\vec{k}$-vectors. $\vec{k}_{\parallel}$ denotes the direction along the carbon nanotube axis while $\vec{k}_{\perp}$ is along the circumference. Depending on whether a $K$-point is included or not, one obtains a (c) metallic or (d) semiconducting density of states (DOS). $E_{ii}$ marks optically allowed transitions.

Figs. II.3(c,d). They play an important role in optical experiments because they strongly enhance resonance features and will later be used for chirality assignment. However, the singularities can also be observed, e.g., via scanning tunnelling spectroscopy [Wil98], electrostatic force microscopy [Heo05] or in transport experiments [Ohn04].

### II.1.2 Interaction of carbon nanotubes with light

#### Optical properties

Light shone on a carbon nanotube will interact with its electronic system (vide supra), creating electron-hole pairs, i.e. excitons. They can directly relax back into the ground state, which is the so-called Rayleigh scattering [Ray71]. The cross section of this process is strongly enhanced when the incident photon is in resonance with an interband

transition $E_{ii}$. This is due to the high density of states at the van-Hove singularities (cf. Fig. II.3(c+d)) and is one ingredient for chirality assignment, similar to what I will show for the Raman spectroscopy [Joh10]. Transitions involving different band indices $E_{ij}$ with $i \neq j$ are strongly suppressed because they need a photon polarization perpendicular to the tube axis whereas it must be parallel for a finite cross section due to the antenna effect [Aji95, Dam99].

The interband transition energies $E_{ii}$ are found to be diameter-dependent as demonstrated in the so-called Kataura plots [Kat99] shown in Fig. II.4. They map the diameter to the optical transition energy for every chirality $(n, m)$. The carbon nanotubes group as a function of their family index

$$\nu := \mathrm{mod}(n - m, 3) \quad \Rightarrow \nu \in [0, 1, 2] \tag{II.7}$$

that divides the semiconducting tubes in eq. (II.6c) in two groups depending on their position with respect to the $K$-point. These families additionally describe a pointed shape in the Kataura plot that leads to the definition of a branch index

$$\nu' := 2n + m. \tag{II.8}$$

The metallic branches $\nu' = 24$ and $\nu' = 27$ are exemplarily marked by the black lines in Fig. II.4. The transition energies $E_{ii}$ are inversely proportional to the diameter, disregarding the spread due to the branching.

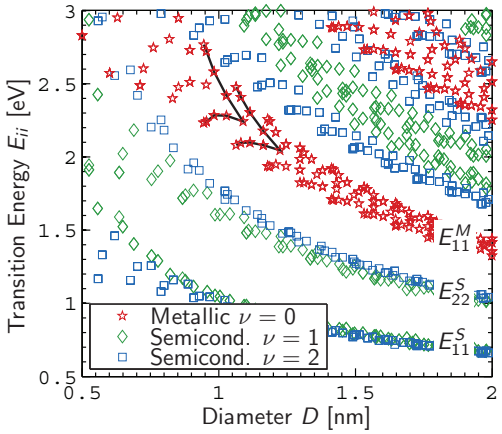


**Figure II.4:** Theoretical Kataura plot calculated in the framework of a non-orthogonal tight-binding model [Pop04]. It maps the diameter to the optical transition energy, with every point in the plot being a specific chirality $(n, m)$. The first intraband transitions $E_{ii}$ are labeled and the metallic branch indices $\nu' = 24$ ($\nu' = 27$) are exemplarily given by the left (right) black trace. All transition energies are rigidly blueshifted by 0.3 eV to account for excitonic effects and electron correlations [Pop04, Mau05].

The displayed Kataura plot will be used for chirality assignment in the Raman experiments. It is calculated with a non-orthogonal tight-binding model [Pop04] that takes the curved CNT geometry into account, in contrast to the zone-folding approximation described in section II.1.1 [Rei02, Rei04, Tho07]. It does not include excitonic effects, i.e. the binding energy of the created electron-hole pair, but a rigid blueshift of the calculated values by 0.3 eV can correct this issue [Pop04, Mau05]. The real transition energies can

additionally be influenced by environmental effects such as bundling [Goß11a, O'C04]. These latter corrections are so small that they can be neglected for the systems discussed in this thesis.

### Raman scattering

An optically created exciton has the possibility to generate or annihilate a phonon instead of directly relaxing back into its ground state. This so-called Raman scattering [Ram28] gives detailed insight into the vibrational and therefore structural properties of the studied carbon nanotube. I will use the various possible Raman processes for a chirality assignment, to determine the integrity of the sample, and to monitor a chemical functionalization in the experimental chapters of this thesis. Notably three phonon modes are important in this context which will be introduced in the following.

The cross section for the Raman process is much smaller than for the Rayleigh scattering because it is a higher order process. The discussed resonance effect thus plays an even more important role for the detectability of the scattered light, since the intensity ratio between on- and off-resonant processes is in the order of $\sim 10^3$ [Dre05].[2] The actual resonance width depends on the phonon mode and ranges between 8 meV for the radial breathing modes [Jor01b] and hundreds of meV for the $G^{\pm}$ modes [Tel09].

The resonance condition can be fulfilled by either the incident ($\hbar\omega_L$) or the scattered ($\hbar\omega'$) photon, i.e.

$$\hbar\omega_L = E_{ii} \quad \rightarrow \quad \text{Incoming resonance} \tag{II.9a}$$

$$\hbar\omega_L - \hbar\omega_{\text{phon}} = \hbar\omega' = E_{ii} \quad \rightarrow \quad \text{Outgoing resonance,} \tag{II.9b}$$

where $\hbar\omega_{\text{phon}}$ denotes the phonon energy. One or two maxima can be observed upon tuning the wavelength of the incoming photon, depending on the relative size of the phonon energy and the resonance width [Tel04, Duq10]. This is demonstrated in Fig. II.5, where the resonance width is assumed to be smaller than the phonon energy as it is the case for the $G^{\pm}$ modes (see next section).

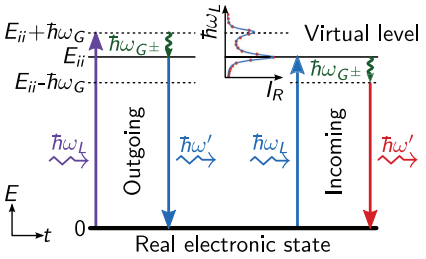


**Figure II.5:** The Raman resonance condition can be fulfilled by the incoming ($\hbar\omega_L$) or outgoing ($\hbar\omega'$) photon. They differ by the phonon energy $\hbar\omega_{G^\pm}$ (of the CNT $G^{\pm}$ phonon, in this example). This results in two maxima of the Raman scattering intensity $I_R$ in function of the incoming photon energy. The sketched asymmetry stems from a violation of the Frank-Condon approximation (data taken from [Duq11]).

[2] Raman scattering was discovered in off-resonant systems where both intermediate states before and after phonon creation are virtual [Ram28]. Resonant processes described here are single-resonant with one real and one virtual intermediate state (cf. Fig. II.5) whereas some materials offer double-resonant conditions, as e.g. the $D$ Mode in graphite [Mau04].

Two additional criteria have to be strictly met for the Raman process. First, the polarization tensor needs to be changed by the vibrating atoms, leading to a multitude of Raman-silent phonon modes that are usually infrared active. Second, energy and momentum need to be conserved. Therefore, only optical phonons in the center of the Brillouin zone can be observed because the maximum transferable momentum from the photon to the phonon is three orders of magnitude smaller than the extend of the Brillouin zone.[3]

### II.1.3 Selected phonon modes in carbon nanotubes

A typical Raman spectrum of a carbon nanotube ensemble is shown in Fig. II.6. Three major modes can be observed that are of particular interest for this work, videlicet the radial breathing modes (RBMs), the defect-induced $D$ mode and the high-energy or $G^{\pm}$ modes (HEMs). They will be discussed in the following. Some of these phonons, namely the $D$ and $G^{\pm}$ modes, are inherited from the graphene similar to the electronic bandstructure, while others (RBMs) are inherent to carbon nanotubes. More detailed descriptions may be found in [Jor03a, Dre05, Tho07].

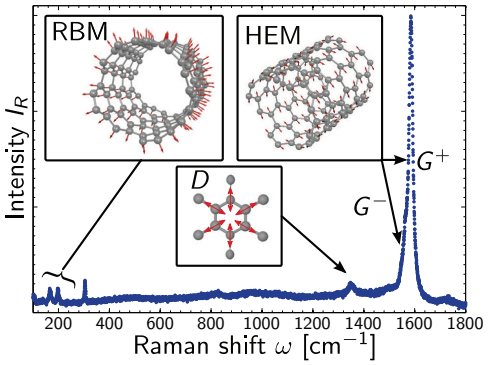


**Figure II.6:** Typical Raman spectrum of a carbon nanotube ensemble, taken at an exciting wavelength of $\lambda_L = 633\,\mathrm{nm}$. Radial breathing and both high-energy modes as well as the defect $D$ mode are highlighted and the respective atom vibrations are sketched. Other maxima are combination and substrate modes that are not investigated in this thesis. The upper insets are adapted from [Tel09].

#### The radial breathing mode

The radial breathing modes (RBMs) are specific to carbon nanotubes and can used for CNT detection in a specimen. They are caused by a coherent radial vibration of the C atoms as sketched in the top left inset of Fig. II.6. The carbon nanotube appears to breathe, which also motivates the name. It can be modeled by a harmonically oscillating cylinder, yielding eigenfrequencies inversely proportional to the diameter, $\omega \sim 1/D$. This proportionality is solely described by material constants, independent of the chiral angle [Dre00], and the corresponding proportionality constant depends only on environmental effects such as bundling or surfactants. This results in a multitude of different

[3] This holds for first-order processes. Higher-order Raman processes like the $D$ mode are also sensitive to phonon modes at the zone border (vide infra).

reported values and even rigid shifts of the RBM frequency.[4] Additionally, multiwalled carbon nanotubes develop new, collective eigenfrequencies due to the van-der-Waals interaction of their shells [Spu10b, Lev11]. All these modes have typical frequencies between $100\,\mathrm{cm}^{-1}$ and $400\,\mathrm{cm}^{-1}$ and resonance widths of $(4\ldots18)\,\mathrm{cm}^{-1}$ [Jor02a].

### The high-energy modes

The high-energy modes (HEMs) have the highest intensity within a carbon nanotube Raman spectrum and stem from a graphitic mode, hence the symbol $G^{\pm}$. The term HEM describes that it is the most energetic branch of the phonon band structure. The benzene rings of the graphene structure are sheared (top right inset in Fig. II.6) and therefore the total intensity of the HEMs is related to the graphitic carbon content of the sample. It reflects the number of (resonant) carbon nanotubes if the amount of amorphous carbon is low. This is usually the case for the systems investigated in this thesis.

The planar degeneracy of the graphene sheet is lifted for carbon nanotubes, resulting in a splitting into a longitudinal (LO) and a transversal (TO) optical mode. They have different energies, with $\omega_{\mathrm{TO}} = \omega_{G^-} < \omega_{\mathrm{LO}} = \omega_{G^+}$ ($\omega_{\mathrm{LO}} = \omega_{G^-} < \omega_{\mathrm{TO}} = \omega_{G^+}$) for semiconducting (metallic) carbon nanotubes [Pis07]. Also the $G^-$ lineshape of the two species differs, whereupon the metallic $G^-$ is generally being broader than its semiconducting counterpart and describes a Breit-Wigner-Fano instead of a Lorentzian line shape. Measurements yielded $\sigma_S \approx 10\,\mathrm{cm}^{-1}$ ($\sigma_M \approx 60\,\mathrm{cm}^{-1}$) for semiconducting (metallic) $G^-$ linewidths [OC05] but the shape and the intensity of the metallic $G^-$ vary strongly between armchair and zigzag CNTs [Wu07, Dam99].

The origin and quantification of these effects has been discussed controversially [Jor02b, Tel05, OC05, Wu07, Pis07]. In conclusion, an increased electron-phonon coupling for the metallic LO mode results in the increased linewidth and a considerable softening that shifts the LO energetically below the TO phonon [Pis07].

Curvature effects lead to a diameter dependence of the $G^-$ mode following

$$\omega_{G^-_{S,M}} = 1591\,\mathrm{cm}^{-1} - \frac{C_{S,M}}{D^2}, \tag{II.10}$$

with different proportionality constants $C_S = 47.7\,\mathrm{cm}^{-1}\cdot\mathrm{nm}^2$ and $C_M = 79.5\,\mathrm{cm}^{-1}\cdot\mathrm{nm}^2$ for semiconducting and metallic carbon nanotubes, respectively [Jor02b]. Also these dependencies are under debate, and environmental effects can modify them even qualitatively [Jor03b, Tel09, Pai06]. Experiments on free-standing CNTs [Mic09] agree with the theoretical descriptions [Jor02b, Pis07] that will be used on a similar system in section IV.2.

### The defect mode

The RBMs and HEMs discussed so far are first-order Raman processes, i.e. they involve one inelastic scattering event that restricts them to the center of the Brillouin zone. The entire zone can be probed in a second-order Raman process if the exciton scatters a

[4] See [Goß11a] for a comprehensive list of parameters.

second time with the lattice. This is the case for the so-called $D$ mode, observed at about $1340\,\mathrm{cm}^{-1}$ but strongly dispersive as a function of the incident photon energy [Tho07]. The associated vibration is given in the lower inset of Fig. II.6 and consists of a radial vibration of the benzene rings. Hence, the mode is again common with any graphitic systems.

The underlying process takes place in the vicinity of a $K$-point at the border of the Brillouin zone (cf. Fig. II.3). The associated phonon causes an intervalley scattering of one of the exciton partners (electron or hole). A second, elastic collision has to scatter it back for recombination as summarized in Fig. II.7. Such a backscattering is suppressed in a perfect graphene lattice as discussed in section II.1.1 and thus this phonon mode requires a structural defect in order to be observed. This process does not differentiate between different kind of defects like vacancies, substitutional atoms, or the chemical groups attached during the functionalization process described later.

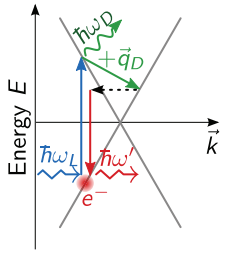


**Figure II.7:** Illustration of the scattering events of the Raman $D$ mode. An electron is vertically scattered by an incoming photon $\hbar\omega_L$ and excites a phonon of wave vector $-\vec{q}_D$ and energy $\hbar\omega_D$. A structural defect is needed to horizontally transfer the electron back to a $\vec{k}$ value where it can recombine, generating a photon of energy $\hbar\omega' = \hbar\omega_L - \hbar\omega_D$.

The $D$ mode intensity is found to scale linearly with the amount of defects in a graphitic sample [Dre00]. It can therefore not be observed on our pristine CVD-grown carbon nanotubes. Its value needs to be normalized to the amount of carbon within the sample by dividing it by the $G$ mode intensity. The resulting ratio is proportional to the number of defects within a carbon nanotube sample [Dre00]. On the other hand, graphitic carbon also shows a $D$ mode, and therefore the structural integrity of the CNTs may be underestimated in a contaminated sample as the one shown in Fig. II.1(b).

### II.1.4 Chemical reactivity of carbon nanotubes

Carbon nanotubes can be decorated with functional groups as I will demonstrate with a tetramanganese complex in the experimental chapters. Such chemical reactions have different kinetics on defects with dangling bonds, on the fullerene-like endcaps, and on the graphene-like walls [Hir02]. The reason is the different degree of the $sp^2$-hybridization, parametrized by the so-called pyramidalization angle [Che03]

$$\theta_P := \sphericalangle(\sigma, \pi) - 90^\circ, \tag{II.11}$$

i.e. the deviation of the $\sigma$ and $\pi$ orbitals from a perfect $sp^2$-hybridization as in graphene. The unsaturated bond of the $sp^3$-fraction leads to an enhanced reactivity of the structure [Had93].



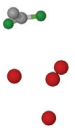

If a carbon nanotube is exposed to an oxidative environment like acids or hot air, it will generate several functional groups such as phenol (CNT−$\overline{\text{O}}$−H), ketone (CNT=O), and carboxylate (CNT−COOH), starting from the aforementioned ends and structural defects. The oxidation can also directly break the graphene lattice if it is strong enough [Hir02, Li11a] and the carbon nanotube wall will eventually exhibit even larger gaps since C atoms may also be removed [Spu08, Spu09] as shown in Fig. II.1(b).[5]

These defects are an important step for a further reaction of the nanotubes. For example, fullerenes can enter and fill the inner hollow [Tsa94, Chi05, Spu09] or molecules can be covalently grafted to these new functional groups [Hir02].

## II.2 InAs nanowires

InAs belongs to the class of III/V-semiconductors. It has a low direct bandgap of 0.354 eV, a low effective mass of $0.023\,m_e$ and a high electron mobility of $4{\cdot}10^4$ cm$^2$/Vs within this material class [Lev96]. This makes it an interesting choice for optoelectronic applications. Of particular interest is, however, usually not the bulk InAs, but its interface to vacuum or other semiconductors (e.g. for terahertz radiation generation [Zha92, Hey01] or for infrared lasing [Le98]). In this context, InAs nanowires receive much attention as they have a large surface-to-volume ratio. Due to their strong spin-orbit coupling, they are also proposed as candidates for spin-based devices [Ind07, NP10].

### Crystal properties

Bulk InAs has a zinc blende structure [Lev96]. However, one often observes axially alternating zinc blende and wurtzite crystal phases when turning to self-organized nanowire growth [Yeh92, Kog92, Dic10a] with a diameter larger than a critical value of some 20 nm [Aki06]. Both structures only differ in their third-nearest neighbours leading to a small energetic difference of about 10 meV per atom [Sch10]. Zinc blende has an ABCABC... stacking sequence in its ⟨111⟩ nanowire growth direction whereas wurtzite behaves as ABAB... in the ⟨0001⟩ growth direction as summarized in Fig. II.8.

This polytypism manifests itself in multiple sections of the crystal phases along the nanowire axis, with the segment lengths determined by the growth conditions. Additionally, there are rotational twinning planes that inverse the zinc blende ABC stacking sequence (ABC*AC*BACBA) and can be regarded as one layer of wurtzite (marked in italic) within the zinc blende [Li11b]. Although the changes are crystallographically subtle, they have a major impact on the electronic properties as discussed in the following section.

### Electronic properties

The wurtzite band gap is larger than the zinc blende one, leading to axial discontinuities in the bandgap $E_G$ and in the conduction band $E_C$, with predictions ranging from

[5] This example shows slightly oxidized carbon nanotubes. The defects may have been enlarged by the high-energetic beam of the transmission electron microscope.

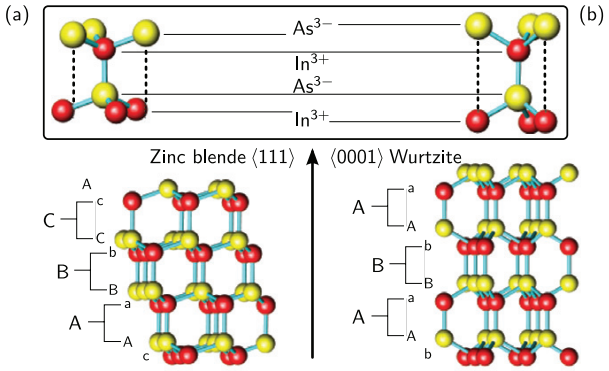


**Figure II.8:** Crystal structure of (a) zinc blende and (b) wurtzite InAs. The ⟨111⟩ and ⟨0001⟩ crystal directions are very similar. The energetic difference between both types only lies in their third-nearest neighbour distance as illustrated in the inset. Adapted from [Dic10a].

116 meV [Zan07] to 290 meV [Mur94] for $\Delta E_G$ and from 23 meV [De10] to 86 meV [Mur94] for $\Delta E_C$. The charge carriers thus experience a potential modulation along their trajectory in the nanowire, leading to a short elastic mean free path $l_e$ in the order of some ten nanometer. Even single crystalline wires exhibit $l_e \approx 100$ nm due to other crystal imperfections like point defects [Han05, Cso08].[6] Therefore, diffusive transport is generally reported for InAs nanowires and universal conductance fluctuations can be observed in low-temperature transport. I will analyze this effect with respect to the polytypism in the experimental chapters.

Another peculiarity of the nanowire geometry is the enhanced surface sensitivity [For09, Du09]. The typical diameters I study in my thesis, around 100 nm, have about half of the charge carriers residing in the outer 15 nm. This is owed to their cylindrical geometry, assuming a radially flat conduction band. Moreover, it is known from the bulk material that InAs exhibits a charge accumulation layer at the surface [Ols96] despite its finite bandgap shown in the bandstructure (exemplarily given for the wurtzite case in Fig. II.9(a)). This is caused by the so-called Fermi level pinning illustrated in Fig. II.9(b+c). This effect is found in all semiconductors, but usually results in a surface depletion layer for charge neutrality reasons. In the case of InN and InAs, on the other hand, the surface states that arise from the discontinuity of the crystal structure are emptied into the bulk conduction band that bends below the Fermi level. A two-dimensional electron gas (2DEG) is formed just underneath the surface [Lüt08], regardless of the crystal structure.

Calculating the electron distribution by iteratively solving the coupled Schrödinger and Poisson equations for a radially symmetric InAs nanowire, one obtains an electron distribution as shown in Fig. II.10 [Dem12]. Here, the conduction band is pinned 160 meV below the surface [Aff01, Smi89]. The electron density and the lowest wavefunctions are

[6] Very few publications can be found claiming longer elastic lengths up to 500 nm [Kre10].



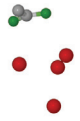

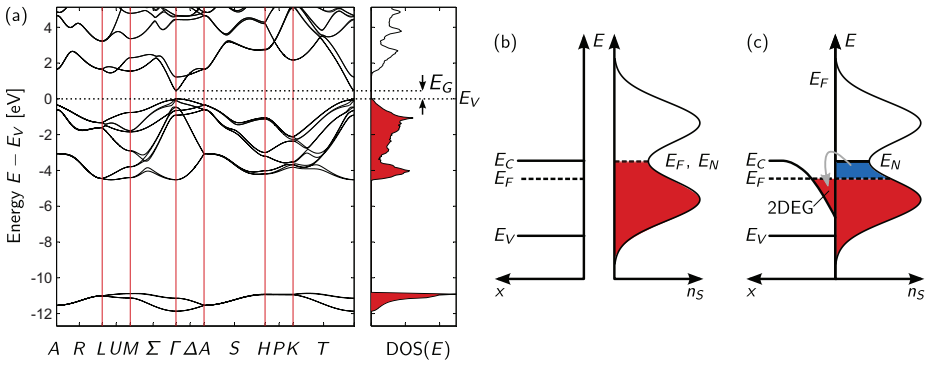


**Figure II.9:** (a) Band structure and resulting density of states (DOS) of wurtzite InAs. The calculation has been performed in a framework using transferable empirical pseudopotentials and including spin-orbit coupling. Adapted from [De10]. (b+c) Mechanism of Fermi level pinning. (b) Far from the surface, the bulk has a uniform conduction band minimum ($E_C$) and valence band maximum ($E_V$). The Fermi level $E_F$ lies in the bandgap. The surface, which is hypothetically disconnected from the bulk, has a donor- and an acceptor-like density of states ($n_S$) that is filled up to the charge neutrality point $E_N$. (c) If brought into contact, Fermi and charge neutrality level do not necessarily coincide. The donor-like states are then emptied into the conduction band that bends below the Fermi level. Adapted from [Lüt08].

peaked some 10 nm beneath the surface for an undoped nanowire. On the other hand, the conduction band becomes flat and the wavefunctions spread throughout the entire wire when including a dopant density similar to the samples investigated in this work.

This should also be the case for the InAs nanowires invested in this thesis. However, no evidence for a surface accumulation layer has been found in transport experiments [Day09, Blö11] in contrast to similar material systems such as InN [Ric08]. This is attributed to the stacking faults described above, resulting in interfacial electric fields [Day09]. The geometrical considerations (vide supra) are obviously unaffected hereof, and electrical transport is expected to be surface-sensitive regardless of the presence of a surface accumulation layer.

## II.3 Conclusions

The carbon nanotubes and the InAs nanowires are geometrically similar, with a surface-sensitive electrical conduction. Material and environmental effects can therefore be easily intertwined. One way to reduce this risk is the suspended sample design that I will use for my transport experiments.

The fabrication of both nanostructures usually remains a statistical process and individual specimens will in general differ from one another, even if grown in the same process. This is especially the case for chemically functionalized carbon nanotubes, where both

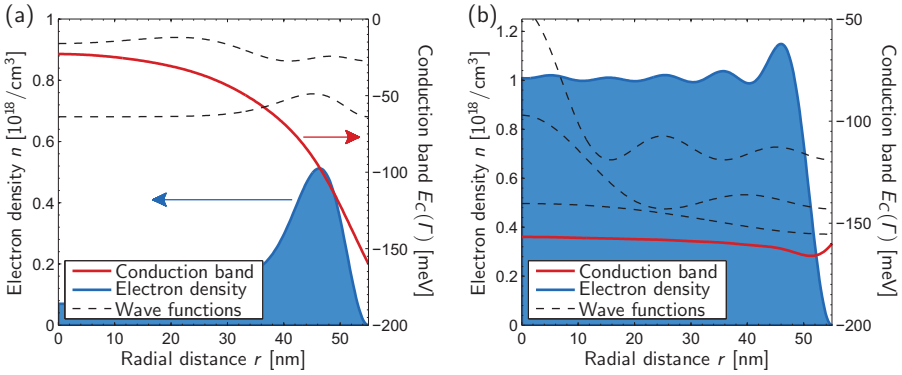


**Figure II.10:** Electron distribution inside InAs nanowires. The electron density is given on the left axis while the minimum of the conduction band (at the $\Gamma$ point) is plotted with the right axis ($E_F := 0$). Calculations are performed with a self-consistent solution of the coupled Schrödinger and Poisson equations [Dem12]. The squares of the lowest wavefunctions in energy are given as black, dashed lines. Their base value corresponds to their energy, the height is an arbitrary unit. Calculations are for an (a) undoped and (b) an $n$-doped wire with $1{\cdot}10^{18}$ cm$^{-3}$ dopant density.

fabrications steps can lead to device-to-device fluctuations. If these modifications cannot be controlled, they should be monitored for an unambiguous interpretation of the experiments. This usually requires various investigation techniques combined on the same nanostructure. I will tackle this issue with a novel sample design developed for this thesis.



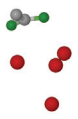

# CHAPTER III

## Metrology and low-temperature transport effects

The measurements presented in the following chapters require some elaborate setups and techniques that shall be introduced in the following. I rely on three methods, namely Raman spectroscopy, transmission electron microscopy, and low-temperature transport. They give complementary information on the investigated nanostructure and will prove to be mandatory for a comprehensive interpretation of the obtained results.

**Resonant Raman spectroscopy** probes the phonon modes and some electronic properties as explained in section III.1 and is therefore related to the structure. It is used to monitor the carbon nanotube's phonons introduced in section II.1.3. I will give an overview on the instrumentation and on the data treatment[1] in the following section III.1.

**High-resolution transmission electron microscopy and spectroscopy** is used for chemical and structural characterization. I will introduce the operation modes important for this thesis and give an overview on the instrumentation in section III.2.

**Low-temperature transport** monitors the interaction of the charge carriers with the atomic lattice and probes the course of individual electrons. I explain several effects in the limit of transparent and opaque contacts, namely universal conductance fluctuations and Coulomb blockade in section III.3. The generation of cryogenic temperatures and the instrumentation are then presented in section III.4.

## III.1 Raman spectroscopy setups

Three Raman setups are used for the characterization of the carbon nanotube specimen, namely two confocal and a Fourier-transform Raman spectrometer that will be introduced in the following.

[1] Additional information can be found in the appendix A.



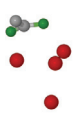

## Confocal Raman spectroscopy

Confocal microscopy greatly reduces the scattering volume of the illuminated sample [Egg67]. Its principle is depicted in Fig. III.1. Light is passed through a pinhole and focused on the region of interest (blue beam). The backscattered light passes a dichromatic mirror and is focused on a second pinhole (green beam). This rejects all photons that were not generated in the (usually diffraction-limited) scattering volume (red beam).

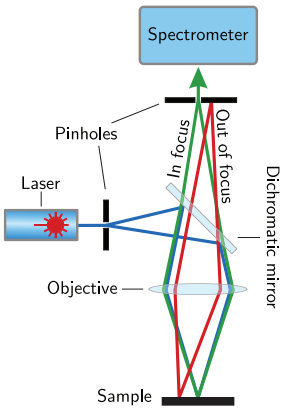


**Figure III.1:** Working principle of a confocal Raman setup. The incoming laser light (blue) passes a pinhole in the focal plane of the objective. The generated Raman light (green) is passed into the spectrometer through a second pinhole. This blocks all radiation from outside the scattering or focal volume (red).

A confocal Raman setup replaces the light source by a laser and analyses the scattered light with a spectrometer after the second pinhole. The spot size, i.e. the investigated volume, is about 1 $\mu$m for all experiments reported in this work. The laser power is kept below 700 $\mu$W to avoid carbon nanotube destruction and heating effects [Fan04]. The measurements presented in section IV.2 on sample $\alpha$, an individual carbon nanotube, were taken in house with a `Horiba Jobin Yvon T64000` at an excitation wavelength $\lambda_L = 487.9864\,\mathrm{nm}$, generated by an $Ar^+$ laser. The spectrometer consists of a triple monochromator and a nitrogen-cooled CCD that provide a spectral resolution of $0.7\,\mathrm{cm}^{-1}$ [Spu10a].

Experiments on the tetramanganese-functionalized carbon nanotubes (samples $\vartheta$) reported in section VII.4 are carried out in collaboration with Asmus Vierck from the group of Prof. Dr. Janina Maultzsch at the TU Berlin. We use a `Horiba Jobin Yvon LabRam HR-800` setup with an exciting laser wavelength $\lambda_L = 632.87\,\mathrm{nm}$ from a He-Ne laser. The spectrometer has a spectral resolution of $2\,\mathrm{cm}^{-1}$ [Goß11a] and it is equipped with a Peltier-cooled CCD. The specimen can be mapped with its motorized sample stage.

The recorded spectra of both setups are calibrated with the lines of a neon lamp, using the `peak-o-mat` software [Kri07]. Spectral information is obtained by its built-in least-squares fitting routine assuming Lorentzian line shapes. This describes my carbon nanotube Raman spectra reasonably well and is also the standard approach in literature [Jor03a, Dre05]. The natural line widths of the lasers are neglected because they are in the order of one per million.

### Fourier-transformed Raman spectroscopy

A `VERTEX 70 FT-IR` spectrometer from `Bruker Optics` is used for the experiments reported in section VII.5. The Nd:YAG laser with $\lambda_L = 1064\,\text{nm}$ illuminates a millimeter-wide area of the sample. It is equipped with a movable mirror in a Michelson interferometer instead of a grating spectrometer. The resulting interferogram is recorded with a nitrogen-cooled CCD and Fourier-transformed using a Blackman-Harris apodization function [Spu10a]. This setup is used for the bulk carbon nanotube specimen (samples $\eta$) presented in chapter VII because it probes a wide area.

## III.2 Transmission electron microscopy

Transmission electron microscopy (TEM) gives the structural and elemental information of thin specimen down to the level of individual atoms by means of an electron probe beam [Kno32, BS12, Gir09], the current information limit lies at 50 pm [Kis08]. Its working principles are sketched in Fig. III.2 and will be introduced in the following subsections. The microscope is operated in ultra-high vacuum conditions ($p < 10^{-8}\,\text{mbar}$) to avoid hydrocarbon deposition and collisions with the residual gas. Electrons are collected with highly sensitive CCDs in bright and dark field positions, each equipped with a scintillator. A more comprehensive introduction can be found in [Wil96, Gro07, Hou07, Len07]

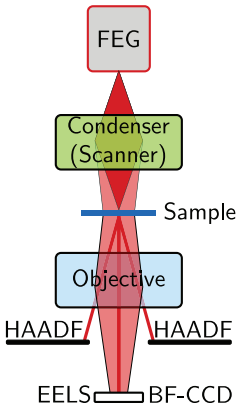


**Figure III.2:** Working principle of a transmission electron microscope. An electron beam is generated in a field emission gun (FEG, gray) and projected by the condenser (green) onto the sample (broad beam). It interacts with the specimen and is focused by the objective lens (blue) onto the bright-field (BF) screen. This can be replaced by an energy-analyzing prism system for electron energy loss spectroscopy and energy-filtered TEM. In STEM mode, the condenser focuses the beam onto a sub-nanometer sized spot that is scanned across the sample. The signal is collected in a high-angle annular dark field detector (HAADF) or the directly transmitted beam is analyzed with EELS.

### Bright-field transmission electron microscopy

The electrons illuminate the area of interest where they interact with the atoms. The microscope is tuned into a regime where energy losses and absorption by the thin specimen can be neglected in high-resolution TEM imaging conditions (HR-TEM). This approach reduces chromatic aberrations, because all projected electrons have the same energy. Car-



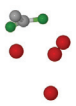

bon nanotubes almost directly fulfill these imaging conditions while the electrons scattered inelastically in the InAs nanowires are actively rejected (vide infra).

A perfectly focused HR-TEM image would not yield any contrast on the viewing plane, i.e. the bright-field CCD, because the elastic scattering events the electrons experience in the specimen only modulate their phase. This phase shift depends on the nuclei Coulomb potential and is thus a spatial function. It is translated into an intensity modulation by an electronic self-interference effect [Len07]. This process is described by the phase contrast transfer function (neglecting spherical aberrations above third order)

$$\mathcal{C}(g) = \epsilon(g)\sin\left[\chi(g)\right], \qquad \text{with } \chi(g) = \frac{\pi}{2}C_S\lambda_e^3 g^4 - \pi\lambda_e Z_f g^2, \tag{III.1}$$

where $g$ is the spatial frequency of the diffracted electrons, $\lambda_e$ the electron wavelength, $C_S$ the spherical aberration, $Z_f$ the defocus, and $\epsilon(g)$ an envelope function. The latter determines the so-called information limit $g_{\max}^{\inf}$ by $\epsilon(g_{\max}^{\inf}) \approx 0$ and depends on $C_S$ and chromatic aberrations. Only spatial frequencies up to, i.e. image details down to, the first sign change of $\chi(g)$ can be monitored which gives the point resolution $g_{\max}^{\text{point}}$. In the so-called Scherzer imaging conditions one tries to push this point as far as possible, resulting in $Z_f = -1.2\sqrt{\lambda_e C_S}$ for optimum point resolution. This was long limited by a lack of diverging electron lenses that could control the spherical aberrations, a detriment that was overcome in 1998 by the introduction of defocusing double-hexapole aberration correctors introduced into the condenser system [Sch36, Sch47, Hai98]. Corrected microscopes can extend the point resolution up to the information limit [Urb09].

The micrographs shown in this work are recorded with bright atom contrast, where a negative spherical aberration is balanced with an overfocus [Thu07].[2] An advanced image treatment is necessary for a quantitative structural analysis as reported for sample $\alpha$ in section IV.2 because the TEM images are a product of complicated interactions of the electrons with the specimen and the TEM lens system [Len06]. The full system is simulated for this purpose and the assumed specimen iteratively refined until measured and simulated image match. This is done using the EMS software [Sta87].

### Dark-field and scanning transmission electron microscopy

The electron beam is focused onto a subnanometer-sized spot and scanned across the sample in scanning transmission electron microscopy (STEM) [Ard38, Hou07]. The scattered electrons are collected with the bright-field CCD[3] or with a high-angle annular dark field detector (HAADF). Only electrons scattered quasi-elastically at high angles[4] are collected by the latter. Such scattering events require a collision with the nuclei and the HAADF intensity $I_H$ depends on the atomic number $Z$. The mechanisms dominant in the carbon nanotube samples are Rutherford scattering with $I_H \sim Z^2$ and inelastic thermal diffusive scattering. Heavier atoms appear thus brighter in the HAADF-STEM images.

[2] So-called negative spherical imaging conditions.

[3] The carbon nanotube specimen are thin enough that TEM and STEM bright field imaging is comparable [Wan95].

[4] High angles in this context are at least three times higher than the semiconvergence angle of the beam, i.e. in the order of $\sim 100\,\text{mrad} \approx 4^\circ$ to the beam axis [Hou07].

### Electron energy loss spectroscopy in the TEM

The techniques described so far rather monitor the specimen structure. It may however also be desirable to learn about its chemical composition. This can be done by analyzing inelastic scattering events in the specimen, what I will use to observe a carbon nanotube tetramanganese functionalization. Electron energy loss spectroscopy (EELS) measures the inelastic interaction of electrons with matter [Hil44]. It exists as two versions, as a low-energetic surface-sensitive investigation tool [Iba82] and as a built-in TEM analysis [Hil44, Ege04]. The beam electrons lose energy by interacting with the specimen electrons, major decay channels are plasmons, spin waves, and ionization. Only core-level excitations are of interest for this thesis because they permit one to monitor the chemical composition of a sample. Even the bonding state of the elements can be analyzed if the fine structure of the core level excitations has a sufficient strength [Ege04]. A magnetic prism, bending the electron beam by 90°, replaces the bright-field CCD to measure the energy loss as illustrated in Fig. III.2. The loss spectrum $I_S$ of a very small scattering volume can be acquired if the microscope is operated in STEM mode. A HAADF-image can obviously be recorded simultaneously.

This procedure measures the energy spectrum to a high precision but drifts inside a real instrument worsen the spatial accuracy. This becomes especially an issue in the functionalized carbon nanotube samples where the thin CNTs themselves easily start to vibrate. A second possibility is thus to operate the instrument in standard bright-field mode as described in section III.2, with the difference that only electrons of a specific energy loss $\Delta E$ can reach the detector.[5] Setting this filter to $\Delta E = 0$, the so-called zero loss peak, is a convenient way to reduce chromatic aberrations of thicker specimen as the InAs nanowires investigated in chapter V. Alternatively, one can acquire a series of images at different $\Delta E$ around an ionization edge. The pre-edge background intensity, that is known to obey an inverse power law $I_S \sim E^{-a}$, can be fitted and extrapolated for every pixel of this image set. This technique is called energy-filter TEM (EF-TEM) or energy-spectroscopic imaging (ESI) and monitors the structure and the elemental repartition of the specimen simultaneously [Rei95].

### Energy-dispersive X-ray spectroscopy

The energy dispersed by the electron beam drives the sample into an excited state. Low-energy losses (plasmons and thermal diffusive scattering) lead to an increased sample temperature that is dispersed into the surrounding. Core level excitations, on the other hand, result in Auger processes and radiative recombination. While the first are usually not further considered, the latter lead to a characteristic X-ray spectrum that can be analyzed in energy-dispersive X-ray spectroscopy (EDX) for chemical mapping. A spatial resolution of 1 nm can be obtained if the instrument is operated in STEM mode [Gro07]. This is usually worsened by stray electrons and multiple scattering events [Ege04]. This becomes an issue again for my experiments with the tetramanganese-decorated carbon

[5] Technically, the detector is set to a fixed value and the acceleration voltage is modified in the opposite direction.



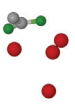

nanotubes where the Mn signal is so small that it has the same size as the one originating from these stray electrons impinging the substrate.

### Instrumentation

The TEM measurements on carbon nanotubes presented in chapters IV, VI (individual carbon nanotube transport devices) and VII (tetramanganese-functionalized carbon nanotube networks) were taken in collaboration with Dr. Lothar Houben from the Ernst Ruska-Center for Microscopy and Spectroscopy with Electrons. Three instruments from `FEI company` have been utilized, depending on the experimental requirements.

- `F20 (S)TEM` from the `Tecnai` series (not aberration-corrected) equipped with an EDX detector having an energy resolution of 136 eV. The acceleration voltage is set to 200 kV (chapter VII).
- `80-300 (S)TEM` from the `Titan` series with an information limit of 1.8 Å at 80 kV acceleration voltage, operated at 80 kV (chapter IV) or 300 kV (chapter VII), respectively. The instrument is equipped with a double-hexapole aberration corrector in the condenser system.
- `60-300 PICO (S)TEM` from the `Titan` series with an information limit of 0.8 Å at 80 kV acceleration voltage, operated at 80 kV (chapters VI and VII). The instrument is equipped with two double-hexapole aberration correctors in the condenser and objective lens systems.

The low acceleration voltages of 80 kV are essential for the microscopy of the individual carbon nanotube transport devices and the long exposure times of the EF-TEM imaging because knock-on damage of C−C bonds in CNTs is found to start at 86 kV [Smi01]. This means that even perfect bonds will break at this energy. Damage is found to occur already at lower energies, starting at pre-existing defects [Spu10a, Kas04]. This low acceleration voltage is accompanied by a loss of resolution. Some experiments on the functionalized carbon nanotube networks, where the tubes are bundled and thus stabilize each other, were therefore conducted at higher acceleration voltages.

TEM measurements on the InAs nanowires, reported in chapter V, are performed in collaboration with Falk Dorn and PD Dr. Thomas E. Weirich from the central facility for electron microscopy of the RWTH Aachen. We use a `FEI F20 TEM` from the `Tecnai` series at an acceleration voltage of 200 kV (not aberration-corrected).

## III.3 Low-temperature transport

Lowering the temperature can lead to classically unexpected electrical transport phenomena like superconductivity [Onn11, Tin75, Sch01], phase-coherent transport [Fow82, Sto85, Lee85], interference effects [Kre10, Cao05], or single-electron tunneling [Cha74, Dek99, Bjö04], depending on the material and experimental conditions. Two of these phenomena are investigated in detail in this thesis, namely the universal conductance fluctuations in

the InAs nanowires in chapter V and Coulomb blockade in carbon nanotubes in chapter VI. Here, I will introduce some important notions and explain the origin of these effects in the following.

### III.3.1 Length scales and transport regimes

Charge carriers can preserve their phase for long time scales up to micro- or even milliseconds at low temperatures. Consequently, larger sections of the sample are phase-coherently probed by the charge carrier. Length scales that quantify the extent and the trajectory of the charge carrier wave function, become accessible by nanotechnological methods. Those relevant for the investigated mesoscopic systems are discussed in this section.

#### Elastic and Fermi length

Only electronic states up to a certain energy are filled in a solid, owing to the Pauli principle and energy minimization. It is called Fermi energy $E_F$ and is given for three dimensions by [Iba09]

$$E_F = \frac{\hbar^2 k_F^2}{2m^*} \tag{III.2a}$$

$$k_F = \sqrt[3]{3\pi^2 n} \tag{III.2b}$$

$$\lambda_F = \frac{2\pi}{k_F} \tag{III.2c}$$

$$v_F = \frac{\hbar k_F}{m^*} \,. \tag{III.2d}$$

Here, $k_F$ is the Fermi wave vector, $\lambda_F$ the Fermi wavelength, $v_F$ the Fermi velocity, $m^*$ the effective mass and $n$ the charge carrier concentration. Only charge carriers within a narrow range around the Fermi energy, $\pm 4k_BT$ around $E_F$, contribute to the electrical transport [Fer26, Sch04, Iba09, Zan99]. They are thus well described by the above quantities. The Fermi wavelength can be considered as the extent of the charge carrier wave function and determines the dimensionality of the transport [Iba09].

Charge carriers traveling through a solid will eventually experience scattering events. These can be divided in two kinds, elastic and inelastic, depending on whether energy and phase information are preserved or not. The physical quantities in this context are lifetimes $\tau$, namely the elastic and inelastic times $\tau_e$ and $\tau_\varphi$. The elastic scattering length $l_e$ is consequently given by

$$l_e = v_F \tau_e = \frac{\hbar \sigma k_F}{n e^2} \,. \tag{III.3}$$

Here, $\sigma$ denotes the conductivity.

#### Ballistic and diffusive transport

The charge carriers traverse the solid in a straight line if the specimen is much smaller than the elastic scattering length, $L \ll l_e$. This transport regime is called ballistic and depicted



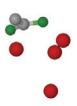

in Fig. III.3(a). Micrometer-long carbon nanotubes often conduct in or at least close to this regime because the bandstructure prohibits many scattering events [Whi98, Kon01, Bie08]. Especially in metallic CNTs long-range, small angle scattering is forbidden because the final state would lie in another valley of the bandstructure (cf. section II.1.1).

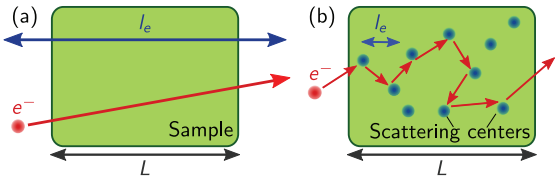


**Figure III.3:** Transport in the (a) ballistic and (b) diffusive regime. (a) The elastic mean free path $l_e$ is much longer than the sample length $L$. (b) Scattering centers like defects or charged impurities force the electron on a diffusive trajectory.

Such a one-dimensional, phase-coherent conductor can be modeled by the Landauer-Büttiker formalism [Lan57, Lan87, Büt85, Büt86]. Electron reservoirs at chemical potential $\mu_i$ are connected through the sample with a reflection and a transmission probability $\mathcal{R}_{ii}$ and $\mathcal{T}_{ij,mn}$, respectively. Here, $i \neq j$ denote the reservoir and $m, n$ the channel number. The current from reservoir $i$ into the sample is then given by

$$I_i = \frac{e}{h}\left[(1-\mathcal{R}_{ii})\mu_i - \sum_{j\neq i}\mathcal{T}_{ij}\mu_j\right] \qquad \text{with} \quad \mathcal{T}_{ij} = \sum_{mn}\mathcal{T}_{ij,mn}\ . \tag{III.4}$$

$N_i$ gives the number of available transport channels from reservoir $i$ into the sample. For ideal contacts, i.e. $\mathcal{R}_{ii} = 0$ and $\mathcal{T}_{ij,mn} = 1$ even an ideal transport channel still has a finite conductance

$$G = N_i G_0 \qquad \text{with} \qquad G_0 = e^2/h = 1/(25.8\,\mathrm{k\Omega})\ , \tag{III.5}$$

that can be understood as a contact resistance. It is $N_i = 2$ in the spin-degenerate case. An ideally contacted, defect-free metallic single-walled carbon nanotube can exhibit a conductance $G = 4e^2/h = 1/(6.5\,\mathrm{k\Omega})$ because CNTs have an additional valley degeneracy (cf. section II.1.1), i.e. two spin-degenerate transport channels. This has been shown experimentally by electrical transport measurements [Kon01].

If the elastic mean free path becomes, on the other hand, much shorter than the sample length, $l_e \ll L$, the charge carrier traverses the specimen diffusively (cf. Fig. III.3(b)). This can be quantified by the diffusion constant [Iba09]

$$\mathcal{D} = \frac{1}{d}v_F^2\tau_e = \frac{1}{d}v_F l_e\ . \tag{III.6}$$

Here, $d$ denotes the dimensionality of the transport. The diffusion constant connects the spread of a charge carrier wave function to a time difference. This relationship is given by

$$\Delta l = \sqrt{\mathcal{D}\Delta t}\ . \tag{III.7}$$

The diffusive transport regime dominates in the investigated InAs nanowires [Wir11]. It can also be modeled by the Landauer-Büttiker formalism because the elastic scattering events that force the charge carrier on its diffusive trajectory conserve its phase. Each of these trajectories corresponds to a transport channel with a conductance quantum $G_0$ [Bee91a, Bee04].

### Phase-coherence and thermal length

Phase coherence is an mandatory ingredient e.g. for quantum computation and most phenomena discussed in this chapter. It is therefore important to study when it gets lost to understand and potentially govern the responsible mechanisms. This will be a leading question in my experiments on the InAs nanowires for which I will introduce some important length scales and effects in the following two sections.

Only energy-conserving events were considered in the above description of diffusive and ballistic transport. The phase of the electron wave is preserved in this case.[6] On the other hand, there are also phase-breaking scatterers that are quantified by the time $\tau_\varphi$ between two such events and the resulting phase-coherence length $l_\varphi$. This quantity considers the coherence of both the spin and the wave function.

The major phase-breaking event is small-angle electron-electron scattering ($ee$) for both carbon nanotubes and InAs nanowires at low temperatures [Liu01, Lin02]. The electrons in the system form a time-dependent background potential that leads to a decoherence of the charge carrier in this so-called Nyquist mechanism [Nyq28, Al'82]. Other, less important mechanisms are large-angle electron-electron ($EE$) and electron-phonon scattering ($e$-ph). A temperature-dependence of the Nyquist mechanism as

$$\tau_{ee,3d} \sim T^{-3/2} \quad \Rightarrow \quad l_\varphi \sim T^{-3/4} \tag{III.8a}$$

$$\tau_{ee,2d} \sim T^{-1} \quad \Rightarrow \quad l_\varphi \sim T^{-1/2} \tag{III.8b}$$

$$\tau_{ee,1d} \sim T^{-2/3} \quad \Rightarrow \quad l_\varphi \sim T^{-1/3} \tag{III.8c}$$

in three, two and one dimension are predicted and measured [Al'82, Lin02, Liu01]. The phase-coherence length dependencies are given for diffusive transport and calculated via eq. (III.7).[7]

The phase-coherence is also affected by thermal smearing apart from the scattering events described above. Due to the uncertainty principle $\Delta E \Delta t \gtrsim \hbar$, charge carriers in similar transport states cannot be discerned. Transport in a solid takes place within an energy window $\Delta E = k_B T$ and with eq. (III.7) the phase-coherence in diffusive transport is lost after a thermal length

$$l_T = \sqrt{\frac{\hbar \mathcal{D}}{k_B T}} \, . \tag{III.9}$$

## III.3.2 Universal conductance fluctuations

In the early 1980s, several groups observed aperiodic, reproducible conductance fluctuations in low-temperature magnetotransport measurements of degenerate semiconductors [Fow82] and disordered metals [Umb84] shown in Fig. III.4. These were called universal conductance fluctuations (UCFs) and attributed to electronic self-interference effects [Sto85, Lee85, Al'85]. They can be observed in various diffusive, mesoscopic systems,

[6] Disregarding spin-flip processes that are energy-conserving yet phase-breaking.
[7] The phase-coherence length scales like the dephasing time in the ballistic case.



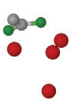

including nanowires and dirty multiwalled carbon nanotubes at low temperatures [Was86, EH10, Lan96]. They can also be measured as a function of gate voltage in semiconducting systems. The subsequent discussion follows [Bee04, Bee91a].

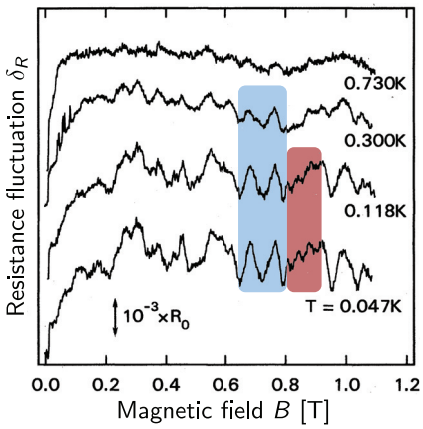


**Figure III.4:** First UCF measurements from Umbach *et al.* [Umb84] on a Au ring at various temperatures. Note that not the conductance but the resistance fluctuations $\delta_R$ are given in units of $R_0 = R(B = 0) = 7.7\,\Omega$. The blue and red areas mark fluctuations of low and high frequency. The low-frequent component is sustained for higher temperatures because it requires a shorter phase-coherence length than the high-frequent component.

A charge carrier traversing a diffusive conductor can take several pathways like a photon passing a double slit. Analogously, the charge carrier interferes with itself reproducibly at a later point if the distance traveled is smaller than the phase-coherence length. This interference can be constructive (cf. Fig. III.5(a)) or destructive (cf. Fig. III.5(b)), resulting in a high or low conductance, respectively. The interference can be tuned inter alia by a magnetic field modifying the relative length of the two paths. The interference then changes periodically from constructive to destructive with a period of one flux quantum $\Phi_0 = h/e$. The analogue in the optical double slit experiment is the horizontal distance from the beam axis. Another quantity that changes the relative phase is the gate voltage tuning the carrier concentration and thus the Fermi wavelength (cf. equation (III.2c)). I will only discuss the magnetic field in the following because this is the case relevant for this work.

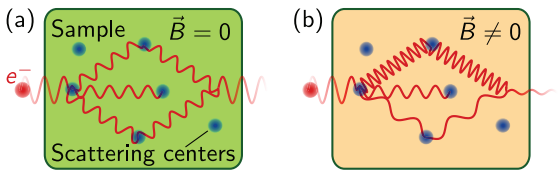


**Figure III.5:** An electron traversing a solid explores several pathways and interferes with itself. (a) Constructive interference, i.e. high conductance. (b) Destructive interference, i.e. low conductance, after changing the relative phase of the two trajectories by a perpendicular magnetic field $\vec{B}$.

In a real diffusive, mesoscopic solid, there are many such self-interfering trajectories. They can be modeled as transport channels in the Landauer-Büttiker formalism (vide supra) because they are phase-coherent [Bee91a, Bee04]. They all enclose a different area

and thus magnetic flux $\Phi$ as shown in Fig. III.6. The overall conductance then changes aperiodically upon changing the magnetic field perpendicular to the sample plane. These are the universal conductance fluctuations

$$\delta_G = \delta_G(B) := G(B) - \langle G(B) \rangle_B \,. \tag{III.10}$$

Here, $\langle \ldots \rangle_B$ denotes the average over the magnetic field. The actual pattern depends on the particular scattering center distribution in the specimen and is like a fingerprint of the device.

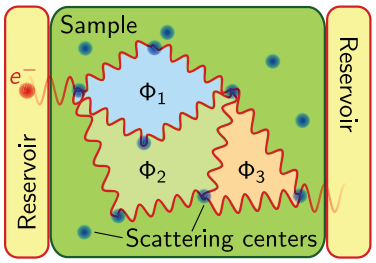


**Figure III.6:** On the origin of the universal conductance fluctuations. Each sub-path encloses a different flux $\Phi$ at a given perpendicular magnetic field $\vec{B}$ and therefore a different change in conductance.

The resulting conductance fluctuations are named universal because the root-mean square of the amplitude obeys

$$\sigma_{\delta_G} = \mathrm{rms}(\delta_G) = \sqrt{\langle (G - \langle G \rangle)^2 \rangle} \approx G_0 = e^2/h \tag{III.11}$$

for all samples, provided $l_T, l_\varphi > L$. The exact magnitude depends on the sample geometry and material [Lee85]. For example, $\sigma_{\delta_G} = 0.73\, G_0$ can be assumed for weak spin-orbit coupling. The possible electron trajectories need to be classified with Feynman diagrams for a rigorous theoretical description [Lee85, Lee86]. Then, also correlations of the various transport channels like common scattering sites have to be taken into account.

### Temperature dependence of the universal conductance fluctuations

The charge carrier must not lose its phase on the self-interference trajectories discussed above. Otherwise, the interference is random and only an average conductance is measured for all magnetic fields. Thus, more and more loops cannot contribute to the UCF pattern anymore upon increasing the temperature, starting with the one enclosing the largest area. This leads to a decrease of the UCF amplitude and maximum frequency with respect to the magnetic field. This is highlighted by the two rectangles in Fig. III.4. The blue one marks a region of low-frequency fluctuations while the red one highlight field values with a faster modulation that vanish already at a lower temperature.

Several regimes for the decay of the UCF amplitude $\sigma_{\delta_G}$ can be identified [Lee85, Bee91a, Bee04]. The below description is derived for channels in a planar, two-dimensional electron gas. However, it has been shown to hold also for the cylindrical material systems used in this work [Lan96, EH10, Yan12].



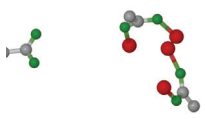

**$l_\varphi \ll L, l_T$** This situation is depicted in Fig. III.7. The sample breaks into $N_\varphi = L/l_\varphi$ phase-coherent sections connected in series, each with a UCF amplitude $\sigma_{\delta_G} = e^2/h$. Because thermal averaging does not take place, the temperature dependence can be derived from stochastic laws

$$\sigma_{\delta_G} = \sqrt{6}\frac{e^2}{h}\left(\frac{l_\varphi}{L}\right)^{3/2}. \tag{III.12}$$

**$l_T \ll l_\varphi < L$** Phase-breaking scattering and thermal averaging occurs in the sample. In each of the $N_\varphi$ sections there are now $N_T = (l_\varphi/l_T)^2$ uncorrelated transport channels, leading to a temperature dependence of

$$\sigma_{\delta_G} = \beta\frac{e^2}{h}\frac{l_T}{l_\varphi}\left(\frac{l_\varphi}{L}\right)^{3/2} = \beta\frac{e^2}{h}\frac{l_T}{L}\sqrt{\frac{l_\varphi}{L}}, \tag{III.13}$$

with $\beta = \sqrt{8\pi/3}$. It is like $N_T$ of the above described systems with $l_\varphi \ll L, l_T$ connected in parallel.

**$l_\varphi \approx l_T < L$** The intermediate case of the above regimes (III.12) and (III.13) can be interpolated [Bee88]:

$$\sigma_{\delta_G} = \sqrt{6}\frac{e^2}{h}\left(\frac{l_\varphi}{L}\right)^{3/2}\left[1+\frac{9}{2\pi}\left(\frac{l_\varphi}{l_T}\right)^2\right]^{-1/2}. \tag{III.14}$$

**$l_T < L < l_\varphi$** Thermal averaging leads to $N_T' = (L/l_T)^2$ uncorrelated transport channels although there are no phase-breaking scattering events in the wire. The UCF amplitude then decays like

$$\sigma_{\delta_G} = \frac{e^2}{h}\frac{1}{\sqrt{N_T'}} = \frac{e^2}{h}\frac{L}{l_T} \sim T^{-1/2}. \tag{III.15}$$

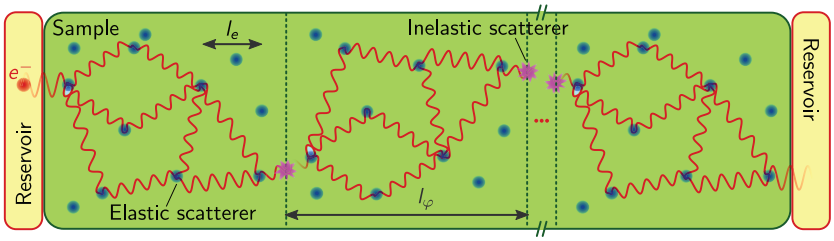


**Figure III.7:** In the transport regime where $l_\varphi \ll L, l_T$, the sample breaks into several smaller, phase-coherent sections connected in series. The resulting UCF amplitude is reduced.

Thus, the temperature dependence of the UCFs can identify the transport regime of the system.

### The correlation field

The maximum UCF frequency (cf. Fig. III.4) in the magnetic field is a measure for the largest enclosed areas [Fri09a, Fri09b] and the phase-coherence length [Sto85, Bee88, Bee91a, Bee04].[8]

The measurable quantity is the correlation field $B_C$, defined via the autocorrelation function $f(\Delta B)$

$$f(\Delta B) = \langle \delta_G(B + \Delta B)\delta(B)\rangle_B \rightarrow f(B_C) := \frac{1}{2}f(0). \tag{III.16}$$

The largest possible enclosed area is given by the outer dimensions of the sample, or, at higher temperatures when $D < l_\varphi < L$, by $A_\varphi = Dl_\varphi$ with $D$ and $L$ being diameter and length of the nanowire. The correlation field is a measure for the field needed to add another flux quantum into this area and thus

$$B_C = \gamma\frac{\Phi_0}{A_\varphi} = \gamma\frac{h}{eDl_\varphi} \Rightarrow l_\varphi = \gamma\frac{h}{eDB_C} = \gamma\frac{\Phi_0}{DB_C}. \tag{III.17}$$

The proportionality constant $\gamma$ is predicted to be between 0.42 and 0.95 for $l_T \gg l_\varphi$ and $l_T \ll l_\varphi$, respectively [Bee88].

### Measuring universal conductance fluctuations

All magnetoresistance curves of the InAs nanowires shown in this work are measured using a standard quasi-static lock-in technique with an ac current bias. The measured quantity is the resistance, not the conductance.[9] Any contact resistances need to be subtracted to obtain the latter.

The conductance obtained from the resistance is composed of a slowly varying background and the UCFs. The former is estimated using a third-order polynomial fit[10] and subtracted from the data. A nice illustration can be found in [Fri09a].

The correlation field is in turn determined from the UCFs by interpolating the autocorrelation function $f_B$ and determining its half maximum. This is again illustrated in [Fri09a].

## III.3.3 Single electron transport and Coulomb blockade

Samples featuring universal conductance fluctuations usually have rather transparent contacts. When these contacts are designed to be more opaque, i.e. when they form tunnel barriers, the charge carriers on the sample become confined and behave like particles in a box. Following basic quantum mechanics, charge and orbital degree of freedom become

[8] In the InAs nanowires, flux-cancellation effects have to be taken into account as discussed in section V.4.
[9] Technically, it is the differential resistance $\mathrm{d}R = \partial V_B/\partial I|_{V_B=0}$ around zero bias, see section III.3.3.
[10] This specific fit is phenomenologically derived and found to describe the background accurately without distorting the UCFs.



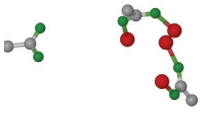

quantized, i.e. one charge carrier at a time is trapped in the specimen. These systems are straightforwardly called single electron transistors or quantum dots.[11]

They have been investigated extensively in the past decades because they probe single electrons and their interaction with the environment using a mesoscopic system [Hou05, Kou01]. They are also model systems for quantum computing [Los98]. Quantum dots can be studied in many material classes, they were first characterized in semiconductor heterostructures [Cha74, Joh92, Tar96, Ash96], metallic nanoparticles [Lam69, Pet01] and thin films [Itt47, Lam50, Gor51]. More recently, progress in nanotechnology made more systems accessible, inter alia nanowires [Bjö04, Sch10], superconductors [Ral95, Fra10], single molecules [Ree97, Par02] and various carbon materials like graphene, fullerenes and CNTs [Par00, Dek99, Pon08, Sta08]. The basic structure in all these experiments is field-effect transistor like as depicted in Fig. III.8, i.e. with a source and a drain electrode connecting the structure via tunnel barriers and a third gate electrode shifting the electronic levels.

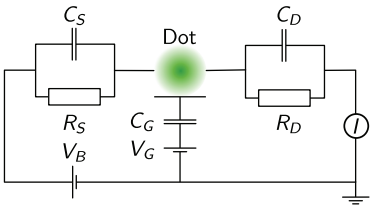


**Figure III.8:** Equivalent circuit diagram of a quantum dot. Source (S) and drain (D) leads are connected via tunnel barriers, represented by a capacitance $C_{S,D}$ and a resistance $R_{S,D}$. The gate electrode is coupled only capacitively. The current $I$ is measured in function of the source-drain $V_{SD}$ and the gate $V_G$ voltages.

Two prerequisites have to be fulfilled in order to observe the typical quantum dot behaviour introduced in the following. First, the charging energy $E_C$ that measures the Coulomb energy to add an extra electron has to be sufficiently large with respect to the thermal energy in order to have a defined, finite number of electrons

$$E_C := e^2/C \gg k_B T. \tag{III.18}$$

Here, $C$ denotes the capacitance of the system. Second, the charge carrier is meant to stay on one energy level defined by the spatial confinement of the quantum dot. These should thus have a much smaller spacing than the charging energy, $\Delta E \ll E_C$. Using the uncertainty relation $\Delta E \Delta t \gtrsim \hbar$ and the typical time constant of a capacitance $\Delta t = RC$, one obtains the requirement for the tunnel resistance

$$R \gg \hbar/e^2 \approx h/e^2 = 1/G_0. \tag{III.19}$$

[11] The term 'quantum dot' is shared among two scientific communities, depending on the energy scale. This thesis exclusively deals with electrically detected, mesoscopic quantum dots, instead of self-assembled, nanometer-sized particles or inclusions that are addressed and read out optically [Eki81, Mur00]

### The constant interaction model

A simple yet powerful way to describe transport through a quantum dot is the so-called constant interaction model [Bee91b, Ave91, Kou01]. The description here largely follows [Han07]. It makes two simplifications:.

1. All Coulomb interactions between the charge carriers are parametrized by a single capacitance $C_\Sigma := C_S + C_D + C_G$, where the summands denote the source, drain, and gate capacitances (see Fig. III.8).

2. The discrete, single-particle energy spectrum is independent from the number of charge carriers on the dot. This means that the electrons only interact via Coulomb repulsion and the Pauli exclusion principle.

The total ground state energy of the $N$-electron system, $\phi(N)$, is then given by the sum of the single particle level energies and the charging of the quantum dot capacitance

$$\phi(N) = \frac{1}{2C}\left(-|e|(N-N_0) + \sum_{S,D,G} C_i V_i\right)^2 + \sum_{i=1}^{N} E_i \ . \tag{III.20}$$

Here, $N_0$ denotes the number of electrons that is needed to compensate the positive background charge induced from the atomic lattice with $N_0 = 0$ for $V_G = 0$. The voltages $V_i$ can obviously be tuned experimentally to drive through its energy spectrum. The single-particle energies $E_i$ depend on the geometry, the material, and the environment like the magnetic field.

The electrochemical potential $\mu_N$ denotes the energetic difference between the $N$ and the $N-1$ electron system. It is defined as

$$\mu_N := \phi(N) - \phi(N-1) = \left(N - N_0 - \frac{1}{2}\right) E_C - \frac{E_C}{|e|} \sum_{S,D,G} C_i V_i + E_N \ . \tag{III.21}$$

The notation is the same as in eq. (III.20), $E_N$ is the highest single-particle level. In contrast to the ground state energy, $\mu_N$ depends linearly on the electron number. If the capacitances are assumed independent of the quantum dot state and $C_S, C_D \ll C_G$, the gate voltage is capable to rigidly shift the entire set of available states in energy. A current $I$ can only flow through the dot if one of these states lies in the bias window, i.e. between the source and drain potentials $\mu_{S,D}$:

$$\begin{array}{lcl} I > 0 & \Leftrightarrow & \mu_S \geq \mu_N \geq \mu_D \\ I < 0 & \Leftrightarrow & \mu_S \leq \mu_N \leq \mu_D \\ I = 0 & \Leftrightarrow & \text{otherwise.} \end{array} \tag{III.22}$$

The magnitude of the current depends on the tunnel rates $\Gamma_{S,D}(N)$ through the barriers. They are in principle different for the various states and for the two contacts.



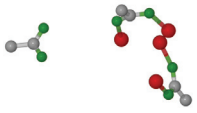

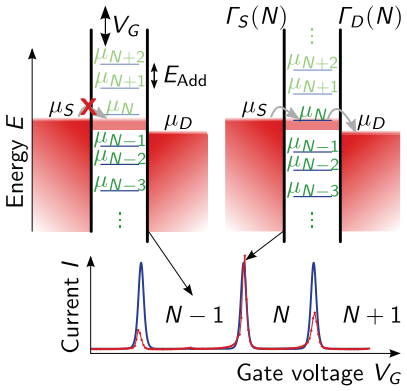


**Figure III.9:** On the origin of Coulomb oscillations, visualizing eq. (III.22). Current can only flow between source (S) and drain (D) if one of the dot chemical potentials, $\mu_N$, is inside the bias window (fainted red) defined by the source and drain potentials $\mu_{S,D}$. Otherwise, the number of charge carriers on the dot is fixed. The dot level position can be tuned by the gate voltage $V_G$. The Coulomb peak height is determined by the tunnel rates $\Gamma_{S,D}$. Overlain in red is a real measurement on a CNT quantum dot where the individual levels have different tunnel rates, i.e. peak heights. The finite peak width results from $V_B, T > 0$ and $\Gamma_{S,D} < \infty$.

This is summarized in Fig. III.9. The number of electrons on the dot is fixed in the so-called Coulomb blockade regions (left) and fluctuates between two values on the Coulomb peaks (right). The distance between two such peaks is called addition energy

$$E_{\mathrm{Add}} := \mu_{N+1} - \mu_N = E_N - E_{N-1} =: E_C + \Delta E \ . \tag{III.23}$$

This term is dominated by the charging energy. $\Delta E$ denotes the level spacing that depends in general on the electron number on the dot. The analogue is the filling of energy levels in an atom. Quantum dots are hence sometimes called artificial atoms [Kou01].

### The stability diagram

The phenomena discussed so far are called linear transport regime because the bias window is so small that it can contain only one energy level at the most. Several quantum dot states can eventually contribute to the transport upon increasing the bias voltage $V_B = \mu_S - \mu_D$. This will in turn stepwise increase the measured current as demonstrated in Fig. III.10. The phenomenon is consequently called Coulomb staircase.

Combining Figs. III.9 and III.10, i.e. modifying both gate and bias voltage, one obtains the so-called stability diagram as shown in Fig. III.11. The regions of Coulomb blockade where the number of charge carriers on the dot is fixed are diamond-shaped and straightforwardly called Coulomb diamonds. The height gives the addition energy $E_{\mathrm{Add}}$ which can be used to convert the gate voltage into an energy with a conversion factor $\alpha_G$, called gate lever arm. The black lines in Fig. III.11 mark the source and drain resonances, i.e. when $\mu_S = \mu_N$ or $\mu_D = \mu_N$. Their slopes represent the source and drain coupling strengths $\alpha_S$ and $\alpha_D$ that are not necessarily equal. It is

$$V_B = \begin{cases} \frac{\alpha_G}{1-\alpha_S} \cdot V_G & \text{source resonance} \\ -\frac{\alpha_G}{\alpha_S} \cdot V_G & \text{drain resonance} \end{cases} \Rightarrow \alpha_G = \frac{\Delta V_B}{\Delta V_G} \ , \tag{III.24}$$

where $\Delta V_B = E_{\mathrm{Add}}$ ($\Delta V_G$) denote the diamond height (full width).

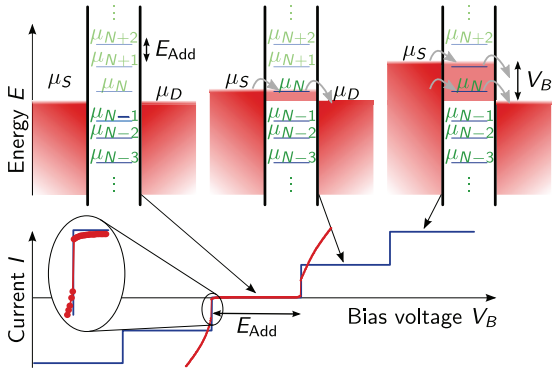


**Figure III.10:** On the origin of the Coulomb staircase. Current can only flow between source (S) and drain (D) if one of the dot chemical potentials, $\mu_N$, is inside the bias window (fainted red) defined by the source and drain potentials $\mu_{S,D}$. Every energy level entering the bias window results in a stepwise increase of the current. The addition energy determines the step width. Overlain in red is a real measurement on a carbon nanotube quantum dot where only first-order tunneling can be observed. The sharp edges of the theoretical curve are for $T = 0$, the real measurement at a finite temperature follows the Fermi-Dirac distribution (cf. inset).

Stability diagrams often do not plot the current $I$ but the differential conductance $\mathrm{d}G := \partial I/\partial V_B$. Only conductance changes are visible in this case. This has the advantage to enhance faint structures such as excited states of the single-particle spectrum. These always belong to a particular $N$-electron ground state discussed so far. When both ground and excited state are within the bias window, the charge carriers have both pathways accessible for transport, but still only one of them can traverse the dot at a time. The conductance is enhanced nevertheless because the number of available states on the dot has increased. The corresponding step in the Coulomb staircase develops additional small substeps appearing as lines parallel to the diamond edges as summarized in Fig. III.12.

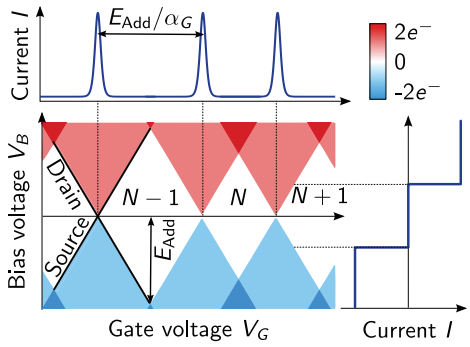


**Figure III.11:** A stability diagram is obtained by varying both, bias and gate voltage and monitoring the current through the quantum dot. Transport is blocked inside the white diamonds where the charge carrier number on the dot is fixed. One resp. two at a time can tunnel in the coloured regions. Positively (negatively) sloped diamond edges have the respective chemical potential $\mu_N$ aligned with $\mu_S$ ($\mu_D$). From the slope of these resonances (depicted in black), the lever arm $\alpha_G$ and the coupling to source and drain can be determined.



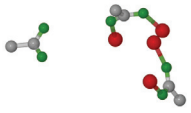

The energy of the excited state can be extracted directly from its starting point at the diamond edge. A stability diagram is thus sufficient to fully characterize a quantum dot since its complete energy spectrum and its capacitive coupling to the environment can be extracted.

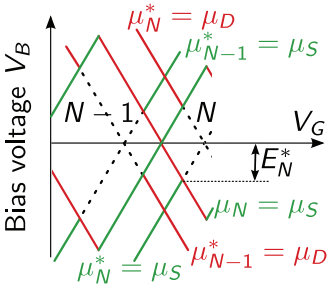


**Figure III.12:** Excited states in a stability diagram. They manifest as lines running parallel to the diamond edge when their chemical potential $\mu_N^*$ is aligned with the one of source (green) resp. drain (red). The starting point at the diamond edge gives the excited state energy $E_N^* = \mu_N^* - \mu_N$.

### Carbon nanotube quantum dots

Quantum dots in carbon nanotubes have been studied extensively since the first measurements on individual [Tan97] and bundled [Boc97] CNTs in the late 1990s. These experiments are often performed on single-walled carbon nanotubes (SWCNT) and reflect the material properties introduced in section II.1, notably the four-fold degeneracy of the bandstructure as explained in Fig. III.13(a). The contacts impose a quantization on the wave vector $\vec{k_\parallel}$ along the axis and the nanotube becomes zero-dimensional. Consequently, a quantum dot is formed with energy levels separated by

$$\Delta = \frac{h v_F}{2L} \approx \frac{1.7\,\mathrm{meV}}{L[\mu\mathrm{m}]}, \tag{III.25}$$

as can be obtained from a particle-in-a-box argument [Tan97]. Here, $v_F$ denotes the Fermi velocity. Furthermore, one often observes a lifting of the degeneracy between the two subbands that originate from the two inequivalent $K$ points, resulting in a finite offset $\delta$ [Sap05]. This four-fold shell filling sequence reflects into a periodicity of the Coulomb diamond pattern from which these parameters can be extracted along with the spin-spin interaction.

These SWCNT quantum dots have been studied and understood in detail. I will therefore study more complicated carbon nanotube structures like bundles and multiwalled CNTs. In the following, I will briefly sketch how the above mentioned properties are expected to evolve into these systems. The four-fold shell filling consequently becomes eight-fold when turning to double-walled carbon nanotubes because the wall index is a good quantum number [Wan08]. So far, this was observed in only two experiments [Moo07, Dat11]. A further increase of the wall number rather leads to diffusive transport, i.e. the appearance of universal conductance fluctuations, or to a return to the four-fold periodicity [Bui02]. This is because not necessarily all CNT walls contribute to the transport. Semiconducting walls are usually non-conductive at the low temperature in these

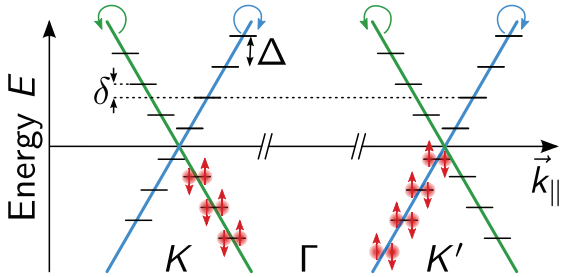


**Figure III.13:** (a) Discrete energy levels are induced on a CNT when it is clamped by tunnel-coupled contacts. They are offset by a length-dependent energy $\Delta$; the two subbands (clock- and counterclockwise propagating electrons) can be offset by $\delta$. Electrons outside the first Brillouin zone are omitted for clarity.

experiments. The different conducting shells also need a sufficient overlap of their wavefunctions to interact [Wan08]. An outer wall could thus shield an inner, better conductive one from the environment [Bui02].

Both the theoretical expectations and experimental findings are therefore ambiguous and it is assumed that the actual behaviour depends on the relative chirality of the shells. Consequently, all above mentioned regimes have been reported in measurements. They have been conducted on sample layouts where the chirality of the carbon nanotube could not be determined, not even the number of walls was definitively known. I will propose a sample design in the next chapter that can possibly overcome this issue and lead to a better comparability between theory and experiment. Based hereupon, I will analyze the room- and low temperature transport characteristics of two triple-walled carbon nanotubes.

This sample design involves a suspension of the transport device. Such quantum dots have in principle two additional advantages over their standard, substrate-bound counterparts. First, they can exhibit very clean transport properties because they are perfectly isolated from a possibly perturbing environment [Ste09a, Cao05, Muo10]. Best performances in this context require the nanotube growth as very last step what drastically limits the choice of contact materials and treatments [Nyg01].

A second advantage is that with this geometry carbon nanotube phonons excited from the transport through the dot [Let09, Sap06, Hüt09, Isl12] or by an external radio frequency radiation [Las09, Ste09b] can be studied. CNT quantum dots usually couple only to longitudinal stretching vibrations; twist, bending and radial breathing modes have a negligible interaction [LeR04, Let09]. The other optically active phonons probed by Raman spectroscopy (see section II.1.3) are too high in energy to be excited by the quantum dot. These vibronic excitations will appear as lines running parallel to the dot edges that are equidistant as predicted for their harmonic potential [CT99].

### Measuring quantum dots

The stability diagrams shown in this work are obtained by sweeping the bias voltage symmetrically around zero[12] for every gate voltage and recording the resulting bias current.

[12] This must not be confused with the bias coupling that is asymmetric as sketched in Fig. III.8. The drain electrode is connected to ground ($V_D \equiv 0$) and the source voltage is swept ($V_S \equiv V_B$).



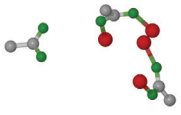

The differential conductance $\mathrm{d}G$ can then be obtained by a numerical derivation. I always use a symmetric approach

$$\mathrm{d}G(V_B = V_0) = \left.\frac{\partial I}{\partial V_B}\right|_{V_0} = \frac{I(V_0 + \Delta V_B) - I(V_0 - \Delta V_B)}{2\Delta V_B} \,, \tag{III.26}$$

where $\Delta V_B$ denotes the sweep step width.

Another possibility to obtain the differential conductance is to modulate the dc bias voltage with a quasistatic ac modulation that is smaller than the dc step width. This leads to an alternating current signal detectable with standard lock-in techniques that can be expanded into a Taylor series

$$I(V_B = V_\mathrm{dc} + V_\mathrm{ac}) = I(V_\mathrm{dc}) + \left.\frac{\partial I}{\partial V_B}\right|_{V_\mathrm{dc}} \cdot V_\mathrm{ac} + \mathcal{O}(V_\mathrm{ac}^2). \tag{III.27}$$

This effectively suppresses noise possibly distorting the dc measurements and can even be used to measure detailed quantum dot properties like spin degeneracies, tunnel barrier asymmetries, and interactions [Rec10].

## III.4 Cryogenics for low-temperature transport experiments

Temperatures close to the absolute zero are needed to observe quantum phenomena (vide supra) because the thermal energy would otherwise smear out all such effects. Three helium cryostats that can operate in the (sub-)Kelvin range, namely a $^4$He flow, a $^3$He cryostat, and a $^3$He/$^4$He dilution refrigerator, are used in this work. Their working principles are explained in detail e.g. in [Hei07] I will therefore only briefly give their specifications and discuss the low-noise electronic setup they are equipped with.

### The utilized cryostats

Electrical transport measurements on carbon nanotube networks reported in chapter VII are performed in a $^4$He flow cryostat that cools with the enthalpy of vaporization of helium. I use a commercial `Oxford Spectrostat` cryostat that provides a temperature range $3.4 \lesssim T \lesssim 300\,\mathrm{K}$ with its helium pump and heater. A normal conducting magnet generates magnetic fields up to 2 T in the sample plane. This cryostat is not connected to the electronic setup described in the following subsection. Instead, transport measurements are performed with a `Keithley 2636` without additional filtering.

The $^3$He cryostat uses the enthalpy of vaporization of the $^3$He isotope and provides temperatures ranging from 300 mK to 30 K. The base temperature can be held for up to two days. I use a top-loading, custom built `Oxford Helios` cryostat that is equipped with a superconducting magnet to generate fields up to 10 T perpendicular to the sample plane. These ingredients, i.e. a temperature range covering two orders of magnitude and the large magnetic fields, are necessary for the phase-coherence measurements via the universal conductance fluctuations in the InAs nanowires described in chapter V.

Even lower temperatures and a continuous operation are needed for the time-consuming (carbon nanotube) quantum dot measurements reported in chapter VI. They can be achieved with a $^3$He/$^4$He dilution refrigerator that cools via the enthalpy of mixing the two isotopes. I use a `Leiden Cryogenics Millikelvin 126-TOF (MNK126-700)` that has a cooling power of 700 $\mu$W at 120 mK and a base temperature of about 25 mK at the mixing chamber resulting in 50 mK at the cold finger where the sample is mounted. It is equipped with a superconducting magnet that can generate fields up to 12 T.

## Electronic setup

The quantum transport measurements reported in chapters V and VI demand low currents and therefore low noise levels. This is achieved by elaborated electronic setups as described in [Goß11a] and shortly introduced in the following.

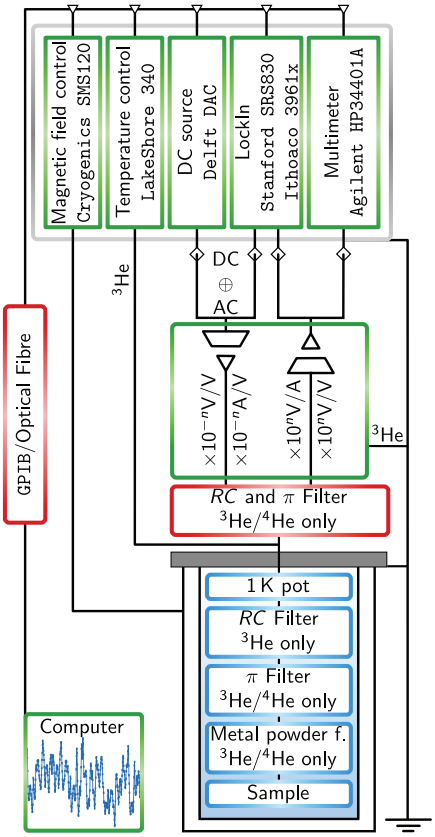


**Figure III.14:** Electronic setup for the quantum transport measurements in the $^3$He and dilution refrigerators. A computer controls the source and readout instruments via the GPIB bus (optical fiber for `Delft DAC` unit). A home (custom from TU Delft) built stage at the $^3$He (dilution) refrigerator decouples the instruments from the sample and converts or (de-)amplifies the signals. The $^3$He cryostat has an *RC* filter stage at 1 K. The dilution refrigerator is instead equipped with *RC* and $\pi$ filters at room temperature and $\pi$ and metal powder filters at the cold finger. The signal lines are thermally anchored at each cooling stage. $^3$He/$^4$He denotes the dilution refrigerator, lines labeled with $^3$He are only connected in the $^3$He setup.



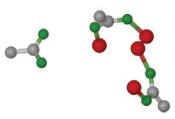

The general idea is to first decouple the input signal, generated by instruments connected to the power grid, galvanically from the sample. This is achieved by isolation amplifiers implemented on battery-driven setups. They also convert the signal amplitude in the range of several volts into smaller voltages or currents. Electron noise of various frequencies is additionally filtered out by several filter stages at room and cryogenic temperatures. This thermal anchoring cools the electrons from ambient to cryogenic temperatures. The thermal equilibrium between the two systems is not perfect, the electron temperature remains a few hundred millikelvin hotter than the above given base or lattice temperatures. The output signal is amplified by several orders of magnitude right outside the cryostat. An isolation amplifier decouples it from the read-out instruments connected to the power grid.

This is summarized in Fig. III.14. The signals are generated by the lock-in amplifiers or by digital-to-analog converters (DACs) built at the TU Delft (`QT-IVVI rack`). The latter are addressed via an optical fiber to decouple the signal additionally from the power grid. Signal conversion, isolation and (de-)amplification is performed in a home ($^3$He cryostat) resp. custom built (`QT-IVVI rack` for the dilution refrigerator) stage. The $RC$-filters cut off at $\geq 30\,\mathrm{Hz}$ in the $^3$He cryostat[13] resp. $1\,\mathrm{kHz}$ in the dilution refrigerator. The $\pi$ filters block in the $10\ldots100\,\mathrm{MHz}$ range, the metal powder (silver epoxy) filters have an attenuation of -50 dBm at 110 MHz.

[13] The exact value depends on the sample resistance.

# CHAPTER IV

## Sample preparation - probing structural and electrical properties

The feature size of information technology devices has shrunk by more than five orders of magnitude in the past decades. This observation, the so-called Moore's law, is currently reaching two physical limits. First, the smallest possible transistor, an atom, is only two orders of magnitude smaller than modern fabrication technology. A corresponding device has been realized recently [Fue12]. Second, today's feature size reaches a limit where smallest deviations of the dopant or defect distribution lead to considerable device-to-device fluctuations that hamper reliability [Lan12]. It is thus vital to understand the influence of small modifications of the crystal structure on electrical transport.

Also in more fundamental nanotechnology research, the control of and knowledge about modifications on the atomic or molecular scale is a key to understand various quantum phenomena. One example for such an intentionally modified structure are carbon nanotube peapods – $C_{60}$ fullerenes (peas) inside carbon nanotubes (pods). Encapsulation is usually shown via transmission electron microscopy (TEM) while the influence on the mutual electronic structure is investigated with quantum transport measurements. With standard sample layouts, only one of these two methods can be applied. Consequently, transport experiments suffer from the ambiguity whether the investigated structure was a filled, a partially filled or an empty CNT. Because of this, the interaction of peas and pods is still under debate [Que02, Utk06, Eli10].

One method to obtain structural and electronic properties at the same time is scanning tunnelling microscopy (STM). It can provide information on the local density of states on an atomic scale and is used to study various nanostructures [Hor02, Fue12, Odo98, Hil08]. It is, though, only sensitive to the surface and demands sample designs incompatible with many other investigation methods. Another technique more sensitive to the bulk is the correlation between Raman spectroscopy and transport experiments [Goß11a, OC05]. Here, the lateral resolution is limited by the wavelength in far-field setups or to some ten nanometers for near-field measurements. In some material systems like carbon nanotubes, the optical modes are highly structure-dependent but results are often ambiguous because, e.g., individual modes can overlap and are then difficult to distinguish.



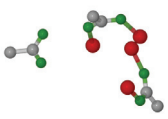

A third, technologically most advanced possibility is the correlation of transmission electron microscopy with (quantum) transport experiments and Raman spectroscopy. These investigation methods offer complementary information on the properties of individual nanostructures. Each technique on its own offers only a limited or ambiguous insight but combined they can comprehensively characterize individual nanostructures. In short, TEM mainly reveals the complete atomic structure down to the identification of individual dopants [BS12]. Quantum transport experiments probe inter alia the electronic states and their dependence on the intra- and intermolecular environment. Raman scattering measures the vibronic properties of solids and individual nanostructures.[1]

Several approaches have been presented to combine these techniques [Muo10, Cos08, All11, Kim05, Obe06] . In this chapter, I will present a sample design that uses a route similar to [Chi05, Wes11]. A prefabricated TEM membrane is patterned and individual nanostructures are selectively grown or placed across the holes. They are subsequently contacted and measured electrically and optically. TEM micrographs are taken as a last step to avoid a premature decomposition due to the electron beam irradiation. Carbon nanotubes and InAs nanowires are the nanostructures investigated in this thesis. In section IV.1, I describe the device fabrication. The comprehensive characterization of an individual triple-walled carbon nanotube demonstrates the application of this sample design in section IV.2. Parts of this chapter have been published in [Fri11], [Flö11a] and [Flö12].

## IV.1 Device fabrication

### IV.1.1 Carbon nanotube growth

There are three major techniques to synthesize carbon nanotubes: arc discharge [Iij91, Ebb92], laser ablation [The96] and (catalytic) chemical vapour deposition (CVD) [Rad52, Bet93, Kon98]. The first two methods produce gram quantities of CNTs and thus most commercially available samples are fabricated in this manner. These nanotubes are usually bundled into ropes containing hundreds of CNTs [The96]. They have to be unbundled by ultrasonication in sodium dodecyl sulfate (SDS) to investigate them on a single-tube level. With a special posttreatment and the use of high-performance liquid chromatography, density gradient ultracentrifugation or DNA decoration it is possible to isolate single chiralities or at least metallicities [Her08, Tu09]. This drastically shortens the CNTs and may leave them decorated with the surfactant.

I choose catalytic CVD growth, following a procedure published elsewhere [Kon98] because the experiments presented here require isolated, high-quality carbon nanotubes. Here, a bimetallic Fe/Mo-catalyst catalytically cracks the precursor gas $CH_4$. Carbon nanotubes grow from the catalyst particles in a vapour-liquid-solid (VLS) process. The molybdenum greatly enhances the efficiency of the actual catalyst Fe by forming an $Fe_2MoO_4$ alloy and suppressing the generation of the catalytically inactive $Fe_2SiO_4$ [Yos09]. The number of nanotube walls can be influenced via the growth temperature [Spu09]. An

[1] These measurement techniques have been introduced in detail in chapter III.

example of an individual, as-grown carbon nanotube with a catalyst particle is given by the atomic force micrograph in Fig. IV.1.

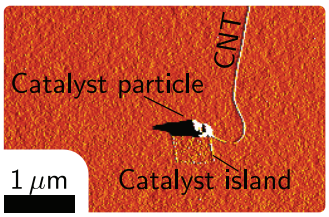


**Figure IV.1:** Atomic force micrograph of an as-grown carbon nanotube on a Si substrate. The active catalyst particle is clearly visible as well as the boundaries of the patterned catalyst island (vide infra).

The quantitative catalyst composition is adjusted according to the desired nanotube density. It consists of a suspension of $Fe(NO_3)_3$, $MoO_2(C_5H_5O_2)_2$ and $Al_2O_3$ (in a ratio of about 4:1:3) in methanol, with the alumina serving as support for the actual catalyst.

The reaction chamber for the CVD process is a tube furnace where the sample is heated in an argon flow[2] of 1.50 l/min. The argon flow is eventually switched off and methane (0.52 l/min) and hydrogen (0.70 l/min) are introduced for 10 min to initiate the growth. The sample is finally cooled down in an argon flow again. A growth temperature of 860°C is chosen which should result in mainly single- and some few-walled CNTs.

### IV.1.2 InAs nanowire growth

InAs nanowires are grown by means of selective-area metalorganic vapour phase epitaxy (SA-MOVPE) [Kum94]. Details of this process are given elsewhere [Aka09, Sla10, Wir11, Sla12]. In short, a GaAs (111)B substrate is spincoated with 30 nm of hydrogen silsesquioxane (HSQ) that is converted to silicon oxide and patterned with a hexagonal hole array with about 500 nm periodicity and 50 nm hole diameter [Aka09].

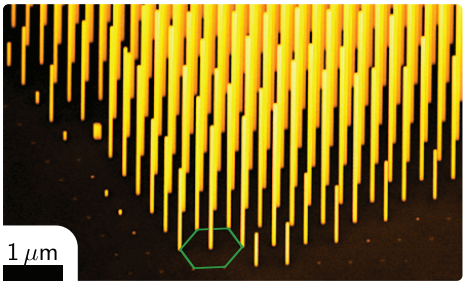


**Figure IV.2:** False-color SEM image of as-grown InAs-nanowires with doping factor 0×. The surface consists of silicon oxide, the nanowires nucleate on hexagonally arranged perforations opening to the underlying GaAs (111)B growth substrate as highlighted by the green hexagon. Image by Sladek adapted from [Wei13].

The precursor gases trimethylindium (TMIn) and arsine ($AsH_3$) are carried in an $N_2$ flow. The As/In ratio is 110, resulting in a growth process limited by the group III precursor TMIn. InAs nanowires selectively nucleate on the bare GaAs substrate at

[2] All flow rates are given at standard conditions.



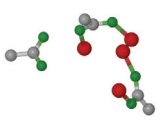

650°C [Aka09] as can be seen in Fig. IV.2. The nanowires can be Si $n$-doped by adding disilane ($Si_2H_6$) to the gas flow. The doping is quantified by a doping factor that gives the partial pressure ratio of dopant and group III precursor gas. A ratio of $p(Si_2H_6)/p(\mathrm{TMIn}) = 7.5{\cdot}10^{-5}$ is defined as unity (1×). Apart from the electrical properties, doping also changes the nanowire morphology with the diameter typically ranging between 80 nm and 120 nm and the length between 2 $\mu$m and 4 $\mu$m. A lower doping generally leads to a higher aspect ratio [Wir11].

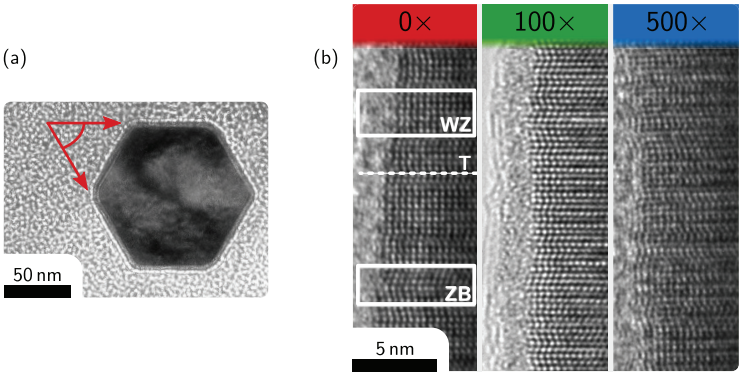


**Figure IV.3:** TEM images of as-grown InAs nanowires. (a) Hexagonal cross section of a nanowire lamella prepared by a focused ion beam. The arrows point to native oxide present on the surface. They draw an angle of 60°. Micrograph by Sladek adapted from [Wei13]. (b) A projection along the nanowire growth direction highlights the crystal phase fluctuations. A wurtzite (WZ) and a zinc blende (ZB) section as well as a twinning boundary (T) are exemplarily marked in the left image. The different doping factors are given on top of each image. Adapted from [Wir11].

The resulting nanowires have a hexagonal shape as shown in Fig. IV.3(a). They are quickly covered by an oxide layer when outside the reaction chamber (cf. Fig. IV.3). The crystal structure fluctuates axially between zinc blende and wurtzite structure as highlighted in Fig. IV.3(b) and introduced in section II.2. The zinc blende segments have additional twinning planes where they inverse their stacking sequence. The amount of wurtzite sections can be tuned by the growth rate but stacking-fault free nanowires have not yet been achieved by this method [Sla12]. Different growth methods like gold-catalysed MOVPE offer perfect crystal arrangements [Joy10] but have other disadvantages like a higher incorporation of impurities [Dic10a, Wir11].

The nanowires are grown in-house by Kamil Sladek from the group of Dr. Hilde Hardtdegen.

### IV.1.3 Nanostructuring of the TEM membranes

I use the well-established technique of electron beam lithography to pattern the TEM membranes. Some standard procedures have to be modified to account for the small size

and fragility of the samples. As a historical remark, the idea of using TEM membranes for lithography is actually rather old, dating from the 1970s [Mol79, Umb84] where it was used to improve feature sizes. Modern, sub-10 nm resolution could be achieved with this technique. It was however not used for TEM analysis and replaced by an improved resist and beam control.

### Electron beam lithography

Structures down to below 10 nm [Vie00, Che93] and samples up to wafer-size can be fabricated using electron beam lithography (e-beam). This is generally reached by covering the sample with an electron-sensitive resist and scanning it with an electron beam [Hei07]. The exposed resist is chemically modified and can be washed away in a developer.[3] The resulting mask is used for a selective metal resp. catalyst deposition or etching.

E-beam lithography has been performed with a `Leica EBPG 5000 Plus` at an acceleration voltage of 50 kV in this work. The electron-sensitive resist is polymethylmethacrylate (PMMA) with a chain length of 600,000 monomers, dissolved in ethyl lactate. The solids content is 7%.[4]

### Workflow

The TEM membranes used in such samples are `DuraSiN DTF-2523` and `DTM-25232` from `Protochips, Inc`. Both consist of a hexagonally shaped, intrinsic silicon frame of 300 $\mu$m thickness, 2.65 mm diameter and a central square opening of $500 \times 500\,\mu\text{m}^2$. Everything is covered with a 200 nm thick sheet of silicon nitride as shown in the cross section in Fig. IV.4(a). These samples have the advantage of being mechanically and chemically robust against the wide temperature range (20 mK... 1300 K) and process solvents used in this work. The `DTF`-series is a plain film in which all observation holes need to be etched manually. This has the advantage of a custom hole pattern but potentially weakens the membrane. The `DTM`-series comes with a mesh of holes already manufactured in the production process. The disadvantage is, on the other hand, a lower accuracy in the e-beam lithography and an electrical leakage through the intrinsic silicon substrate.[5] An illustration of the samples is given in Fig. IV.4.

The general process flow is given in Fig. IV.5. A mild oxygen plasma treatment is mandatory (300 W, 2 min) to ensure resist adhesion. This generally smoothens the surface and converts the silicon nitride to silicon oxide [Use10]. The sample is baked out at 180°C in air for 15 min and spincoated with the `AR-P 669.07` PMMA resist at $7{,}000\,\text{min}^{-1}$ for 35 s. The PMMA solvent evaporates in a 12 min bake-out at 180°C.

The small size of the samples and the presence of holes demands for a rather viscous resist with a high solids content. Therefore, a double-layer resist structure that usually ensures

[3] This is a description for positive resists which are used exclusively in this work. Negative resists behave oppositely.

[4] `AR-P 669.07` from `Allresist GmbH`.

[5] This leakage is in the order of MΩ to GΩ depending on temperature and can be neglected against typical InAs nanowire resistances and metallic or small bandgap CNTs.



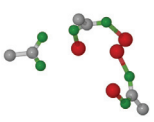

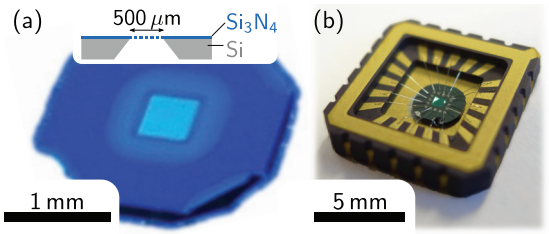


**Figure IV.4:** (a) A DTF-2523 substrate used in this work. The outer, 300 $\mu$m thick silicon frame (dark blue) has a square central opening (light blue) which is covered with a silicon nitride film as shown by the sketched cross section on top. (b) A bonded DTM-25232 mesh.

a pronounced undercut cannot be applied. The large secondary electron cone however produces a sufficient undercut for a reliable lift-off [Hei07, Goß11a]. Since the scattering volume of the membranes is reduced compared to the bulk silicon frame, they need an electron dose twice as high. All structures are developed in AR600-55 from Allresist GmbH for 1 min. Isopropanol alcohol serves as stopper.

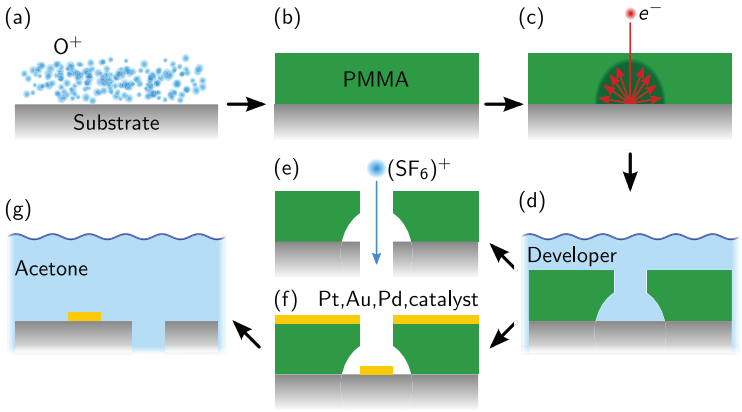


**Figure IV.5:** Workflow summarizing the process steps performed on a membrane. (a) The substrate is exposed to an oxygen plasma. (b) The substrate is spincoated with AR-P 669.07 PMMA resist and (c) the desired structures are exposed to an electron beam. (d) The exposed structures dissolve in the AR600-55 developer and (e) the membrane is etched with a reactive ion beam (RIBE) or (f) metal resp. catalyst is deposited. (g) Finally, the remaining PMMA is dissolved in acetone.

First, a coordinate system needs to be defined for the subsequent process steps. This is either done with positive metal markers (5 nm Ti as sticking layer, 60 nm Pt) on the prefabricated DTM mesh or with negative etched markers for the DTF films (cf. Fig. IV.6). The structures are transferred into the $Si_3N_4$ with an $SF_6$ reactive ion beam etch (RIBE) for $2 \times 3 : 15$ min. The remaining resist is washed away in acetone. The etched samples are additionally cleaned in an oxygen plasma (600 W, 2 h). Nevertheless, some PMMA can remain as will be shown in section IV.2.

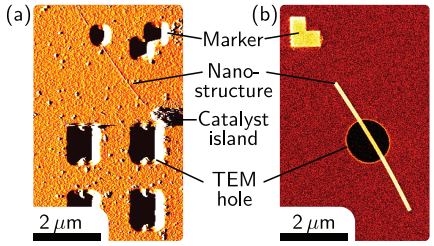


**Figure IV.6:** Nanostructures on a TEM membrane, ready for contacting. (a) AFM image of a custom etched DTF film with catalyst island and as-grown CNT. The negative markers also serve as observation holes. (b) SEM micrograph of a DTM mesh with positive markers and a selectively placed InAs nanowire.

Carbon nanotubes are grown directly on the sample with the CVD process described in section IV.1.1. The catalyst can be deposited selectively as small islands for this purpose. These are tailored as $500 \times 500\,\mathrm{nm}^2$ squares with electron beam lithography. Relatively harsh lift-off conditions need to be applied to avoid a redeposition of the catalyst particles [Goß11a]. The samples are held in hot, stirred acetone (55°C, $380\,\mathrm{min}^{-1}$, 30 s) because the ultrasonic treatment described therein would destroy the membranes. Nevertheless, some catalyst particles adhere to the borders of the holes. An atomic force micrograph of a CNT grown from a catalyst island is shown in Fig. IV.6(a).

The InAs nanowires, on the contrary, need to be transferred from their host substrate onto the membrane. They can be placed precisely across individual holes by means of an indium needle [Flö11a, Flö12]. It is pressed against an as-grown nanowire (cf. Fig. IV.2) using micromanipulators which will result in a rupture at the wire base. Van-der-Waals-forces stick the wire to the tip until it is placed on the membrane (cf. Figs. IV.7 and IV.6(b)). The nanowires need a minimum length of about 2 μm and 20 nm diameter for this transfer process. The placement precision is mainly limited by the optical microscope and is below 1 μm.

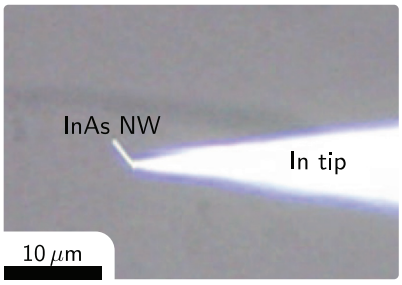


**Figure IV.7:** Optical microscope image of an InAs nanowire attached to an In tip as seen during the transfer process. The nanowire is glued to the tip via Van-der-Waals-forces. Adapted from [Flö11a].

The nanostructures on the membrane need to be imaged relative to the previously defined coordinate system to locate and precisely contact them. Here, scanning electron microscopy (SEM) and atomic force microscopy (AFM) are the two available options. The SEM was either equipped with a cold trap or operated in ultra high vacuum conditions to avoid deposition of amorphous carbon. While the InAs nanowires were exclusively located using an SEM, the carbon nanotubes were imaged using both SEM or AFM. Example micrographs may be found in Fig. IV.6.



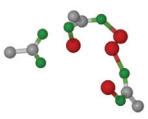

In a final step, contacts are patterned to the nanostructures using again e-beam lithography. Various metals and thicknesses are chosen depending on the targeted measurements. Details for all samples presented in this thesis are listed in table C.3 in the appendix.

## IV.2 Comprehensive characterization of an individual carbon nanotube transport device

I will present a comprehensive characterization of an individual triple-walled carbon nanotube in the following to prove the applicability of the above presented sample design. The atomic structure is measured by high-resolution transmission electron microscopy and is needed to interpret correctly the Raman spectroscopic data that is linked to the electronic structure. This combined dataset agrees with the room temperature electrical resistivity and helps to determine the active transport channel.

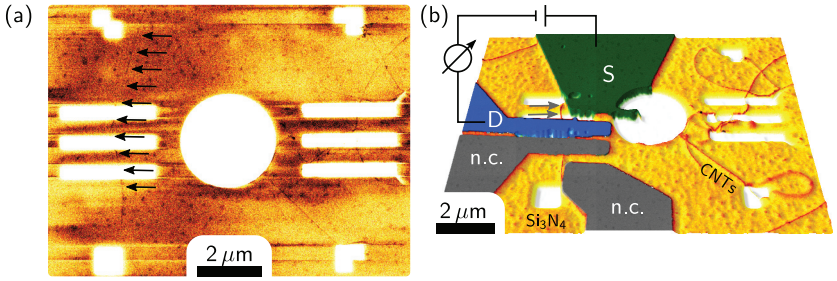


**Figure IV.8:** SEM micrographs of sample $\alpha$, an individual, contacted carbon nanotube. The secondary electron yield is inverted for clarity. (a) As-grown CNTs before contacting. They are only barely visible due to charging effects. The arrows mark the later contacted CNT running across the TEM observation slits. (b) The same structures after contacting. Almost no charges build up during the SEM imaging. The contact configuration is sketched, source (S) and drain (D) are highlighted. The gray contacts (n.c.) are kept floating throughout the measurements. The height profile is extracted from the inverted secondary electron yield and is a guide to the eye.

An individual carbon nanotube marked by the black arrows in Fig. IV.8(a) is processed as described in the first part of this chapter (sample $\alpha$). The resulting transport device is depicted in Fig. IV.8(b). The slightly arched CNT segment between the gold electrodes (black arrows in Fig. IV.8(b)) has a length of 1.44 $\mu$m. Room-temperature transport measurements are carried out in a probe station equipped with a `Keithley 2400` multimeter, Raman spectroscopy was performed in a confocal `Horiba Jobin Yvon T64000` Raman setup at an excitation wavelength $\lambda_L = 487.9864$ nm with $\sim 420\,\mu$W output power to avoid nanotube destruction. High-resolution TEM measurements (HR-TEM) were acquired in a `FEI Titan 80-300` microscope. Images were taken at 80 kV acceleration voltage with a negative spherical aberration $C_S = -52\,\mu$m and an overfocus $Z_f = +17$ nm, resulting in optimized phase contrast with uniform contrast transfer up to the information limit of

about 1.8 Å and negligible residual point spread. Carbon atoms appear bright against the background under these conditions (see section III.2).

The visibility of the carbon nanotubes shown in Fig. IV.8 (a) before and (b) after contacting differs strongly although both images are recorded in the same microscope under identical conditions (5 kV acceleration voltage using a `Zeiss Gemini` column). Additionally, the membrane in Fig. IV.8(a) has a non-homogeneous secondary electron yield before electrode deposition.

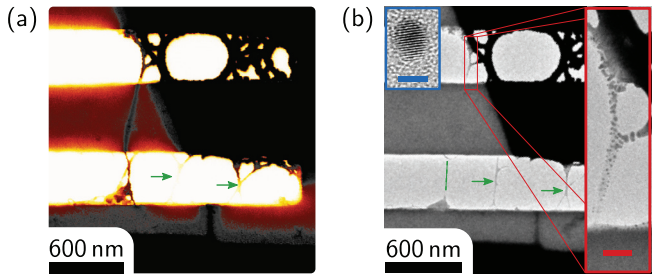


**Figure IV.9:** (a) SEM and (b) TEM micrographs of sample $\alpha$. The arrows point to structures fading out in SEM imaging while clearly bridging the gap in the TEM measurement. In (b), the dashed line indicates the CNT position before destruction. Left and right inset are magnifications of a Au nanoparticle hosted in the amorphous matrix (scale bar 3 nm) and of the upper half of the device (scale bar 50 nm), respectively.

A close-up of the device's electrically active part is given in Fig. IV.9(a). Again, the contacted CNT is clearly visible in the SEM image. There are additional structures bridging the bottom slit that fade out the further they are from the upper contact (cf. arrows in Fig. IV.9(a)). These structures exhibit a homogeneous intensity in the TEM micrograph in Fig. IV.9(b). They consist of an amorphous material that hosts some crystalline nanoparticles. This same substance also covers the upper half of the CNT device as shown in the red (right) inset. An individual nanoparticle from another sample region is displayed in the blue (left) inset. The lattice constant and the contrast identifies it as a gold droplet deposited during contact evaporation. The lower half of the sample is completely embedded in the amorphous material without nanoparticles. The carbon nanotube was destroyed during TEM imaging albeit the low acceleration voltage of 80 kV.

A HR-TEM analysis reveals that the investigated CNT has three walls. It is largely hosted in the amorphous matrix described above and touched by several gold nanoparticles just below the top (source) contact as can be seen in the very right of Fig. IV.10(a+b). The short completely free section can be used to determine the diameter.

Fig. IV.10(c) demonstrates the necessity to calculate nanotube diameters with the refined model as described in section III.2. The maxima of the linescan of the part denoted by arrows in Fig. IV.10(a) should mark the tube walls since the image is taken under bright atom contrast. The real tube diameters marked in red deviate up to 1.5 Å from these maxima. The following analysis of the Raman data with the unrefined diameters would



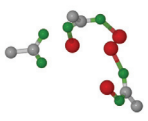

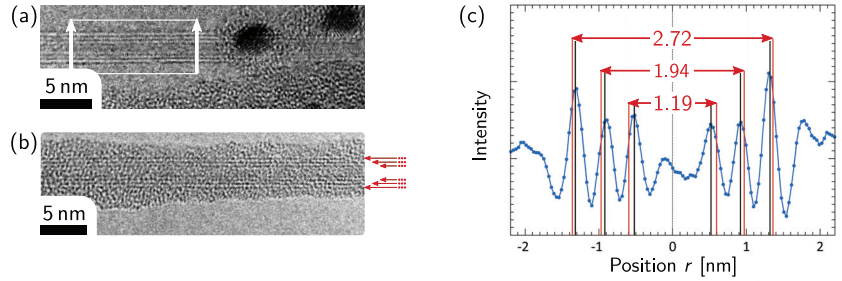


**Figure IV.10:** High-resolution TEM analysis with bright atom contrast of sample $\alpha$. (a) Clean CNT section close to the source (upper contact in Fig. IV.9(b)). Three walls are well resolved. On the right, the CNT is covered with gold nanoparticles and amorphous material. White arrows mark the section used for the linescan on the right. (b) Most of the device is completely covered with amorphous material and only barely discernible (walls indicated by red arrows). (c) Averaged intensity scan taken between the arrows in part (a). While the black lines indicate the scan maxima, the refined, real wall diameters are marked and given in nanometers by the red numbers.

give a wrong chirality assignment. The real, refined diameters are $D = 1.19\,\text{nm}$, $1.94\,\text{nm}$ and $2.72\,\text{nm}$, respectively. These values are within $0.5\,\text{Å}$ of the intershell distance of multiwalled CNTs [Sai93], indicating that the individual shells are not strained.

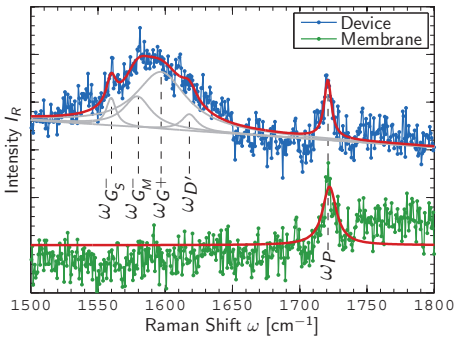


**Figure IV.11:** High-energy Raman modes of sample $\alpha$, measured in a confocal Raman setup with an excitation wavelength $\lambda_L = 488\,\text{nm}$. The bottom graph is measured on a CNT-free part of the membrane. Curves are offset for clarity. All fits are Lorentzian with linear background determined by a least-squares algorithm.

The high-energy Raman spectrum (cf. section II.1.3) of device $\alpha$ is given in Fig. IV.11. I observe three modes that can be assigned to the CNT, namely a narrow $G^-$ band at $\omega_{G_S^-} \approx 1560\,\text{cm}^{-1}$ with $\sigma_S \approx 9\,\text{cm}^{-1}$, a broader one with $\omega_{G_M^-} \approx 1580\,\text{cm}^{-1}$ and $\sigma_M \approx 25\,\text{cm}^{-1}$, and the $G^+$ mode at $\omega_{G^+} \approx 1597\,\text{cm}^{-1}$. Errors from the least-squares fit are in the order of $1\,\text{cm}^{-1}$. The $D'$ band at $\omega_{D'} \approx 1618\,\text{cm}^{-1}$ is a graphitic defect mode and may arise from the carbon nanotube or the amorphous material [Tan01, Nos12]. The line at $\omega_P = 1721\,\text{cm}^{-1}$ is also present on a CNT-free part of the membrane (cf. lower trace) and is attributed to PMMA contamination as discussed in the following section.

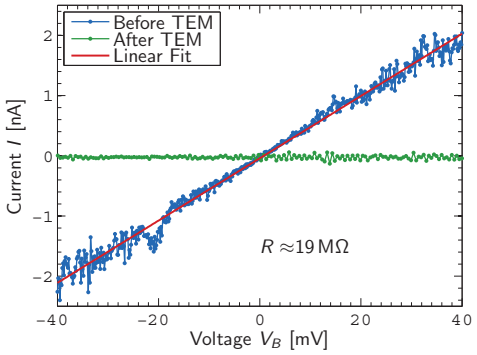


**Figure IV.12:** Room-temperature current-voltage characteristics of device $\alpha$. It was destroyed during the TEM measurement (cf. Fig. IV.9).

The resistance is measured as indicated in Fig. IV.8(b) at room temperature in a probe station. The investigated segment shows an ohmic behaviour with a resistance $R \approx 19\,\mathrm{M\Omega}$ as shown in Fig. IV.12. No current flow between the electrodes could be monitored after the destruction during the TEM measurement (cf. Fig. IV.9(b)). Thus, there are no parasitic resistances in the system, neither through the substrate nor through the other structures bridging the TEM observation slits and the observed resistance can be clearly attributed to the CNT device.

### IV.2.1 Joint interpretation

A linear $IV$-curve requires a metallic CNT as active device. This is supported by the Raman measurements where one of the $G^-$ modes is rather broad ($\sigma_M \approx 25\,\mathrm{cm}^{-1}$). which is typical for metallic CNTs because of their strong electron-phonon coupling [OC05, Jor02b]. Thus, these two measurements mutually support each other.

Besides the carbon nanotube high energy modes, a peak at $\omega_P = 1721\,\mathrm{cm}^{-1}$ contributes to the Raman spectrum that is also present on the substrate (cf. Fig. IV.11). It can be attributed to the C=O bond in the ester carbonyl group of the PMMA resist. The absence of the unpolymerized C=C bond at $\omega = 1640\,\mathrm{cm}^{-1}$ indicates a complete polymerization [Pal01]. This explains the PMMA resistance to the standard lift-off recipe and identifies the amorphous material that hosts the carbon nanotube.

The PMMA can additionally be identified by its insulating properties. The spiderweb-like structures bridging the observation slits in Fig. IV.9 are only barely visible in the SEM micrographs. They are quickly obscured by charging effects despite being physically connected to the electrodes. The TEM measurements are much less affected thereof. The same mechanism is at work in Fig. IV.8. Only carbon nanotubes connected to the metal electrodes and membrane regions nearby can disperse the charges induced by the SEM and yield a clear image. Also the unusually high resistance of the metallic CNT can be explained by a PMMA-contaminated interface between the contact and the actual device.



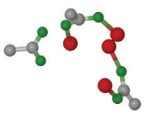

The fitting results need additional support as the Raman signal-to-noise ratio is rather poor. The $G^-$ mode is known to be diameter dependent as described in section II.1.3 [Jor02b, Pis07]. Diameters $D_M = (2.7 \pm 0.3)\,\mathrm{nm}$ ($D_S = (1.24 \pm 0.04)\,\mathrm{nm}$) can be assigned to the $G^-$ frequencies of the metallic (semiconducting) mode, according to these literature measurements and theoretical frameworks. This fits well to the outer and inner diameter determined in the TEM measurement and confirms the mode assignment. The TEM analysis is mandatory for a correct interpretation of this Raman data because a reasonable fit could also be obtained with a different model. One could a priori, e.g., assume a second semiconducting $G^-$ mode at $\omega_{G_S^-} \approx 1540\,\mathrm{cm}^{-1}$. The corresponding diameter, $D_S \approx 0.9\,\mathrm{nm}$, is clearly not observable in the TEM measurements.

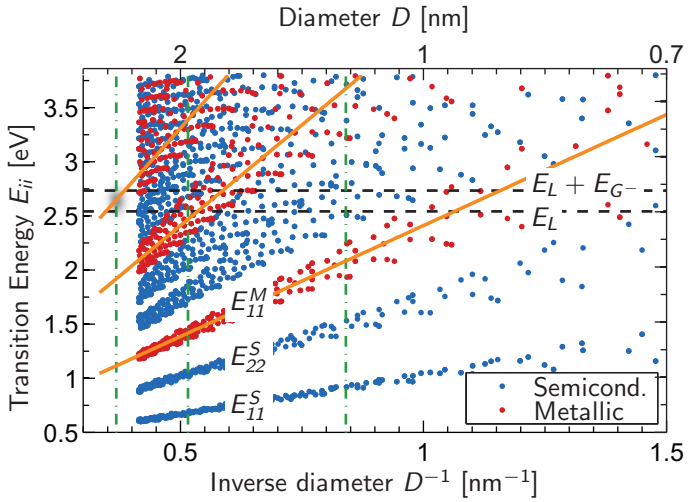


**Figure IV.13:** Kataura plot calculated by Popov and Henrard [Pop04]. Transition energies are blueshifted by 0.3 eV. The green, dash-dotted lines indicate the diameters observed in the TEM measurement (cf. Fig. IV.10). The horizontal, dashed lines indicate the used laser line $E_L = 2.54\,\mathrm{eV}$ in Fig. IV.11, and this line offset by the $G^-$ phonon frequency $E_{G^-}$, respectively. Each point stands for a specific $(n, m)$ chirality. Shaded regions denote barely fulfilled resonance conditions. The solid orange lines are linear fits to the armchair metallic transition energies $E_{11}^M$, $E_{22}^M$ and $E_{33}^M$.

Furthermore, it is likely that at least part of the current flows through the outer shell since it is metallic. The middle wall remains silent in the Raman measurement as it is probably off-resonant. The $G^-$ frequency would be around $\omega_{G_M^-} \approx 1570\,\mathrm{cm}^{-1}$ ($\omega_{G_S^-} \approx 1580\,\mathrm{cm}^{-1}$) for a metallic (semiconducting) shell according to its diameter $D = 1.94\,\mathrm{nm}$. I cannot exclude that a broad metallic $G_M^-$ mode is hidden behind the signal from the outer and inner shells, neither that the one outlying data point at $1580\,\mathrm{cm}^{-1}$ stems from a weak semiconducting $G_S^-$ mode. The resonance conditions derived from the Kataura plot would justify both, a metallic or semiconducting shell (cf. Fig. IV.13). Fitting with an additional

$G^-$ mode at the mentioned frequencies becomes unreliable and shifts the above discussed $G^-$ modes considerably.

The low Raman signal strength is attributed to an only barely fulfilled resonance condition. Because Raman processes in carbon nanotubes have a small cross section only resonant Raman scattering is observed as explained in section II.1.3. Either the incoming or the scattered photon must have the energy of a real electronic transition. On this basis it is possible to calculate so-called Kataura plots that map the diameter and the optical transitions for various CNT chiralities. Such a plot is given in Fig. IV.13, calculated with a non-orthogonal tight-binding model [Pop04]. All transition energies are rigidly blue shifted by 0.3 eV to account for excitonic effects and electron correlations [Pop04, Mau05].

Although the large diameter of the outermost tube is beyond the calculated values, Fig. IV.13 clearly shows that the observed metallic $G^-$ Raman mode belongs to the $E_{33}^M$ transitions because the experimentally probed region ($D = 2.72\,\text{nm}$, $\lambda_L = 488\,\text{nm}$) intersects with the extrapolation of the $E_{33}^M$ branch. A further assignment of chiral indices is not possible.

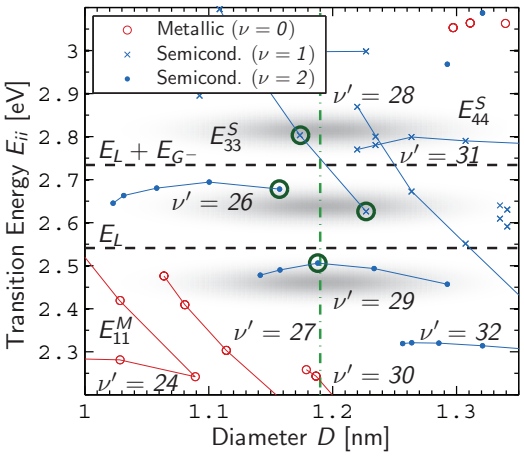


**Figure IV.14:** Closeup of the Kataura plot shown in Fig. IV.13. The green, dash-dotted lines indicate again the diameters observed in the TEM measurement (cf. Fig. IV.10). The black line gives the used laser energy $E_L = 2.54\,\text{eV}$ in Fig. IV.11, and this energy offset by the $G^-$ phonon frequency $E_{G^-}$, respectively. Each point stands for a specific $(n, m)$ chirality. Shaded regions denote barely fulfilled resonance conditions. Family index $\nu$, branch number $\nu'$ and transition energies are given for some selected chiralities. Green circles denote most likely candidates for the innermost wall of sample $\alpha$.

On the contrary, the innermost, semiconducting carbon nanotube can be further encircled. It is unlikely that it has a transition energy within the RBM resonance window of 120 meV around the incoming laser light at $\lambda_L = 488\,\text{nm} = 2.54\,\text{eV}$ because no radial breathing mode could be observed [Fan04, Par06]. The low Raman signal strength additionally indicates that also the resonance condition for the high-energy modes is just barely met. Only the outgoing resonance at $E_L + E_{G^-}$ has to be considered additionally since the incoming resonance coincides with the RBM resonance window. The innermost shell is expected to lie within the shaded regions of Fig. IV.14, assuming a full width at half maximum (FWHM) $2\Gamma \approx 80\,\text{meV}$ of the HEM resonances [Duq10, Duq11] and a measurement uncertainty $\sigma_D \approx 1\,\text{Å}$ on the nanotube diameters measured in the TEM. They are centered at $D = 1.19\,\text{nm}$ and $E = E_L - \Gamma$, $E = E_L + E_{G^-}/2$, and $E = E_L + E_{G^-} + \Gamma$,



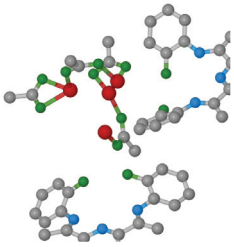

respectively. The observed semiconducting $G_S^-$ mode thus either belongs to the $E_{33}^S$ transition of the $\nu = 2$ family (branches $\nu' = 26$ or $\nu' = 29$), to the $E_{33}^S$ transition of the $\nu = 1$ family (branches $\nu' = 28$ or $\nu' = 31$), or to the $E_{44}^S$ transition of the latter ($\nu' = 31$). Best matches are the encircled (12,5), (10,8), (9,8), and (11,6) carbon nanotubes.

**Summary**

- A novel sample design is presented with which transport, Raman spectroscopy, and transmission electron microscopy measurements can be combined on individual (self-assembled) nanostructures. It uses commercially available $Si_3N_4$ TEM membranes and standard e-beam lithography.
- It is used for the comprehensive characterization of an individual, triple-walled carbon nanotube as a proof of principle. Each measurement technique on its own gives either an incomplete or ambiguous picture of this transport device.
- The electrical transport of this particular device is mainly mediated by the outer, metallic shell identified by means of all measurement techniques. Its measured resistance is relatively large, a result from PMMA residues identified in the TEM and Raman measurements.
- The outer shell's Raman response can be attributed to the $E_{33}^M$ transition.
- I can assign the innermost shell to few semiconducting branches and sort out four chiralities that are likely to describe this nanotube combining the Raman resonance condition and the diameter measured in the TEM.

# CHAPTER V

## Monitoring structural influences on quantum transport in InAs nanowires

Self-assembled semiconductor nanowires receive, like carbon nanotubes, considerable interest to pursue the miniaturization of nanoelectronic devices [Sam04, Li06, Yan10b]. They are also considered to introduce entirely new capabilities like quantum computing [Ind07] or even used to demonstrate concepts in elementary particle physics [Mou12, Das12]. Some III/V compounds with a low bandgap as, e.g., InAs, InN or InSb are ideal candidates in this regard because they exhibit a surface accumulation layer that offers Schottky-barrier free contacts which facilitate the integration into electronic circuits [Tsu70, Nog91, Fri09b, Fri10, Wir11].

These nanowires can be tuned into several transport regimes, depending on the experimental conditions. Their classical electrical properties like electron concentration, resistances or mobilities are studied as a function of the chemical and electronic environment at room temperature [Du09, Wir11]. Various quantum effects start to dominate the transport upon turning to cryogenic temperatures. Single-electron tunneling [Sho07, Sch10], localization effects [EH10, Han05] or conductance fluctuations [Fri09b, Blö11] have been observed. The proximity effect can be studied in the nanowires when brought into contact with superconductors [Doh05, Fri10].

Standard sample layouts suffer from two factors that can strongly influence the respective transport experiments. The charge carrier distribution and the high aspect ratio lead to an enhanced sensitivity of the transport to the environment (cf. section II.2). This can be a benefit for applications like gas sensing [Du09]. On the other hand, an interaction with the substrate can mask or distort the investigated transport phenomena [Wei13].

Also, it is usually not possible to directly correlate observed transport phenomena to an exact defect distribution since the latter is unknown as it is not accessible in standard transport experiments. The usual approach is to study a number of nanowires of the same growth run in a transmission electron microscope (TEM) and to compare their average defect density and distribution with the transport data [Fuh07, Blö11, Wir11].



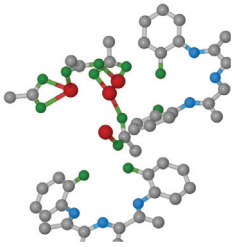

Sometimes, additional measurements such as dark field microscopy [Sch10] or atomic force microscopy [Day10] are used on the investigated transport device. However, no insight on the precise atomic arrangement can be obtained by these means.

The sample layout introduced in chapter IV directly tackles these issues. The suspended geometry of the nanowires avoids possible substrate interactions. A TEM measurement reveals quantitatively the polytypism of the wurtzite and zinc blende crystal structures of the actual measured device. Although the defect distribution is usually rather homogeneous within one growth run, a one-to-one comparison of crystallographic and transport data sets may reveal connections that could pass unnoticed otherwise.

In this chapter, I will present universal conductance fluctuation measurements that probe inter alia the phase-coherence length (section V.2) along with TEM micrographs of the very same investigated nanowire segments (section V.3) and interpret their results jointly (section V.4). Parts of this chapter have been published in [Fri12a], [Fri12b] and [Flö11a].

## V.1 Sample layout

One TEM membrane (named ℵ hereafter) with four InAs nanowires ($\aleph_1$ to $\aleph_4$) has been prepared as described in section IV.1. A positive marker structure has been used and the suspended device length is about 1 $\mu$m. The InAs nanowires have a diameter and length of $\sim 110\,\mathrm{nm}$ and $\sim 4\,\mu\mathrm{m}$, respectively and are moderately $n$-doped (doping factor 100×). Contacts consisting of a Ti/Au bilayer (10 nm/120 nm) are defined in a two- (wires $\aleph_2$ and $\aleph_3$), three- (wire $\aleph_4$), and four-terminal (wire $\aleph_1$) configuration. The nanowires were exposed to an oxygen ion beam and an $Ar^+$ plasma prior to metal deposition to remove PMMA residues and the native oxide layer in order to ensure a good contact transparency. Exemplarily, samples $\aleph_1$ and $\aleph_4$ are shown in Fig V.1. Room-temperature measurements of nanowires from similar growth conditions yield a mobility $\mu \approx 1000\,\mathrm{cm}^2/\mathrm{Vs}$ and an electron concentration $n \approx 1 \cdot 10^{18}\,\mathrm{cm}^{-3}$. These values could not be determined from wires $\aleph_1$ to $\aleph_4$ directly because the lack of a gate. Although the exact values could deviate, they do not have any impact on the temperature dependences discussed in the following sections.

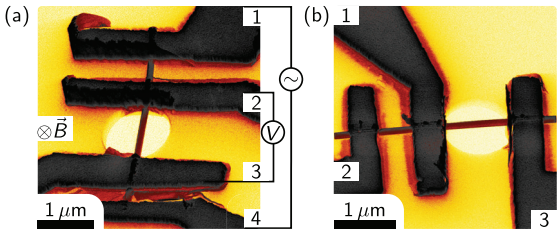


**Figure V.1:** Scanning electron micrographs of samples (a) $\aleph_1$ and (b) $\aleph_4$. The color scale of the secondary electron yield is inverted for clarity. The four-terminal measurement configuration sketched in (a) translates to (b) if contact 3 serves both as voltage and current probe. The suspended middle sections are investigated in TEM.

## V.2 Transport measurements

The wires were measured at cryogenic temperatures in a $^3$He cryostat (cf. section III.4) between 0.35 K and 30 K. The resistance was obtained using a lock-in amplifier[1] at an excitation frequency of 17.3 Hz and currents given in table V.1. They are chosen differently as to have a similar signal-to-noise ratio in all measurements. A magnetic field up to 7 T was applied perpendicular to the wire axis as sketched in Fig. V.1(a). Only measurements of wire segments suspended across the TEM holes are reported if not mentioned otherwise, with dimensions given in table V.1.

| Sample | ℵ$_1$ | ℵ$_2$ | ℵ$_3$ | ℵ$_4$ |
|---|---|---|---|---|
| Length [$\mu$m] | 1.16 | 1.47 | 1.31 | 0.9 |
| Diameter [nm] | 111 | 103 | 116 | 113 |
| ac excitation [nA] | 5 | 2 | 3 | 3 |

**Table V.1:** Measurement settings for samples ℵ.

The resistance at low temperatures fluctuates as a function of the magnetic field as shown in Fig. V.2. This can be attributed to the universal conductance fluctuations (UCFs) introduced in section III.3.2. The contact resistance is estimated by the difference of the two- and four-terminal measurement and amounts to $2 \cdot 600\,\Omega$. It stays constant for all investigated temperatures ($0.35\,\mathrm{K} \leq T \leq 30\,\mathrm{K}$) and needs to be subtracted to determine the wire conductance.

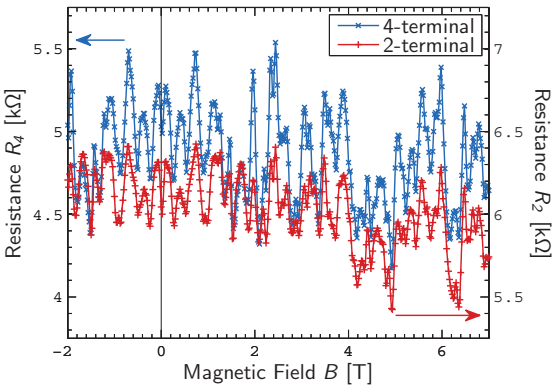


**Figure V.2:** Magnetoresistance of sample ℵ$_1$, measured in four- (left axis) and two-terminal (right axis) configuration. The active device region is between contacts 2 and 3 in Fig. V.1. The measurements are performed at 0.35 K.

I observe similarly shaped resistance and therefore conductance fluctuations in the two- and four-terminal configuration measuring the same wire section. Both traces are symmetric under a reversal of the magnetic field. Magnetotransport measurements are expected to be symmetric in a two-terminal configuration and asymmetric for multiple ter-

[1] `Ithaco 3961B`, analog output monitored with an `Agilent HP3458A`.



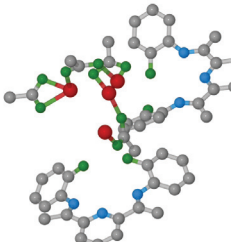

minals [Ons31, Cas45, Büt86, Büt88]. This has been observed inter alia for InN nanowires [Fri09b, Fri09a]. In the material systems investigated here, InAs nanowires [Han05, Blö11], but also in other materials like indium tin oxide nanowires [Yan12], the voltage probes in a four-terminal configuration tend to couple so strongly to the system that it becomes effectively a two-terminal measurement with symmetric UCFs. This is primarily a quantum effect, i.e. the voltage probes act as scattering centers that break the phase coherence. It could also mean that the contact resistance slightly deviates from the estimated value.

The universal conductance fluctuations $\delta_G$ are extracted from the magnetoresistance curves as described in section III.3.2. All fluctuation patterns reproduce themselves for all investigated temperatures with a decreasing amplitude as shown in Fig. V.3(a) and (b) exemplarily for wires $\aleph_1$ and $\aleph_4$, respectively. As mentioned in section III.3.2, the particular pattern is a fingerprint of the probed wire section. Therefore, the two surface plots in Fig. V.3 that stem from distinct nanowires are different while the two curves of Fig. V.2 fall on top of each other because they probe the very same wire section.

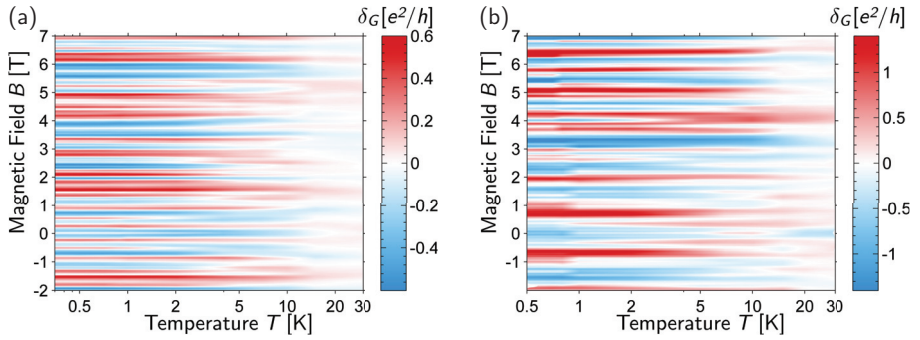


**Figure V.3:** Universal conductance fluctuation $\delta_G$ in units of $e^2/h$ of wires (a) $\aleph_1$ and (b) $\aleph_4$ as a function of temperature and magnetic field at $T = 0.35\,\mathrm{K}$. Measurements are taken in a four- and three-terminal configuration, respectively. (a) The leftmost measurement at $T = 0.35\,\mathrm{K}$ corresponds to the blue resistance curve of Fig. V.2.

The root mean square of the UCFs, $\sigma_{\delta_G}$, is shown in a double-logarithmic plot in Fig. V.4(a) to quantify the decreasing amplitude with increasing temperature. All wires $\aleph$ show a similar behaviour. The amplitude remains constant up to a temperature of about 1 K. After a short transition for $1\,\mathrm{K} \lesssim T \lesssim 3\,\mathrm{K}$, it decreases exponentially with increasing temperature like

$$\sigma_{\delta_G} \sim T^{-0.70\pm0.04} \qquad \text{for } T \geq 3\,\mathrm{K}. \tag{V.1}$$

This can be explained with the phase-coherence length being longer or comparable to the contact separation for $T \leq 1\,\mathrm{K}$. For higher temperatures, several phase-breaking mechanisms break the wires into smaller phase-coherent sections. The exponent of the above temperature dependence in eq. (V.1) matches the value predicted in eq. (III.13) for a one-dimensional diffusive transport with $l_T \ll l_\varphi < L$ (vide infra).

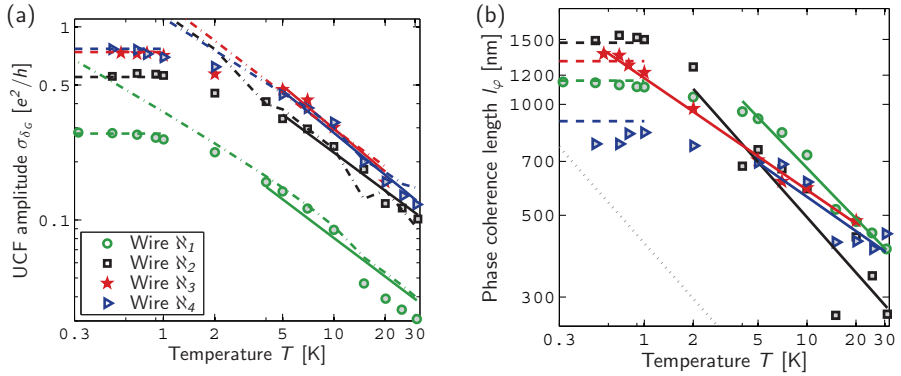


**Figure V.4:** (a) UCF amplitude $\sigma_{\delta_G}$ and (b) phase-coherence length $l_\varphi$ versus temperature $T$ of samples ℵ. Measured values are given as open symbols sharing the same color code for both plots. The solid lines are exponential fits for elevated temperatures. (a) The dashed lines mark the maximum amplitude when the entire wire is phase-coherent. The dash-dotted lines are the amplitude values calculated from $l_\varphi$ in (b) via eq. (III.13). (b) The dashed lines mark the contact separations that coincide with $\max(l_\varphi)$. The dotted line gives the thermal length $l_T$.

The phase-coherence length $l_\varphi$ can be determined via the correlation field $B_C$ as described in section III.3.2. The result is displayed in Fig. V.4(b). I observe a similar behaviour as for the UCF amplitude, i.e. a saturation below 1 K and an exponential decrease for elevated temperatures ($T \gtrsim 3\,\mathrm{K}$). Only $l_\varphi$ of wire $\aleph_3$ decreases in the entire temperature range. The maximum, constant value of $l_\varphi$ matches the contact separations given in table V.1 and by the dashed lines in Fig V.4 when assuming $\gamma \approx 2$ in eq. (III.17). This value is higher than the theoretical expectations [Bee88, Bee91a, Bee04, Lee87] what can be attributed to a flux cancellation (vide infra). The temperature dependence of the phase coherence length agrees with the above explanation that the entire wire is phase-coherent for $T < 1\,\mathrm{K}$.

Remarkably, two distinct dephasing rates of the phase-coherence length are observed upon increasing the temperature. It is

$$l_\varphi \sim T^{-0.5} \text{ — (wires } \aleph_1, \aleph_2) \quad \| \quad l_\varphi \sim T^{-0.3} \text{ — (wires } \aleph_3, \aleph_4) \tag{V.2}$$

for the various samples ℵ. I measure in the regime where $l_T \ll l_\varphi$ as indicated by the dotted line in Fig. V.4(b) that gives the evolution of $l_T(T)$. Here, the UCF amplitude depends mainly on $l_T$ as predicted by eq. (III.13) and all wires follow the same exponential decrease. Indeed, $\sigma_{\delta_G}(T)$ calculated from $l_\varphi$ and $l_T$ nicely reproduces the measured values as shown in Fig. V.4(a). The proportionality constant $\beta$ has to be modified by a factor between 0.5 (wire $\aleph_1$) and 2 (wire $\aleph_2$). [Yan12, Fri09b]

The thermal length $l_T$ calculated with eq. (III.9) is given in Fig. V.4(b) by the gray dotted line. It is slightly below the contact separation distance even for $T < 1\,\mathrm{K}$ where the wires



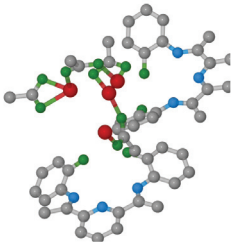

seem completely phase-coherent, i.e. with a constant UCF amplitude. The calculated curve could indeed be underestimated given the uncertainties on the electron concentration that cannot be measured directly. Also the resistivity might be overestimated because the inner voltage probes couple to the wire as demonstrated by the symmetric four-terminal magnetotransport measurement, leading to an underestimation of $l_T$.

On the other hand, the underestimation of $l_T$ can only be slight because the decay exponent of the UCF amplitude $\sigma_{\delta_G}$ averaged for all wires in eq. (V.1) predicts thermal averaging to be the dominant phase-breaking mechanism at elevated temperatures [Bee91a, Bee04]. Indeed, the theoretical prediction given in eq. (III.13) for $l_T \ll l_\varphi < L$ quantitatively models $\sigma_{\delta_G}(l_T, l_\varphi)$ as shown in Fig. V.4(a).

In this $l_T \ll l_\varphi$ regime, the proportionality constant $\gamma$ that relates the phase-coherence length with the correlation field via eq. (III.17) is predicted to be $\gamma = 0.95$ [Bee88, Bee91a, Bee04, Lee87]. The cited theory has been developed for wires made from two-dimensional planar electron gases, inter alia they do not respect the cylindrical shape of the probed samples. This morphology can lead to a flux cancellation observed in InAs nanowires grown by molecular beam epitaxy (MBE) [Blö11]. This effect overestimates the correlation field which is the measurable quantity and in turn underestimates the phase-coherence length. I used $\gamma \approx 2$ to account for this behaviour. Blömers *et al.* [Blö11] obtain a considerably smaller value $\gamma \approx 1.4$. They measure, however, in the opposite regime where $l_T \gg l_\varphi$ and a smaller theoretical value $\gamma = 0.45$ is predicted.

The prefactor $\beta$ that is used to calculate the UCF amplitude from the phase-coherence length via eq. (III.13) may suffer from similar geometrical effects. This should rather lead to a constant deviation like in the above discussion for $\gamma$. It is therefore more likely that the contact resistances deviate from the estimated values. In particular the two-terminal wires do not offer any possibility to measure the contacts which can indeed differ from device to device. This leads to a wrong measurement of the amplitude, but the phase-coherence length and temperature dependences are not affected. This would explain the distinct values of $\beta$ for different wires and contact configurations.

The error on the various fitting parameters like $\gamma$ and the decay exponents is estimated to be around 10% after one thermal cycle to room temperature [Sch12]. The same holds for unsuspended wire segments that show the same temperature dependences. Only the factor $\beta$ can be different what can be explained by a deviation of the contact resistances. A three-terminal measurement of the unsuspended section of wire $\aleph_4$ (named $\aleph_4'$) is given exemplarily in Fig. V.5. The same temperature dependences of $\sigma_{\delta_G}$ and $l_\varphi$ as in $\aleph_4$ can be found, the value for $\gamma$ is $\sim 10\%$ smaller and $\beta = 0.35$ deviates by 65% from the value of the suspended section.

One advantage of the used sample design introduced in chapter IV with the suspended nanostructures is the absence of detrimental substrate influences. The measured wire sections are largely suspended and hence there are, e.g., no trapped charges that temporarily modify the transport characteristics [Day07]. The measurements presented above are indeed rather smooth and reproducible, also compared to similar measurements using the same electronic setup [Fri09b, Fri09a].

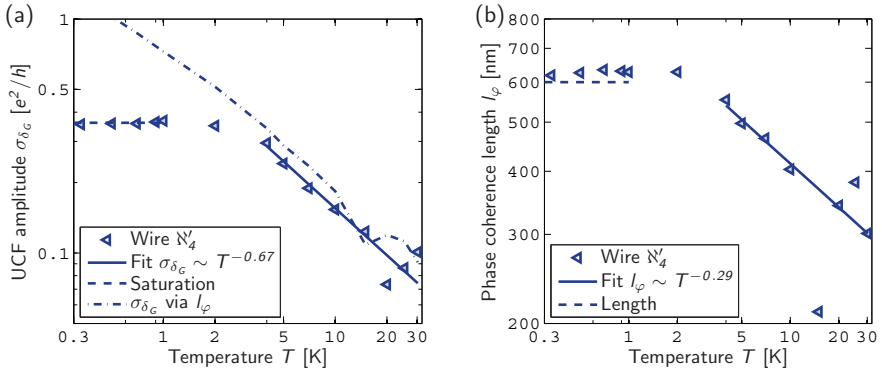


**Figure V.5:** Double-logarithmic plots of (a) UCF amplitude $\sigma_{\delta_G}$ and (b) phase-coherence length $l_\varphi$ versus temperature of sample $\aleph_4'$, the unsuspended segment of wire $\aleph_4$. Both plots use identical symbol and colour codings as Fig. V.4. Fit results should be compared to eqs. (V.1) and (V.2).

The origin of the different decoherence rates shown in Fig. V.4(b) is thus unclear at this point. The dominant Nyquist dephasing mechanism in eqs. (III.8) relates a temperature dependence $l_\varphi \sim T^{-0.5}$ to two-dimensional and $l_\varphi \sim T^{-0.3}$ to one-dimensional transport [Al'82, Lin02].

All wires were picked from within a growth area of a few micrometer. The resulting transport devices are only a few hundred micrometer apart from each other on the membrane. The nanowires do not show any systematic differences in terms of length, shape, suspended resp. supported segments, diameter or contact shape on the length scales accessible by scanning electron microscopy as displayed in Fig. V.1.

There are also microscopic influences on the electronic transport and the dephasing mechanisms besides the dimensionality. They could lie within the crystal phase mixing, which is a fingerprint of every nanowire and related to defect scattering and the electron density. The Nyquist mechanism is sensitive to the latter via the number of states a charge carrier can scatter in and out [Al'82]. Additionally, the phase coherence length depends on the diffusion constant $\mathcal{D}$ via eq. (III.7). This reflects in turn the disorder in the crystal with two main contributions, the crystal phase boundaries and point defects like dopants.

Consequently, polytypism is discussed as the origin of various transport phenomena. The conductivity and its temperature dependence were shown to depend on the degree of crystal phase mixing [Wal12, The11, Day09]. The wurtzite phases can act as tunnel barriers for quantum point formation as measured via the capacitance for controlled [Dic10b] and uncontrolled [Sch10, Wei13] crystal phase mixing.

These measurements, however, lacked a direct correlation of the crystal structure with the transport characteristics of the very same nanowire. Statistical fluctuations of the wire properties, notably of the crystal stacking sequence or the dopant distribution could distort the interpretation of these measurements.



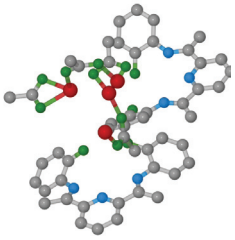

## V.3 Transmission electron microscopy measurements

This issue can be directly tackled by using my novel sample design because the wires can be investigated by high-resolution transmission electron microscopy (HR-TEM). It has an atomic resolution and could reveal a possible structural or crystallographic origin of the discussed transport behaviour. The crystallography, in particular the polytypism (cf. section II.2), is shown and analyzed for different length scales in the following.

This HR-TEM investigation was performed as a last step to avoid any electron beam damage. A complete breakdown as for the carbon nanotube sample $\alpha$ (cf. sec. IV.2) is not expected but still structural changes like sputtering of the surface could be induced [Ege04]. All measurements in this section have been performed in a `FEI Tecnai F20` microscope operated at an acceleration voltage of 200 kV. Acquisition time was set to 1 s and images recorded at 115 k-, 490 k- and 880 k-fold resolution. The samples are oriented along the [1000] wurtzite and the [011] zinc blende zone axis, respectively, because in this direction stacking faults are clearly visible [Day09].

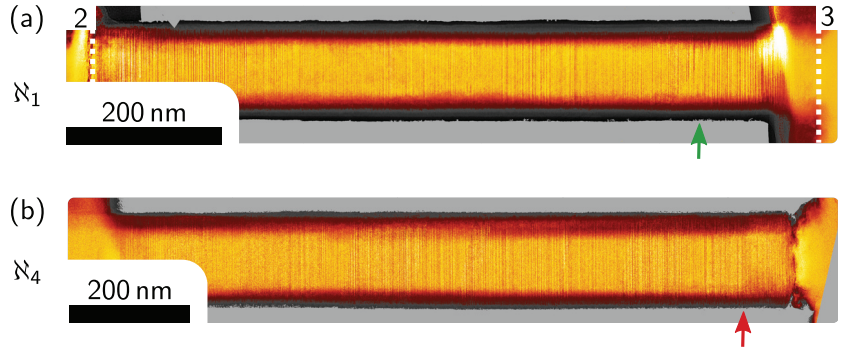


**Figure V.6:** Low-magnification TEM micrographs of the suspended sections of wires (a) $\aleph_1$ and (b) $\aleph_3$. The images are stitched from several individual micrographs. The arrows mark the approximate sites of the HR-TEM measurements in Fig. V.7. In (a), the dashed lines indicate the extremities of contacts 2 and 3 in Fig. V.1(a).

Low-magnification TEM measurements, stitched from several individual micrographs, are shown in Fig. V.6(a) of wire $\aleph_1$ that follows a $l_\varphi \sim T^{-0.5}$ dependence and of $\aleph_3$ in Fig. V.6(b) with $l_\varphi \sim T^{-0.3}$, respectively. The overlay has been performed by aligning prominent features of the oxide layer. The vertical fringes are due to stacking faults between different crystal structures. Again, no systematic differences can be observed.

Information down to the level of individual atomic planes can be obtained from high-resolution TEM measurements. Example micrographs of wires $\aleph_1$ and $\aleph_3$ are given in Fig. V.7(a) and (b), respectively. Wurtzite and zinc blende crystal phases can be observed as indicated. The zinc blende regions often contain twinning planes that inverse the stacking sequence and can be regarded as atomically thin wurtzite inclusions (cf. section II.2). All wires are covered by a 3–4 nm thick amorphous layer. This should consist mainly of

indium oxide [Sho07] and possibly some PMMA residues [Fri10]. It does not vary between the individual wires.

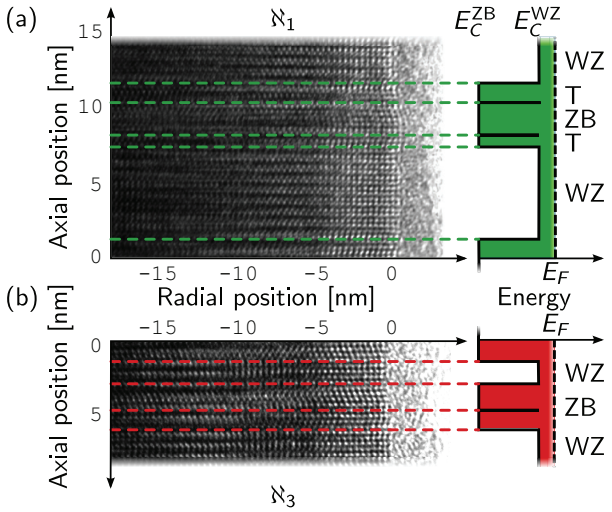


**Figure V.7:** High-resolution TEM micrographs of wires (a) $\aleph_1$ and (b) $\aleph_3$ along with a schematics of the conduction band profile $E_C$ of the wurtzite (WZ) and zinc blende (ZB) crystal phases with twinning planes (T). The shaded regions denote filled electronic states below the Fermi energy $E_F$. The micrographs are taken from sites marked in Fig. V.6.

In summary, all four investigated samples ℵ reveal a very similar morphology, device geometry, and polytypism. A grouping as measured in the different dephasing rates in transport experiments (vide supra) cannot be observed.

## V.4 Joint interpretation

In this section, I will discuss the transport measurements with respect to the crystal structure. The latter provides a direct mapping of the polytypism and hence the conduction band profile along the current flow. I obtain a Fermi wavelength of about 20 nm via eq. (III.2c) using the estimated electron concentration $n \approx 1 \cdot 10^{18}\,\mathrm{cm}^{-3}$. Because I cannot observe any crystal phases of this length I expect the Fermi energy to lie above the conduction band of both the wurtzite and the zinc blende phase. This assumption goes along with a metallic conductance measured at room temperature (not shown) and is expected for such $n$-doping growth conditions. A resulting band profile is sketched in the right parts of Fig. V.7.

A statistical analysis of the wurtzite and zinc blende segment lengths quantifies the polytypism. The result is given in Fig. V.8. Wire $\aleph_2$ could not be aligned properly with the electron beam to obtain these quantitative results. This statistics reflects the potential



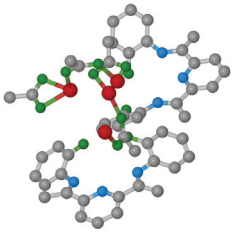

fluctuation periodicity as sketched in the right parts of Fig. V.7 and introduced in sec. II.2. All samples show a similar behaviour and have an average wurtzite segment length of 3 nm determined by a Poisson fit to the distribution displayed in Fig. V.8(a). The zinc blende segments turn out to be harder to identify and the statistical analysis is less clear as shown part (b) of the figure. Both distributions do not exhibit any differences on the scale of the individual crystal planes for all nanowires.

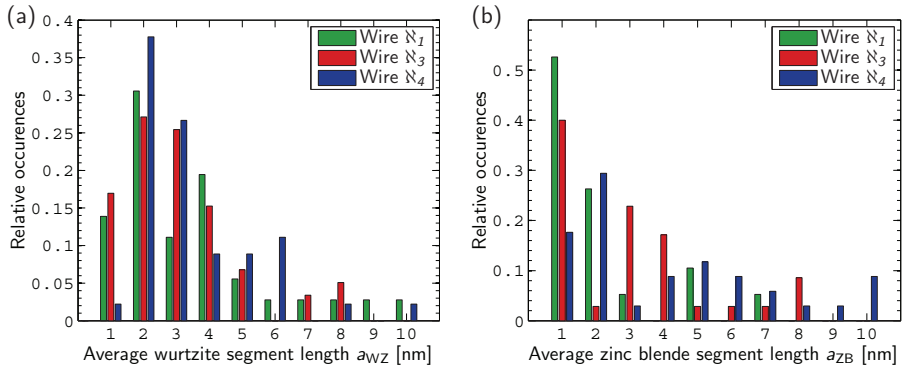


**Figure V.8:** Distribution of the axial (a) wurtzite and (b) zinc blende segment length for wires ℵ. Data is extracted from HR-TEM measurements as demonstrated in Fig. V.7.

The twinning boundaries inside the zinc blende phases are sketched as discontinuities in the conduction band in Fig. V.7 owing to their wurtzite stacking sequence. They are, on the other hand, two pieces of zinc blende crystal connected with a 180° twist. The symmetry of their wavefunctions at the $\Gamma$ point leads to a transmission close to unity even for low electron energies. This has been calculated for isolated and periodic twinning planes in GaAs, a material system similar to InAs [Iko93].[2] Their influence on the current flow in the presented devices should thus be small and is not considered any further.

I can thus conclude that the presented distinct temperature dependences of the phase-coherence length have their origin in properties that cannot be extracted from the TEM measurements. One possibility is a varying local Si dopant and defect distribution that affects the diffusion constant. Only much heavier impurities like gold inclusions could be monitored up to now [BS12]. Another candidate is strain resulting, e.g., from the suspended geometry, the clamping by the contacts, and the different thermal expansion coefficients of the InAs and the underlying $Si_3N_4$ membrane.

One possibility to probe the potential barriers or steps inside the nanowires, not restricted to the polytypism discussed in this chapter, are holographic measurements. This TEM technique monitors the interference of two electron beams, one reference beam passed

[2] The argument does not hold for other points of the Brillouin zone like the $M$ point with different symmetries. These points are not relevant for the presented low-energy transport.

through the vacuum and a second one transmitted through the current-carrying specimen [Lic08]. My sample design can be readily adapted for these measurements to further encircle the origin of the different decoherence behaviours.

### Summary

- Four suspended InAs nanowires are investigated with low-temperature magnetotransport and HR-TEM measurements. Clearly resolved and reproducible conductance fluctuations can be found for temperatures up to 30 K and magnetic fields up to 7 T. The HR-TEM micrographs reveal a rapid change between wurtzite and zinc blende crystal phases along the nanowire axis.

- The nanowires are found to be in the $l_T \ll l_\varphi < L$ regime in the temperature range $3\,\mathrm{K} \lesssim T \lesssim 30\,\mathrm{K}$ where the UCF amplitude decays like $\sigma_{\delta_G} \sim T^{-0.7}$. It has a constant value for $T \lesssim 1\,\mathrm{K}$, which is attributed to a completely phase-coherent wire.

- The phase-coherence length shows two distinct dephasing rates, $l_\varphi \sim T^{-0.5}$ and $l_\varphi \sim T^{-0.3}$ for the different samples. Its saturation value at lowest temperatures matches the contact separation if flux cancellation effects are taken into account.

- The HR-TEM measurements are very similar for all nanowires in terms of diameter, length, oxide layer thickness, and polytypism. The average wurtzite segment length is found to be $\sim 3\,\mathrm{nm}$. A grouping as for the phase-coherence length cannot be observed.

- The distinct transport behaviours therefore originate from properties that cannot be extracted from the TEM measurements, namely a dopant and point defect distribution or (thermal) strain.



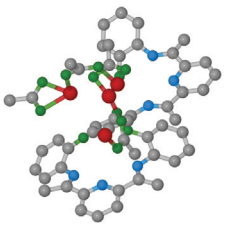

# CHAPTER VI

## Analysis of quantum transport features in complex carbon nanotube structures

The vast majority of carbon nanotube low-temperature transport experiments is reported to be on single-walled CNTs (SWCNTs). There are few exceptions of bundles [Ida00, Goß11b], multi-walled CNTs (MWCNTs) [Bui02, Moo07] or undetermined nanotube structures [Qua07]. These various CNT derivatives are expected to show fundamentally different transport behaviours. It is though experimentally difficult to distinguish one from the other with the standard surface-sensitive techniques used for device fabrication, namely atomic force or scanning electron microscopy. Also, when turning to the transport experiment, one metallic carbon nanotube could be the dominant channel and the measurement effectively probes an individual single-walled CNT [Wan08]. Results are often ambiguous once the characteristic four-fold shell filling introduced in section III.3.3 cannot be observed due to interactions of the transport channel with an a priori unknown environment.

The sample design introduced in chapter IV can be helpful in this context, since one can unambiguously identify the investigated carbon nanotube structure with this approach. The room-temperature transport measurement capabilities of the layout have been presented in section IV.2 and its compatibility with different material systems in chapter V. I will report on quantum dot measurements on two carbon nanotube devices in the following, namely on a bundle of two SWCNTs and on a triple-walled CNT. These are, to my knowledge, the first reported measurements on such structures. The stability diagrams of both systems turn out to be rather complex, but with the knowledge of the exact structure it is possible to assign specific transport features to the actual components.

## VI.1 Sample layout

Carbon nanotube samples have been grown on a TEM membrane using the process described in section IV.1. They have been located by AFM and contacted with Cr/Pd (2 nm/60 nm) contacts, deposited with molecular beam epitaxy. Example SEM images



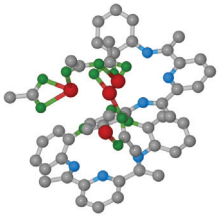

of the two investigated devices are shown in Fig. VI.1. Hereafter, they will be named $\zeta$ (Fig. VI.1(a)) and $\xi$ (Fig. VI.1(b)), respectively. It becomes apparent that sample $\zeta$ is a rope of at least two carbon nanotubes as can be seen by the branching highlighted with the blue arrows and the white dashed lines in Fig. VI.1(a).

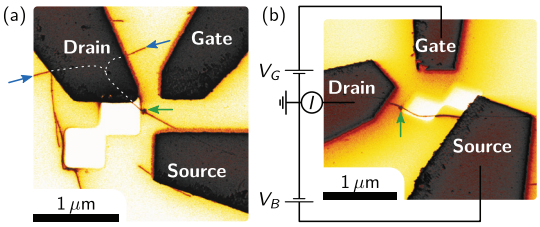


**Figure VI.1:** SEM images of samples (a) $\zeta$ and (b) $\xi$. The color scale of the secondary electron yield is inverted for clarity. The green arrows point to metal droplets discussed along with the transport data. (a) The blue arrows point to the rope ends that split up in the middle of the drain contact. It is traced by the dashed white line. (b) The micrograph is taken at a tilt of 40°. The sketched contact scheme is equivalent to Fig. III.8.

The results of a room-temperature pre-characterization of the two samples in a probe station is shown in Fig. VI.2. Both exhibit a linear transport with low resistances of 52 kΩ (sample $\zeta$) and 220 kΩ (sample $\xi$), as shown in part (a). The gate trace of sample $\xi$ is given in Fig. VI.2(b) and shows a $p$-type semiconducting behaviour for the explored gate range. Larger $|V_G|$ were avoided in order to prevent electrical destruction of the sensitive devices. No gate trace is shown for sample $\zeta$ because it has a gate leakage of about 0.5 GΩ that freezes out at the cryogenic temperatures of the following quantum dot measurements.

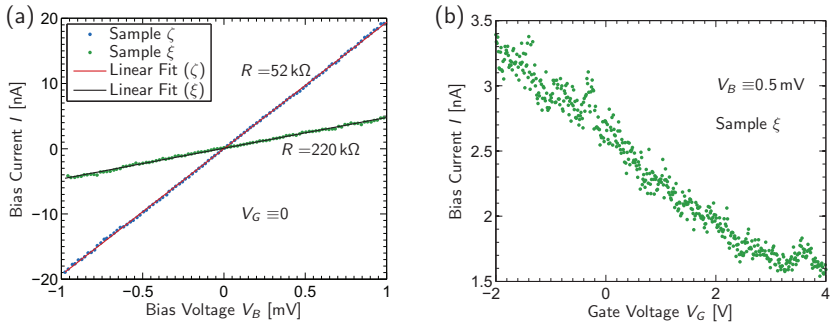


**Figure VI.2:** Room temperature characterization of samples $\zeta$ and $\xi$. (a) Resistance measurements of both samples, together with linear fits. (b) Gate trace of sample $\xi$ showing a $p$-type dependence.

All quantum transport measurements are performed in the `Leiden Cryogenics` dilution refrigerator described in section III.4 at its base temperature. The experiments are voltage-driven with the `Delft` electronic unit described in section III.4.[1]

[1]The sole exception is the extended diamond measurement with $V_G > 4$ V of sample $\xi$ that uses an

## VI.2 Sample ζ – a thin rope

### VI.2.1 Transmission electron microscopy measurements

The sample structure is determined with the transmission electron microscope after the transport experiments (vide infra) to avoid premature irradiation damage (see sample α in section IV.2). I will first present these results because many of the quantum transport features can only be understood with this knowledge. The measurements were performed in a `FEI Titan 60-300 Pico` microscope at 80 keV primary electron energy. The membrane is, presumably due to local resist thickness variations, not entirely etched through, resulting in blurred micrographs. About 15 nm of $Si_3N_4$ are left in the holes underneath the carbon nanotubes, estimated from the energetic broadening of the electron beam due to quasielastic scattering. All images are thus recorded in a strong overfocus to achieve a reasonable contrast. Atoms appear bright under these conditions, CNT walls are doubled on their outside by an interference effect.

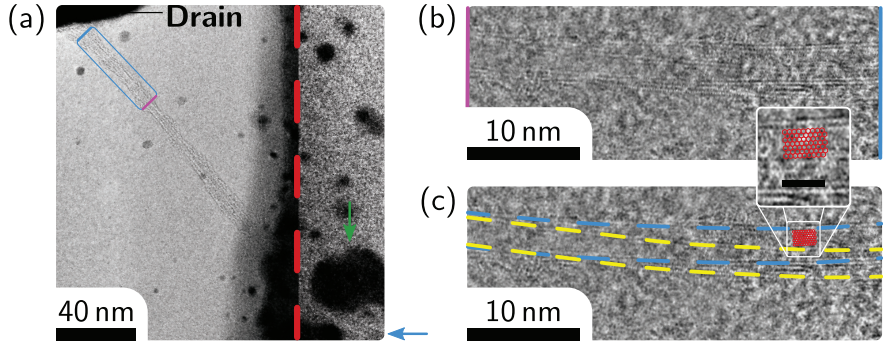


**Figure VI.3:** HR-TEM micrographs of sample ζ with bright atom contrast. (a) Low-magnification measurement covering the entire suspended region. The drain contact (cf. Fig. VI.1(a)) is visible at the top. The image brightness is enhanced right from the dashed red line (on the membrane). The green arrow points to the metal droplet also visible in the SEM images, the blue arrow to the CNT on the membrane. The dark spots around the nanotube are metal droplets. The blue rectangle is magnified in (b). Magnification of the blue rectangle in (a), oriented as indicated by the magenta and blue lines. The sample is a two-fold bundle of single-walled carbon nanotubes, i.e. each of their shells appears as two bright lines in this strong overfocus. Some graphene hexagons are visible despite the noisy background. (c) Same as (b) but with the tube walls and hexagons retraced. Scale bar of the inset is 2 nm. (b+c) The high magnification micrographs are averaged from 20 records.

A low-magnification micrograph is given in Fig. VI.3(a). The carbon nanotube is largely covered by an amorphous material that can stem from an attempt to further ablate the

`Agilent HP3245A` for the gate voltage.



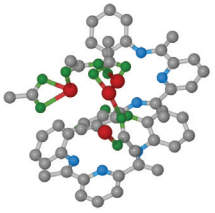

membrane underneath the hole after the transport measurements.[2] Some crystalline metal droplets reside on the membrane that originate from the contact deposition, as also observed for sample $\alpha$ reported in section IV.2. The large metal droplet marked by the green arrow in Fig. VI.1(a) is also visible in the TEM image.

High-resolution TEM images were recorded in the region marked by the blue rectangle in Fig. VI.3(a) and are displayed in parts (b+c). Twenty measurements of 500 ms each were performed in quick succession to expose the actual device more clearly. They are overlaid and averaged leading to a reduction of the white noise caused by the remaining $Si_3N_4$. The overlay process was facilitated by one of the crystalline metal droplets [The98]. A bundle of two single-walled carbon nanotubes appears clearly against the slightly structured background.[3] They have uncorrected diameters of 2.6 nm and 2 nm for the upper and lower CNT (blue and yellow line in (c)). These values are fairly large for individual single-walled CNTs under these growth conditions. The error on the diameter is expected to be below 10% what agrees with the deviations of the corrected and as-measured values of sample $\alpha$ (cf. section IV.2).

The micrographs even reveal some graphene hexagons of the upper carbon nanotube that are tentatively retraced in red in the inset of Fig. VI.3(b+c). The CNT is armchair and thus metallic, with the (19,19) chirality being the most likely candidate because it has a diameter $D = 2.58$ nm calculated via eq. (II.1b). This agrees with the low ohmic resistance observed in the room-temperature transport measurements. A likewise identification for the second CNT is not possible because it is mostly hidden by the upper one. The nanotubes reside on top of each other for the entire hole width except for the depicted section just before the drain contact.

### VI.2.2 Transport measurements

#### Quantum dot location

Sample $\zeta$ exhibits many Coulomb peaks in the investigated gate region $-1\,\mathrm{V} \leq V_G \leq 2\,\mathrm{V}$ as shown in Fig. VI.4 (top trace). It is thus a defined quantum dot for which the number of electrons can be controlled by the gate voltage (cf. section III.3.3). There is no sign of a transport gap, i.e. an empty quantum dot, in the investigated gate region as is expected for a metallic carbon nanotube. The pattern does not show any regularity like the fourfold shell filling discussed in section III.3.3. Additionally, the quantum dot does not close completely at several positions despite the low excitation voltage of $50\,\mu$V.

Some peaks do not have a gate voltage dependence like $\sim \cosh^{-2}(V_G)$ as expected for standard Coulomb oscillations [Bee91b], but look rather Fano-like with one steep shoulder. These two cases, the standard and the Fano-like peak shape, are demonstrated by fits of two neighbouring oscillations taken from the gate trace and displayed in Fig. VI.5. A Fano-shape is in general an indication for competing transport channels [Sel11, Fan61]. It

[2] The device was protected by PMMA and the backside of the membrane was etched with the RIBE process described in section IV.1.3.

[3] Counterintuitively, single walls appear as two bright lines due to the strong overfocus.

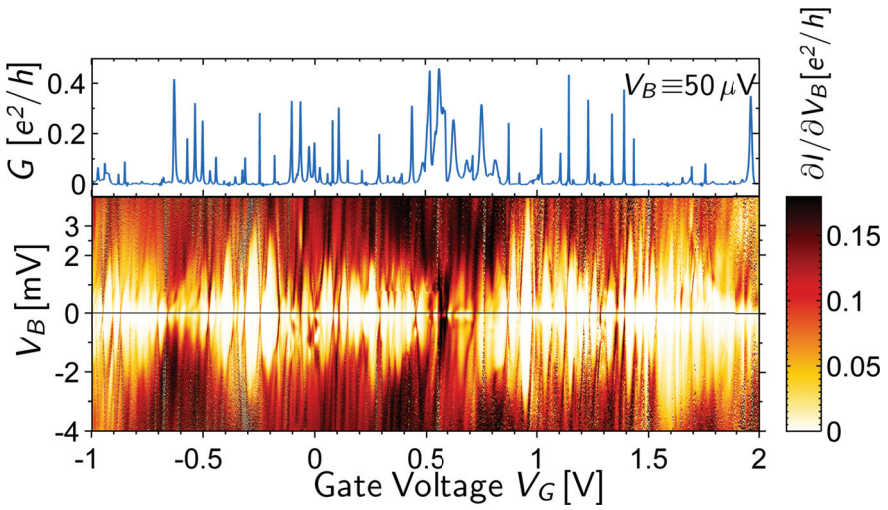


**Figure VI.4:** All measured Coulomb diamonds of sample ζ (bottom graph) along with a gate trace taken at a constant bias voltage $V_B = 50\,\mu$V (top graph). The stability diagram is composed of four individual measurements. The horizontal line highlights $V_B = 0$.

should be noted that here the origin is not the standard Fano effect as I will discuss in the analysis of the Coulomb diamonds.

The full stability diagram of sample ζ is shown in the bottom graph of Fig. VI.4. A dominant Coulomb diamond pattern can be seen that exhibits full blockade (white regions). These diamonds are described best by assuming coupling to the source and drain electrodes as $\alpha_S \approx 330\,\mathrm{mV/V}$ and $\alpha_D \approx 670\,\mathrm{mV/V}$ and a gate lever arm with $\alpha_G \approx 100\,\mathrm{meV/V}$. The pattern breaks down for the same gate voltages where the Coulomb oscillations do not fully close ($V_G \approx -0.7\,\mathrm{V}, 0\,\mathrm{V}, +0.6\,\mathrm{V}$). This modulates the diamond height throughout the pattern. Such a behaviour is expected for parallel quantum dots with the individual dots coupled differently to the gate, following classical Kirchhoff circuit laws [Goß11a]. Corresponding resonances inside the blocked regions can be found in some Coulomb diamonds (not shown). It is not possible to quantitatively separate the two patterns, i.e. the diamond structure and the beating, because the other features that I will discuss in this section hamper this analysis.

The two patterns stem from two parallel dots that are formed in the two strands of the bundle. This is also the basic reason why the stability diagram is so complex, as the quantum dots are not independent from each other but experience different forms of mutual coupling. The precise knowledge of the structure will be mandatory to interpret the transport data. I will therefore first narrow the quantum dot location before I analyze the additional features that modify the Coulomb diamonds.



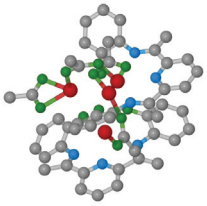

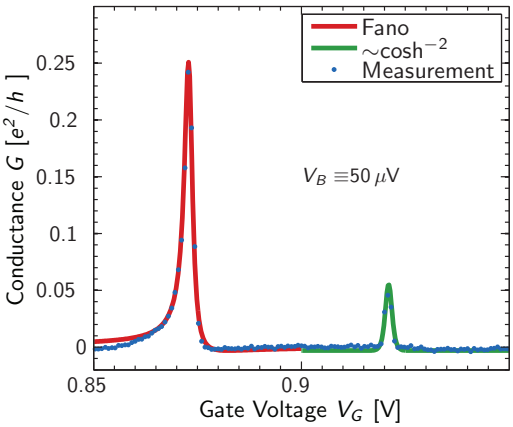


**Figure VI.5:** Two neighbouring Coulomb peaks of the gate trace shown in the upper part of Fig. VI.4. They are fitted with a Fano line shape and the standard $\sim \cosh^{-2}(V_G)$ dependence.

The two-fold bundle has two different sections, i.e. a substrate-bound and a freestanding one. The structure might have a kink at the border of the hole, locally distorting the band structure. Additionally, this environmental change can induce a potential step and break the device into a serial double dot. This is obviously not the case for these measurements because a multitude of Coulomb peaks is observable in the gate trace shown in Fig. VI.4. A serial dot would experience stochastic Coulomb blockade, i.e. that for any gate voltage at least one of the two serial dots is in blockade and no current can flow [Ruz92]. The possible quantum dot locations are thus the entire bundle or only one of the two sections, with the other serving as contact. These two cases can be discriminated by the length $L$ of the quantum dot.

A length estimation from the energy level distance via eq. (III.25) is not possible because the four-fold shell filling cannot be observed. Nevertheless, it can be roughly estimated by the addition energy as defined in eq. (III.18), assuming $E_C \approx E_{\mathrm{Add}} \approx 3\,\mathrm{meV}$ and a capacitance-over-plane model

$$C = \frac{2\pi\epsilon_0\epsilon_r L}{\operatorname{arccosh}(\Delta x/D)}, \tag{VI.1}$$

where $250\,\mathrm{nm} < \Delta x < 350\,\mathrm{nm}$ is the gate distance, $D$ the diameter determined with the TEM and $\epsilon_{\mathrm{Vac}} = 1 \leq \epsilon_r < 7.5 = \epsilon_{\mathrm{Si_3N_4}}$ the effective dielectric constant. A quantum dot length of $0.6\,\mu\mathrm{m} < L < 4.6\,\mu\mathrm{m}$ can be obtained, where the lower bound determined with $\epsilon_r = 7.5$ is certainly underestimated. The variation of the gate distance has a minor impact. The measured device lengths are $L = 150\,\mathrm{nm}$ for the suspended and $L = 600\,\mathrm{nm}$ for the substrate-bound section and I do thus not expect the quantum dot to be formed in the freestanding part only because it is too short.

A second indication for the quantum dot location in the substrate-bound area is the absence of vibronic excited states in the stability diagram. A subsection of the full gate range is shown in Fig. VI.6 where the non-equidistant excitation spectrum of one Coulomb

diamond is retraced by the blue lines at $V_G \approx -0.35\,\mathrm{V}$. I will not analyze these excitations any further because there are no identical diamonds or spectra that can be used in order to get a thorough statistic and reliable energy values. In summary, I assume the quantum dot to be located in the entire device or only in the substrate-bound part.

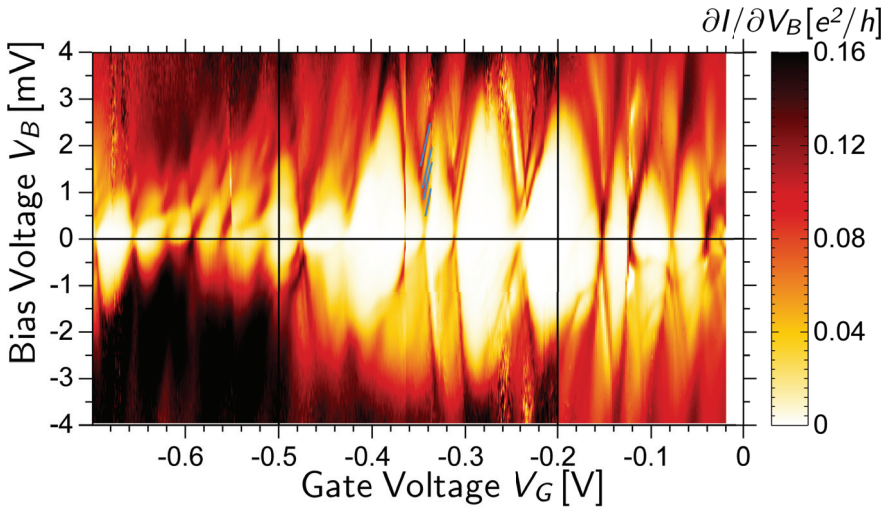


**Figure VI.6:** Low-noise lock-in measurement of a subset of the Coulomb diamonds presented in Fig. VI.4. The blue, slanted lines at $V_G \approx -0.35\,\mathrm{V}$ trace a set of excited states. The diagram is stitched from three measurement, indicated by the black vertical lines. The horizontal line highlights $V_B = 0$.

### Capacitively coupled quantum dots

The stability diagram in Fig. VI.6 was measured with a lock-in technique to suppress the high noise level of the DC-measurement (cf. Fig. VI.4). Even the lock-in measurement still suffers from some gate-dependent noise, prominent examples are the artefacts at $V_G \approx -0.7\,\mathrm{V}, -0.25\,\mathrm{V}$. These positions are reproducible and appear in both stability diagrams (Figs. VI.4 and VI.6). Such a gate-dependence is an indication that the noise has its origin on the sample and not in the electronic setup. It could be a nearby object that, just like a quantum dot, gets charged and discharged depending on its electrostatic environment. This change of state in turn modifies the electrical field at the quantum dot, causing a fluctuating resistance. Indeed, the device is partially decorated with PMMA remnants and has several metal droplets in its vicinity as can be seen in Fig. VI.3.

I will discuss such a mechanism in the following, namely a so-called gate switch that will turn out to be responsible for the Fano-like shape of some Coulomb peaks (vide supra). Two such gate switches seem to occur at first glance in the Coulomb diamonds in Fig. VI.6, namely at $V_G = -0.36\,\mathrm{V}$ and $V_G = -0.55\,\mathrm{V}$ where two lines of almost vertical slope run



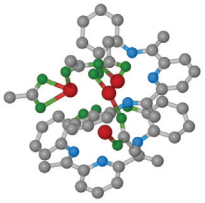

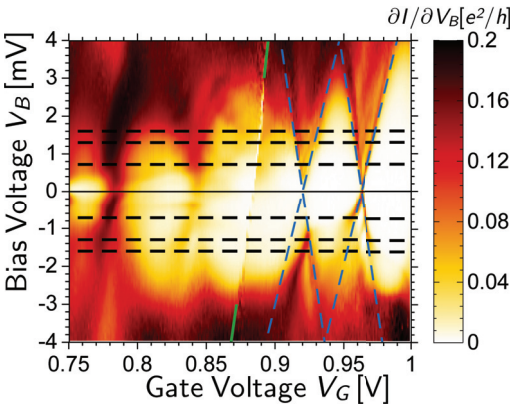


**Figure VI.7:** Gate switch with finite slope $\mathrm{d}V_B/\,\mathrm{d}V_G \approx 290\,\mathrm{mV/V}$, indicated by the two green lines. Gate traces at $V_B$ values shown by the black dashed lines are given in Fig. VI.10. The solid horizontal line indicates $V_B = 0$. The blue, dashed lines trace the Coulomb diamond edges that have a clearly different slope than the gate switch.

through the stability diagram. These events are usually ascribed to a stochastic charging or discharging of a nearby nano-object, a charge trap in the gate dielectric, or, in my case, in the $Si_3N_4$ membrane. This results in an effectively different electrostatic environment at the sample, i.e. the gate voltage seems to have switched. The stability diagram can be healed by a rigid shift of the gate voltage on one side of the switching line. A standard, stochastic gate switch happens instantaneously and presents itself as a perfectly vertical line in the stability diagram. Additionally, the gate voltage positions are not reproducible.

These last two criteria are clearly not fulfilled for my measurements. I observe several of these ostensible gate switches that all have a steep but finite slope and reproducibly take place for the same gate voltages. A close-up of the most pronounced event at $V_G = +0.9\,\mathrm{V}$ is shown in Fig. VI.7. It has a finite slope $\mathrm{d}V_B/\,\mathrm{d}V_G \approx +290\,\mathrm{mV/V}$. This value is clearly larger than the Coulomb diamond source resonance with $\sim 250\,\mathrm{mV/V}$ determined by the dominant diamonds in Figs. VI.6 and VI.7 and exemplarily highlighted in the latter (dashed blue lines). The stability diagrams right and left from the gate switch can be concatenated by cutting along the switching line and rigidly shifting the right part by $\Delta V_G \approx -20\,\mathrm{mV}$ as shown in Fig. VI.8.

Such events have been observed in single-molecule break junctions and interpreted as an interaction between a main or transfer quantum dot and a capacitively coupled spectator dot, namely a gold droplet or a second part of the molecule not directly involved in the transport [Med11, Sel11].[4]

The reasoning of this model is summarized in Fig. VI.9 and goes as follows. Both dots are in Coulomb blockade but differently coupled to the environment. The spectator dot has a highly asymmetric coupling, e.g. $\Gamma_S \gg \Gamma_D$. This results in a stable occupation even outside the blockade region because an electron from the source will stay for a long time on the dot and will be replaced immediately if it can finally tunnel into the drain. The opposite happens when the current flow is reversed (i.e. the dot will be uncharged most of

[4] The two publications on the same measurement differ in regard of the nature of the second island, i.e. the spectator dot. Both assumptions are compatible with my interpretation and experimental situation.

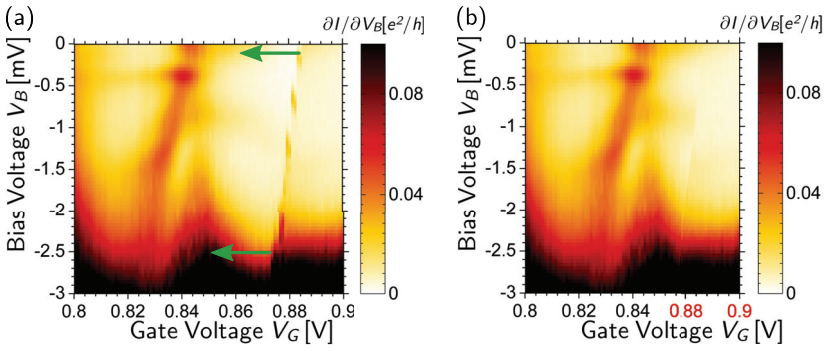


**Figure VI.8:** Closeup of the gate switch measurement of Fig. VI.7. (a) The gate switch can be removed by shifting the Coulomb diamonds on its right by $\Delta V_G \approx -20\,\mathrm{mV}$ to the left as indicated by the green arrows. (b) Result of this operation. The corrected gate values are marked in red.

the time). The total charge of this spectator dot therefore only changes when its diamond edge is crossed.

The transfer dot is responsible for the dominating Coulomb diamond pattern and can have an arbitrary coupling to source and drain. It is capacitively coupled to the spectator dot, which means that it feels a change of the spectator dot charge state. This results in a different electrostatic environment, just as for the above described stochastic gate switches. The difference is, however, that the switches in the transfer-spectator dot system are reproducible because both dots would have a clearly defined charge stability diagram if they could be measured independently. This hypothetical situation is sketched in Fig. VI.9.

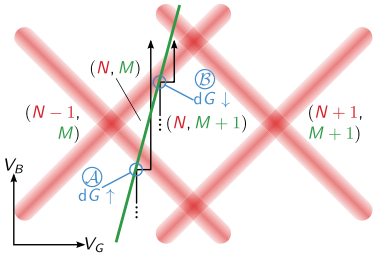


**Figure VI.9:** Visualization of the gate switching model on the hypothetically separated stability diagrams of the transfer (red) and spectator dot (green) [Sel11]. The red lines are the Coulomb diamond edges of the transfer dot with finite level broadening. The green line traces the spectator dot source resonance. Bias sweeps of the full system effectively follow the black, rectangular trajectories. The number pairs give the occupancy of the transfer ($N$) and spectator ($M$) dot. Events $\mathcal{A}$ and $\mathcal{B}$ are discussed in the text.

The electrostatic environment of the transfer dot is suddenly more positive when the bias voltage crosses a spectator diamond (source) resonance from below (events $\mathcal{A}$ and $\mathcal{B}$). The effect is therefore just as if the gate voltage had instantaneously switched and a bias voltage trace of the combined system effectively takes a trajectory as sketched by the black arrows in Fig. VI.9. The lower, left line results in an increased differential conductance at the spectator dot edge (event $\mathcal{A}$) because the bias trace switches to a region of increased



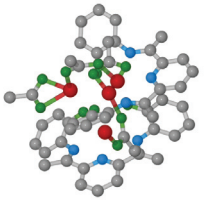

conductance. The opposite happens for the upper right bias voltage values where the transfer dot is switched into a region of lower conductance (event $\mathcal{B}$).

As a result, asymmetrical, Fano-shaped dips and peaks feature in the gate traces. This behaviour must not be confused with the standard Fano effect because the latter needs one quantized and one continuous state [Fan61].

These Fano-like Coulomb oscillations can indeed be observed in my transport measurements (cf. Fig VI.5). Similar shapes can be found for negative bias values where the differential conductance is expected to rise. Dips can be observed for positive biases. This is summarized in Fig. VI.10 where six gate traces across the mentioned gate switch in Fig. VI.7 are exemplarily shown. Especially the dips are highly asymmetrically shaped and strongly resemble the theoretical expectation [Sel11].

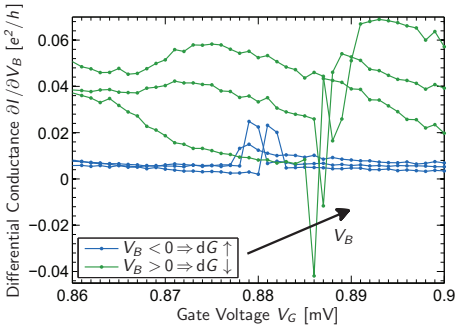


**Figure VI.10:** Gate traces across the switch as indicated by the black lines in Fig. VI.7. It is $V_B = (\pm 0.72,\ \pm 1.3,\ \pm 1.6)\,\mathrm{mV}$. The finite slope of the gate switch translates to a shift of the maxima and minima and the $V_B$ values increase from left to right.

The measured data can apparently be well described with the model of the spectator and transfer dot. Interpretations of measurements performed on standard sample layouts would need to stop at this point. Here, the knowledge of the microscopic structure of the transport device enables me to take the analysis one step further and to discuss the physical manifestation of the two dots.

The transfer dot is one or both strands of the carbon nanotube bundle because it connects the source and drain electrodes. One could in principle imagine that the spectator dot resides in the second strand. This would mean that these similar constituents behave very differently. A further analysis will additionally show that the two carbon nanotubes hybridize (vide infra). They thus form the transfer dot together.

A likely candidate for the spectator dot is the metallic grain that can be seen in both the scanning and transmission electron micrographs (green arrows in Figs. VI.1(a) and VI.3(a)). It seems to touch the transfer dot and thus has a strong capacitive influence and also a connection to the source and drain contacts. It can also give a hint on the extent of the transfer dot. The above analysis of the capacitance, using eq. (VI.1) determined the transfer dot to reside either in the entire bundle or only in the substrate-bound part, with the suspended segment serving as drain contact.

Only the source resonance is visible for the discussed gate switch, meaning that it is strongly source coupled. This would not be possible if the suspended rope segment serves

as drain lead because the metallic grain, i.e. the spectator dot, would then be connected to the drain. A similar gate switch at $V_G = -0.55\,\mathrm{V}$ indicated by green arrows in Fig. VI.11 is, on the other hand, drain coupled. The electrode coupling of the spectator dot is then gate-dependent. The transfer dot must fill the entire bundle length in this case because a spectator dot located at the source (drain) of the transfer dot cannot be strongly drain (source) coupled. These opposing behaviours could in principle also be a sign for two independent spectator dots. On the other hand, the micrographs do not show two similar elements that could account for two separate dots. Therefore, a transfer dot formed across the entire bundle length seems the most likely case.

The discussed gate switching model can in principle differentiate between a metallic island, i.e. a quantum dot with a continuous excitation spectrum, and a standard quantum dot with discrete excitation lines, by the appearance of a fine structure close to the switch [Sel11]. The resolution of my measurements does not permit a distinction between the two possibilities. I can nevertheless determine the interaction energy via

$$E_{ST} = e\alpha_G \Delta V_G \approx 2\,\mathrm{meV}, \tag{VI.2}$$

where $\Delta V_G \approx 20\,\mathrm{mV}$ denotes the effective gate switch. This is one order of magnitude smaller than the interaction energy between a nanoparticle and a molecule in a migration break junction [Sel11] and about tenfold larger than the interdot charging energy of parallel carbon nanotube quantum dots [Goß11a].

#### Hybridization in a carbon nanotube quantum dot

Apart from the gate switch, one can observe a second remarkable feature in the stability diagram shown in Fig. VI.11. Some of the Coulomb diamond edges deviate from their straight line and bend away from the diamond and asymptotically approach a shallower slope as traced by the dotted lines. I will denote the steep slope of the dominating diamond as main resonance and the shallower slope of the asymptotic lines as secondary resonance hereafter, following the nomenclature of the later used model [Goß11a, Goß11b]. They stem from a main and secondary quantum dot that together constitute the transfer dot of the discussion above.

The edges bend away so far that they even enter the neighbouring Coulomb diamond and lead to a finite current inside. Such a resonance inside the blocked region is often attributed to inelastic cotunneling that can in principle be gate dependent [Hol08]. This mechanism requires an excited state that cannot be observed here. Even if it was hidden in the highly conductive region outside the diamonds, the inelastic cotunneling could not explain the avoided crossing. Corresponding measurements reported in literature have indeed a different shape [Hol08].

A finite current inside a blocked region can readily be explained by two parallel quantum dots. The composed system shows a finite conductance as long as the blockade in one of the two dots is lifted. These are two independent[5] first-order processes that should in principle be stronger than the second-order pertubative cotunneling mechanism. At this point, my

[5] In the limit of non-interacting quantum dots that I will discuss first.



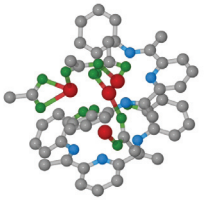

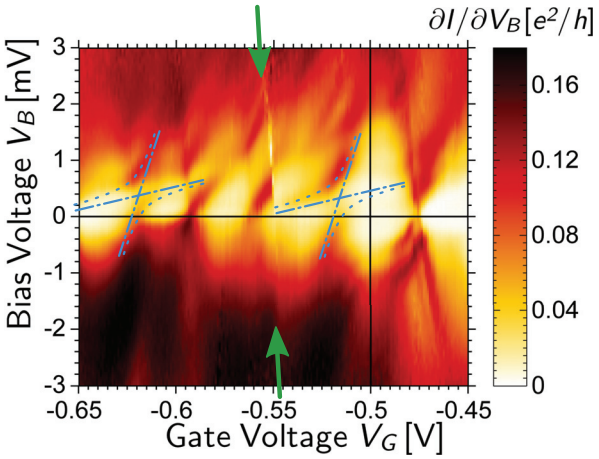


**Figure VI.11:** Close-up of the stability diagram in Fig. VI.6. The green arrows point to another gate switch with a finite slope. The blue lines highlight regions of avoided crossings. The vertical black line indicates the stitching between two different measurements, the horizontal one $V_B = 0$.

sample design can again enable to access valuable information. The transmission electron micrographs presented in section VI.2.1 unambiguously show that the device consists of a two-fold carbon nanotube bundle. These two strands form the two parallel quantum dots. First indications for this system were already present in the full stability diagrams (vide supra). This demonstrates again the advantages of my sample design because the (maximum) number of parallel dots can be easily determined and thus the risk of possible misinterpretations can be reduced.

Two uncoupled, parallel quantum dots would result in a simple addition of their differential conductance, i.e. of their Coulomb diamond pattern, as can be directly derived from the Kirchhoff circuit laws. This is not the case in my measurements and the occurrences of secondary resonances do not form a straight line as one can see, e.g., for the two traced features in Fig. VI.11. This is partially caused by the gate switches discussed before. The Coulomb diamonds do not represent a consecutive filling sequence because the gate switches in between (green arrows). Both slopes, of the main and secondary resonance, can be found throughout the entire stability diagram. Especially the main resonance can describe most Coulomb diamonds. For the following I will focus on the part of the stability diagram shown in Fig. VI.11. The full model of the system, including the spectator dot, is given in Fig. VI.12.

The bent diamond edges cannot be explained by two uncoupled quantum dots. They actually describe a so-called anti- or avoided crossing, meaning that the main and secondary resonance lines must not cross, i.e. a course as drawn by the dash-dotted lines in Fig. VI.11 is not possible. Instead, they both break up at the crossing point and one main and one secondary resonance line form a common resonance as sketched by the dotted lines.

Such avoided crossings have already been observed in a carbon nanotube peapod [Eli10] and a thick CNT rope [Goß11a, Goß11b]. Both systems are modeled as capacitively as

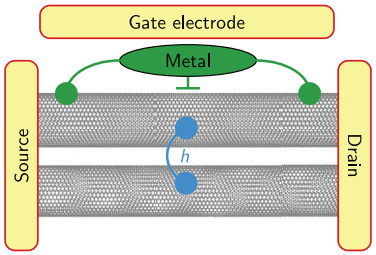


**Figure VI.12:** Sketch of all circuit elements of sample $\zeta$. Two carbon nanotubes (the upper is a (19,19) armchair) form the transfer dot. They hybridize with an amplitude $h$ and are capacitively coupled to a nearby metallic grain. I cannot observe a capacitive coupling between the two strands.

well as tunnel coupled parallel quantum dots. The tunnel coupling leads to a hybridization of the individual quantum dots. In my sample, the two strands of the rope form this new molecule-like system.

The tunnel coupling is parametrized by an hybridization integral or amplitude $h$ in the cited model [Eli10, Goß11b, Goß11a].[6] The authors assume the same sign for the matrix tunneling elements from the leads into the main as well as into the secondary dot because they are formed by similar molecules in a single junction [Goß11b, Goß11a]. This enables them to determine the nature of the hybridization. A pronounced conductance peak bending into the diamond and a suppressed second part of the avoided crossing are interpreted as a bonding state with $h < 0$, the opposite as an antibonding state with $h > 0$. The magnitude of $h$ is determined by the nearest distance between the expected, uncoupled crossing point (of the dash-dotted line in Fig. VI.11) and the actual course of the hybridized resonance (dotted line). A capacitive coupling between the two strands, also accounted for in the model, is too small to be observable in my transport data.

Here, I find $h \approx +0.3\,\mathrm{meV}$, i.e. hybridization via an antibonding state for both traced events. The magnitude agrees with the reported measurements on a thick carbon nanotube rope [Goß11b, Goß11a]. The less pronounced avoided crossings in between (i.e. at $V_G = -0.6\,\mathrm{V}$ and $-0.55\,\mathrm{V}$) have $h < 0$, i.e. they are in a bonding configuration. This means that the antibonding state can contribute to the transport if the bonding state is not available. The hybridization integral additionally seems to be strongly gate-dependent. The two resonances with a different sign cannot arise from two distinct side dots that possibly have a different coupling to the electrodes because the entire system is composed of only two carbon nanotubes, i.e. one main and one side dot.

## VI.3 Sample $\xi$ – a triple-walled carbon nanotube

### VI.3.1 Transmission electron microscopy measurements

The HR-TEM measurements of sample $\xi$ (full device depicted in Fig. VI.1(b)) are even more masked by the only partial etching of the $Si_3N_4$ membrane as observed for sample $\zeta$ discussed above. Imaging conditions are identical and listed in section VI.2.1. Again, 20 images of this time 1 s integration time were averaged to obtain the micrograph shown

[6] The original publications use the symbol $t$ that is already assigned to the time in my thesis.



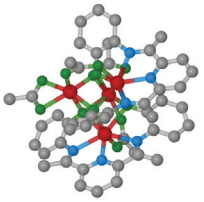

in Fig. VI.13(a). A triple-walled carbon nanotube can be distinguished feebly from the background (i.e. four maxima on each side in the strong overfocus). An intershell distance of $\sim 0.37\,\mathrm{nm}$ can be observed, a value close to the one measured for sample $\alpha$ (cf. section IV.2) and to the multiwalled CNT interlayer distance of $\sim 0.34\,\mathrm{nm}$ [Sai93]. This agrees with the expected error below 10%.

The tube diameters measured in the linescan of Fig. VI.13(b) are very large, namely 4.2 nm, 4.9 nm and 5.7 nm. It is unlikely that an inner wall would be overseen in the noisy TEM image because the growth condition were set to produce mostly single-walled carbon nanotubes (SWCNTs) with a low content of double-walled CNTs and very few CNTs of even more walls. Usually, SWCNT diameters of $\sim 2\,\mathrm{nm}$ are observed for the used growth process [Spu10a, Kon98].

On a standard sample layout that only permits surface-sensitive characterization methods, only the outer diameter would be determined routinely by e.g. atomic force microscopy. One would then, without the knowledge of the inner structure, rather assume a bundle of several single- and maybe a double-walled carbon nanotubes for the transport device. This could easily lead to misinterpretations.

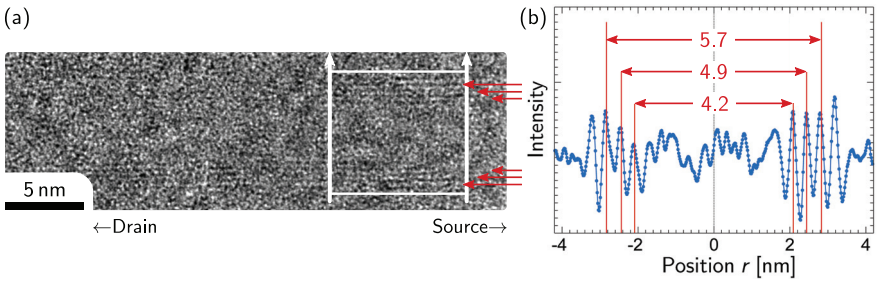


**Figure VI.13:** (a) HR-TEM micrograph of sample $\xi$ averaged from 20 records. The source contact is located right from the displayed region. A triple-walled carbon nanotube sets apart weakly from the background. (b) Linescan of the area marked with a white rectangle in part (a) in direction of the arrows. Diameters are given in nanometer as determined from the raw linescan.

## VI.3.2 Transport measurements

### Stochastic Coulomb blockade

My measurements show the first reported example of quantum transport in a triple-walled carbon nanotube. Experimental and theoretical results exist for double-walled CNTs (DWCNTs) [Wan08, Moo07, Dat11] and thick multi-walled CNTs (MWCNTs) [Bui02] as introduced in section III.3.3. Extrapolating these results, one would expect twelve-, eight,- or fourfold periodic Coulomb diamond pattern, because the respective number of walls needs to contribute to the transport with a sufficient overlap of the wavefunctions.

Neither of these periodicities can be observed in the stability diagram shown in Fig. VI.14 although the Coulomb diamonds seem to follow a regular structure on first sight. There-

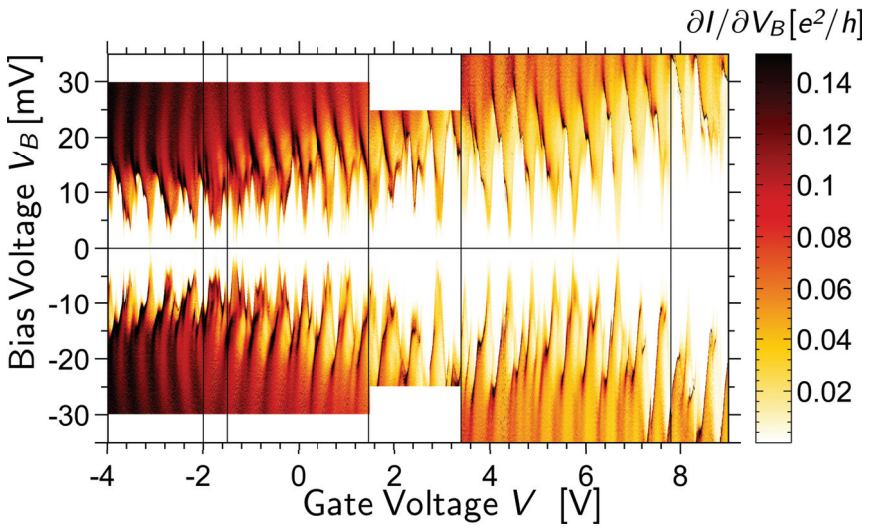


**Figure VI.14:** All measured Coulomb diamonds of sample $\xi$. The stability diagram is composed of five individual measurements separated by the black vertical lines. The horizontal line highlights $V_B = 0$.

fore, I assume that only one shell contributes to the electrical transport. This is not necessarily the semiconducting one that was measured by the room-temperature gate sweep (cf. Fig. VI.2). It is possible that the room temperature transport probed a constant metallic and a semiconducting contribution, tunable by the gate voltage. The quantum dot cannot be emptied as expected for a metallic carbon nanotube, which is an indication that the room-temperature gate measurement effectively probe a shell frozen out at the cryogenic temperatures presented here.

The conductance around $V_B = 0$ is largely suppressed and the diamonds do not close. Consequently, gate traces yield a finite conductance only when applying a large bias in the order of at least 0.5 mV. This value is too high to ensure a linear transport regime that is mandatory for any further analysis of the Coulomb oscillations (not shown).

This can be explained by the so-called stochastic Coulomb blockade of a serial quantum dot, i.e. a series connection of $N_{QD}$ ($N_{QD} \geq 2$) individual dots [Ruz92]. This is a fundamentally different situation than the parallel dot behaviour discussed for sample $\zeta$ in the precedent section. At low biases, the resistance of the $N_{QD}$ dots must be added up to get the resistance of the entire system. As, stochastically, at least one quantum dot is in Coulomb blockade for any gate voltage, all Coulomb oscillations are suppressed.

These individual quantum dots are likely to have a different coupling to the gate because they are not necessarily at the same distance. Also their coupling to the current leads is different since some are located closer to the source while others are closer to the drain. Finally they might differ in size, leading to $N_{QD}$ distinct charging energies $E_C$.



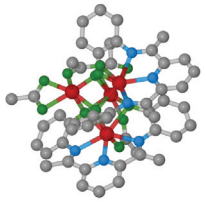

Judging from the scanning electron micrograph shown in Fig. VI.1(b), one could expect up to three individual quantum dots residing in sample $\xi$. Two dots would then be formed in the two substrate-bound sections close to the contacts while a third one resides in the suspended segment.[7] The barriers would be induced by the potential steps from the substrate or from the kinks at the edges of the observation hole. This could not be observed in the quantum transport measurements on sample $\zeta$ (vide supra) where the quantum dot most likely fills the entire device length.

A second possibility would be that the barrier is induced by the metal droplet marked with the green arrow in Fig. VI.1(b), resulting in only two dots. Indeed, most of the features and diamond edges can be described by only two sets of slopes $\mathrm{d}V_B/\,\mathrm{d}V_G \approx (170\,|\,-160)\,\mathrm{mV/V}$ and $(50\,|\,-56)\,\mathrm{mV/V}$ as sketched in Fig. VI.15 by the blue and green line, respectively. They can be found for the diamond edges themselves, with sometimes an individual diamond exhibiting both positive (negative) slope values. The shallower (green) slopes are additionally observed outside the diamonds. This latter observation will be explained in the next section. Therefore, a serial double quantum dot is sufficient to explain the transport data.

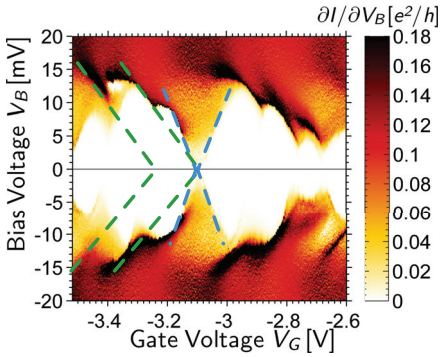


**Figure VI.15:** Subset of the Coulomb diamonds of sample $\xi$ shown in Fig. VI.14. The dotted, green (blue) lines exemplarily trace some edges and excitations in the stability diagram displaying the major slopes. Most of the features meet at $V_B = 0$ as illustrated. The horizontal line highlights $V_B = 0$.

The connection of the device structure and its transport behaviour can be further validated by comparing the length scales. This is possible relating the charging energy $E_C$ (cf. eq. (III.18)) and the capacitance calculated from eq. (VI.1). I assume that the two quantum dots have a similar distance to the gate.[8] Their capacitances then scale linearly with the device lengths. An upper bound for the addition energy can be extracted from the minimum height of the Coulomb diamonds and yields a ratio of about 4:1 for the green (blue) diamonds or slope sets shown in Fig. VI.15.[9] This means that one quantum dot is

[7] The section lengths from left to right in Fig. VI.1(b) for the unsuspended, suspended and unsuspended parts are 250 nm, 500 nm, and 380 nm, respectively.

[8] The distance to the gate varies from 760 nm to 830 nm, i.e. by less than 10%.

[9] A more quantitative analysis of the diamond heights is only possible if the voltage drops across the individual dots are taken into account. This is performed in the next section and yields $E_C \approx 15\,\mathrm{meV}$ ($E_C \approx 4\,\mathrm{meV}$) for the two dots.

about four times longer than the other one. The ratio matches with the individual dot lengths if the barrier separating the two dots is indeed induced by the metal droplet.

### Stability diagram of a serial double quantum dot

The two slope sets of the Coulomb diamonds result in a sawtooth-shaped diamond pattern. I will introduce in the following two models that can explain such a shape, excluding and including a capacitive coupling of the two serial dots.

A serial dot can be described as resistances connected in series as introduced for the stochastic Coulomb blockade (vide supra). Provided that the charge carriers can disperse their energy during the tunneling process, e.g. by bosonic excitations [Ota04], serial quantum dots show voltage drops across each of its constituents, just as a classical resistance network [Jør06, Ish01, Mak09]. Hence, the bias voltage values for the source and drain resonances of the individual quantum dots will add up, giving rise to a sawtooth-like shape for the full system.

This is demonstrated for two diamond edges in Fig. VI.16(a). The addition of the green and black lines that sketch assumed individual Coulomb diamonds results in the blue trace. It has a sawtooth like shape and roughly describes the blockade region. The quantum dot responsible for the larger, green diamond has its Coulomb peaks, i.e. crossing points with the line $V_B = 0$, whenever the resulting superstructure almost closes, namely at $V_G \approx 4.4\,\mathrm{V}$, $4.9\,\mathrm{V}$, and $5.4\,\mathrm{V}$. The teeth of the superstructure denote the Coulomb peaks of the smaller, black diamonds. Using these requirements, slopes of $(64\,|\,-70)\,\mathrm{mV/V}$ for the bigger, green and $(150\,|\,-90)\,\mathrm{mV/V}$ for the smaller, black diamond pattern describe the overall shape best. These values are different from the slopes of the blockade pattern itself (vide supra) because it is not the individual quantum dots but the full system that is measured. The green and black diamonds yield the charging energies used in the discussion of the dot lengths presented earlier.

The blue line traced in Fig. VI.16(a), i.e. the addition of the two individual quantum dots, qualitatively reproduces the measured shape of the Coulomb blockade region. A quantitative agreement exactly describing the diamond edges cannot be achieved. Additionally, the lines of high differential conductance outside the blockade region cannot be explained unambiguously. I ascribe them to excited states or to the two-electron tunneling regime of the larger, green diamond since they are parallel to its edge. The two-tuples $(N, M)$ in Fig. VI.16(a) denote the charge state of the entire system with $N$ and $M$ giving the number of electrons on the quantum dot responsible for the black and green diamond pattern, respectively.

An effect that has been disregarded so far is a mutual capacitive interaction of the dots. It has been observed in single molecular and nanowire quantum dots [Lie03, Fuh07] that a sawtooth-like diamond shape can originate from a gate switching analogous to the spectator dot mechanism discussed for sample $\zeta$ (cf. section VI.2.2). The situation here is different however because there is no designated spectator dot. On the contrary, the current flows through both serial dots. Nevertheless, the charge in each of them is



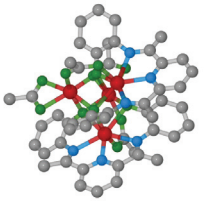

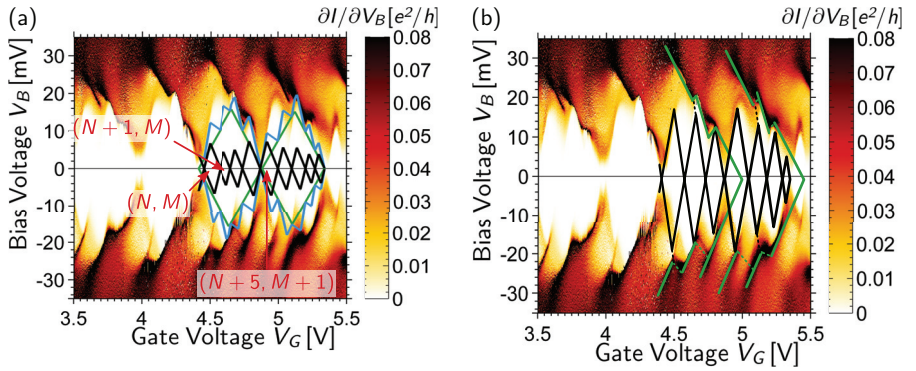


**Figure VI.16:** Two mechanisms to explain the sawtooth-like Coulomb diamond shape of sample $\xi$ (subset from Fig. VI.14). The horizontal line highlights $V_B = 0$. (a) The two diamond patterns simply add up in the limit of negligible capacitive interdot coupling. Two indices $(N, M)$ are needed to describe the charge state of the combined system. (b) If the capacitive interdot coupling is sufficiently strong, one dot could induce gate switches to the other once its electron number changes from $N$ to $N + 1$.

increased by an integer number whenever the gate voltage progresses from one diamond to the next. This is capacitively felt by the other dot.

A resulting pattern is illustrated in Fig. VI.16(b) where the diamond edge sketched by the green line (correspoding to the larger diamond in part (a) of the figure) switches whenever the charge state of the black diamond is increased.

Again, the model can only partially describe the stability diagram. It fits to the lines of enhanced conductance outside the Coulomb blockade region, but would require an unreasonably high leakage current through the quantum dot generating the larger, green diamond to account for the finite current inside some parts of the blockade region of the green dot (e.g. at $V_G \approx 4.9\,\mathrm{V}$ and $5.4\,\mathrm{V}$).

Both models neglect effects (the capacitive coupling and the voltage drops, respectively) that the other takes into account and cannot describe the full stability diagram. Therefore, a combination of the two models probably sketches the physics best. Such a modeling remains speculative because the quantum dots cannot be emptied [Ota04, Fuh07] or measured individually to extract their exact gate couplings [Jør06].

Again, the observed transport measurements are closely related to the structure of the device. Only knowing the diameter and the stability diagram, as would be the case for a standard sample layout, might have resulted in a different interpretation of the data. If one had assumed another structure, e.g. a bundle with only one transport channel, most of the discussed features would probably be explicable as well. This would clearly not meet the real, physical structure.

A remarkable finding is the contamination of the sample with the metal droplets and the PMMA coating. At least the smaller metal particles are invisible to a routine SEM

or AFM investigation on standard sample layouts, the same holds for the PMMA. Even the two larger metal droplets could possibly pass unnoticed in AFM measurements if the contact spacing is too small. Some of these contaminations might be due to the hole edges or to the mild lift-off conditions that owe to the fragility of the membranes. On the other hand, the fabrication steps are not very different to standard processes. Nevertheless, such impurities are rarely taken into account for the interpretation of transport measurements reported in literature although they can have a major impact as I have shown in this analysis.

## Summary

- Two carbon nanotube systems are characterized with low-temperature transport measurements, revealing Coulomb blockade. The observed effects can only be explained if one considers the actual structure of the devices as obtained in a subsequent TEM analysis.

- Sample $\zeta$, a two-fold bundle of single walled carbon nanotubes, shows signs of parallel quantum dot conductance. These dots are formed within the two strands of the bundle and spread over the entire device length.

- The stability diagram features several reproducible gate switches with a finite slope. They can be attributed to the charging and discharging of a nearby quantum dot, called spectator dot, coupled highly asymmetrically to the source and drain contacts. The gate potential felt by the transfer dot is switched whenever a spectator diamond edge is crossed because its charge state can only change at these points. This spectator dot is expected to reside in a gold particle touching the carbon nanotube bundle.

- The two strands of the transfer dot experience a hybridization. Both, bonding and antibonding states are observed to contribute to the quantum transport.

- Sample $\xi$, an individual triple-walled carbon nanotube, shows a typical behaviour of a serial double quantum dot with a stochastic Coulomb blockade, i.e. no transport for small bias voltages. The two dots are induced by a metal droplet. The stability diagram can be explained with only one shell contributing to the conductance.

- The Coulomb blockade regions have a sawtooth-like shape. This can be qualitatively explained by adding the voltage drops across each of the two dots. A capacitive interdot coupling might be responsible for the quantitative differences, effectively leading to gate switches as for the parallel dots.

- The quantum dots of both systems are not affected by a possible potential barrier between a substrate-bound and a freestanding part, not even if the nanotube structure is kinked at these points.



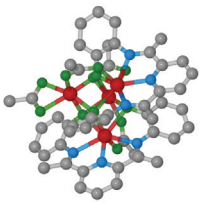

- Both systems are measured in fundamentally different transport regimes. Also, the role of individual structural elements like a metal droplet is distinct. The comparison to the structure, only possible with my novel sample design, helps to correctly interpret the experimental findings.

# CHAPTER VII

## Carbon nanotube functionalization with $\{Mn_4\}$ complexes

Carbon nanotubes have been studied to quite some extent and are consequently well characterized [Rei08, Jor10]. Their properties can additionally be tuned by modifying their chemistry and the environment [Goß11a, Hir02]. Carbon nanotubes are a very suitable system in this context because they offer a rich chemistry due to their base material carbon and can serve as a bridge into the molecular world due to their mesoscopic size. Such a functionalization can be exploited in the emerging field of molecular spintronics [Bog08] or for more fundamental investigations such as quantum computing [Ard03].

Another peculiar property of carbon nanotubes is their one-dimensionality that provides a controlled alignment of molecules on their outside [Ban05, Str03] or on their inside [Smi98, Spu09, Shi08]. Two CNTs can also be used to contact individual molecules between their ends [Guo06, Guo07, Guo09]. The base material carbon and the actual atomic arrangement offer various ways to carry out these functionalizations. An orbital interaction drives the fullerene encapsulation for endohedral functionalization [Oka01] and is one possibility to graft molecules on the carbon nanotube outside [Bog08, Bog10, Urd11]. This technique has the advantage to leave the CNT intact[1] but the van-der-Waals forces forming the bond between tube and molecule remain relatively weak. The result is a feeble interaction and a poor reproducibility of the orientation between molecule and carbon nanotube. Electrostatic interaction with chemically modified CNTs results in stronger bonds [BN12].

In this chapter, I will present a versatile route to covalently graft (magnetic) molecules onto carbon nanotubes, based on a carboxylate ligand exchange. This leads to a direct bonding between the CNT and the metallic atoms without the need of an organic linker as for other covalent functionalization techniques [Bah02, Hir05]. The presented complexes can withstand such a direct reaction, because the acetate is not needed to stabilize the core, in contrast to other magnetic molecules targeted for functionalization experiments [Man08]. I choose a tetramanganese(II) complex with an antiferromagnetic ground

[1] Standard endohedral functionalization demands for an opening of the nanotubes, e.g. by oxidation, which leads to additional defects [Spu09].



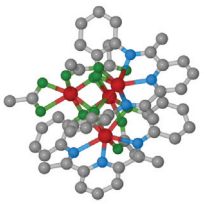

state. This Mn core can be replaced by different elements like Co, changing the magnetic character of the complex, or the number of atoms can be increased to modify the magnetism further. The cluster ligand can be replaced to tune the interatomic coupling character of the core. The degree of functionalization can be controlled by the number of carboxylate functions on the carbon nanotube sidewall which in turn depends on the degree of oxidation. The grafting success is monitored with transmission electron microscopy, Raman spectroscopy, and CNT network conductance. Parts of this chapter have been reported in [Flö11b, Slo12, Sae12] and published in [Mey12].

## VII.1 The {$Mn_4$} complex

The molecular magnet of choice for this thesis consists of a stable, cubane $Mn_4O_4$ core (cf. Fig. VII.1(a)) that is structurally induced by a rigid pentadentate pyridine ligand, abbreviated $LH_2$ (cf. Fig. VII.1(c)). The full cluster and its constituents are depicted in Fig.VII.1. They also form a flip-book animation running on the bottom right page margins to identify the individual parts of the assembled structure more easily. The actual chemical reaction pathway is slightly different.

The cluster is synthesized in-house by Dr. Claire Besson following a procedure published elsewhere [Kam09]. Its general structure is

$$[Mn_4L_2A_4] := Mn_4\,[2,6\text{–bis}(1\text{–}(2\text{–hydroxyphenyl})\text{iminoethyl})\text{–pyridine}]_2\,A_4, \qquad \text{(VII.1)}$$

where $A^-$ is an acetate, trifluoroacetate, or benzoate group. Structure (VII.1) will be abbreviated as {$Mn_4$} in the following. Only clusters with acetate, i.e. $CH_3COO^-$, are studied in this work. Two of these groups bridge two equivalent Mn sites of the core. Of each of these Mn sets, one Mn atom additionally chelates with another acetate. The entire {$Mn_4$} cluster has a size of about 32 Å.

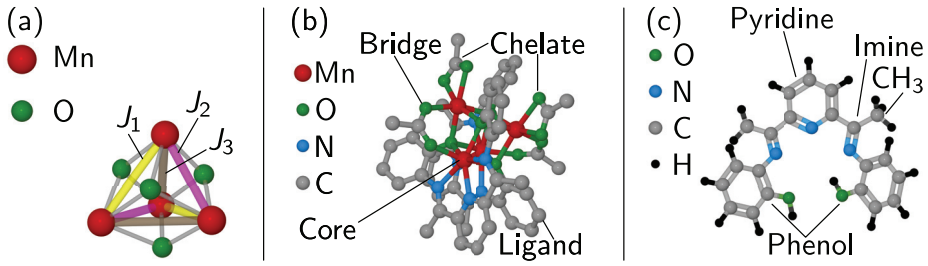


**Figure VII.1:** The {$Mn_4$} complex and its constituents. (a) The four Mn atoms of the $Mn_4O_4$ magnetic core have three different exchange couplings $J_i$ for symmetry reasons, induced by the O atoms (thin gray bonds). (b) The full {$Mn_4$} complex with core, two ligands and four acetates in chelating and bridging position. H atoms and double bonds are omitted for clarity. (c) The $LH_2$ ligand. The O atoms of the outer phenol groups become part of the core, with the Mn replacing the corresponding H atoms.

The Mn atoms each have a ground state spin $S_{Mn} = 5/2$ and an average distance of 3.43 Å. Their interaction is mediated via the four O atoms that originate from the ligand phenol group and can be described by the Hamiltonian

$$\hat{H}_{\{Mn_4\}} = -2J_1(\hat{S}_A\hat{S}_D + \hat{S}_B\hat{S}_C) - 2J_2(\hat{S}_A\hat{S}_B + \hat{S}_C\hat{S}_D) - 2J_3(\hat{S}_A\hat{S}_C + \hat{S}_B\hat{S}_D) + \sum_{i=A}^{D} g\mu_B\hat{S}_i B, \tag{VII.2}$$

where $A \dots D$ denote the four Mn atoms and the $J_i$ phenomenologically describe the three symmetry-induced different interaction paths (cf. Fig. VII.1(a)). These paths must not be confused with direct bonds. They depend on the wave function overlap within the Mn-O-Mn system and can be slightly tuned by withdrawing electrons from the core, i.e. by replacing the ligand. Magnetization measurements of the chosen ligand configuration yield best fits for $J_1 = -2.2\,\mathrm{K}$, $J_2 = -1.1\,\mathrm{K}$, $J_3 = -0.1\,\mathrm{K}$, resulting in a ground state antiferromagnetic intramolecular coupling, i.e. $S_{\{Mn_4\}} = 0$ [Kam09]. Only a strong magnetic field in the order of 30 T dominates the ligand-induced coupling and leads to a paramagnetic behaviour of the four Mn atoms, resulting in $S_{\{Mn_4\}}(B \gtrsim 30\,\mathrm{T}) = 10$. The Néel temperature is in the order of some 10 K but the low-field susceptibility approaches that of uncoupled $S = 5/2$ paramagnets only at room temperature.

## VII.2 Grafting $\{Mn_4\}$ complexes onto carbon nanotubes

The $\{Mn_4\}$ complexes can covalently attach to oxdiation-induced carboxyl (COOH)-groups of the carbon nanotubes (cf. section II.1.4). Chemically, one of the cluster's chelate acetate groups is replaced by the CNT carboxyl group:

$$\mathrm{CNT{-}CO_2H} + [\mathrm{Mn_4L_2(CH_3CO_2)_4}] \longrightarrow \mathrm{CNT{-}CO_2{-}[Mn_4L_2(CH_3CO_2)_3]} + \mathrm{CH_3CO_2H}, \tag{VII.3}$$

as illustrated at the end of the flip book animation on the bottom right corner of the page.

The reaction pathway (VII.3) was established on commercially available powder carbon nanotube samples in the framework of this thesis. Our results are reported in [Flö11b, Sae12, Mey12] and will be briefly summarized here. The rest of this chapter will then exclusively treat experiments performed on CVD-grown carbon nanotubes (see section IV.1.1) because they can be implemented straightforwardly into transport devices with the lithographic procedures introduced in the previous chapters.

We oxidized the carbon nanotube powder samples and suspended them in acetonitrile together with the $\{Mn_4\}$ cluster. The suspension was stirred and sonicated to ensure a thorough mixing. The reacted carbon nanotubes could be filtered out and washed. This approach yields gram amounts of the reacted compound in a shorter time than the below reported procedure on the substrates because of the good mixing from the sonication and stirring steps.

Thermogravimetric analysis (TGA) and magnetization measurements in a superconducting quantum interference device (SQUID) as well as Raman and absorption spectroscopy were conducted on this reaction product. The TGA measurements yield a catalytic effect of the functionalization and $Mn_2O_3$ can be detected in the combustion residue.



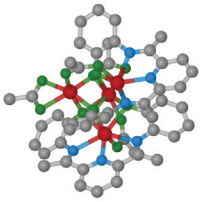

This demonstrates a successful decoration at least with the Mn core; TGA in a nitrogen atmosphere also provides evidence of the ligand. These measurements are given in the appendix B or are published in [Mey12], respectively.

The SQUID measurements of the reacted product are not a simple superposition of the constituents' magnetization curves. Instead, the hybrids approach a paramagnetic coupling already for weaker fields than the bare {$Mn_4$} complex. This indicates that a reaction has taken place, resulting in a slightly different intramolecular coupling of the Mn atoms. This interaction is weaker because the carbon nanotube is more electron-withdrawing than the original acetate group but still present, i.e. the core is still intact.

Raman spectroscopy yields results similar to the ones presented later on the CVD-grown carbon nanotubes. Inter alia, they show that the washing and filtering procedure indeed removes unreacted {$Mn_4$} complexes from the solution. The thus established functionalization routine can be adapted to CVD-grown carbon nanotubes as described in the following. `DuraSiN DTM-25233` transmission electron microscopy (TEM) membranes and amorphous quartz were chosen as substrates for the carbon nanotube growth described in section IV.1.1. The type of substrate depends on the experiments to be carried out later, with the membranes being suitable for TEM and Raman spectroscopy and the quartz for transport measurements and Fourier-transformed Raman spectroscopy. The as-grown carbon nanotubes are subsequently oxidized in air at 450°C with oxidation times reported in tables VII.1 and VII.2. These conditions are known to be harsh enough to not only attack the strongly pyramidized endcaps and pre-existing defects (cf. section II.1.4) but to also break the carbon nanotube sidewalls and generate new functional groups at these positions [Spu09].

| **Sample** | $\vartheta_{A00}$ | $\vartheta_{A02}$ | $\vartheta_{00}$ | $\vartheta_{01}$ | $\vartheta_{02}$ | $\vartheta_{03}$ | $\vartheta_{30}$ |
|---|---|---|---|---|---|---|---|
| Substrate | $Si_3N_4$ | $Si_3N_4$ | $Si_3N_4$ | $Si_3N_4$ | $Si_3N_4$ | $Si_3N_4$ | $Si_3N_4$ |
| Oxidation [min] | 0 | 2 | 0 | 1 | 2 | 3 | 30 |
| Functionalization | $CH_3CN$ | | {$Mn_4$} | {$Mn_4$} | {$Mn_4$} | {$Mn_4$} | {$Mn_4$} |
| TEM | — | | Titan | — | Titan | Pico | Tecnai |

**Table VII.1:** Fabrication parameters for functionalization investigation on samples $\vartheta$, fabricated on `DuraSiN DTM-25233` TEM membranes. Oxidation is performed at 450°C for the given time before functionalization. Samples $\vartheta_{A00}$ and $\vartheta_{A02}$ have been treated with pure acetonitrile only. Measurements in the `FEI Pico` microscope are carried out at 80 keV primary electron energy, the `FEI Titan 80-300` is operated at 300 keV and the `FEI Tecnai F20` at 200 keV.

Functionalization is carried out by immersing the samples into a 2.2 mM solution of {$Mn_4$} in acetonitrile ($CH_3CN$) for 8 d. The {$Mn_4$} clusters reach the carbon nanotubes by diffusion.[2] Subsequently, the samples are rinsed three times and put into a new beaker with pure acetonitrile for 4 d. The latter is repeated once without rinsing. Some samples

[2] Vigorous stirring and sonication as reported for the powder samples would destroy the membranes and detach the van-der-Waals-bound tubes from the substrate [Mey12].

| Sample | $\eta_{ox}$ | $\eta_{A02}$ | $\eta_{00}$ | $\eta_{02}$ | $\eta_{30}$ | $\eta^C_{ref}$ | $\eta^C_{00}$ | $\eta^C_{30}$ |
|---|---|---|---|---|---|---|---|---|
| Oxid. [min] | 0...60 | 2 | 0 | 2 | 30 | 0 | 0 | 30 |
| Functional. | — | $CH_3CN$ | $\{Mn_4\}$ | $\{Mn_4\}$ | $\{Mn_4\}$ | — | $\{Mn_4\}$ | $\{Mn_4\}$ |

**Table VII.2:** Fabrication parameters for functionalization transport measurements. The $\eta$ series is fabricated on amorphous quartz substrates. Pt contacts (70 nm thickness) have been evaporated on the as-grown networks. Oxidation is performed at 450°C before functionalization. Sample $\eta_{A02}$ has been treated with pure acetonitrile ($CH_3CN$) only.

are only treated with pure acetonitrile for 16 d to distinguish the impact of the solvent from the $\{Mn_4\}$ cluster.[3]

The sample nomenclature is as follows. Functionalized carbon nanotubes fabricated on the TEM membranes are denoted $\vartheta$, with the index giving the oxidation time. Samples treated with pure acetonitrile only (no $\{Mn_4\}$) have an additional $A$ in their index. The same indexing holds for the $\eta$ series which compromises all quartz substrate samples on which electrical resistivity measurements have been performed. The temperature and magnetic field dependence of the electrical transport have been measured for samples denoted with a superscript $C$.

## VII.3 Structural and elemental analysis in the transmission electron microscope

### Spectroscopic detection of the manganese

The natural question after the carbon nanotube functionalization is whether it was successful. If the result is positive, the density of the $\{Mn_4\}$ clusters and the structural integrity of the carbon nanotubes are of interest. All these issues can be investigated with a transmission electron microscope.[4] A third aspect, the chemical nature of the functionalization, will be analyzed using Raman spectroscopy.

Oxidation in air at 450°C is known to introduce a considerable amount of defects. The CNT walls partially decompose if carried out for 30 min [Spu09, Spu10a]. One should therefore expect a sufficient amount of carboxylate groups that can attach the clusters on sample $\vartheta_{30}$. Fingerprints of manganese can indeed be found in both available elemental analysis techniques, energy-dispersive X-ray (EDX) and electron energy loss spectroscopy (EELS) as shown in Figs. VII.2 and VII.3.

All EDX spectra of sample $\vartheta_{30}$ show the presence of manganese along with carbon, nitrogen, oxygen, and silicon by their $K\alpha$ lines. The Mn $K\beta$ shell can also be observed in several measurements (not shown). An exemplary spectrum is given in Fig. VII.2(a), together with a dark-field STEM image of the probed CNT acquired simultaneously. The scanned area only contains a bundle that is inhomogeneously decorated with a heavy

[3] Marked as acetonitrile functionalization in tables VII.1 and VII.2.
[4] All reference energies for the EDX and EELS measurements in this section are extracted from [Tho09].



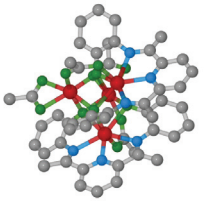

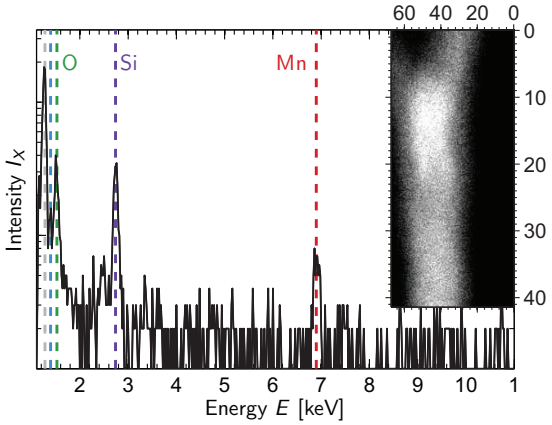


**Figure VII.2:** EDX semi-logarithmic spectrum of sample $\vartheta_{30}$. The Mn, Si, O, N, and C $K\alpha$ lines are marked (the latter two in blue and gray, respectively). The measurement has been performed on the CNT bundle shown in the inset (HAADF STEM mode). Scale is in nm.

element that the EDX spectrum identifies as Mn. Nevertheless, a prominent peak from the Si $K\alpha$ shell can be seen although the $Si_3N_4$ membrane is several hundred nanometers away. The Si peak is present in all spectra, regardless if they are taken in bright-field mode, if the electron beam is scanned as in Fig. VII.2 or if it is held stationary on a carbon nanotube. Further measurements additionally show signatures of the catalyst particles, Fe and Mo, that should also not reside on the CNTs. The presence of these elements can be attributed to scattered and stray electrons that probe the sample non-locally [Ege09].

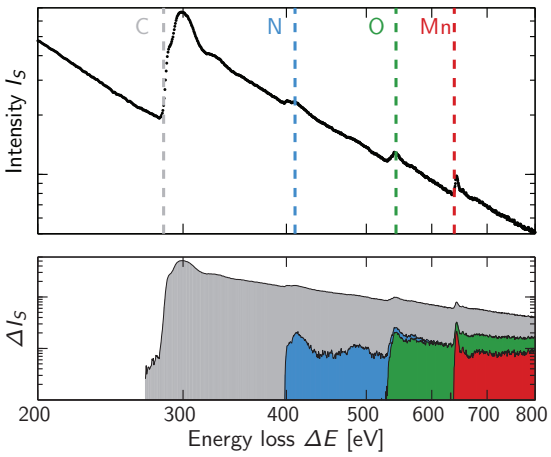


**Figure VII.3:** Double-logarithmic dark-field EEL spectrum of sample $\vartheta_{30}$. The binding energies of the C, N, O $K$ shell and the Mn $L$ shell are indicated. The bottom graph gives the intensities with the respective pre-edge background subtracted.

Electron energy loss spectroscopy performed in scanning TEM mode (STEM) does not suffer from this drawback because the focused electron beam probes the sample very locally. Consequently, only the expected elements carbon, nitrogen, oxygen, and manganese

can be observed on the carbon nanotubes as shown in Fig. VII.3. This particular spectrum has been acquired by scanning across a CNT bundle over a length of about 50 nm. All five investigated carbon nanotubes of sample $\vartheta_{30}$ exhibit signals from the C, N, and O $K$ as well as from the Mn $L$ shell. Their presence is additionally highlighted by the bottom graph where a pre-edge background $\sim E^{-a}$ has been subtracted.

### Repartition of the $\{Mn_4\}$ decoration

The existence of Mn on sample $\vartheta_{30}$ is thus unambiguously proven. The second point of interest is its distribution on the carbon nanotubes. A very direct approach is bright-field imaging of the sample. A typical micrograph is given in Fig. VII.4(a). It shows a small bundle of CNTs that is thickly covered by an amorphous material. The CNT walls can hardly be distinguished against this decoration. Only very few undecorated CNT segments can be found and are merely nanometer-long throughout the entire sample. They are additionally highly defective. These findings agree with the expected functionalization mechanism via carbon nanotube defects. It is also a first indication that these oxidation conditions are too strong to have reliable transport devices. The actual Mn repartition cannot be determined in this amorphous decoration.

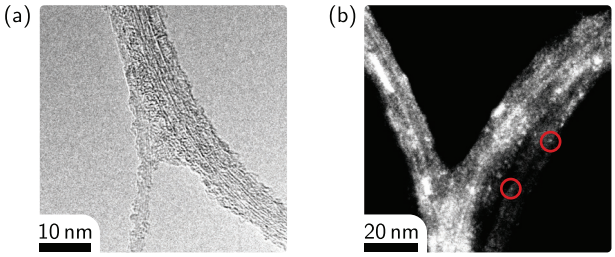


**Figure VII.4:** (a) Bright field TEM and (b) high-angle annular dark field STEM micrographs of different CNT bundles on sample $\vartheta_{30}$. Red circles denote bright, few-atom sized spots.

There is another imaging mode available that can resolve this issue better. A high-angle annular dark field scanning TEM (HAADF STEM) micrograph is given in Fig. VII.4(b). This technique is sensitive to heavy atoms, i.e. to the manganese distribution because Mn is by far the heaviest element in my samples as shown by the EELS measurements. Bright spots of various sizes can be seen on the entire bundle. The largest ones have a diameter up to 10 nm. The smallest spots (red circles) are mobile under the electron beam irradiation and have sizes comparable to few or even single atoms.

The thick coverage observed for the strongly oxidized sample $\vartheta_{30}$ could deteriorate contact interfaces. The large agglomerates shown in Fig. VII.4(b) tenfold surpass the expected core diameter of a single $\{Mn_4\}$ complex. This amassment could be partially due to a destruction of the $\{Mn_4\}$ under the electron beam and a subsequent clustering of the mobile atoms or molecular fractions. However, even the first frame on a virgin part of the sample displays similar agglomerations. It seems thus unlikely to have only the controlled, covalent bonding of individual complexes but rather both, a chemical attachment on the numerous defects but also an additional physisorption of complexes, resulting in large,



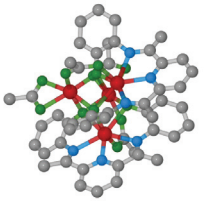

bright agglomerates. The influence of few covalently attached clusters on the carbon nanotube transport properties certainly cannot be studied with this system although it gives valuable information on the success of the chemical functionalization.

This issue may be solved, along with a better understanding of the reaction dynamics, by turning to shorter oxidation times. This should, as discussed in the introductory section II.1.4, result in a smaller number of carboxylate groups on the CNT sidewalls, i.e. less anchoring points. Three samples have been investigated in this regime, namely $\vartheta_{00}$ (not oxidized), $\vartheta_{02}$ (2 min oxidized) and $\vartheta_{03}$ (3 min oxidized). They all seem to be far less decorated with heavy atoms as exemplarily shown in Fig. VII.5(a+b) for samples $\vartheta_{02}$ and $\vartheta_{00}$, respectively.

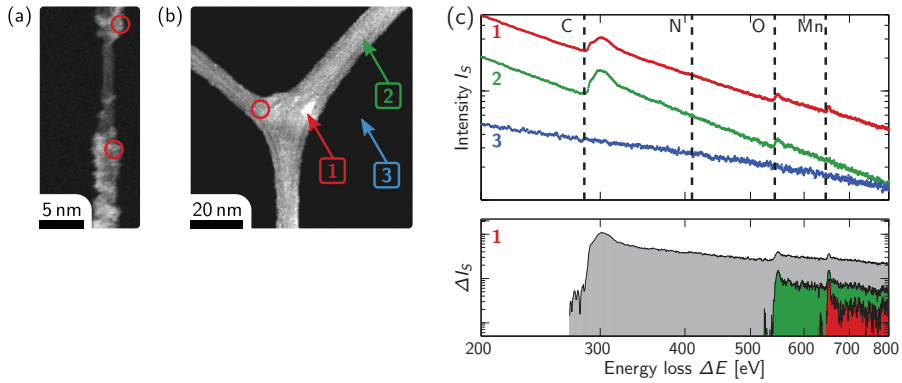


**Figure VII.5:** (a) HAADF STEM micrograph of sample $\vartheta_{02}$. The circles indicate bright, subnanometer-sized spots. (b) HAADF STEM micrograph of sample $\vartheta_{00}$. The arrows mark the points measured with EELS. (c) Double-logarithmic EEL spectra of sample $\vartheta_{00}$ on the points indicated in (b). The binding energies of the C, N, O $K$ shell and the Mn $L$ shell are given. Curves are offset for clarity. The bottom graph shows the intensities of trace 1 (on bright scatterer) with the respective pre-edge background subtracted.

The HAADF STEM micrograph in Fig. VII.5(a) displays an individual CNT or a very small bundle partially decorated with a uniform material. Some brighter spots can be found like the smallest ones in Fig. VII.4(b) with sizes ranging on the level of individual to few atoms. They are again mobile under the electron beam irradiation. This can be observed on all parts of this sample $\vartheta_{02}$. Occasionally a single, larger agglomerate resides on the tubes. Indeed, these mild oxidation conditions lead to a much weaker Mn functionalization and largely suppresses the clustering of the $\{Mn_4\}$ complexes. The smallest spots should be attributed to individual Mn atoms or small molecular fractions that come from $\{Mn_4\}$ clusters destroyed under the electron beam, judging from their scattering strength.

The same holds for the completely unoxidized yet functionalized sample $\vartheta_{00}$ shown in Fig. VII.5(b). This specific micrograph exhibits one of these isolated larger agglomerates

along with several small bright spots as in Figs. VII.5(a) and VII.4(b). Three EEL spectra have been taken on this bundle with the electron beam centered on the agglomerate, some 30 nm away from it but still on the bundle and one in the vacuum as indicated by the arrows. They are meant to identify the chemical composition of these structural elements to further support the assumptions above that are made from the scattering intensity.

These spectra are given in Fig. VII.5(c). The reference background spectrum does not show any ionization edges as expected. The spectrum on the agglomerate clearly exhibits signals from the C and O $K$ and the Mn $L$ shells. This is additionally highlighted by the bottom graph that gives the intensities of this trace with the respective pre-edge background subtracted. Nitrogen cannot be distinguished from the background.

The Mn signal vanishes when moving towards other regions of the bundle as demonstrated by the middle trace in Fig. VII.5(c). The O ionization edge can though still be observed. It is not possible to measure a Mn signal anywhere on samples $\vartheta_{00}$ and $\vartheta_{02}$ but on the agglomerates. Also an integration along a few square nanometer of such a CNT bundle only results in a sizable O ionization edge.

Therefore, the assignment of the (mobile) bright spots in the HAADF micrographs as Mn atoms cannot be directly supported by the spectroscopic measurements because the scattering intensity falls below the detection threshold. On the other hand, Mn is the only heavy element present in all EEL spectra taken on all samples $\vartheta$. These bright spots can thus nevertheless reliably be assigned to Mn atoms. Spectra with a sizable O but no Mn edge should also be expected since there is a number of oxygen-containing groups like phenols and ketones that the $\{Mn_4\}$ cluster cannot react with. It is also possible that some of the carboxylate groups have not been functionalized despite the long reaction time, e.g. because they were not accessible.

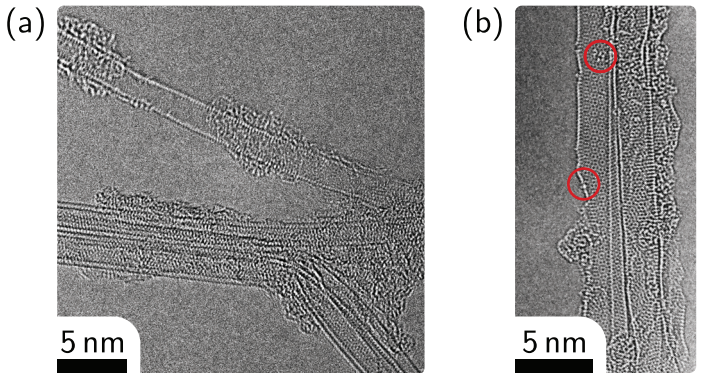


**Figure VII.6:** HR-TEM images of sample $\vartheta_{03}$. (a) Typical bundle and SWCNT with partial decoration. (b) Second bundle with a CNT wall damaged by the electron beam irradiation. Red circles denote some particularly intense spots attributed to the $\{Mn_4\}$ complex.

The bright-field TEM images of the shortly oxidized samples $\vartheta_{00}$, $\vartheta_{02}$ and $\vartheta_{03}$ are also very similar to each other. Two micrographs of sample $\vartheta_{03}$ are given exemplarily in



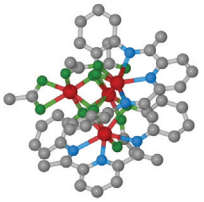

Fig. VII.6. The CNTs exhibit free sections that can be several tens of nanometers long, especially when being part of a bundle. Some tubes decompose, starting from already present defects when exposed to the electron beam as shown in Fig. VII.6(b). Some individual spots of the micrograph, two of them exemplarily marked by the red circles, are considerably brighter than the rest of the image, a behaviour not observed on pristine carbon nanotubes. This is attributed to individual Mn atoms or intact $\{Mn_4\}$ clusters. These spots are a few nanometers apart.

The HAADF-STEM and the bright-field HR-TEM measurements yield complementary information. The first technique is more sensitive to differences in the atomic number but it is difficult to image the morphology of the carbon nanotubes. Bright-field TEM is more suited for this purpose and distinguishes individual carbon atoms in the CNT lattice and the amorphous coverage. Its focal depth is, on the other hand, so small that Mn atoms outside the focal plane remain unnoticed. Most of the coverage is thus due to the wet chemistry applied for functionalization that is generally known to contaminate carbon nanotubes [Spu08].

A combination of EELS and bright-field imaging, the energy-filtered TEM, can unambiguously monitor the Mn repartition on the tubes (cf. section III.2). It is exemplarily performed on sample $\vartheta_{03}$ and displayed in Fig. VII.7. The image was taken using an energy window of $(640\ldots660)\,\mathrm{eV}$ with the background extrapolated from five pre-edge measurements. The Mn is found to be on some isolated positions, three of them exemplarily marked by the red circles. Spots of feeble intensity are noise from the detector and the background determination.

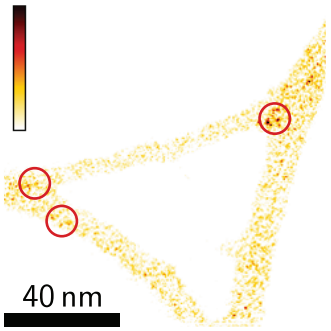


**Figure VII.7:** Energy-filtered TEM (EF-TEM) micrograph of sample $\vartheta_{03}$. The color scale gives the intensity of the image accepting only electrons with an energy loss of $(640\ldots660)\,\mathrm{eV}$ with respect to an extrapolated pre-edge background. Red circles mark some single Mn atoms or $\{Mn_4\}$ clusters.

To summarize, using the chemical and structural TEM imaging techniques I have shown that the $\{Mn_4\}$ carbon nanotube functionalization procedure, developed on CNT powder samples, has been successfully adapted for CNTs grown on substrate. The Mn decoration strength can be controlled by the oxidation time and varies between a complete coverage for the strongly oxidized sample $\vartheta_{30}$ to nanometer-separated Mn atoms. This density is in the range of other reported surface functionalization procedures [BN12] and slightly denser than the grafting of bigger molecules [Bog10, Zha08].

TEM measurements are rather elaborate and have special requirements on the sample design. An analysis of transport devices is only possible with an advanced layout as

presented in the previous chapters. Even then, the TEM measurements are only element-sensitive but cannot probe the chemistry of the grafting process. The low EELS signal and the weakness of the bonds render an analysis of the core level fine structure impossible that yield the chemical states of the elements.

Both issues can be addressed by Raman spectroscopy. Compared to the TEM, it is a relatively simple and straightforward technique and can be applied to almost any sample. Additionally, it is noninvasive and sensitive to the chemistry and can in principle distinguish between chemi- and physisorption. Raman spectra of the very same samples presented in this section are therefore analyzed in the following.

#### Summary

- The carbon nanotube functionalization with the $\{Mn_4\}$ complex has been analyzed systematically with different spectroscopic and microscopic TEM techniques to monitor the success and the degree of the decoration.
- EDX (sample $\vartheta_{30}$) and EELS measurements unambiguously show the existence of Mn on the CNTs. The Mn signal is localized to certain areas on the CNTs that appear bright in the HAADF STEM measurements. The density of these agglomerates can be controlled by the oxidation strength.
- The $\{Mn_4\}$ clusters disintegrate under the electron beam irradiation and the Mn atoms become mobile or cluster together. A TEM analysis of individual devices must therefore be the last in a series of measurements.
- Typical Mn distances, as determined by bright- and dark field TEM imaging as well as EF-TEM measurements, are several nanometers for mild oxidation conditions. This is comparable to other functionalization procedures. The repartition of the Mn is homogeneous as would be expected for the proposed reaction pathway.

## VII.4 Raman spectroscopy measurements

### Raman spectra of the constituents

The TEM measurements cannot provide a routine investigation of a successful functionalization because they require special sample layouts as presented in chapter IV and possibly damage the carbon nanotubes. Raman spectroscopy, on the other hand, is a non-invasive technique that is sensitive to chemical and structural properties of the CNTs [Fil03, Spu10b, Goß11a]. It is furthermore compatible with many sample layouts.

Having shown the successful decoration with $\{Mn_4\}$ clusters in the antecedent section, I will now turn to Raman spectroscopy measurements on the very same samples $\vartheta$ as investigated in the TEM. Two questions are of particular interest in this context, namely whether it is actually possible to detect the decoration by means of Raman spectroscopy and whether the $\{Mn_4\}$ is chemically attached or just physisorbed.



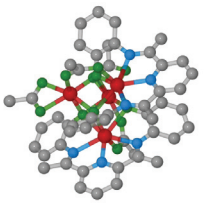

All Raman spectra in this section have been collected in a `Horiba Jobin Yvon LabRam HR-800` confocal Raman spectrometer at an exciting laser wavelength $\lambda_L = 632.87\,\mathrm{nm}$ with an intensity of $700\,\mu\mathrm{W}$. The spot size is in the order of $1\,\mu\mathrm{m}$. The samples have been automatically mapped, covering a region of about $100\,\mu\mathrm{m}$ to avoid misinterpretation due to local inhomogeneities of the functionalization. Spectra with a poor signal-to-noise ratio, resulting from an unfulfilled resonance condition with the carbon nanotubes in the laser spot, have been rejected.

The spectra of the pristine materials, i.e. the $\{Mn_4\}$ clusters and carbon nanotubes, are given in Fig. VII.8(a). The CNTs displayed by the lower, green curve have been oxidized in air for 2 min at 450°C like sample $\vartheta_{02}$. Consequently, they exhibit a small $D$ mode along with the $G^{\pm}$ modes at $\omega_D = (1328 \pm 2)\,\mathrm{cm}^{-1}$, $\omega_{G^-} = (1573 \pm 1)\,\mathrm{cm}^{-1}$ and $\omega_{G^+} = (1597 \pm 1)\,\mathrm{cm}^{-1}$, respectively. The $D/G$ ratio is about 0.06 which is about 1.5-fold larger than on a pristine sample as expected from previous measurements [Slo12, Mey12, Sae12].

The crystallized $\{Mn_4\}$ cluster displays 23 peaks in this wavenumber range as shown by the upper red trace, in strong contrast to the simple CNT spectrum. It is not necessary to assign these modes to specific molecular vibrations of the complex because the composition of the compound is known and verified by crystallization [Kam09]. Consequently, the spectrum can be divided into four parts, based on the peak repartition and the tabulated Raman frequencies of the contained organic groups [Pre09, Soc04]. These regions are colour-coded in Fig. VII.8(a).

**$<1230\,\mathrm{cm}^{-1}$** Seven modes of medium intensity with frequencies as expected for vibrations of CO and aromatic rings (orange-shaded region).

**$(1230 \ldots 1360)\,\mathrm{cm}^{-1}$** Five modes of medium to strong intensity. They can be attributed to COO-metal compounds, with the metal being Mn in this case (blue-shaded region).

**$(1360 \ldots 1500)\,\mathrm{cm}^{-1}$** Five modes of medium intensity. COO-metal vibrations and asymmetric $CH_3$ bending modes are expected in this wavenumber region. The most intense peak at $1455\,\mathrm{cm}^{-1}$ is probably caused by an asymmetric $CH_3$ bending (yellow-shaded region).

**$>1500\,\mathrm{cm}^{-1}$** Six modes of strong and medium intensity can be observed. Pyridine, benzene rings, and carboxylates exhibit Raman signals in this region. The two most intense modes at $1552\,\mathrm{cm}^{-1}$ and $1565\,\mathrm{cm}^{-1}$ are tentatively assigned to the pyridine that has a strong and narrow vibrational band there (magenta-shaded region).

### Raman spectra of the reacted carbon nanotubes

Exemplary Raman spectra of the reacted carbon nanotubes are given in Fig. VII.8(b+c). They are typical for the entire map taken on the respective specimen. The maps of an

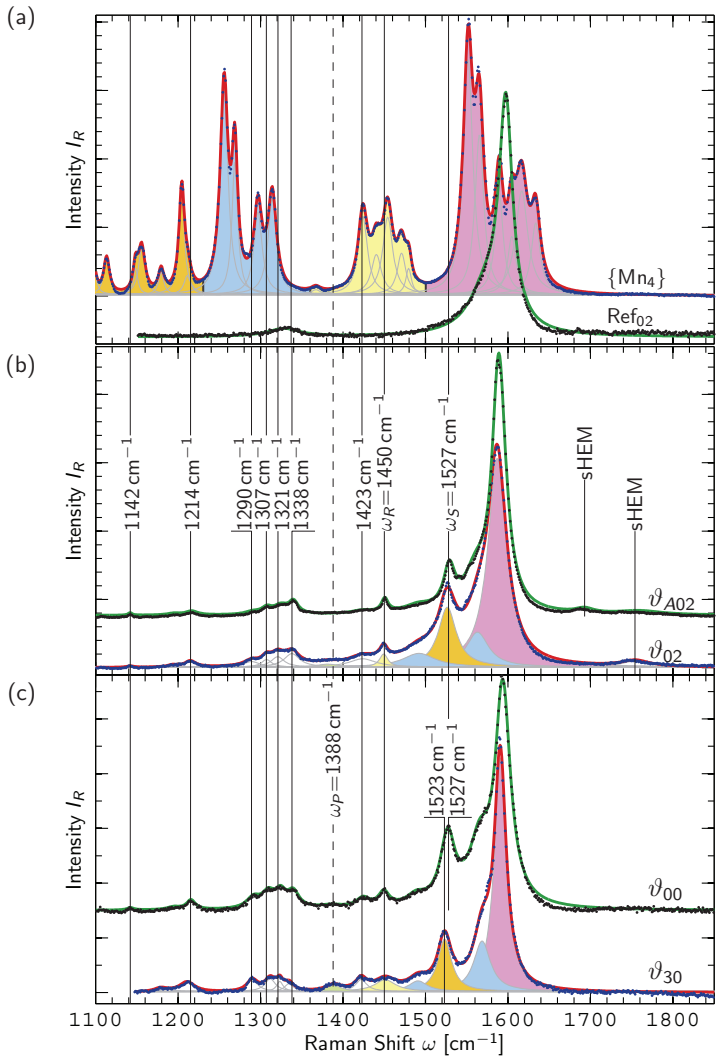


**Figure VII.8:** Example Raman spectra of (a) the $\{Mn_4\}$ complex (red) along with pristine carbon nanotubes oxidized for 2 min (green), (b) samples $\vartheta_{A02}$ (green) and $\vartheta_{02}$ (red), and (c) samples $\vartheta_{00}$ (green) and $\vartheta_{30}$ (red). The exciting wavelength is $\lambda_L = 633$ nm. All spectra are normalized to the $G^+$ mode and offset for clarity after subtraction of a linear background. Dots give measurement points, the thick solid lines are fits composed of a sum of Lorentzians (thin, gray lines). Some of the modes discussed hereafter are further highlighted. Vertical lines and text labels give averaged mode positions of all samples $\vartheta$.



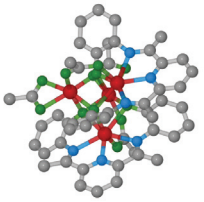

individual sample only vary in the signal-to-noise ratio of the single spectra, not in their shape.[5] Samples $\vartheta_{01}$ and $\vartheta_{03}$ have a spectral response very similar to sample $\vartheta_{02}$ (red, lower trace in part (b)) and are therefore not plotted separately. The same holds for samples $\vartheta_{A00}$ and $\vartheta_{A02}$ that have been treated with acetonitrile only. Thus, all statements in this section made for the depicted spectrum of sample $\vartheta_{A02}$ hold for the entire Raman map as well as for all spectra of sample $\vartheta_{A00}$. The same applies analogously to the other samples $\vartheta$.

All samples $\vartheta$ exhibit a multitude of Raman modes. The most prominent ones are indicated by the vertical lines in Fig. VII.8, the numbers are peak positions averaged for all samples $\vartheta$ with a standard deviation of $\sim 1\,\mathrm{cm}^{-1}$ if not mentioned otherwise in the text. All subfits are Lorentzian and have been omitted for the upper traces for clarity.

The discussions of the Raman spectra are conducted against the background of the TEM measurements presented in the previous section VII.3 and the experiments on the bulk functionalized carbon nanotubes [Mey12, Sae12]. The presence of Mn has been unambiguously proven on these very same samples $\vartheta$ and the reaction procedure has been successfully implemented on the very similar CNT powder specimen.

A comparison with the above discussed {$Mn_4$} modes shows that the hybrid systems have a Raman spectrum that is not a simple superposition of the pristine materials. Moreover, even samples $\vartheta_{A00}$ and $\vartheta_{A02}$ (acetonitrile-treatment only) share most of the peaks (green, upper trace in part (b)). The first is a sign of a chemical reaction because the hybrid system will develop new eigenmodes. The second indicates that the solvent acetonitrile also modifies the carbon nanotubes what has to be considered for a further analysis. In the following paragraphs, I will briefly discuss the spectral features of Fig. VII.8(b+c), i.e. of all samples $\vartheta$. Some modes will be further analyzed in the next subsections.

The most prominent carbon nanotube modes, the $G^{\pm}$ or high energy modes (HEMs), are still present in the hybrid spectra. They are marked magenta for the $G^{+}$ and blue for the $G^{-}$ modes. This is a first spectral evidence that the CNTs are still intact after the functionalization process because amorphous carbon or graphene only displays a single $G$ mode. It obviously agrees with the findings of the TEM measurements in the previous section. The $G^{\pm}$ modes exhibit an additional, sharp peak at $\omega_S = (1527 \pm 1)\,\mathrm{cm}^{-1}$ ($\omega_S = (1523 \pm 0.4)\,\mathrm{cm}^{-1}$ for sample $\vartheta_{30}$) that will be named $S$ in this work (orange fit). Two Lorentzian curves are required to fit the $G^{-}$ mode accurately what is probably an artefact due to the additional fit of the $S$ mode. The $S$ mode itself cannot be interpreted as a $G^{-}$ mode for several reasons that I will discuss in the end of this subsection.

Some spectra show a small and usually asymmetric maximum between $1650\,\mathrm{cm}^{-1}$ and $1900\,\mathrm{cm}^{-1}$ at various positions. It can be found for all, even as-grown samples. These peaks should therefore be assigned to the CNTs themselves. They are attributed to the so-called super-HEMs (sHEMs) [Tel09]. This is a second-order overtone of an infrared active phonon and thus requires a resonance of the CNT with the exciting laser light. The energy of the underlying phonon is additionally diameter-dependent. This is why the observed maxima change in position and intensity.

[5] The one exception is the sHEM mode which is due to a resonance condition as will be discussed.

Another Raman feature commonly observed on carbon nanotubes and also present in Fig. VII.8(a) is the $D$ mode. It is superimposed by three additional peaks between $1290\,\mathrm{cm}^{-1}$ and $1340\,\mathrm{cm}^{-1}$ in all spectra of all reacted samples $\vartheta$ as shown in Fig VII.8(b+c). This hampers an unambiguous assignment of the individual frequencies and intensities. The obtained position values fluctuate unsystematically by $\sim 5\,\mathrm{cm}^{-1}$ between individual spectra.

Some additional minor features, not present in the spectra of the pristine materials of Fig. VII.8(a), appear away from the $D$ mode and the HEMs. Two weak modes at $\omega \approx (1142 \pm 5)\,\mathrm{cm}^{-1}$ and $(1214 \pm 1)\,\mathrm{cm}^{-1}$ can be observed. The latter exhibits a shoulder at lower energies. They can again be found in all measured spectra of all samples $\vartheta$, although they are sometimes too weak to yield a reliable fit.

A prominent mode appears at $\omega_R = (1450 \pm 1)\,\mathrm{cm}^{-1}$, highlighted in yellow, and will be named $R$ in this work. It will be attributed to an asymmetric $CH_3$ bending and discussed in detail later in this section because it changes as a function of the chemical treatment and oxidation time as can be directly seen in Fig. VII.8(c). It is accompanied by a shoulder at $\omega = (1423 \pm 5)\,\mathrm{cm}^{-1}$.

So far, the discussed modes could be observed in all spectra, regardless if they were treated with the $\{Mn_4\}$ cluster or with acetonitrile only.[6] There is, however, one spectral feature that can only be observed on $\{Mn_4\}$-functionalized samples. It is particularly strong in the spectrum of sample $\vartheta_{30}$ and marked by the green Lorentzian subfit and the dashed vertical line $\omega_P = (1388 \pm 1)\,\mathrm{cm}^{-1}$. It will be named $P$ hereafter. This mode is strong in all spectra of $\vartheta_{30}$ but appears only in very few of the shorter oxidized samples $\vartheta_{00}$ to $\vartheta_{03}$ with an intensity similar to $\vartheta_{30}$. Most of these curves are either flat or slightly arched upwards in the wavenumber region between $1365\,\mathrm{cm}^{-1}$ and $1405\,\mathrm{cm}^{-1}$. All spectra of the samples $\vartheta_{A00}$ and $\vartheta_{A02}$ with only acetonitrile treatment are either flat or have a downward curvature in this region.[7] This behaviour is summarized in Fig. VII.9 that is a magnification of Fig. VII.8(b+c) around $\omega_P$. A more quantitative analysis of the intensities will follow in the next subsection. It is already clear at this point that the $P$ mode must not be related to only physisorbed $\{Mn_4\}$ clusters because the pristine $\{Mn_4\}$ Raman spectrum (Fig. VII.8(a)) does not exhibit any mode at $\omega_P$.

To conclude this subsection, I will now discuss the origin of the $S$ mode (orange in Fig. VII.8). At a first glance, its position and shape suggest to interpret it as a semiconducting $G^-$ mode. The carbon nanotube responsible for it would have a diameter $D \approx 0.9\,\mathrm{nm}$ calculated from eq. (II.10). This is a rather narrow CNT that is extremely well in resonance with the incoming laser light. Only very few CNTs meet this criterion, namely the (7,6), (8,3) and (10,3) chiralities using the Kataura plot in Fig. IV.13 [Pop04]. It is already rather unlikely that they should be produced in abundance during the CVD growth. With [Jor01a]

$$\omega_{\mathrm{RBM}} = \frac{248\,\mathrm{cm}^{-1}}{D[\mathrm{nm}]} \approx 287\,\mathrm{cm}^{-1} \qquad \text{(VII.4)}$$

[6] Disregarding the sHEM that depends on the nanotube chirality (vide supra).

[7] Fit results are more reliable if one includes a Lorentzian in this wavenumber region for all samples $\vartheta$ as in Fig. VII.8(b+c) to describe the background.



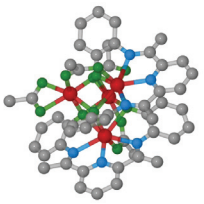

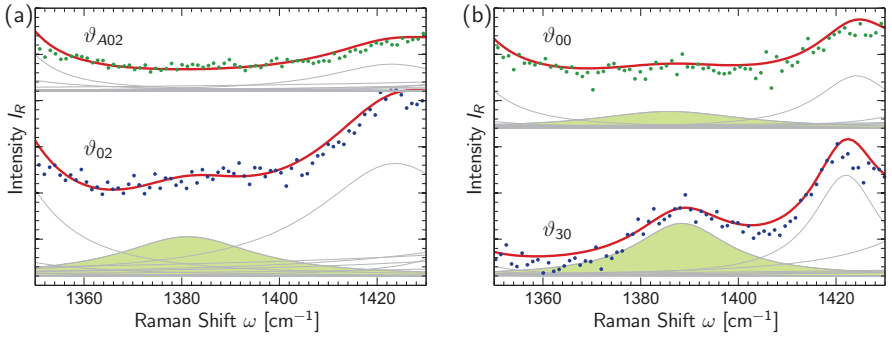


**Figure VII.9:** Magnification of Fig. VII.8(b+c) around the $P$ mode. Spectra are from (a) samples $\vartheta_{A02}$ (green) and $\vartheta_{02}$ (red) and (b) samples $\vartheta_{00}$ (green) and $\vartheta_{30}$ (red). The exciting wavelength is $\lambda_L = 633\,\mathrm{nm}$. All spectra are normalized to their $G^+$ modes and offset for clarity after subtraction of a linear background. Dots give measurement points, the thick solid lines are fits composed of a sum of Lorentzians (thin, gray lines). The subfit for the $P$ mode is highlighted in green.

one obtains an RBM frequency that cannot be observed as shown by the dashed line in Fig. VII.10. Even if the absolute numerical value was wrong, one should still observe one prominent RBM mode in all spectra which is not the case. A dominant, narrow CNT diameter can also not be observed in the TEM measurements (cf. previous section VII.3). Finally, the $S$ mode cannot be observed on as-grown and only oxidized samples (see Fig. VII.8(a)). It is therefore related to the functionalization procedure. This is also indicated by a shift of the position for the strongly oxidized sample $\vartheta_{30}$ that will be briefly analyzed in the following subsection.

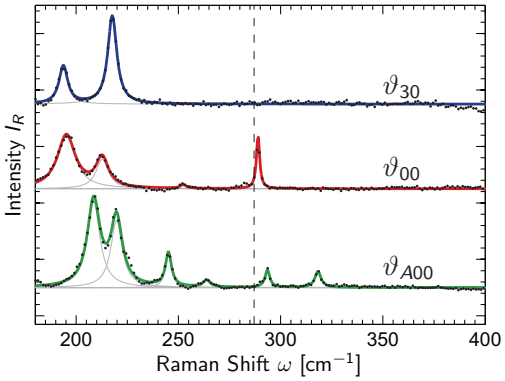


**Figure VII.10:** Raman spectra of the RBM region of samples $\vartheta_{A00}$, $\vartheta_{00}$, and $\vartheta_{30}$ from bottom to top (black dots). They are offset for clarity after removal of a quadratic background. The fit is a sum of Lorentzians (solid lines). The vertical dashed line gives the RBM frequency that would result if the $S$ mode was a $G^-$ mode.

The radial breathing modes also provide a definite proof that the samples $\vartheta$ do contain carbon nanotubes. This obviously agrees with the TEM measurements but also shows that

the spectral features discussed in this section must be attributed to chemically modified but structurally largely intact carbon nanotubes and not to amorphous carbon or unrolled CNTs.

The general observation of this overall discussion of the Raman spectra in Fig. VII.8(b+c) is that all samples $\vartheta$ show a rather similar response on first sight. This is especially the case for the mildly respectively not oxidized samples $\vartheta_{00}$ and $\vartheta_{02}$, also compared to $\vartheta_{A02}$ that has been treated with acetonitrile only. Two differences are the position and intensity of the sHEM and the RBMs which is due to a resonance effect of the carbon nanotubes. Therefore, most of the modifications from the pure CNT spectrum mentioned above should be attributed to a reaction with the acetonitrile and not to the $\{Mn_4\}$ cluster.

According to the TEM measurements and to the reaction pathway, a Raman signal originating from or at least related to the $\{Mn_4\}$ functionalization should be strongest for sample $\vartheta_{30}$. Indeed, the corresponding spectra do show some differences, namely in the $P$ and $R$ mode intensities and the $S$ mode position. This is a starting point for a further analysis of the spectra in the following subsections. There, I will compare the different oxidation strengths of the $\{Mn_4\}$-functionalized carbon nanotubes with the samples that have been treated in acetonitrile only to reveal trends in the data.

For this analysis, one has to keep in mind that the $R$ and $S$ modes must be attributed to a reaction with the acetonitrile because they also appear in the spectrum of sample $\vartheta_{A02}$. Nevertheless, they depend on the degree of decoration because they are clearly differnt in sample $\vartheta_{30}$. The $P$-mode, on the other hand, must be attributed to the $\{Mn_4\}$-functionalization as such because it cannot be found in any spectrum of samples $\vartheta_{A00}$ and $\vartheta_{A02}$.

### The *S* and *P* modes

The $S$ mode of sample $\vartheta_{30}$ is slightly red-shifted by about $4\,\mathrm{cm}^{-1}$ to $\omega_S = (1523.0 \pm 0.4)\,\mathrm{cm}^{-1}$. This is shown in Fig. VII.11 where the results of the least-squares fits of the entire maps of all measured samples are reported. Sample $\vartheta_{30}$, denoted by the crosses, has a spectrum that is clearly distinct from the other samples. This cannot be explained with a simple calibration error because, e.g., the $R$ mode does not shift correspondingly. Additionally, the $S$ positions of the intentionally functionalized samples $\vartheta_{00}$ to $\vartheta_{03}$ are also slightly redshifted.

This shift is a first indication that the $\{Mn_4\}$ cluster modifies the electronic structure of the functionalized carbon nanotubes although the origin of the $S$ peak remains unknown. This interaction depends on the degree of $\{Mn_4\}$ coverage that was found to be by far strongest for sample $\vartheta_{30}$ in the TEM measurements.

A mode that only appears for the $\{Mn_4\}$ functionalized samples is the $P$ peak. Consequently, I attribute it to the CNT-$\{Mn_4\}$ hybrid system. In the following, I will correlate its intensity to the degree of oxidation and to the number of carbon nanotubes. A similar analysis will be made fo the $R$ mode in the next subsection.

The degree of functionalization can be quantified by normalizing the $P$ with the $G$ mode, i.e. with the number of carbon nanotubes. The degree of functionalization is expected to



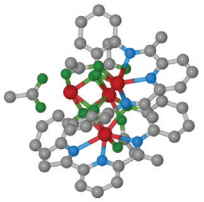

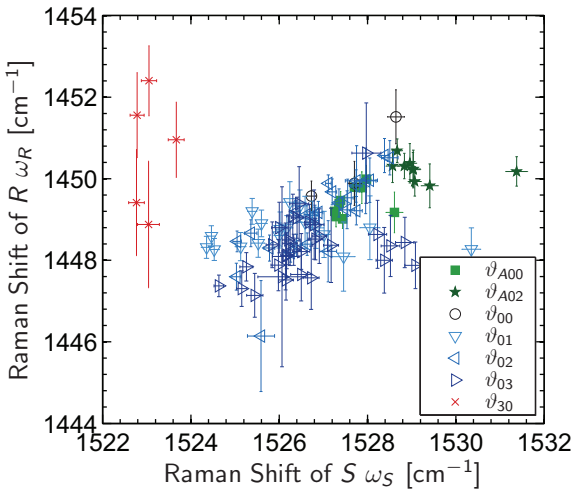


**Figure VII.11:** Positions of the $R$ and $S$ modes of samples $\vartheta$. Filled symbols denote the not-functionalized samples $\vartheta_{A00}$ and $\vartheta_{A02}$, open ones the shortly oxidized and functionalized $\vartheta_{00}$ to $\vartheta_{03}$ and crosses $\vartheta_{30}$ with 30 min of oxidation. Error bars are from the least-squares fits as in Fig. VII.8.

depend on the COOH group density if it is carried out as described in section VII.2. The total defect density, i.e. all deviations from a simple carbon nanotube wall like tube ends, holes, or attached chemical groups, is determined by the $D/G$ ratio [Dre00]. The $D$ mode is thus not a direct measure of the COOH density but the two are still intimately linked (cf. sections II.1.3 and II.1.4).

The $D$ mode is masked by several surrounding peaks and a least-squares fit becomes unreliable. The $P$ mode obviously cannot be fitted in samples $\vartheta_{A00}$ and $\vartheta_{A02}$ because it is absent. It is furthermore often of an intensity too low to be fitted reliably in samples $\vartheta_{00}$ to $\vartheta_{03}$. A numerical integration of the modes as described in appendix A is thus the preferred analysis procedure. This approach can obviously not at all distinguish the true $D$ mode from its surroundings. I therefore use the full area between 1240 cm$^{-1}$ and 1370 cm$^{-1}$ that I call $\tilde{D}$. The true $D$ mode is the major component of $\tilde{D}$ because it is $\tilde{D}/G \approx D/G$ when compared to pristine CNT spectra as the one given in Fig. VII.8(a). Numerically integrated and fitted areas follow the same trend discussed below but it is less accentuated for the latter.

The result of this analysis is shown in Fig. VII.12. It seems that the oxidation time does not have an influence on the $\tilde{D}/G$ ratio and that the values are rather scattered. One reason might be the three additional, acetonitrile-related modes that mask the true $D$ peak. The scatter in the data becomes larger when turning to the least-squares fit result. A second reason for the scattering can be local inhomogeneities in the sample, i.e. that certain areas contain more amorphous carbon that leads to an overestimation of the carbon nanotube $D$ intensity.

The numerically integrated $P/G$ is plotted against the $\tilde{D}/G$ ratio in Fig. VII.12. Negative values shaded in gray stand for an absent $P$ mode, i.e. an overall downward curvature. Measurements with $|P/G| \leq 10^{-3}$ seem to be flat. As expected from their shape, all

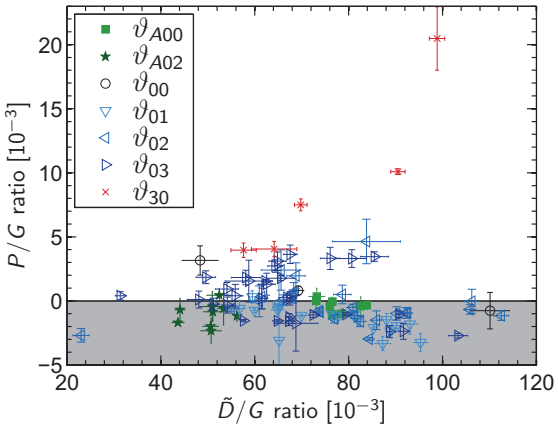


**Figure VII.12:** (a) Numerically integrated relative intensity of the $P$ mode vs. that of the $\tilde{D}$ mode, i.e. the $D$ mode superimposed with its surrounding signals. Symbols in the gray area denote an absent $P$ mode. Filled symbols stand for acetonitrile-only, open ones for shortly oxidized and functionalized samples and crosses for 30 min oxidation. Error bars estimate the uncertainty on the background determination.

spectra from samples $\vartheta_{A00}$ and $\vartheta_{A02}$ do not show any sign of a $P$ mode. The mildly oxidized and $\{Mn_4\}$ functionalized samples $\vartheta_{00}$ to $\vartheta_{03}$ sometimes do and sometimes do not exhibit a sizable $P$ mode. Sample $\vartheta_{03}$, that experienced the strongest oxidation, also shows the highest intensity within this subset. Sample $\vartheta_{30}$, finally, clearly has the strongest $P$ mode. It is, according to the reaction pathway and to the TEM measurements, the most decorated specimen. The $P$ mode, although it cannot be attributed to a specific vibration, can therefore be used for a spectroscopic detection of a successful functionalization. It must not be attributed to the acetonitrile because it cannot be observed in the respective samples $\vartheta_{A00}$ and $\vartheta_{A02}$ and also cannot be related to only physisorbed $\{Mn_4\}$ clusters because the pristine $\{Mn_4\}$ Raman spectrum does not exhibit any mode there.

### The *R* mode and the concept of sterical hindrance

Another difference in the spectra of the various samples $\vartheta$ is the shape and intensity of the $R$ peak. It becomes smaller and broader for sample $\vartheta_{30}$ which also reflects in the increased uncertainty of the peak position (cf. Fig. VII.11). This will be analyzed as for the $P$ mode in the previous subsection (cf. Fig. VII.12).

Fig. VII.13 shows the numerically integrated $R/G$ versus the $\tilde{D}/G$ ratio for all measured spectra. The samples fall into three groups. The long-oxidized samples $\vartheta_{30}$ show a relatively low $R/G$ ratio except for one spectrum that suffers from a poor signal-to-noise ratio. The shortly or not at all oxidized samples $\vartheta_{00}$ to $\vartheta_{03}$ fall in the middle of the graph while samples $\vartheta_{A00}$ and $\vartheta_{A02}$ (acetonitrile treatment only) have the highest $R/G$ relative to their $\tilde{D}/G$ ratios. This behaviour is highlighted by the gray area in Fig. VII.13.

This $R$ mode must be attributed to either physisorped acetonitrile ($CH_3CN$) molecules or to a reaction with the carbon nanotubes because it can also be found on samples $\vartheta_{A00}$ and $\vartheta_{A02}$ that have not been exposed to the $\{Mn_4\}$ complex.



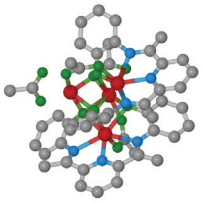

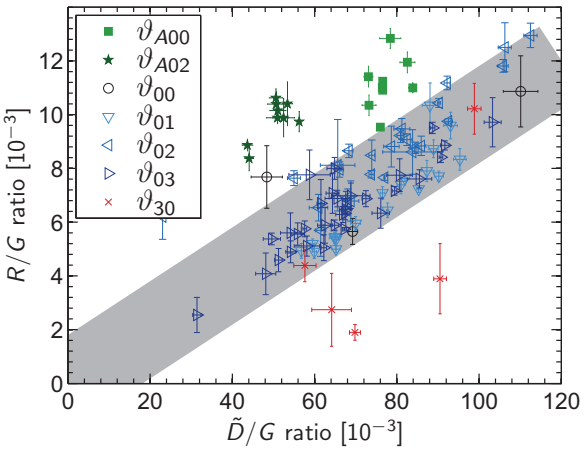


**Figure VII.13:** Numerically integrated relative intensity of the $R$ mode vs. that of the $\tilde{D}$ mode, i.e. the $D$ mode superimposed with its surrounding signals. The gray bar highlights the region of the shortly resp. not oxidized and {$Mn_4$}-treated samples. Filled symbols stand for acetonitrile-only, open ones for shortly oxidized and functionalized samples and crosses for 30 min oxidation. Error bars estimate the uncertainty on the background determination.

Pure acetonitrile exhibits four modes in the investigated wavenumber region, namely at 1373 $cm^{-1}$, 1406 $cm^{-1}$, 1447 $cm^{-1}$, and 1519 $cm^{-1}$. The first and third one are assigned to $CH_3$ deformations, the second one is a combination mode between a $CH_3$ rocking and a CC bending [Nee64]. The $R$ mode that is strongest for samples $\vartheta_{A00}$ and $\vartheta_{A02}$ (acetonitrile treatment only) lies within this wavenumber region and agrees in energy with a $CH_3$ bending observed on correspondingly functionalized carbon nanotubes [Bas05]. The other acetonitrile modes cannot be found, indicating that the $CH_3CN$ molecules are not simply physisorbed on the carbon nanotubes.

The transfer of the $CH_3$ group from the acetonitrile molecule to the carbon nanotube can most likely be explained by a two-step process, namely a hydrolysis of the acetonitrile and an esterification of the CNT. The first step is very slow but starts right after the production of the acetonitrile.

Acetonitrile contains trace amounts of water that react via

$$CH_3CN + 2\,H_2O \longrightarrow CH_3COOH + NH_3 \qquad \text{(VII.5)}$$

to acetic acid. When the carbon nanotubes are immersed for two weeks in the acetonitrile, the following reaction will eventually take place despite the low concentration of the acetic acid

$$CH_3COOH + CNT{-}OH \longrightarrow CNT{-}O(C{=}O)CH_3 + H_2O. \qquad \text{(VII.6)}$$

A direct esterification of the carbon nanotubes is possible but expected to be much slower than the presented process because it happens on the timescale of reaction (VII.6). Both schemes require OH groups the acid molecules can access. They are generated by the oxidation [Li11a] and are already present in small amounts on the as-grown CNTs. Some of these sites are blocked if the carbon nanotube is decorated with the large {$Mn_4$} clusters as illustrated in Fig. VII.14. This would explain why the {$Mn_4$}-free samples $\vartheta_{A00}$ and

$\vartheta_{A02}$ have the highest $R/G$ ratio compared to their $\tilde{D}/G$ ratio while sample $\vartheta_{30}$ falls well below the shortly oxidized samples $\vartheta_{00}$ to $\vartheta_{03}$ as shown in Fig. VII.13. The acetonitrile-only samples $\vartheta_{A00}$ and $\vartheta_{A02}$ give full access to the OH sites (upper side of the illustration) while the strong $\{Mn_4\}$ coverage of sample $\vartheta_{30}$ (lower side), as confirmed in the TEM measurements, sterically hinders process (VII.6). A continuous oxidation can furthermore lead to a significantly higher concentration of COOH compared to OH groups, i.e. less $CH_3$ functionalization sites at all because some of the OH will react to COOH [Ger11].

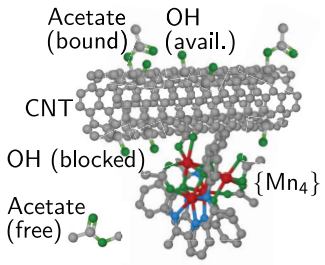


**Figure VII.14:** Illustration of the concept of sterical hindrance. A $\{Mn_4\}$-decorated carbon nanotube (bottom side) has less available OH sites for a acetate functionalization than a pristine one (upper side). Molecule sizes are to scale.

The $R$ mode has not been observed in as-prepared dispersions of CNTs in acetonitrile, taken at the same excitation wavelength [Deb11]. The authors could, on the other hand, detect an appreciable downshift of the $G$ mode position that they attributed to an interaction of the $\pi$ electron systems of the carbon nanotubes and the C≡N bond of the acetonitrile. This cannot be measured for my samples, again indicating that the acetonitrile molecules are fully removed as such and that the changes in the Raman spectra should be attributed to chemical reactions that only happen on the longer time scales of the week-long functionalization process.

### Comparison of the *P*, *R*, and *S* modes

The concept of sterical hindrance of $CH_3$ decoration agrees with the expected reaction of the $\{Mn_4\}$ cluster with COOH sites on the carbon nanotubes. It furthermore agrees with the expectation that stronger oxidized CNTs offer more attachment sites for the cluster as measured with the TEM. They show a much stronger decoration for sample $\vartheta_{30}$ which agrees with a greater number of blocked OH sites. It is, on the other hand, only an indirect proof of functionalization.

The $S$ mode as such must also be attributed to a reaction of the carbon nanotubes with the acetonitrile. There seems to be an electronic interaction with the $\{Mn_4\}$ cluster, leading a redshift (see Fig. VII.11). The $P$ mode, on the other hand, seems to be directly related to the $\{Mn_4\}$ functionalization because it cannot be observed on samples $\vartheta_{A00}$ and $\vartheta_{A02}$ which were only treated with acetonitrile (cf. Fig. VII.12). Both phenomena remain phenomenological because an assignment to a specific vibrational mode of the CNT-$\{Mn_4\}$ system is not possible in the framework of this thesis. They are both not a simple combination of the constituents because neither the Raman spectrum of the $\{Mn_4\}$ nor the one of the carbon nanotubes has a feature in this region.



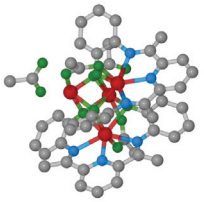

A further comparison of the $R/G$ ratio that gives an indirect proof of $\{Mn_4\}$ functionalization to the possibly more directly depending $P$ mode intensity and $S$ mode position, i.e. a combination of the data displayed in Figs. VII.11 and VII.12 is given in Fig. VII.15. The relationship of the $P/G$ with the $R/G$ ratio is given in part (a). Fig. VII.15(b) shows the relationship of the $S$ mode position with the $R/G$ ratio. The data point at $R/G \approx 0.01$ of sample $\vartheta_{30}$ that is apart from the other values in both plots originates from a spectrum with a poor signal-to-noise ratio and is not further considered. An evolution from samples $\vartheta_{A00}$ (no $\{Mn_4\}$ treatment) to the strongly oxidized $\vartheta_{30}$ can be observed in both plots, with the second strongest oxidized sample $\vartheta_{03}$ (right-pointing triangles) being closest to $\vartheta_{30}$ especially in part (a).

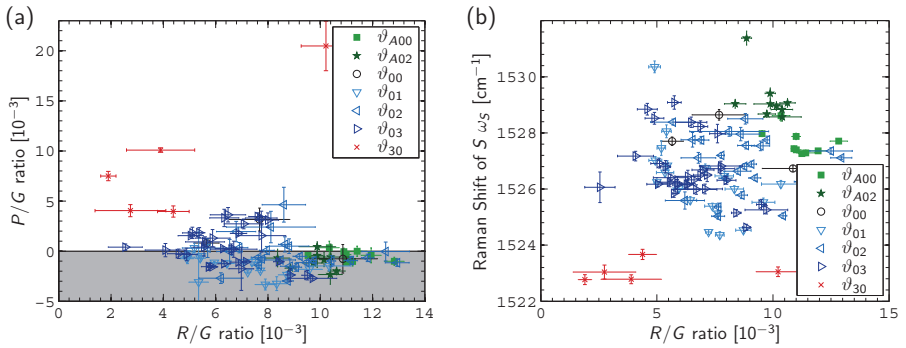


**Figure VII.15:** (a) Comparison of $P$ to the $R$ mode intensities calculated by numerical integration, both normalized to the $G$ mode. (b) Position of the $S$ mode vs. numerically integrated $R/G$ ratio. In both plots, filled symbols denote the not-functionalized, open ones the shortly oxidized and functionalized samples and crosses the 30 min oxidation. Error bars estimate the uncertainty on the background (numerically integrated data) resp. on the fit parameter (position of $S$).

The tendencies of the discussed $P$, $R$, and $S$ modes therefore agree with each other and also with the expected chemical functionalization route, i.e. stronger decoration for longer oxidation times. Some individual Raman spectra of samples $\vartheta_{00}$ to $\vartheta_{03}$ resemble to the ones of sample $\vartheta_{30}$ in regard of these modes, a behaviour not observed for the not $\{Mn_4\}$-treated samples $\vartheta_{A00}$ and $\vartheta_{A02}$. This can be explained by the non-homogeneous Mn decoration measured with HAADF STEM (Figs. VII.4(b) and VII.5(a+b)). All functionalized samples have areas with a Mn agglomeration. If the laser is focused on a region with several of these spots, a signal comparable to the most densely decorated sample $\vartheta_{30}$ should be expected.

To summarize, the $P$, $R$, and $S$ modes can serve as spectroscopic evidence for a $\{Mn_4\}$ functionalization as shown by the comparison of the TEM and Raman measurements. This is an important aspect for the integration of $\{Mn_4\}$-decorated carbon nanotubes into transport devices because Raman spectroscopy can be used more easily for a routine investigation and does not require the elaborate sample design introduced in

the previous chapters. It is also a non-invasive technique and can be applied before the transport experiments. It has, on the other hand, a much worse spatial resolution unless turning to near-field microscopy.

The TEM and Raman experiments do not give much information about a possible integration of $\{Mn_4\}$-functionalized carbon nanotubes into electrical transport devices. The $D/G$ ratio that is not much larger than for pristine CNTs is a first hint that an integration should be feasible in terms of integrity of the carbon nanotubes. I will further investigate this issue in the next section and analyze the impact of functionalization upon electrical transport properties. A third aspect will be the defect evolution with the oxidation time which is an important aspect for the functionalization procedure.

#### Summary

- Raman measurements of the $\{Mn_4\}$ cluster, the samples $\vartheta_{A00}$ and $\vartheta_{A02}$ that have been treated with acetonitrile but not functionalized further, and samples $\vartheta_{00}$ to $\vartheta_{30}$ that have been treated with a $\{Mn_4\}$ solution are presented in the wavenumber region between $1100\,cm^{-1}$ and $1850\,cm^{-1}$.
- The $\{Mn_4\}$ cluster displays a multitude of peaks grouped in four wavenumber regions that are attributed to its various organic components.
- The majority of the spectral changes due to the $\{Mn_4\}$ functionalization process must be attributed to a reaction with the solvent acetonitrile. Three modes, named $P$, $R$, and $S$ show a dependence with the degree of $\{Mn_4\}$ decoration as determined from the TEM measurements.
- The $P$ mode only appears in spectra that have been treated with the $\{Mn_4\}$ complex. It is a new mode of the hybrid system because it cannot be observed in the constituent spectra. The $S$ mode red-shifts for strong $\{Mn_4\}$ decoration. Both may serve as spectroscopic evidence for a successful functionalization.
- An indirect evidence for $\{Mn_4\}$ functionalization is a reduced $R$ mode which is attributed to a $CH_3$ group originating from the acetonitrile. The large $\{Mn_4\}$ cluster sterically hinders this reaction, and intentionally functionalized samples thus show a reduced $R$ mode intensity.

## VII.5 Transport measurements on functionalized carbon nanotube networks

### Influence of oxidation and functionalization on room-temperature conductivity

The TEM and Raman measurements lead to the conclusion that 30 min oxidation time strongly modifies the carbon nanotube reactivity to the $\{Mn_4\}$ cluster. The first minutes of oxidation, on the other hand, show a weak but finite modification of this reactivity.



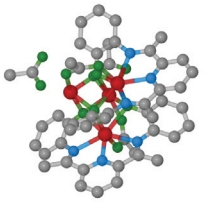

These results cannot clarify whether the degree of decoration is a continuous process with time or rather changes abruptly after a certain degree of oxidation. Another aspect that has not been addressed so far is the integrability of the functionalized carbon nanotubes into (quantum) transport devices.

Both issues, the time dependence of the reactivity to the $\{Mn_4\}$ complex as well as the influence on the conductivity are addressed in the following transport experiments. These are carried on carbon nanotube networks and as a function of oxidation time, functionalization, temperature, and magnetic field. The oxidation is furthermore monitored via the network Raman response.

This has been done by contacting an as-grown carbon nanotube network with 70 nm thick Pt pads on an amorphous quartz substrate using electron gun evaporation with a shadow mask (samples $\eta$). The contact separations are between 0.2 mm and 4 mm. The electrical measurements in this subsection have been carried out at room temperature in a probe station[8] in a four-terminal configuration with a current-biased sweep between $\pm 10\,\mu$A. Fourier-transformed Raman spectra are recorded at an excitation wavelength of $\lambda_L = 1064$ nm in a `VERTEX 70 FT-IR` spectrometer from `Bruker Optics`. This Raman setup has the advantage to probe a large section of the network at once with its millimeter-sized focus. This reduces the sensitivity to local variations of the network. Oxidation has been performed at 450°C in air as for the functionalization experiments reported above.

Typical resistance curves are given by the coloured traces in Fig. VII.16 that are normalized to the resistivity of the respective pristine nanotube network, i.e. contact combination. The oxidation behaviour of the conductivity neither depends on the contact distance nor on the network density. The resistance drops to about 40% of its original value within the first 7 min of oxidation. It has a minimum after about 10 min and starts increasing again until it saturates at about $(55 \ldots 65)\%$ of the value at $t = 0$. This evolution is attributed to the network alone and not to the contacts because all measurements are conducted in a four-probe configuration. The $D/G$ ratio that is concurrently monitored rises by a factor of about 1.5 during the first minute of oxidation and then saturates within its measurement accuracy.[9]

This evolution can be divided into four regions that can be explained by the different oxidation states of the carbon nanotubes (see section II.1.4):

**(0 . . . 1) min:** The $D/G$ ratio almost doubles while the resistance drops by about one third of its original value. A rising $D/G$ ratio indicates the creation of defects as is expected for an oxidation. These are predominantly phenol (OH) and ketone (C=O) groups [Zha03] that are expected to reduce the resistivity via chemical $p$-doping [Pan04]. Other possible mechanisms that cause a resistance decrease like crosslinks between different CNTs or shells of a multiwalled carbon nanotube [Kis04, Mik03] are unlikely under these rather mild oxidation conditions because they require two defects being created within a subnanometer distance.

[8] `Süss MicroTec EP6`, equipped with `Keithley 2400` and `2420` multimeters.

[9] The exact temporal development in the first minutes depends on the sample and the data analysis (numerical integration or fit). A saturation only after 2 min oxidation time can also be observed.

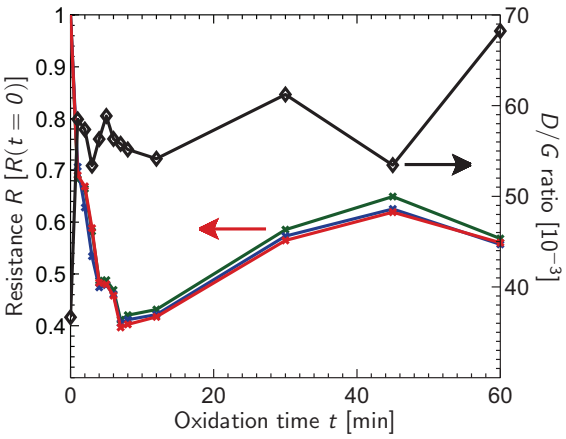


**Figure VII.16:** Normalized resistance for different network sections (coloured traces) and averaged $D/G$ ratio (black) of the CNT network on sample $\eta_{\text{ox}}$ as a function of oxidation time $t$ at 450°C. $D/G$ ratios have been calculated numerically from Raman spectra recorded at an excitation wavelength $\lambda_L = 1064\,\text{nm}$. The variation on the $D/G$ ratio due to the position on the network is in the order of 10%.

**(1...7) min:** The $D/G$ ratio remains constant while the resistance decreases further to about 40% of its original value. The first can be attributed to two effects, namely an equilibrium between the removal of amorphous carbon, the creation of new defects, and a change of the defect nature while keeping their number constant [Zha03]. It is likely that both mechanisms are at work because the removal of amorphous carbon should result in less perturbations on the $\pi$ electron system of the CNTs what agrees with the reduced resistance. Changing the initial defects to their next oxidation state, i.e. carboxylate groups (COOH) [Ger11], does not change the nature of the doping [Wan06] and should not strongly modify the resistance.

**(7...12) min:** The network resistance goes through a minimum while the $D/G$ ratio remains constant. This is a crossover from the regime of the first minutes of oxidation to the next state where the destruction of carbon nanotubes starts to dominate over the beneficial doping effects.

**$\geq$12 min:** The resistance rises while the $D/G$ ratio remains approximatively constant. The defects created so far enlarge further, resulting in a partial decomposition of the carbon nanotubes. This has been reported for similar experimental conditions [Spu09] and is observed on the few uncovered sections of sample $\vartheta_{30}$ in the TEM measurements (not shown). The resistance values for $t \geq 45\,\text{min}$ become unreliable because the contacts started to degrade. The $D/G$ ratio remains still constant because the oxidation mainly enlarges existing defects. Indeed, the overall Raman signal intensity is observed to drop continuously from one oxidation step to the next [Slo12] what agrees with the ongoing removal of amorphous carbon and the decomposition of carbon nanotubes (not shown).

The carbon nanotube conductance properties are thus altered by the oxidation but the CNT network remains sufficiently intact to mediate an electrical current. The effects of



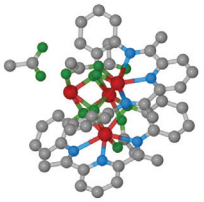

the second functionalization step, i.e. the ligand exchange and treatment with acetonitrile will be investigated in the following. Four samples of the $\eta$ series have been prepared for this purpose, $\eta_{00}$, $\eta_{02}$, $\eta_{30}$, and $\eta_{A02}$ which have undergone a functionalization with $\{Mn_4\}$ or acetonitrile after various oxidation times as listed in table VII.2.

The Raman spectra of these samples do not change before or after functionalization (not shown). This is due to an unfulfilled resonance condition of the $\{Mn_4\}$ cluster at this excitation wavelength (cf. Fig B.3 in appendix B). The network resistivity drops from its as-grown value depending on the oxidation duration as can be seen in Fig. VII.17. This decrease agrees with the above measurements on sample $\eta_{ox}$.

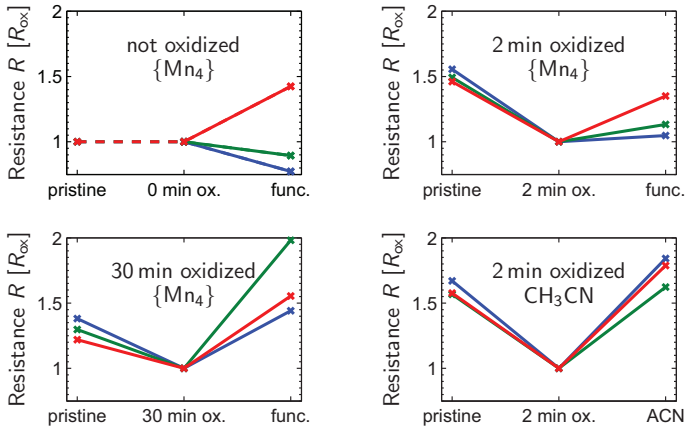


**Figure VII.17:** Network resistance in dependence of the functionalization, normalized to the value before functionalization. Every trace denotes a different contact combination, i.e. network section.

The resistivity dependence on functionalization gives rather ambiguous results but some general trends can be extracted. The resistance rises again after functionalization in most of the samples. This rise is strongest for sample $\eta_{A02}$ which was immersed in pure acetonitrile only. The intentionally $\{Mn_4\}$-functionalized samples $\eta_{02}$ and $\eta_{30}$ show a weaker increase, $\eta_{02}$ even has network sections where the resistivity remains constant. The not-oxidized sample $\eta_{00}$ does not have a clear development after contact deposition, the resistance rises for higher network densities and drops for lower densities as determined by the initial resistance.

These findings of the resistance dependence upon treatment with the acetonitrile and the $\{Mn_4\}$ complex agree with the concept of sterical hindrance of the unintended functionalization with $CH_3$ by the $\{Mn_4\}$ cluster, as reported in the previous section VII.4. According to their Hammett parameters, a phenol group ($C_6H_5OH$) will have stronger doping effects on the carbon nanotube than a toluene group ($C_6H_5CH_3$) [Ham37]. The exchange reaction $CNT{-}COOH \longrightarrow CNT{-}COO\{Mn_4\}$ should, on the other hand, not significantly alter the character of the carboxylate group. If the treatment with pure ace-

tonitrile replaces the phenol by toluene groups, the carbon nanotube doping decreases and the nanotube resistance consequently increases. This agrees with the observation in Fig. VII.17 (lower right). If a mildly oxidized sample is functionalized with $\{Mn_4\}$ clusters, on the other hand, some of the OH sites are blocked and the resistance increase is less pronounced (cf. Fig. VII.17, top row). This effect should be strongest for the harshly oxidized sample $\eta_{30}$ but instead the resistance is found to increase almost as strong as for the not functionalized sample $\eta_{A02}$. Here, the decoration is so strong as observed in the TEM measurements (cf. Fig VII.4) that the carbon nanotube $\pi$ system and thus the current flow are perturbed.

An optimal amount of oxidation can be found for the preparation of transport devices comparing the resistivity with the Raman and TEM measurements. The conditions of sample $\vartheta_{30}$ are too harsh for a reliable construction of a transport device consisting of an individual carbon nanotube because CNTs start to decompose and the decoration is too strong to detect the effect of single $\{Mn_4\}$ clusters on the transport. Completely unoxidized carbon nanotubes, on the other hand, may statistically not offer any reaction sites on the contacted region of the transport device. A mild oxidation in the order of a few minutes as for samples $\vartheta_{01}$ to $\vartheta_{03}$ should result in reliably, but not too densely functionalized CNTs. The oxidation should be shorter than seven minutes where the network resistivity is observed to rise again, i.e. to pass into the regime with severe defect concentration.

### Variable range hopping in carbon nanotube networks

The temperature dependence of the conductivity as well as the magnetoresistance of three samples has been investigated to determine the influence of the $\{Mn_4\}$ functionalization on these properties. They are named $\eta^C_{\text{ref}}$ for a pristine carbon nanotube network and $\eta^C_{00}$ ($\eta^C_{30}$) for a $\{Mn_4\}$-functionalized samples with no (30 min) prior oxidation. The fabrication was carried out as for the above discussed $\eta$ series. Magnetotransport measurements have been carried out in a $^4$He flow cryostat (cf. section III.4) equipped with a `Keithley 2636` multimeter.

All samples show a monotonous increase of their resistance upon decreasing temperature; two exemplary curves of samples $\eta^C_{00}$ and $\eta^C_{30}$ are depicted in Fig. VII.18. Such a dependence is a property of the carbon nanotube network. These can exhibit a variable range hopping (VRH) transport [Mot69, Mot79, Kim98, Efr75]. In this regime, commonly found in strongly disordered systems, the current is not mediated via a conduction band but the electrons hop from one localized state or impurity to the next. It is ostensive for a carbon nanotube network that the charge carriers have to migrate from one CNT to the next and that a single CNT also tends to split into several conductive islands due to intertube interactions.

The electrons choose a trajectory in a way to minimize both the energetic and spatial distance between neighbouring islands. The resistance is then given by

$$R(T) = R_0 \exp\left[\left(\frac{T_0}{T}\right)^{\left(\frac{1}{d+1}\right)}\right], \tag{VII.7}$$



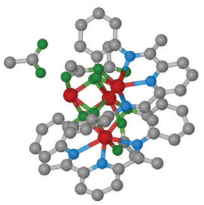

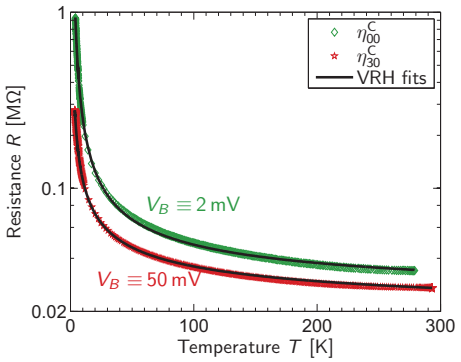


**Figure VII.18:** Resistance vs. temperature of samples $\eta^C_{00}$ (upper green) and $\eta^C_{30}$ (lower red curve), in the low- and high bias regime, respectively. Fits are according to eq. VII.7.

where $R_0$ and $T_0$ are fitting parameters and $d$ gives the dimension of the transport [Mot79]. The temperature curves indeed show these dependences as illustrated by the black curves in Fig. VII.18 that are the results of least-squares fits to the data. The dimensionality of the transport is sensitive to the applied bias voltage and ranges between $d = 1.2$ for $V_B = 2\,\mathrm{mV}$ and $d = 1.8$ for $V_B = 50\,\mathrm{mV}$. It is also slightly influenced by the network density. The electrical transport in the flat carbon nanotube network is obviously limited to two dimensions (high bias) and Coulomb interactions [Yan10a, Jai07] further reduce the dimensionality at low electron energies (low bias). These behaviours have been reported for several experiments on carbon nanotube networks [Jai07, Kim98, Yan10a]. Other models like thermal fluctuation-induced tunneling [Sal08] or weak localization [Yan10a], also reported for carbon nanotube networks and disordered systems, do not agree with the measured data.

The networks exhibit a nonohmic behaviour for temperatures $T \lesssim 20\,\mathrm{K}$ as is demonstrated in Fig. VII.19 for the strongly functionalized sample $\eta^C_{30}$. This is expected in the variable range hopping model where the energy for the transition from one site to the next is provided by the temperature or, alternatively, by the electric field if the voltage across the network is sufficiently large [Gra92],

$$V_B > \frac{k_B T}{e} \cdot \frac{1}{r} \cdot \Delta x, = \mathcal{O}(0.1\,\mathrm{V}) \; . \tag{VII.8}$$

Here, $r$ denotes the typical distance between two sites and $\Delta x$ is the contact separation. In this case, the resistance can be approximated by [Kim01, Gra92]

$$R(V_B, T) = R(V_B = 0, T) \exp\left(\frac{e V_B r}{k_B T \Delta x}\right) . \tag{VII.9}$$

Indeed, all three samples can be described by this dependence for sufficient bias voltages as shown in Fig. VII.20 with fits for $|V_B| \geq 0.5\,\mathrm{V}$.

Samples $\eta^C_{\mathrm{ref}}$ and $\eta^C_{30}$ have a negative magnetoresistance for temperatures below 200 K. A corresponding curve for $T = 3.6\,\mathrm{K}$ is shown in Fig. VII.21 where it reaches $\Delta R/R_0 :=$

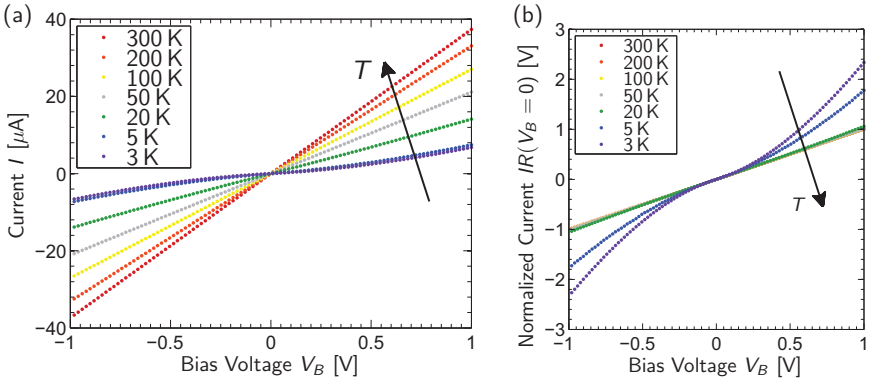


**Figure VII.19:** $IV$-characteristics of sample $\eta^C_{30}$ between 4 K and room temperature. (a) As-measured curves. (b) Current is normalized to the differential resistance at $V_B = 0$ to accentuate the non-ohmic character for $T < 20$ K.

$(R(B) - R(B = 0))/R(B = 0) = 3.5\%$ for $B = 1$ T for both samples. Thus, the magnetoresistance behaviour is not modified by the presence of the magnetic Mn(II) ions in the vicinity of the carbon nanotubes at these low fields. This is due to the $S = 0$ antiferromagnetic ground state of the $\{Mn_4\}$ complex that breaks up only at much higher fields as shown by the SQUID measurement (see appendix B, Fig. B.3(a)).

The low-field magnetoresistance of both samples can again be explained by the variable range hopping model. Here, a suppression of destructive interference of the forward moving electrons leads to a decrease of the resistance [Rai93, Vav05, Fuk79]. The mechanism is similar to the universal conductance fluctuations introduced in section III.3.2 and also involves a magnetic flux enclosed in a current loop [Vav05]. This particular finding is

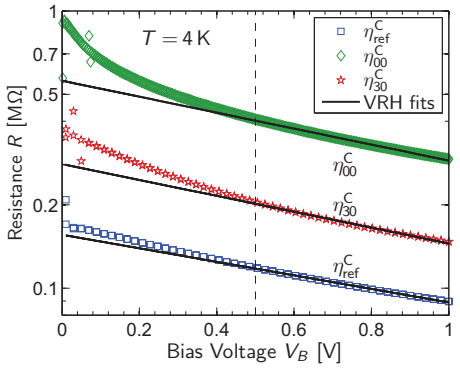


**Figure VII.20:** Resistance vs. bias voltage of samples $\eta^C_{\text{ref}}$ (blue), $\eta^C_{00}$ (green), and $\eta^C_{30}$ (red). The gray fits are according to eq. (VII.9) for $|V_B| > 0.5$ V (dashed line). Temperature is $T = 4$ K.

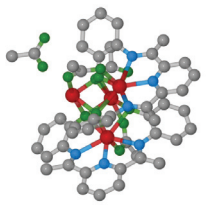

also expected for weak localization [Vav05] but it could not describe the previous resistance measurements. Therefore, the variable range hopping model is expected to be the dominant mechanism also for the magnetoresistance.

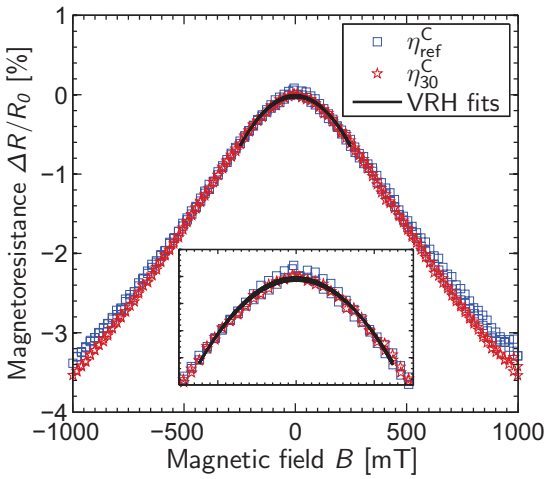


**Figure VII.21:** Magnetoresistance vs. magnetic field of samples $\eta^C_{ref}$ (blue) and $\eta^C_{30}$ (red). The black fits are quadratic for $|B| < 250\,\mathrm{mT}$ and magnified in the inset (blow-up for $|B| < 300\,\mathrm{mT}$). Temperature is $T = 3.6\,\mathrm{K}$ and bias voltage is $V_B = 400\,\mathrm{mV}$.

In summary, the low-temperature transport measurements can all be explained with variable range hopping commonly observed in carbon nanotube networks. The functionalization process does not alter the dependences on temperature as well as on electrical and low magnetic fields. This agrees with the transport measurements at room temperature where most changes could be attributed to doping effects. The strong decoration after 30 min of oxidation does not significantly alter the network properties reported in this section although the functionalization process itself leads to a clear resistance increase. The low-field magnetoresistance is not affected by the functionalization because the Mn(II) ions remain in their $S = 0$ ground state.

## Summary

- The resistance of a carbon nanotube network reduces upon oxidation due to $p$-doping of the generated groups. If the conditions become too harsh, the network starts to decompose and the resistance rises again. An optimum oxidation time for the functionalization process of some few minutes can be derived from these findings.
- The effects of the unintended $CH_3$ functionalization and the sterical hindrance of this process by the $\{Mn_4\}$ clusters can also be observed in the resistance change before and after the grafting process.
- The low-temperature transport properties of pristine and $\{Mn_4\}$ functionalized carbon nanotube networks can be explained by variable range hopping. The magne-

toresistance is not affected by the $\{Mn_4\}$ clusters because they remain in their $S = 0$ ground states for the investigated low fields.

## VII.6 Conclusions and outlook

The functionalization of carbon nanotubes with an antiferromagnetic tetramanganese complex by a carboxylate ligand exchange has been monitored with high-resolution transmission electron microscopy and spectroscopy, Raman scattering, and electrical transport. Only the combination of these techniques can comprehensively characterize the functionalization process.

The TEM measurements clearly detect the presence of Mn on the samples and show a dependence of the degree of decoration with oxidation strength as is expected from the chemical ligand exchange process. The transport experiments confirm this oxidative defect generation via the doping effects of the various groups. Raman measurements show one mode (the $P$-mode) that is directly attributed to the $\{Mn_4\}$ cluster and can monitor the increasing decoration upon stronger oxidation. They also detect an unintentional esterification of the carbon nanotubes from the acetonitrile solvent that is sterically hindered by the $\{Mn_4\}$ complexes.

The presented results are an important step towards devices for spintronic applications made of individual, functionalized carbon nanotubes. For this, the $\{Mn_4\}$ cluster needs to be replaced by a molecular magnet with a finite spin in its ground state. This could e.g. be a $\{Co_4\}$ cluster that is identical to the studied $\{Mn_4\}$ complex except for the metal ions and their intramolecular coupling. Therefore, all experiences gathered on the $\{Mn_4\}$ like the chemical functionalization process, its detectability in Raman spectroscopy, or the optimum oxidation strength can be directly applied to a $\{Co_4\}$ decoration. These carbon nanotube hybrids would have the advantage to have the magnetic center very close to the transport channel due to the cluster geometry.

The experience with the carboxylate ligand exchange and the carbon nanotube chemistry can also pave the way for a different class of materials, the so-called spin crossover complexes [Bou11, Med11]. These have two metastable states, a low- and a high-spin configuration that can be switched by various stimuli like temperature, light, and, most interesting for the transistor-like carbon nanotube devices, electric fields [Bou11]. These transitions can be rather sharp and spin lifetimes infinitively long. They would, however, need a grafting via an amine backbone because a direct ligand exchange would be too harsh. Nevertheless, this reaction involves the same carboxylate defects as studied in this chapter for the $\{Mn_4\}$ complex. The spin crossover complex would also have free ligands that could serve as spectroscopic handle for Raman scattering or for the elemental analysis in the TEM to monitor the integrity of the molecules.



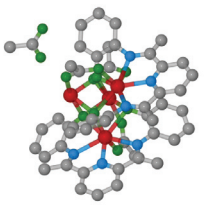

**Summary**

- Carbon nanotube functionalization with a tetramanganese(II) complex, based on a carboxylate ligand exchange, has been investigated with TEM, Raman, and electrical transport measurements. These measurements can only be interpreted jointly.
- The TEM spectroscopy reveals the presence of Mn on the samples. The decoration with the $\{Mn_4\}$ clusters increases with the oxidation time because more COOH attachment sites are created. The mildly oxidized samples have a typical cluster distance of several nanometers.
- The Raman spectrum of the hybrid system has contributions from the $\{Mn_4\}$ complex and the solvent acetonitrile. The latter also depends on the degree of decoration via a sterical hindrance mechanism. The dependence on the oxidation time can be reproduced.
- Resistivity measurements on oxidized and functionalized carbon nanotube networks detect an oxidative doping and agree with the results obtained by the other techniques. They furthermore hint to use an oxidation time of a few minutes to have a sizable amount of COOH defects and to preserve, at the same time, the structural integrity of the carbon nanotubes.
- Low-temperature magnetotransport measurements on these networks detect a variable range hopping mechanism that is not affected by the functionalization. The cluster remains in its $S = 0$ ground state for fields below 1 T.

# CHAPTER VIII

## Conclusions and outlook

This thesis presents experiments that connect the structure of various nanoscaled assemblies, namely carbon nanotubes, tetramanganese-decorated carbon nanotubes, and InAs nanowires, to their electrical and optical properties. This is achieved by correlating experimental techniques that probe a multitude of physical properties on the very same specimen. The presented correlation of transmission electron microscopy, Raman spectroscopy, and low-temperature quantum transport can thoroughly describe the sample, with each technique contributing information not accessible by the others.

This correlation is possible with a novel sample design that I have developed in the course of this thesis. It is fabricated by standard electron beam lithographic methods on a commercial transmission electron microscopy membrane. This setup is compatible with a variety of nanostructures and fabrication procedures because it is inert against almost any chemical environment and stable over a wide temperature range.

The capability of this sample design has been demonstrated by a comprehensive characterization of an individual triple-walled carbon nanotube transport device. I could determine the shell diameters by high-resolution transmission electron microscopy and compare these results to a Raman spectrum and to the electrical resistance of the specimen. With this information in hand, I can in turn narrow the identification of the innermost wall to a few possible semiconducting chiralities and pinpoint the outermost wall as the most likely metallic transport channel.

I have measured Coulomb blockade on two additional carbon nanotube devices with this sample design. They consist of a two-fold bundle of single-walled carbon nanotubes and an individual triple-walled carbon nanotube, respectively, as determined unambiguously by high-resolution transmission electron microscopy. These are, to my knowledge, the first reported quantum transport measurements unambiguously conducted on such systems. Both stability diagrams clearly deviate from a simple carbon nanotube pattern and can only be interpreted with the knowledge of their structure.

The two strands of the bundle turn into two parallel, tunnel-coupled quantum dots at cryogenic temperatures. The full system develops new molecular orbitals of bonding and



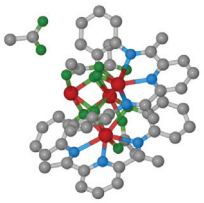

antibonding character. I can observe both cases, demonstrating that the also antibonding orbitals can contribute to the electrical transport. This hybridized quantum dot system is additionally capacitively coupled to a nearby metallic island. This leads to reproducible apparent gate switches that produce asymmetric, Fano-shaped gate traces.

The second, triple-walled carbon nanotube device has only one shell that defines its electrical transport characteristics. It breaks into a serial double quantum dot with a capacitive coupling, leading to a sawtooth-like shape of the Coulomb diamonds.

The interpretation of the above measurement results on structurally simple systems was only possible by the joint interpretation of several experimental techniques. The presented strategy becomes even more crucial when turning to an intended increase of complexity by fabricating hybrid molecular structures as, e.g., functionalized carbon nanotubes. They potentially have new properties that can be exploited for future spintronic devices. Such a functionalization needs to be monitored because the quantitative degree remains a statistical process.

I have characterized the covalent grafting of tetramanganese complexes onto carbon nanotubes by an exchange of carboxylate groups. Their degree of functionalization can be controlled by the oxidation time, i.e. the number of defects induced on the carbon nanotubes. Transmission electron microscopy directly demonstrates the successful decoration and repartition of the manganese. These results are compared to Raman spectroscopy measurements that are found to depend indirectly on the degree of functionalization.

The antiferromagnetic $S = 0$ ground state of the complex limits its applicability for spintronic devices. On the other hand, its manganese core can readily be replaced by different metals, leading to a finite magnetic moment. The experience on covalent carbon nanotube chemistry, gained by the experiments in this thesis, widens the choice of molecules to, e.g., molecular magnets or spin crossover complexes [Med11]. This latter class of materials has a magnetic center that can have two configurations, a low- and a high-spin–state. They are structurally distinct, leading to long lifetimes and sharp transitions. Switching is inter alia possible via an electric field and could be directly implemented into the field effect transistor structure of the transport devices [Med11]. An exemplary complex with an iron(II) center is sketched in Fig. VIII.1 [Cec01].

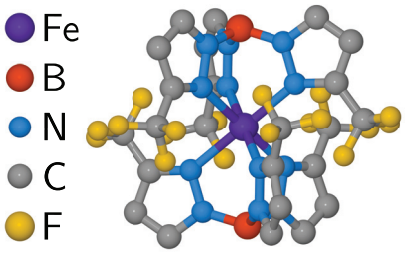


**Figure VIII.1:** Example of a spin crossover complex [Cec01]. It is an polypyrazolylborato iron (II) complex where the iron can has two metastable spin states. A nanotube could be connected by replacing one of the $CF_3$ groups with an amine. The others could be replaced by spectroscopy handles for Raman and transmission electron microscopy measurements.

The ligands of the tetramanganese or spin crossover complexes can be altered to make them directly detectable in transmission electron microscopy and Raman scattering by

incorporating heavy elements and Raman-active functional groups. This would yield information on the integrity of the clusters after the functionalization.

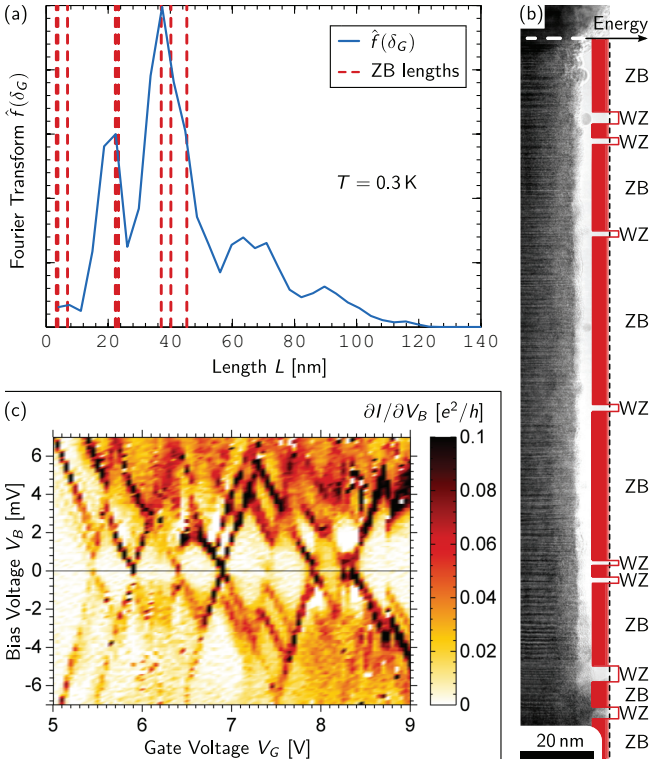


**Figure VIII.2:** Preliminary results on InAs nanowires. (a) The Fourier transform of the universal conductance fluctuations yields the size of the enclosed areas [Fri09b]. One dimension is limited by the nanowire diameter, the resulting length of the second side is given by the blue line. The vertical dashed lines indicate the zinc blende (ZB) segment lengths as determined by transmission electron microscopy. (b) TEM measurement taken under the same conditions as in chapter V. The conduction band minimum of the wurtzite (WZ) and zinc blende (ZB) crystal phases is sketched relative to the Fermi energy (vertical dashed line). The nanowire is contacted above the white dashed line. (c) Exemplary quantum dot measurement on an InAs nanowire at $T = 0.35\,\mathrm{K}$ that is yet to be investigated in the TEM.

The correlation of different investigation methods is not only important for carbon nanotubes but also for other self-assembled nanostructures such as InAs nanowires. I have measured the temperature dependence of the phase coherence length via universal conductance fluctuations on four such devices. They exhibit two distinct behaviours although the nanowires have a statistically identical stacking fault density as determined by high-



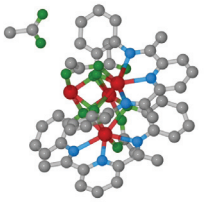

resolution transmission electron microscopy. These differences are thus attributed to point defects or to thermal strain during the cooling cycle.

Recent experiments performed with my novel sample layout on InAs nanowires suggest a direct influence of the stacking faults on the universal conductance fluctuation pattern itself. The size of some closed trajectories that are responsible for the fluctuations correlates with the area of the zinc blende segments. These results are given in Fig. VIII.2(a+b) where the Fourier transform of the universal conductance fluctuations taken at $T = 0.3\,\mathrm{K}$ is correlated to the zinc blende segment length. This relationship should be confirmed with additional measurements on nanowires of different stacking fault densities.

Another issue still under debate is the quantum dot formation in InAs nanowires. The size, estimated from the charging energy via a capacitive model, does not correspond to the contact spacing in most reported measurements [Sch10, Dic10b]. The barriers are thus assumed to be formed between two wurtzite segments. The presented sample layout is therefore the most promising way to validate this assumption. A stability diagram has already been taken on such a system and is shown in Fig. VIII.2(c). The length scale of this quantum dot experiment is now to be compared to a high-resolution transmission electron microscopy measurement, revealing the crystal structure. An effective sample length can also be extracted by tuning the nanowire into a Fabry-Pérot regime [Kre10]. This requires a good decoupling from the environment for which my sample design is perfectly suited.

Holographic measurements with the transmission electron microscope probe the potential landscape of the specimen. If a current flows through the nanostructure one obtains the voltage drops with nanometer precision [Lic08]. This experiment can be conducted with my novel sample design to directly study the influence of individual defects and functional groups on the electrical resistance.

These conducted and proposed experiments have the potential to accurately compare theory and experiment because small variations of a nanostructure, indistinguishable in standard transport measurements, can be identified and modeled. This can help to resolve ongoing debates on established material systems like carbon nanotubes and InAs nanowires but also thoroughly characterize emerging compounds like functionalized carbon nanotubes, $MoS_2$, or topological insulators.

# Appendix

## A Numerical integration of the Raman signals

The numerical integration of the Raman signals of the CNT-{$Mn_4$} hybrids is illustrated in Fig.A.1 by analyzing the $R$ mode of an arbitrary spectrum of sample $\vartheta_{03}$. Numerical integration boundaries for the various modes are given in table A.1. The background is assumed linear and determined by taking the average intensity in a region up to $\Delta\omega = 5\,\mathrm{cm}^{-1}$ symmetrically around the integration boundaries. This $\Delta\omega$ is varied to estimate an error on the background. The mode intensities are then averaged values for these various backgrounds with integration performed by a trapezoidal rule. Error bars give the respective standard deviation.

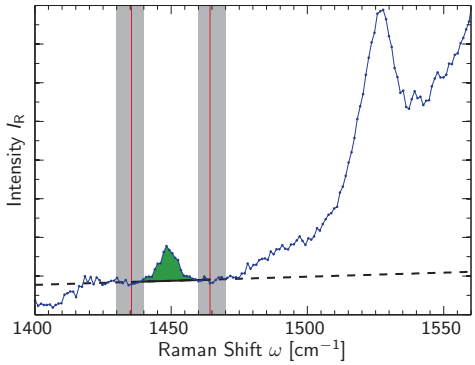


**Figure A.1:** Routine for numerical integration of the Raman spectra, exemplarily shown for an $R$ mode of sample $\vartheta_{30}$. Trapezoidal integration is performed between the red lines. A linear background is estimated by averaging the intensity in the shaded regions and given by the dashed line.

The integration boundaries for the $S$ and $G$ mode overlap as given in table A.1. The numerically integrated $S$ mode intensity is therefore subtracted from the likewise determined $G$ mode value.

This numeric integration is sometimes more reliable than a least-squares fit, especially if modes of low intensity or above a large background need to be described. Two converged fits using the same model but with only slightly different starting conditions[1] can converge

[1] Both are chosen by eye using the `peak-o-mat` software [Kri07] and describe the data equally well.



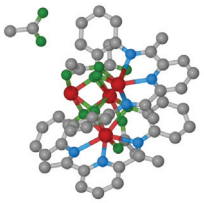

| Mode | $\tilde{D}$ | $P$ | $R$ | $S$ | $G$ |
|---|---|---|---|---|---|
| Lower bound [$cm^{-1}$] | 1240 | 1365 | 1435 | 1508 | 1465 |
| Upper bound [$cm^{-1}$] | 1370 | 1405 | 1465 | 1545 | 1675 |

**Table A.1:** Integration boundaries for the Raman spectra of the $\{Mn_4\}$-functionalized samples $\vartheta$.

into rather different fits as illustrated in Fig. A.2, using the same spectrum as for Fig. A.1. A convergence as for the lower, red trace was chosen if possible.

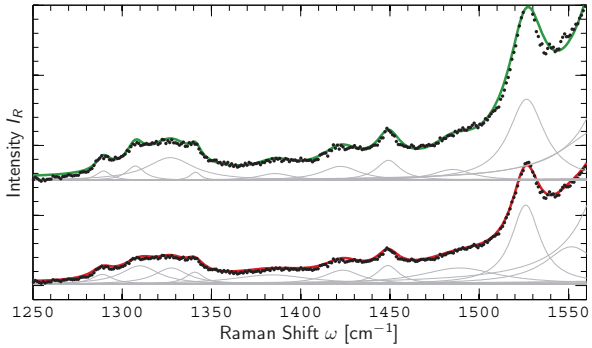


**Figure A.2:** Two converged least-squares fits of the same spectrum of sample $\vartheta_{03}$ as used in Fig. A.1, sharing the same model and almost identical starting conditions. Large differences can especially be observed for the $D$, $P$, and $R$ modes.

# B Additional information on the $\{Mn_4\}$ complexes

The bulk $\{Mn_4\}$ complex and the $\{Mn_4\}$-carbon nanotube hybrids have been investigated by several other investigation methods to establish the chemical functionalization process. This section gives additional SQUID magnetization measurements and a UV-vis absorption spectrum in Fig. B.3.

The magnetization curve of the reacted $\{Mn_4\}$-CNT hybrids is not the sum of its constituents. In fact, the carbon nanotubes withdraw electrons from the Mn core and weaken the antiferromagnetic coupling. The attached cluster can therefore reach the paramagnetic already at weaker magnetic fields. A similar effect has been shown by replacing the acetate in the ligand with a more electron-withdrawing trifluoroacetate [Kam09]. This is a clear indication that a reaction with the carbon nanotubes takes place, leaving the clusters largely intact. This is the process expected from reaction VII.3.

The UV-vis spectrum shows that the $\{Mn_4\}$ cluster is completely off-resonant for long wavelengths $\lambda \geq 1000\,\text{nm}$. Changing the solution agent only slightly shifts the maxima around $\lambda = 400\,\text{nm}$.

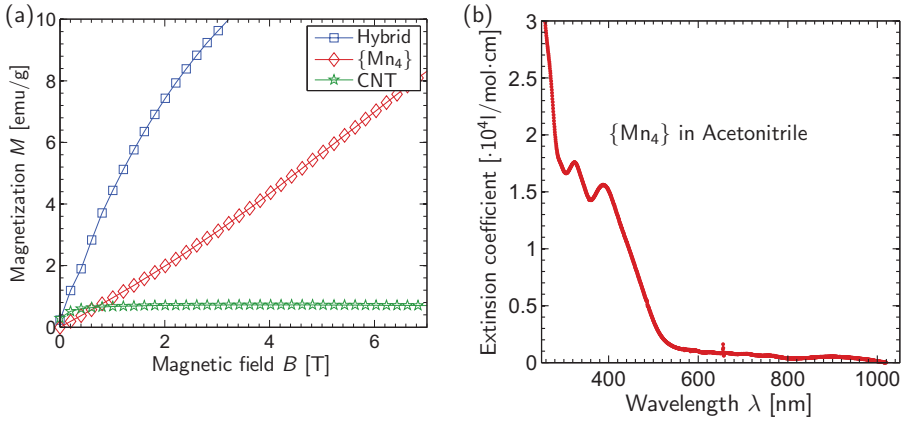


**Figure B.3:** (a) SQUID magnetization measurement on the reacted $\{Mn_4\}$-CNT hybrids, the $\{Mn_4\}$ cluster, and bulk CNTs (from top to bottom). Magnetization is normalized to the composition of the hybrids. (b) UV-vis absorption spectrum of the $\{Mn_4\}$ complex, dissolved in acetonitrile.

A thermogravimetric analysis of the bulk $\{Mn_4\}$-CNT hybrid is furthermore published in [Mey12].

## C Process parameters

A comprehensive list of all process parameters used for the samples prepared as described in chapter IV and with measurements presented in chapters IV (sample $\alpha$), V (sample $\aleph$), and VI (samples $\zeta$ and $\xi$) are given in table C.3.

The $\{Mn_4\}$-decorated samples presented in the chapter VII are prepared on DuraSiN `DTM-25233` meshes (samples $\vartheta$) or on amorphous quartz substrates, respectively. Carbon nanotube CVD growth has been done with CVD for 10 min at a temperature of 860°C. The CNT networks on the quartz substrates have Pt contacts of 70 nm thickness defined by a shadow mask with electron gun evaporation in a `Leybold L560`.

| | **Membrane** | **Substrate** |
|---|---|---|
| Current [nA] | 2 | 2 resp. 15 |
| Dose [$\mu$C/cm$^2$] | 1000 | 500 |
| Resolution [nm] | 12.5 | 12.5 resp. 50 |

**Table C.2:** Process parameters for the electron beam lithography performed on the samples reported in chapters IV, V and VI. The second set of numbers for writing on the substrate are the coarse parameters for the outer parts of the contacts.



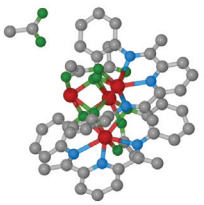

| | **Sample $\alpha$** | **Samples $\zeta, \xi$** | **Samples א** |
|---|---|---|---|
| Internal name | ATR6 | LGR14 | NKR1 |
| Type | CNT | CNT | InAs NWs |
| Chapter | IV | VI | V |
| DuraSiN | DTF-2523 | | DTM-25232 |
| Preparation | Oxygen Plasma (2 min, 600 W, 200 ml/min, TePla 300) | | |
| Spincoating | 12 min@180°C; AR-P669.07, 7,000 $min^{-1}$, 35 s; 12 min@180°C | | |
| e-beam (marker) | Both (fine) | | Membrane only |
| Development | 1 min@AR600-55, 20 s@IPA | | |
| Marker structure | $2 \times 3 : 15$ min $SF_6$ RIBE | | 5 nm Ti/60 nm Pt |
| Lift-off | 3 d@Acetone, Oxygen Plasma (1 h, 600 W, TePla 300) | | |
| e-beam (catalyst) | Membrane only | | — |
| Development | 1 min@AR600-55, 20 s@IPA | | — |
| Lift-off | 30 s@Acetone, 55°C, 380 $min^{-1}$ | | — |
| Growth | CVD: 10 min@860°C | | MOVPE |
| Locating | SEM | AFM | SEM |
| e-beam (contacts) | Both (3×) | Both | |
| Development | 1 min@AR600-55, 20 s@IPA | | |
| Cleaning (RIBE) | — | | 2 s $O_2$ RIBE |
| Cleaning (plasma) | — | | 30 s $Ar^+$ |
| Contacts | 5 nm Ti/60 nm Au | 2 nm Cr/60 nm Pd | 10 nm Ti/120 nm Pt |
| Lift-off | 3 d@Acetone | | |
| Imaging | SEM | | |

**Table C.3:** Process parameters used for the samples with individual nanostructures investigated in this work. The settings for electron beam lithography (e-beam) are listed in C.2. The machine used for reactive ion beam etching (RIBE) is an Oxford Ionfab 300+.

## Danksagung

Diese Arbeit ist in der ersten Person Singular verfasst – was natürlich eigentlich nicht stimmt, weil es viele liebe Menschen gibt, die zu ihrem Gelingen beigetragen haben. Diesen möchte ich an dieser Stelle ganz herzlich danken:

Zuerst wäre da **Prof. Dr. Claus M. Schneider** zu nennen, an dessen Institut ich die Arbeit anfertigen durfte. Er hat uns Doktoranden immer wunderbar den Rücken freigehalten und mir auch bei dieser photoemissionsfreien Dissertation viele wichtige Ratschläge gegeben.

**Prof. Dr. Thomas Schäpers** hat sich sofort dazu bereit erklärt, die Zweitkorrektur zu übernehmen und mir auch viel bei der Interpretation der InAs-Messdaten geholfen. Außerdem, und das finde ich noch viel wichtiger, habe ich auch persönlich und menschlich sehr viel von Dir lernen dürfen. Vielen lieben Dank dafür!

Meiner Arbeitsgruppenleiterin und inoffiziellen Doktormutter, **Dr. Carola Meyer**, möchte ich für die Betreuung der letzten drei Jahre ganz herzlich danken. An der guten Stimmung in der nanotube-Gruppe bist Du sicher nicht unschuldig! Und dass Du Dich hochschwanger durch meine wirren Ausführungen zum Quantentransport in komplexen Kohlenstoffnanoröhrenstrukturen gekämpft hast, ist alles andere als selbstverständlich.

Nun folgen einige höchst ungerechte Gruppendanksagungen. Ich hoffe, jeder von Euch fühlt sich persönlich angesprochen, aber bei einer Einzeldanksagung würde ich auch noch die letzte Seitenzahlbegrenzung für diese Doktorarbeit sprengen.

Da wäre natürlich zuerst unsere **nanotube-Gruppe**, mit denen jede Laborarbeit Spaß gemacht hat. **Dr. Karin Goß** hat mich in die Geheimnisse der Coulomb-Blockade in Kohlenstoffnanoröhren eingeführt und mir auch beim Interpretieren und Schreiben viel geholfen. Vor und nach Feierabend war es immer lustig mit Dir! Auch mit **Michael Schnee** hatte ich immer etwas zu lachen, im Büro, im Labor, und auch abends. **Dr. Christian Spudat** hat mir die Kohlenstoffnanoröhrensynthese beigebracht, sicherlich wichtig für diese Arbeit. Und dann sind da noch **Cate Morgan, Peter Weber, Dominik Metten, Lidia Saptsova, Victoria Guana Zapata** und vor allem **Fabian Fritz**, die mir immer geholfen haben.

Sehr viel zum Gelingen dieser Arbeit haben natürlich auch „meine“ Studentinnen und Studenten beigetragen: **Marlou Slot**, die eine Bachelor- auf Masterarbeitsniveau geschrie-



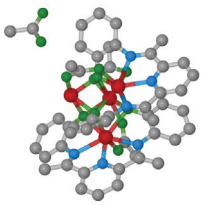

ben hat; **Anna-Katharina Saelhoff** und **Henrik Flötotto**, die die {$Mn_4$}-Funktionalisierung etabliert und vermessen haben; and of course **Mark Brunson** and **Francisco Pelaez III** who made it all the way from the US to solder and to bring good humour! Und schließlich ist da noch **Martin Schuck**, der sich auf eine interinstitutionelle Diplomarbeit eingelassen und die InAs-Arbeiten ein gutes Stück weitergebracht hat. Liebe Gutachter und Leser, dass die Doktorarbeit so lang ist, liegt nicht an mir, sondern an ihnen!

Ein Nullsummenspiel hingegen ist die **Kaffeerunde**, bestehend aus der nanotube-Gruppe und Freunden: Der Kaffee steigert sicher die Konzentration und damit die Produktivität. Aber (Chef, bitte weghören) diesen Zeitgewinn haben wir direkt wieder durch die halbfachlichen Gespräche zunichte gemacht. Dafür war zumindest die Studienfahrt ins Ruhrgebiet in unserer Freizeit.

**Dr. Claire Besson** hat den Ligandenaustausch entwickelt, alle Schritte vom Mn-Atom zur {$Mn_4$}-dekorierten Kohlenstoffnanoröhre durchgeführt und mir immer wieder sehr geduldig die Chemie erklärt. Außerdem hat sie mir sehr viele sehr gute Korrekturvorschläge gemacht. Et enfin, merci bien que tu m'as laissé te parler en français bien que je ne le sache guère!
An dieser Stelle möchte ich auch **Prof. Dr. Paul Kögerler** für die gute Zusammenarbeit danken und dafür, dass ich an Eurem FT-Raman-Aufbau messen durfte.

**Lothar Houben** hat die Kohlenstoffnanoröhren-TEM-Aufnahmen angefertigt. Mir kam es vor wie „einfach so", als Du die einzelnen Kohlenstoffatome durch hundert Lagen $Si_3N_4$ hindurch aufgelöst hast. Wer es nicht glaubt, schaue in Kapitel VI nach.

Die **Berliner**, genauer gesagt **Asmus Vierck, Prof. Dr. Janina Maultzsch** und **Matthias Müller**, haben die Raman-Spektren der {$Mn_4$}-Hybride aufgenommen und diskutiert und mich in die Geheimnisse von `peak-o-mat` eingeführt.

**Dr. Stefan Trellenkamp** hat die Elektronenstrahllithographie übernommen und das Design der TEM-Membrane diesbezüglich mitentwickelt. Außerdem hat er mir immer wieder geduldig die absoluten Grundlagen erklärt.

Eine Schlüsselstellung für diese Arbeit hat sicher auch **René Borowski**: Ohne Dich hätte ich keinen Reinraum und kein RIBE-Ätzen zur Verfügung gehabt, das wären drei Kapitel weniger. Und während der Prozesse haben wir uns wunderbar übers Laufen unterhalten. Gleichzeitig möchte ich mich auch bei den anderen **PGI-Reinraumverantwortlichen** bedanken.

Der Meister der Kälte ist **Herbert Kertz**. Selbst wenn ich wollte, hatte ich meist keine Chance, die Kryostaten zu füllen, weil Du es schon erledigt hattest. In diesem Zusammenhang geht ein zweiter Dank an **Prof. Dr. Thomas Schäpers** und seine **Arbeitsgruppe**, die mich in ihrem Magnetlabor aufgenommen, unterstützt, begrillt und sehr gut unterhalten haben. Danke, dass ich eine Art externes Gruppenmitglied sein durfte!

Zurück zur ganz praktischen Hilfe: **Thomas Jansen**, **Michael Schnee** und **Hans Wingens** haben meine Proben metallisiert. **Stephany Bunte** hat sie dann geschnitten und **Hans Peter Bochem** die Messungen am Rasterelektronenmikroskop durchgeführt.

**Dr. Frank Matthes**, **Dr. Julius Mennig** und **Sarah Fahrendorf** haben mich mitunter auch selbst REM-Aufnahmen an ihrem Nanospintronicclustertool anfertigen lassen.

Bei elektronischen Problemen konnte ich mich immer an **Jürgen Lauer, Heinz Pfeiffer** und **Norbert Schnitzler** wenden. **Bernd Küpper** und **Konrad Bickmann** waren meine Ansprechpartner, wenn es um Mechanik oder Nichts (vulgo: Vakuum) ging. Und **Margret Frey** hat alle Kämpfe mit der Verwaltung für mich ausgefochten.

Eine Initialzündung für die Messungen an den InAs Nanodrähten kam von **Kilian Flöhr**, als er mir vorschlug, seine Indiumnadelmethode einfach mal für die Positionierung der Drähte auf den Membranen auszuprobieren.
Die Drähte an sich wurden mir von **Kamil Sladek** aus der Gruppe von **Dr. Hilde Hardtdegen** zur Verfügung gestellt. Die anschließenden Diskussionen der Messungen, auch mit **Dr. Beata Kardynal**, haben mir sehr geholfen.
**Falk Dorn** und **Dr. Markus Heidelmann** aus der Gruppe von **PD Dr. Thomas E. Weirich** haben die TEM-Aufnahmen der InAs-Nanodrähte gemacht.

**Prof. Dr. Maarten R. Weegewijs** hat sich einmal die Messdaten der Quantenpunkte aus Kapitel VI angeschaut und mir direkt eine Musterlösung gegeben.

Als Lektoren möchte ich den bereits genannten und außerdem **Michael Schnee, Moritz Plötzing, Marlou Slot, Fabian Fritz**, **Sebastian Heedt** und **Anne Frielinghaus** danken.

**Paul, dem Elektron** danke ich für die gute Zusammenarbeit.

Bei meinen **Freunden**, die bis hierhin noch keine Erwähnung gefunden haben, möchte ich mich ganz herzlich dafür bedanken, dass ich nicht nur in den letzten drei Jahren immer auf Euch zählen durfte! Ich wusste, dass ich bei Euch immer ein offenes Ohr und auch einfach Erdung in der Welt jenseits der Physik finden konnte.
Bei meinen **Eltern** und meiner **Familie** möchte ich mich bedanken, dass Ihr mich unterstützt habt, egal, was ich auch gemacht habe. Und ich weiß, dass ich mich auch in Zukunft auf Euch verlassen kann!



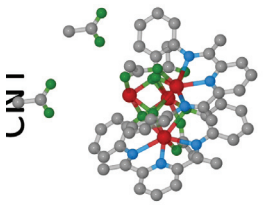

## Bibliography


[Aff01] C. Affentauschegg and H. H. Wieder. *Properties of InAs/InAlAs heterostructures.* Semiconductor Science and Technology **16**, 8, 708 (2001). URL http://stacks.iop.org/0268-1242/16/i=8/a=313. 17

[Aji95] H. Ajiki and T. Ando. *Carbon Nanotubes: Optical Absorption in Aharonov-Bohm Flux.* Japanese Journal of Applied Physics, Supplement **34**, 107 (1995). URL http://jjap.jsap.jp/link?JJAPS/34S1/107/. 11

[Aka09] M. Akabori, K. Sladek, H. Hardtdegen, T. Schäpers, and D. Grützmacher. *Influence of growth temperature on the selective area MOVPE of InAs nanowires on GaAs (111) B using $N_2$ carrier gas.* Journal of Crystal Growth **311**, 15, 3813 (2009). ISSN 0022-0248. URL http://dx.doi.org/10.1016/j.jcrysgro.2009.06.015. 45, 46

[Aki06] T. Akiyama, K. Sano, K. Nakamura, and T. Ito. *An Empirical Potential Approach to Wurtzite–Zinc-Blende Polytypism in Group III–V Semiconductor Nanowires.* Japanese Journal of Applied Physics **45**, 9, L275 (2006). URL http://dx.doi.org/10.1143/JJAP.45.L275. 16

[Al'82] B. L. Al'tshuler, A. G. Aronov, and D. E. Khmelnitsky. *Effects of electron-electron collisions with small energy transfers on quantum localisation.* Journal of Physics C: Solid State Physics **15**, 36, 7367 (1982). URL http://stacks.iop.org/0022-3719/15/i=36/a=018. 29, 63

[Al'85] B. Al'tshuler. Флуктуации остаточной проводимости неупорядоченных проводников *(Fluctuations in the extrinsic conductivity of disordered conductors).* Журнал Экспериментальной и Теоретической Физики (ЖЭТФ) (Soviet Journal of Experimental and Theoretical Physics Letters) **41**, 530 (1985). URL http://www.jetpletters.ac.ru/ps/1470/article_22425.pdf. 29

[All11] C. S. Allen, M. D. Elkin, G. Burnell, B. J. Hickey, C. Zhang, S. Hofmann, and J. Robertson. *Transport measurements on carbon nanotubes structurally characterized by electron diffraction.* Physical Review B: Condensed Matter and Materials Physics **84**, 115444 (2011). URL http://dx.doi.org/10.1103/PhysRevB.84.115444. 44




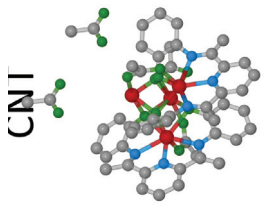

[Ard38] M. von Ardenne. *Das Elektronen-Rastermikroskop*. Zeitschrift für Physik A Hadrons and Nuclei **109**, 9, 553 (1938). ISSN 0939-7922. URL http://dx.doi.org/10.1007/BF01341584. 24

[Ard03] A. Ardavan, M. Austwick, S. C. Benjamin, G. A. D. Briggs, T. J. S. Denni s, A. Ferguson, D. G. Hasko, M. Kanai, A. N. Khlobystov, B. W. Lovett, G. W. Morley, R. A. Oliver, D. G. Pettifor, K. Porfyrakis, J. H. Reina, J. H. Rice, J. D. Smith, R. A. Taylor, D. A. Williams, C. Adelmann, H. Mariette, and R. J. Hamers. *Nanoscale solid-state quantum computing*. Philosophical Transactions of the Royal Society of London. Series A:Mathematical, Physical and Engineering Sciences **361**, 1808, 1473 (2003). URL http://dx.doi.org/10.1098/rsta.2003.1214. 89

[Ash96] R. C. Ashoori. *Electrons in artificial atoms*. Nature **379**, 6564, 413 (1996). URL http://dx.doi.org/10.1038/379413a0. 34

[Ave91] D. V. Averin, A. N. Korotkov, and K. K. Likharev. *Theory of single-electron charging of quantum wells and dots*. Physical Review B: Condensed Matter and Materials Physics **44**, 12, 6199 (1991). URL http://link.aps.org/doi/10.1103/PhysRevB.44.6199. 35

[Avo08] P. Avouris, M. Freitag, and V. Perebeinos. *Carbon-nanotube photonics and optoelectronics*. Nature Photonics **2**, 6, 341 (2008). ISSN 1749-4885. URL http://dx.doi.org/10.1038/nphoton.2008.94. 2

[Bah02] J. L. Bahr and J. M. Tour. *Covalent chemistry of single-wall carbon nanotubes*. Journal of Materials Chemistry **12**, 7, 1952 (2002). ISSN 0959-9428. URL http://dx.doi.org/10.1039/B201013P. 89

[Bai88] M. N. Baibich, J. M. Broto, A. Fert, F. N. Van Dau, F. Petroff, P. Etienne, G. Creuzet, A. Friederich, and J. Chazelas. *Giant Magnetoresistance of (001)Fe/(001)Cr Magnetic Superlattices*. Physical Review Letters **61**, 21, 2472 (1988). URL http://link.aps.org/doi/10.1103/PhysRevLett.61.2472. 1

[Ban05] S. Banerjee, T. Hemraj-Benny, and S. Wong. *Covalent Surface Chemistry of Single-Walled Carbon Nanotubes*. Advanced Materials **17**, 1, 17 (2005). ISSN 1521-4095. URL http://dx.doi.org/10.1002/adma.200401340. 89

[Bas05] A. Bassil, P. Puech, G. Landa, W. Bacsa, S. Barrau, P. Demont, C. Lacabanne, E. Perez, R. Bacsa, E. Flahaut, A. Peigney, and C. Laurent. *Spectroscopic detection of carbon nanotube interaction with amphiphilic molecules in epoxy resin composites*. Journal of Applied Physics **97**, 3, 034303 (2005). URL http://dx.doi.org/10.1063/1.1846136. 108

[Bau10] J. Baugh, J. S. Fung, J. Mracek, and R. R. LaPierre. *Building a spin quantum bit register using semiconductor nanowires*. Nanotechnology **21**, 13, 134018

(2010). ISSN 0957-4484. URL http://stacks.iop.org/0957-4484/21/i=13/a=134018. 2

[Bee88] C. W. J. Beenakker and H. van Houten. *Flux-cancellation effect on narrow-channel magnetoresistance fluctuations*. Physical Review B: Condensed Matter and Materials Physics **37**, 6544 (1988). URL http://dx.doi.org/10.1103/PhysRevB.37.6544. 32, 33, 61, 62

[Bee91a] C. Beenakker and H. van Houten. *Quantum Transport in Semiconductor Nanostructures*. In H. Ehrenreich and D. Turnbull (eds.), *Semiconductor Heterostructures and Nanostructures*, volume 44 of *Solid State Physics*, pp. 1 – 228. Academic Press (1991). URL http://dx.doi.org/10.1016/S0081-1947(08)60091-0. 28, 30, 31, 33, 61, 62

[Bee91b] C. W. J. Beenakker. *Theory of Coulomb-blockade oscillations in the conductance of a quantum dot*. Physical Review B: Condensed Matter and Materials Physics **44**, 4, 1646 (1991). URL http://link.aps.org/doi/10.1103/PhysRevB.44.1646. 35, 72

[Bee04] C. W. J. Beenakker and H. van Houten. *Quantum Transport in Semiconductor Nanostructures*. ArXiv:cond-mat **0412664**, 1 (2004). URL http://arxiv.org/pdf/cond-mat/0412664v1.pdf. 28, 30, 31, 33, 61, 62

[Bet93] D. S. Bethune, C. H. Klang, M. S. de Vries, G. Gorman, R. Savoy, J. Vazquez, and R. Beyers. *Cobalt-catalysed growth of carbon nanotubes with single-atomic-layer walls*. Nature **363**, 6430, 605 (1993). URL http://dx.doi.org/10.1038/363605a0. 44

[Bie08] M. Biercuk, S. Ilani, C. Marcus, and P. McEuen. *Electrical Transport in Single-Wall Carbon Nanotubes*. In *Carbon Nanotubes*, volume 111 of *Topics in Applied Physics*, pp. 455–493. Springer Berlin / Heidelberg (2008). ISBN 978-3-540-72864-1. URL http://dx.doi.org/10.1007/978-3-540-72865-8_15. 28

[Bin82] G. Binnig, H. Rohrer, C. Gerber, and E. Weibel. *Tunneling through a controllable vacuum gap*. Applied Physics Letters **40**, 2, 178 (1982). URL http://dx.doi.org/10.1063/1.92999. 1

[Bin89] G. Binasch, P. Grünberg, F. Saurenbach, and W. Zinn. *Enhanced magnetoresistance in layered magnetic structures with antiferromagnetic interlayer exchange*. Physical Review B: Condensed Matter and Materials Physics **39**, 7, 4828 (1989). URL http://link.aps.org/doi/10.1103/PhysRevB.39.4828. 1

[Bjö04] M. T. Björk, C. Thelander, A. E. Hansen, L. E. Jensen, M. W. Larsson, L. R. Wallenberg, and L. Samuelson. *Few-Electron Quantum Dots in Nanowires*. Nano Letters **4**, 9, 1621 (2004). URL http://dx.doi.org/10.1021/nl049230s. 26, 34



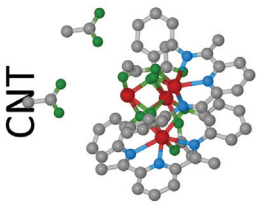

[Blö11] C. Blömers, M. I. Lepsa, M. Luysberg, D. Grützmacher, H. Lüth, and T. Schäpers. *Electronic Phase Coherence in InAs Nanowires*. Nano Letters **11**, 9, 3550 (2011). URL http://dx.doi.org/10.1021/nl201102a. 18, 57, 60, 62

[BN12] C. Bosch-Navarro, E. Coronado, C. Martí-Gastaldo, B. Rodríguez-González, and L. M. Liz-Marzán. *Electrostatic Anchoring of $Mn_4$ Single-Molecule Magnets onto Chemically Modified Multiwalled Carbon Nanotubes*. Advanced Functional Materials **22**, 5, 979 (2012). ISSN 1616-3028. URL http://dx.doi.org/10.1002/adfm.201102227. 89, 98

[Boc97] M. Bockrath, D. H. Cobden, P. L. McEuen, N. G. Chopra, A. Zettl, A. Thess, and R. E. Smalley. *Single-Electron Transport in Ropes of Carbon Nanotubes*. Science **275**, 5308, 1922 (1997). URL http://www.sciencemag.org/content/275/5308/1922.abstract. 38

[Bog08] L. Bogani and W. Wernsdorfer. *Molecular spintronics using single-molecule magnets*. Nature Materials **7**, 3, 179 (2008). ISSN 1476-1122. URL http://dx.doi.org/10.1038/nmat2133. 89

[Bog10] L. Bogani, R. Maurand, L. Marty, C. Sangregorio, C. Altavilla, and W. Wernsdorfer. *Effect of sequential grafting of magnetic nanoparticles onto metallic and semiconducting carbon-nanotube devices: towards self-assembled multi-dots*. Journal of Materials Chemistry **20**, 11, 2099 (2010). ISSN 0959-9428. URL http://dx.doi.org/10.1039/B917111H. 89, 98

[Bou11] A. Bousseksou, G. Molnar, L. Salmon, and W. Nicolazzi. *Molecular spin crossover phenomenon: recent achievements and prospects*. Chemical Society Reviews **40**, 6, 3313 (2011). ISSN 0306-0012. URL http://dx.doi.org/10.1039/C1CS15042A. 119

[BS12] M. Bar-Sadan, J. Barthel, H. Shtrikman, and L. Houben. *Direct Imaging of Single Au Atoms Within GaAs Nanowires*. Nano Letters **12**, 5, 2352 (2012). ISSN 1530-6984. URL http://dx.doi.org/10.1021/nl300314k. 23, 44, 66

[Bui02] M. R. Buitelaar, A. Bachtold, T. Nussbaumer, M. Iqbal, and C. Schönenberger. *Multiwall Carbon Nanotubes as Quantum Dots*. Physical Review Letters **88**, 15, 156801 (2002). URL http://link.aps.org/doi/10.1103/PhysRevLett.88.156801. 38, 39, 69, 82

[Büt85] M. Büttiker, Y. Imry, R. Landauer, and S. Pinhas. *Generalized many-channel conductance formula with application to small rings*. Physical Review B **31**, 10, 6207+ (1985). URL http://dx.doi.org/http://dx.doi.org/10.1103/PhysRevB.31.6207. 28

[Büt86] M. Büttiker. *Four-terminal phase-coherent conductance*. Physical Review Letters **57**, 1761 (1986). URL http://dx.doi.org/10.1103/PhysRevLett.57.1761. 28, 60

[Büt88] M. Büttiker. *Symmetry of Electrical Conduction*. IBM Journal of Research and Development **32**, 3, 317 (1988). URL http://dx.doi.org/10.1147/rd.323.0317. 60

[Cao05] J. Cao, Q. Wang, D. Wang, and H. Dai. *Suspended Carbon Nanotube Quantum Wires with Two Gates*. Small **1**, 1, 138 (2005). ISSN 1613-6829. URL http://dx.doi.org/10.1002/smll.200400015. 26, 39

[Cas45] H. B. G. Casimir. *On Onsager's Principle of Microscopic Reversibility*. Review of Modern Physics **17**, 2-3, 343 (1945). URL http://dx.doi.org/10.1103/RevModPhys.17.343. 60

[Cec01] P. Cecchi, M. Berrettoni, M. Giorgetti, G. Gioia Lobbia, S. Calogero, and L. Stievano. *The effect of the 3-trifluoromethyl substituent in polypyrazolylborato complexes on the iron(II) spin state; X-ray diffraction and absorption and Mößbauer studies*. Inorganica Chimica Acta **318**, 1–2, 67 (2001). ISSN 0020-1693. URL http://dx.doi.org/10.1016/S0020-1693(01)00399-1. 122

[Cha74] L. L. Chang, L. Esaki, and R. Tsu. *Resonant tunneling in semiconductor double barriers*. Applied Physics Letters **24**, 12, 593 (1974). URL http://dx.doi.org/10.1063/1.1655067. 26, 34

[Cha01] J.-C. Charlier and S. Iijima. *Growth Mechanisms of Carbon Nanotubes*. In M. Dresselhaus, G. Dresselhaus, and P. Avouris (eds.), *Carbon Nanotubes*, volume 80 of *Topics in Applied Physics*, pp. 55–81. Springer Berlin / Heidelberg (2001). ISBN 978-3-540-41086-7. URL http://dx.doi.org/10.1007/3-540-39947-X_4. 7

[Che93] W. Chen and H. Ahmed. *Fabrication of 5–7 nm wide etched lines in silicon using 100 keV electron-beam lithography and polymethylmethacrylate resist*. Applied Physics Letters **62**, 13, 1499 (1993). URL http://dx.doi.org/10.1063/1.109609. 47

[Che03] Z. Chen, W. Thiel, and A. Hirsch. *Reactivity of the Convex and Concave Surfaces of Single-Walled Carbon Nanotubes (SWCNTs) towards Addition Reactions: Dependence on the Carbon-Atom Pyramidalization*. ChemPhysChem **4**, 1, 93 (2003). ISSN 1439-7641. URL http://dx.doi.org/10.1002/cphc.200390015. 15

[Che08] J.-H. Chen, C. Jang, S. Xiao, M. Ishigami, and M. S. Fuhrer. *Intrinsic and extrinsic performance limits of graphene devices on $SiO_2$*. Nature Nanotechnology **3**, 4, 206 (2008). ISSN 1748-3387. URL http://dx.doi.org/10.1038/nnano.2008.58. 9



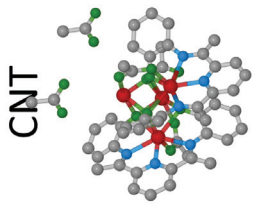

[Chi05] S. B. Chikkannanavar, D. E. Luzzi, S. Paulson, and A. T. Johnson. *Synthesis of Peapods Using Substrate-Grown SWNTs and DWNTs: An Enabling Step Toward Peapod Devices*. Nano Letters **5**, 1, 151 (2005). URL `http://dx.doi.org/10.1021/nl049854y`. 16, 44

[CN09] A. H. Castro Neto, F. Guinea, N. M. R. Peres, K. S. Novoselov, and A. K. Geim. *The electronic properties of graphene*. Reviews of Modern Physics **81**, 109 (2009). URL `http://dx.doi.org/10.1103/RevModPhys.81.109`. 8

[Cos08] P. Costa, D. Golberg, G. Shen, M. Mitome, and Y. Bando. *ZnO low-dimensional structures: electrical properties measured inside a transmission electron microscope*. Journal of Materials Science **43**, 1460 (2008). ISSN 0022-2461. URL `http://dx.doi.org/10.1007/s10853-007-2307-1`. 44

[Cso08] S. Csonka, L. Hofstetter, F. Freitag, S. Oberholzer, C. Schönenberger, T. S. Jespersen, M. Aagesen, and J. Nygård. *Giant Fluctuations and Gate Control of the g-Factor in InAs Nanowire Quantum Dots*. Nano Letters **8**, 11, 3932 (2008). URL `http://dx.doi.org/10.1021/nl802418w`. 17

[CT99] C. Cohen-Tannoudji, B. Diu, and F. Laloë. *Quantenmechanik: Teil 1&2*. De Gruyter (1999). URL `http://d-nb.info/951321668/about/html`. 39

[Dam99] M. Damnjanović, I. Miloscaronević, T. Vuković, and R. Sredanović. *Full symmetry, optical activity, and potentials of single-wall and multiwall nanotubes*. Physical Review B: Condensed Matter and Materials Physics **60**, 2728 (1999). URL `http://link.aps.org/doi/10.1103/PhysRevB.60.2728`. 11, 14

[Das12] A. Das, Y. Ronen, Y. Most, Y. Oreg, M. Heiblum, and H. Shtrikman. *Evidence of Majorana fermions in an Al - InAs nanowire topological superconductor*. ArXiv:cond-mat **7073**, 1 (2012). URL `http://arxiv.org/abs/1205.7073`. 57

[Dat11] S. Datta, S. Wang, C. Tilmaciu, E. Flahaut, L. Marty, M. Grifoni, and W. Wernsdorfer. *Electronic transport properties of double-wall carbon nanotubes*. Physical Review B: Condensed Matter and Materials Physics **84**, 035408 (2011). URL `http://dx.doi.org/10.1103/PhysRevB.84.035408`. 38, 82

[Day07] S. A. Dayeh, C. Soci, P. K. L. Yu, E. T. Yu, and D. Wang. *Influence of surface states on the extraction of transport parameters from InAs nanowire field effect transistors*. Applied Physics Letters **90**, 16, 162112 (2007). URL `http://dx.doi.org/10.1063/1.2728762`. 62

[Day09] S. A. Dayeh, D. Susac, K. L. Kavanagh, E. T. Yu, and D. Wang. *Structural and Room-Temperature Transport Properties of Zinc Blende and Wurtzite InAs Nanowires*. Advanced Functional Materials **19**, 13, 2102 (2009). ISSN 1616-3028. URL `http://dx.doi.org/10.1002/adfm.200801307`. 18, 63, 64

[Day10] S. A. Dayeh. *Electron transport in indium arsenide nanowires*. Semiconductor Science and Technology **25**, 2, 024004 (2010). URL http://stacks.iop.org/0268-1242/25/i=2/a=024004. 58

[De10] A. De and C. E. Pryor. *Predicted band structures of III-V semiconductors in the wurtzite phase*. Physical Review B: Condensed Matter and Materials Physics **81**, 155210 (2010). URL http://dx.doi.org/10.1103/PhysRevB.81.155210. 17, 18

[Deb11] J. Debgupta, B. A. Kakade, and V. K. Pillai. *Competitive wetting of acetonitrile and dichloromethane in comparison to that of water on functionalized carbon nanotube surfaces*. Physical Chemistry Chemical Physics **13**, 32, 14668 (2011). ISSN 1463-9076. URL http://dx.doi.org/10.1039/C1CP21121H. 109

[Dek99] C. Dekker. *Carbon nanotubes as molecular quantum wires*. Physics Today **52**, 5, 22 (1999). ISSN 0031-9228. URL http://dx.doi.org/10.1063/1.882658. 26, 34

[Dem12] N. Demarina. *Solution of coupled Schrödinger and Poisson equations in structures with axial symmetry*. Mäuschen Corporation (2012). 17, 19

[Dic10a] K. A. Dick, P. Caroff, J. Bolinsson, M. E. Messing, J. Johansson, K. Deppert, L. R. Wallenberg, and L. Samuelson. *Control of III/V nanowire crystal structure by growth parameter tuning*. Semiconductor Science and Technology **25**, 2, 024009 (2010). URL http://dx.doi.org/10.1088/0268-1242/25/2/024009. 16, 17, 46

[Dic10b] K. A. Dick, C. Thelander, L. Samuelson, and P. Caroff. *Crystal Phase Engineering in Single InAs Nanowires*. Nano Letters **10**, 9, 3494 (2010). URL http://dx.doi.org/10.1021/nl101632a. 63, 124

[Dir28] P. A. M. Dirac. *The Quantum Theory of the Electron*. Proceedings of the Royal Society of London. Series A **117**, 778, 610 (1928). URL http://rspa.royalsocietypublishing.org/content/117/778/610.short. 8

[Doh05] Y.-J. Doh, J. A. van Dam, A. L. Roest, E. P. A. M. Bakkers, L. P. Kouwenhoven, and S. De Franceschi. *Tunable Supercurrent Through Semiconductor Nanowires*. Science **309**, 5732, 272 (2005). URL http://dx.doi.org/10.1126/science.1113523. 57

[Dre95] M. Dresselhaus, G. Dresselhaus, and R. Saito. *Physics of carbon nanotubes*. Carbon **33**, 7, 883 (1995). ISSN 0008-6223. URL http://dx.doi.org/10.1016/0008-6223(95)00017-8. 7

[Dre00] M. S. Dresselhaus and P. C. Eklund. *Phonons in carbon nanotubes*. Advances in Physics **49**, 6, 705 (2000). ISSN 0001-8732. URL http://dx.doi.org/10.1080/000187300413184. 13, 15, 106



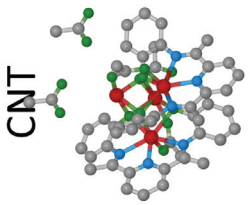

[Dre01] M. Dresselhaus and P. Avouris. *Introduction to Carbon Materials Research.* In M. Dresselhaus, G. Dresselhaus, and P. Avouris (eds.), *Carbon Nanotubes*, volume 80 of *Topics in Applied Physics*, pp. 1–9. Springer Berlin / Heidelberg (2001). ISBN 978-3-540-41086-7. URL http://dx.doi.org/10.1007/3-540-39947-X_1. 7

[Dre05] M. Dresselhaus, G. Dresselhaus, R. Saito, and A. Jorio. *Raman spectroscopy of carbon nanotubes.* Physics Reports **409**, 2, 47 (2005). ISSN 0370-1573. URL http://dx.doi.org/10.1016/j.physrep.2004.10.006. 12, 13, 22

[Du09] J. Du, D. Liang, H. Tang, and X. P. Gao. *InAs Nanowire Transistors as Gas Sensor and the Response Mechanism.* Nano Letters **9**, 12, 4348 (2009). URL http://dx.doi.org/10.1021/nl902611f. 2, 17, 57

[Duq10] J. G. Duque, H. Chen, A. K. Swan, E. H. HÃ¡roz, J. Kono, X. Tu, M. Zheng, and S. K. Doorn. *Revealing new electronic behaviours in the Raman spectra of chirality-enriched carbon nanotube ensembles.* physica status solidi (b) **247**, 11-12, 2768 (2010). ISSN 1521-3951. URL http://dx.doi.org/10.1002/pssb.201000350. 12, 55

[Duq11] J. G. Duque, H. Chen, A. K. Swan, A. P. Shreve, S. Kilina, S. Tretiak, X. Tu, M. Zheng, and S. K. Doorn. *Violation of the Condon Approximation in Semiconducting Carbon Nanotubes.* ACS Nano **5**, 6, 5233 (2011). URL http://dx.doi.org/10.1021/nn201430z. 12, 55

[Ebb92] T. W. Ebbesen and P. M. Ajayan. *Large-scale synthesis of carbon nanotubes.* Nature **358**, 6383, 220 (1992). URL http://dx.doi.org/10.1038/358220a0. 44

[Efr75] A. L. Efros and B. I. Shklovskii. *Coulomb gap and low temperature conductivity of disordered systems.* Journal of Physics C: Solid State Physics **8**, 4, L49 (1975). ISSN 0022-3719. URL http://stacks.iop.org/0022-3719/8/i=4/a=003. 115

[Ege04] R. Egerton, P. Li, and M. Malac. *Radiation damage in the TEM and SEM.* Micron **35**, 6, 399 (2004). ISSN 0968-4328. URL http://dx.doi.org/10.1016/j.micron.2004.02.003. 25, 64

[Ege09] R. F. Egerton. *Electron energy-loss spectroscopy in the TEM.* Reports on Progress in Physics **72**, 1, 016502 (2009). URL http://stacks.iop.org/0034-4885/72/i=1/a=016502. 94

[Egg67] M. D. Egger and M. Petran. *New Reflected-Light Microscope for Viewing Unstained Brain and Ganglion Cells.* Science **157**, 3786, 305 (1967). URL http://www.sciencemag.org/content/157/3786/305.abstract. 22

[EH10] S. Estévez Hernández, M. Akabori, K. Sladek, C. Volk, S. Alagha, H. Hardtdegen, M. G. Pala, N. Demarina, D. Grützmacher, and T. Schäpers. *Spin-orbit coupling and phase coherence in InAs nanowires.* Physical Review B: Condensed Matter and Materials Physics **82**, 235303 (2010). URL `http://dx.doi.org/10.1103/PhysRevB.82.235303`. 30, 31, 57

[Eki81] A. I. Ekimov and A. A. Onushchenko. Квантовый размерный эффект в трехмерных микрокристаллах полупроводников *(Quantum size effect in three-dimensional microscopic semiconductor crystals).* Журнал Экспериментальной и Теоретической Физики (ЖЭТФ) (Soviet Journal of Experimental and Theoretical Physics Letters) **34**, 345 (1981). URL `http://www.jetpletters.ac.ru/ps/1517/article_23187.pdf`. 34

[Eli10] A. Eliasen, J. Paaske, K. Flensberg, S. Smerat, M. Leijnse, M. R. Wegewijs, H. I. Jørgensen, M. Monthioux, and J. Nygård. *Transport via coupled states in a $C_{60}$ peapod quantum dot.* Physical Review B: Condensed Matter and Materials Physics **81**, 155431 (2010). URL `http://dx.doi.org/10.1103/PhysRevB.81.155431`. 43, 80, 81

[Fan61] U. Fano. *Effects of Configuration Interaction on Intensities and Phase Shifts.* Physical Review **124**, 6, 1866 (1961). URL `http://link.aps.org/doi/10.1103/PhysRev.124.1866`. 72, 78

[Fan04] C. Fantini, A. Jorio, M. Souza, M. S. Strano, M. S. Dresselhaus, and M. A. Pimenta. *Optical Transition Energies for Carbon Nanotubes from Resonant Raman Spectroscopy: Environment and Temperature Effects.* Physical Review Letters **93**, 147406 (2004). URL `http://dx.doi.org/10.1103/PhysRevLett.93.147406`. 22, 55

[Fer26] E. Fermi. *Sulla quantizzazione del gas perfetto monoatomico.* Rendiconti Lincei **3**, 145 (1926). URL `http://arxiv.org/abs/cond-mat/9912229`. 27

[Fey60] R. P. Feynman. *There's Plenty of Room at the Bottom.* Engineering and Science **23**, 22 (1960). URL `http://calteches.library.caltech.edu/1976/1/1960Bottom.pdf`. 1

[Fil03] A. G. S. Filho, A. Jorio, G. G. Samsonidze, G. Dresselhaus, R. Saito, and M. S. Dresselhaus. *Raman spectroscopy for probing chemically/physically induced phenomena in carbon nanotubes.* Nanotechnology **14**, 10, 1130 (2003). URL `http://stacks.iop.org/0957-4484/14/i=10/a=311`. 99

[Flö11a] K. Flöhr, M. Liebmann, K. Sladek, H. Y. Günel, R. Frielinghaus, F. Haas, C. Meyer, H. Hardtdegen, T. Schäpers, D. Grützmacher, and M. Morgenstern. *Manipulating InAs nanowires with submicrometer precision.* Review of Scientific Instruments **82**, 11, 113705 (2011). URL `http://dx.doi.org/10.1063/1.3657135`. 44, 49, 58



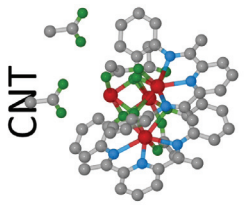

[Flö11b] H. Flötotto. *Herstellung und Charakterisierung von Carboxylatcluster–Kohlenstoffnanoröhrenverbindungen*. Bachelor thesis, Rheinisch-Westfälische Technische Hochschule Aachen (2011). 90, 91

[Flö12] K. Flöhr, H. Y. Günel, K. Sladek, R. Frielinghaus, H. Hardtdegen, M. Liebmann, T. Schäpers, and M. Morgenstern. *Preparing InAs nanowires for functionalized STM tips*. In J. Heber, D. Schlom, Y. Tokura, R. Waser, and M. Wuttig (eds.), *Frontiers in electronic materials*, p. 692. Nature Conference Frontiers in Electronic Materials 2012, Aachen, Weinheim: Wiley-VCH-Verlag (2012). URL http://d-nb.info/1023698269/about/html. 44, 49

[For09] A. C. Ford, J. C. Ho, Y.-L. Chueh, Y.-C. Tseng, Z. Fan, J. Guo, J. Bokor, and A. Javey. *Diameter-Dependent Electron Mobility of InAs Nanowires*. Nano Letters **9**, 1, 360 (2009). URL http://dx.doi.org/10.1021/nl803154m. 17

[Fow82] A. B. Fowler, A. Hartstein, and R. A. Webb. *Conductance in Restricted-Dimensionality Accumulation Layers*. Physical Review Letters **48**, 3, 196 (1982). URL http://dx.doi.org/10.1103/PhysRevLett.48.196. 26, 29

[Fra10] S. de Franceschi, L. Kouwenhoven, C. Schonenberger, and W. Wernsdorfer. *Hybrid superconductor-quantum dot devices*. Nature Nanotechnology **5**, 10, 703 (2010). ISSN 1748-3387. URL http://dx.doi.org/10.1038/nnano.2010.173. 34

[Fri09a] R. Frielinghaus. *Phasenkohärenter Transport durch Indiumnitrid-Nanodrähte, kontaktiert mit Normal- und Supraleitern*. Master's thesis, Rheinisch-Westfälische Technische Hochschule Aachen (2009). URL http://www.visel.net/ausbildung/vorlesungen. 33, 60, 62

[Fri09b] R. Frielinghaus, S. E. Hernández, R. Calarco, and T. Schäpers. *Phase-coherence and symmetry in four-terminal magnetotransport measurements on InN nanowires*. Applied Physics Letters **94**, 25, 252107 (2009). URL http://dx.doi.org/10.1063/1.3159626. 33, 57, 60, 61, 62, 123

[Fri10] R. Frielinghaus, I. E. Batov, M. Weides, H. Kohlstedt, R. Calarco, and T. Schäpers. *Josephson supercurrent in Nb/InN-nanowire/Nb junctions*. Applied Physics Letters **96**, 13, 132504 (2010). URL http://dx.doi.org/10.1063/1.3377897. 57, 65

[Fri11] R. Frielinghaus, K. Goß, S. Trellenkamp, L. Houben, C. M. Schneider, and C. Meyer. *Comprehensive characterization of an individual carbon nanotube transport device*. physica status solidi (b) **248**, 11, 2660 (2011). ISSN 1521-3951. URL http://dx.doi.org/10.1002/pssb.201100081. 44

[Fri12a] R. Frielinghaus, K. Flöhr, K. Sladek, T. E. Weirich, S. Trellenkamp, H. Hardtdegen, T. Schäpers, C. M. Schneider, and C. Meyer. *Monitoring structural in-*

*fluences on quantum transport in InAs nanowires*. Applied Physics Letters **101**, 6, 062104 (2012). URL http://dx.doi.org/10.1063/1.4742326. 58

[Fri12b] R. Frielinghaus, K. Sladek, K. Flöhr, L. Houben, S. Trellenkamp, T. E. Weirich, M. Morgenstern, H. Hardtdegen, T. Schäpers, C. M. Schneider, and C. Meyer. *Structural influences on electronic transport in nanostructures*. In J. Heber, D. Schlom, Y. Tokura, R. Waser, and M. Wuttig (eds.), *Frontiers in electronic materials*, p. 692. Nature Conference Frontiers in Electronic Materials 2012, Aachen, Weinheim: Wiley-VCH-Verlag (2012). URL http://d-nb.info/1023698269/about/html. 58

[Fue12] M. Fuechsle, J. A. Miwa, S. Mahapatra, H. Ryu, S. Lee, O. Warschkow, L. C. L. Hollenberg, G. Klimeck, and M. Y. Simmons. *A single-atom transistor*. Nature Nanotechnology **7**, 4, 242 (2012). ISSN 1748-3387. URL http://dx.doi.org/10.1038/nnano.2012.21. 43

[Fuh07] A. Fuhrer, L. E. Fröberg, J. N. Pedersen, M. W. Larsson, A. Wacker, M.-E. Pistol, and L. Samuelson. *Few Electron Double Quantum Dots in InAs/InP Nanowire Heterostructures*. Nano Letters **7**, 2, 243 (2007). URL http://dx.doi.org/10.1021/nl061913f. 57, 85, 86

[Fuk79] H. Fukuyama and K. Yoshida. *Negative Magnetoresistance in the Anderson Localized States*. Journal of the Physical Society of Japan **46**, 1, 102 (1979). URL http://dx.doi.org/10.1143/JPSJ.46.102. 117

[Gei07] A. K. Geim and K. S. Novoselov. *The rise of graphene*. Nature Materials **6**, 3, 183 (2007). ISSN 1476-1122. URL http://dx.doi.org/10.1038/nmat1849. 8, 9

[Ger11] I. Gerber, M. Oubenali, R. Bacsa, J. Durand, A. GonÃ§alves, M. F. R. Pereira, F. Jolibois, L. Perrin, R. Poteau, and P. Serp. *Theoretical and Experimental Studies on the Carbon-Nanotube Surface Oxidation by Nitric Acid: Interplay between Functionalization and Vacancy Enlargement*. Chemistry – A European Journal **17**, 41, 11467 (2011). ISSN 1521-3765. URL http://dx.doi.org/10.1002/chem.201101438. 109, 113

[Gir09] Ç. Ö. Girit, J. C. Meyer, R. Erni, M. D. Rossell, C. Kisielowski, L. Yang, C.-H. Park, M. F. Crommie, M. L. Cohen, S. G. Louie, and A. Zettl. *Graphene at the Edge: Stability and Dynamics*. Science **323**, 5922, 1705 (2009). URL http://www.sciencemag.org/content/323/5922/1705.abstract. 23

[Gor51] C. Gorter. *A possible explanation of the increase of the electrical resistance of thin metal films at low temperatures and small field strengths*. Physica **17**, 8, 777 (1951). ISSN 0031-8914. URL http://www.sciencedirect.com/science/article/pii/0031891451900985. 34



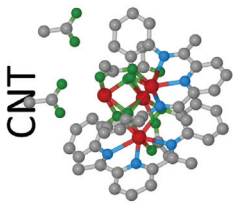

[Goß11a] K. Goß. *Interactions between parallel carbon nanotube quantum dots*. Ph.D. thesis, Universität Duisburg-Essen, Jülich, Germany (2011). URL http://hdl.handle.net/2128/4522. 12, 14, 22, 41, 43, 48, 49, 73, 79, 80, 81, 89, 99

[Goß11b] K. Goß, S. Smerat, M. Leijnse, M. R. Wegewijs, C. M. Schneider, and C. Meyer. *Spin-dependent electronic hybridization in a rope of carbon nanotubes*. Physical Review B: Condensed Matter and Materials Physics **83**, 201403 (2011). URL http://dx.doi.org/10.1103/PhysRevB.83.201403. 7, 69, 79, 80, 81

[Gra92] S. M. Grannan, A. E. Lange, E. E. Haller, and J. W. Beeman. *Non-Ohmic hopping conduction in doped germanium at $T < 1\,K$*. Physical Review B: Condensed Matter and Materials Physics **45**, 8, 4516 (1992). URL http://link.aps.org/doi/10.1103/PhysRevB.45.4516. 116

[Gro07] W. Grogger, B. Schaffer, C. Span, W. Rechberger, G. Kothleitner, and F. Hofer. *Advanced Nanoanalysis in Transmission Electron Microscopy: Overview*. In K. Urban (ed.), *38th IFF Spring School: Probing the Nanoworld–Microscopies, Scattering and Spectroscopies of the Solid State*, chapter C1. Forschungszentrum Jülich, Zentralbibliothek (2007). URL http://d-nb.info/983539421. 23, 25

[Guo06] X. Guo, J. P. Small, J. E. Klare, Y. Wang, M. S. Purewal, I. W. Tam, B. H. Hong, R. Caldwell, L. Huang, S. O'Brien, J. Yan, R. Breslow, S. J. Wind, J. Hone, P. Kim, and C. Nuckolls. *Covalently Bridging Gaps in Single-Walled Carbon Nanotubes with Conducting Molecules*. Science **311**, 5759, 356 (2006). URL http://dx.doi.org/10.1126/science.1120986. 89

[Guo07] X. Guo, A. Whalley, J. E. Klare, L. Huang, S. O'Brien, M. Steigerwald, and C. Nuckolls. *Single-Molecule Devices as Scaffolding for Multicomponent Nanostructure Assembly*. Nano Letters **7**, 5, 1119 (2007). URL http://dx.doi.org/10.1021/nl070245a. 89

[Guo09] X. Guo and C. Nuckolls. *Functional single-molecule devices based on SWNTs as point contacts*. Journal of Materials Chemistry **19**, 31, 5470 (2009). ISSN 0959-9428. URL http://dx.doi.org/10.1039/B900331M. 89

[Had93] R. C. Haddon. *Chemistry of the Fullerenes: The Manifestation of Strain in a Class of Continuous Aromatic Molecules*. Science **261**, 5128, 1545 (1993). URL http://www.sciencemag.org/content/261/5128/1545.abstract. 15

[Hai98] M. Haider, S. Uhlemann, E. Schwan, H. Rose, B. Kabius, and K. Urban. *Electron microscopy image enhanced*. Nature **392**, 6678, 768 (1998). ISSN 0028-0836. URL http://dx.doi.org/10.1038/33823. 24

[Ham37] L. P. Hammett. *The Effect of Structure upon the Reactions of Organic Compounds. Benzene Derivatives*. Journal of the American Chemical Society **59**, 1, 96 (1937). URL http://dx.doi.org/10.1021/ja01280a022. 114

[Ham92] N. Hamada, S. Sawada, and A. Oshiyama. *New one-dimensional conductors: Graphitic microtubules*. Physical Review Letters **68**, 1579 (1992). URL http://dx.doi.org/10.1103/PhysRevLett.68.1579. 9

[Ham10] M.-H. Ham, J. H. Choi, A. A. Boghossian, E. S. Jeng, R. A. Graff, D. A. Heller, A. C. Chang, A. Mattis, T. H. Bayburt, Y. V. Grinkova, A. S. Zeiger, K. J. Van Vliet, E. K. Hobbie, S. G. Sligar, C. A. Wraight, and M. S. Strano. *Photoelectrochemical complexes for solar energy conversion that chemically and autonomously regenerate*. Nat Chem **2**, 11, 929 (2010). ISSN 1755-4330. URL http://dx.doi.org/10.1038/nchem.822. 2

[Han05] A. E. Hansen, M. T. Björk, C. Fasth, C. Thelander, and L. Samuelson. *Spin relaxation in InAs nanowires studied by tunable weak antilocalization*. Physical Review B: Condensed Matter and Materials Physics **71**, 205328 (2005). URL http://dx.doi.org/10.1103/PhysRevB.71.205328. 17, 57, 60

[Han07] R. Hanson, L. P. Kouwenhoven, J. R. Petta, S. Tarucha, and L. M. K. Vandersypen. *Spins in few-electron quantum dots*. Review of Modern Physics **79**, 4, 1217 (2007). URL http://link.aps.org/doi/10.1103/RevModPhys.79.1217. 35

[Hei07] T. Heinzel. *Mesoscopic Electronics in Solid State Nanostructures*. John Wiley & Sons (2007). ISBN 9783527409327. URL http://d-nb.info/98082608X. 2, 40, 47, 48

[Hen06] F. Hennrich, C. Chan, V. Moore, M. Rolandi, and M. O'Connell. *The element carbon*. In *Carbon Nanotubes*, pp. 1–18–. CRC Press (2006). URL http://dx.doi.org/10.1201/9781420004212.ch1. 5

[Heo05] J. Heo and M. Bockrath. *Local Electronic Structure of Single-Walled Carbon Nanotubes from Electrostatic Force Microscopy*. Nano Letters **5**, 5, 853 (2005). URL http://dx.doi.org/10.1021/nl0501765. 10

[Her08] M. C. Hersam. *Progress towards monodisperse single-walled carbon nanotubes*. Nature Nanotechnology **3**, 7, 387 (2008). ISSN 1748-3387. URL http://dx.doi.org/10.1038/nnano.2008.135. 44

[Her10] L. G. Herrmann, F. Portier, P. Roche, A. L. Yeyati, T. Kontos, and C. Strunk. *Carbon Nanotubes as Cooper-Pair Beam Splitters*. Physical Review Letters **104**, 2, 026801 (2010). URL http://link.aps.org/doi/10.1103/PhysRevLett.104.026801. 1

[Hey01] J. N. Heyman, P. Neocleous, D. Hebert, P. A. Crowell, T. Müller, and K. Unterrainer. *Terahertz emission from GaAs and InAs in a magnetic field*. Physical Review B: Condensed Matter and Materials Physics **64**, 085202 (2001). URL http://dx.doi.org/10.1103/PhysRevB.64.085202. 16



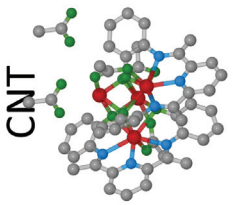

[Hil44] J. Hillier and R. F. Baker. *Microanalysis by Means of Electrons*. Journal of Applied Physics **15**, 9, 663 (1944). URL http://dx.doi.org/10.1063/1.1707491. 25

[Hil08] E. Hilner, U. Håkanson, L. E. Fröberg, M. Karlsson, P. Kratzer, E. Lundgren, L. Samuelson, and A. Mikkelsen. *Direct Atomic Scale Imaging of III–V Nanowire Surfaces*. Nano Letters **8**, 11, 3978 (2008). URL http://dx.doi.org/10.1021/nl802500d. 43

[Hir02] A. Hirsch. *Functionalization of Single-Walled Carbon Nanotubes*. Angewandte Chemie International Edition **41**, 11, 1853 (2002). URL http://dx.doi.org/10.1002/1521-3773(20020603)41:11<1853::AID-ANIE1853>3.0.CO;2-N. 15, 16, 89

[Hir05] A. Hirsch and O. Vostrowsky. *Functionalization of Carbon Nanotubes*. In A. Schlüter (ed.), *Topics in Current Chemistry*, volume 245, pp. 193–237–. Springer Berlin Heidelberg (2005). URL http://dx.doi.org/10.1007/b98169. 89

[Hof09] L. Hofstetter, S. Csonka, J. Nygård, and C. Schonenberger. *Cooper pair splitter realized in a two-quantum-dot Y-junction*. Nature **461**, 7266, 960 (2009). ISSN 0028-0836. URL http://dx.doi.org/10.1038/nature08432. 1

[Hol08] J. V. Holm, H. I. Jørgensen, K. Grove-Rasmussen, J. Paaske, K. Flensberg, and P. E. Lindelof. *Gate-dependent tunneling-induced level shifts observed in carbon nanotube quantum dots*. Physical Review B: Condensed Matter and Materials Physics **77**, 16, 161406 (2008). URL http://link.aps.org/doi/10.1103/PhysRevB.77.161406. 79

[Hor02] D. J. Hornbaker, S.-J. Kahng, S. Misra, B. W. Smith, A. T. Johnson, E. J. Mele, D. E. Luzzi, and A. Yazdani. *Mapping the One-Dimensional Electronic States of Nanotube Peapod Structures*. Science **295**, 5556, 828 (2002). URL http://dx.doi.org/10.1126/science.1068133. 43

[Hou05] H. van Houten, C. W. J. Beenakker, and A. A. M. Staring. *Coulomb-Blockade Oscillations in Semiconductor Nanostructures*. arXiv:cond-mat **0508454**, 1 (2005). URL http://arxiv.org/pdf/cond-mat/0508454v1. 34

[Hou07] L. Houben. *Fundamentals and applications of HAADF STEM*. In K. Urban (ed.), *38th IFF Spring School: Probing the Nanoworld -– Microscopies, Scattering and Spectroscopies of the Solid State*, chapter C1. Forschungszentrum Jülich, Zentralbibliothek (2007). URL http://d-nb.info/983539421. 23, 24

[Hüt09] A. K. Hüttel, B. Witkamp, M. Leijnse, M. R. Wegewijs, and H. S. J. van der Zant. *Pumping of Vibrational Excitations in the Coulomb-Blockade Regime in a Suspended Carbon Nanotube*. Physical Review Letters **102**, 22, 225501 (2009). URL http://link.aps.org/doi/10.1103/PhysRevLett.102.225501. 39

[Iba82] H. Ibach and D. Mills. *Electron Energy Loss Spectroscopy and Surface Vibrations*. Academic Press (1982). 25

[Iba09] H. Ibach and H. Lüth. *Festkörperphysik: Einführung in die Grundlagen*. Springer-Lehrbuch. Springer, 7 edition (2009). ISBN 9783540857945. URL http://www.springer.com/materials/book/978-3-540-85794-5. 27, 28

[Ida00] T. Ida, K. Ishibashi, K. Tsukagoshi, B. Alphenaar, and Y. Aoyagi. *Quantum-dot transport in carbon nanotubes*. Superlattices and Microstructures **27**, 5–6, 551 (2000). ISSN 0749-6036. URL http://dx.doi.org/10.1006/spmi.2000.0871. 69

[Iij91] S. Iijima. *Helical microtubules of graphitic carbon*. Nature **354**, 6348, 56 (1991). URL http://dx.doi.org/10.1038/354056a0. 44

[Iko93] Z. Ikonić, G. P. Srivastava, and J. C. Inkson. *Electronic properties of twin boundaries and twinning superlattices in diamond-type and zinc-blende-type semiconductors*. Physical Review B: Condensed Matter and Materials Physics **48**, 17181 (1993). URL http://dx.doi.org/10.1103/PhysRevB.48.17181. 66

[Ind07] K. M. Indlekofer and T. Schäpers. *On the Possibility of Using Semiconductor Nanocolumns for the Realization of Quantum Bits*. ArXiv:cond-mat **0703520**, 1 (2007). URL http://arxiv.org/pdf/cond-mat/0703520v1. 2, 16, 57

[Ish01] K. Ishibashi, M. Suzuki, T. Ida, and Y. Aoyagi. *Formation of coupled quantum dots in single-wall carbon nanotubes*. Applied Physics Letters **79**, 12, 1864 (2001). URL http://dx.doi.org/10.1063/1.1403295. 85

[Isl12] J. O. Island, V. Tayari, A. C. McRae, and A. R. Champagne. *Few-Hundred GHz Carbon Nanotube Nanoelectromechanical Systems (NEMS)*. Nano Lett. **12**, 9, 4564 (2012). ISSN 1530-6984. URL http://dx.doi.org/10.1021/nl3018065. 39

[Itt47] A. Itterbeek and L. Greve. *Measurements on the electrical resistivity of thin nickel films*. Experientia **3**, 7, 278 (1947). ISSN 0014-4754. URL http://dx.doi.org/10.1007/BF02164168. 34

[Jai07] M. Jaiswal, W. Wang, K. A. S. Fernando, Y.-P. Sun, and R. Menon. *Magnetotransport in transparent single-wall carbon nanotube networks*. Physical Review B: Condensed Matter and Materials Physics **76**, 11, 113401 (2007). URL http://link.aps.org/doi/10.1103/PhysRevB.76.113401. 116

[Joh92] A. T. Johnson, L. P. Kouwenhoven, W. de Jong, N. C. van der Vaart, C. J. P. M. Harmans, and C. T. Foxon. *Zero-dimensional states and single electron charging in quantum dots*. Physical Review Letters **69**, 10, 1592 (1992). URL http://link.aps.org/doi/10.1103/PhysRevLett.69.1592. 34



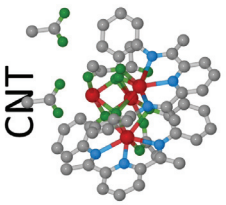

[Joh10] D. Y. Joh, L. H. Herman, S.-Y. Ju, J. Kinder, M. A. Segal, J. N. Johnson, G. K. L. Chan, and J. Park. *On-Chip Rayleigh Imaging and Spectroscopy of Carbon Nanotubes*. Nano Letters **11**, 1, 1 (2010). ISSN 1530-6984. URL `http://dx.doi.org/10.1021/nl1012568`. 11

[Jor01a] A. Jorio, R. Saito, J. H. Hafner, C. M. Lieber, M. Hunter, T. McClure, G. Dresselhaus, and M. S. Dresselhaus. *Structural $(n, m)$ Determination of Isolated Single-Wall Carbon Nanotubes by Resonant Raman Scattering*. Physical Review Letters **86**, 6, 1118 (2001). URL `http://link.aps.org/doi/10.1103/PhysRevLett.86.1118`. 103

[Jor01b] A. Jorio, A. G. Souza Filho, G. Dresselhaus, M. S. Dresselhaus, R. Saito, J. H. Hafner, C. M. Lieber, F. M. Matinaga, M. S. S. Dantas, and M. A. Pimenta. *Joint density of electronic states for one isolated single-wall carbon nanotube studied by resonant Raman scattering*. Physical Review B: Condensed Matter and Materials Physics **63**, 24, 245416 (2001). URL `http://link.aps.org/doi/10.1103/PhysRevB.63.245416`. 12

[Jor02a] A. Jorio, C. Fantini, M. S. S. Dantas, M. A. Pimenta, A. G. Souza Filho, G. G. Samsonidze, V. W. Brar, G. Dresselhaus, M. S. Dresselhaus, A. K. Swan, M. S. Ünlü, B. B. Goldberg, and R. Saito. *Linewidth of the Raman features of individual single-wall carbon nanotubes*. Physical Review B: Condensed Matter and Materials Physics **66**, 11, 115411 (2002). URL `http://link.aps.org/doi/10.1103/PhysRevB.66.115411`. 14

[Jor02b] A. Jorio, A. G. Souza Filho, G. Dresselhaus, M. S. Dresselhaus, A. K. Swan, M. S. Ünlü, B. B. Goldberg, M. A. Pimenta, J. H. Hafner, C. M. Lieber, and R. Saito. *G-band resonant Raman study of 62 isolated single-wall carbon nanotubes*. Physical Review B: Condensed Matter and Materials Physics **65**, 155412 (2002). URL `http://dx.doi.org/10.1103/PhysRevB.65.155412`. 14, 53, 54

[Jor03a] A. Jorio, M. A. Pimenta, A. G. S. Filho, R. Saito, G. Dresselhaus, and M. S. Dresselhaus. *Characterizing carbon nanotube samples with resonance Raman scattering*. New Journal of Physics **5**, 1, 139 (2003). ISSN 1367-2630. URL `http://stacks.iop.org/1367-2630/5/i=1/a=139`. 13, 22

[Jor03b] A. Jorio, M. A. Pimenta, A. G. Souza Filho, G. G. Samsonidze, A. K. Swan, M. S. Ünlü, B. B. Goldberg, R. Saito, G. Dresselhaus, and M. S. Dresselhaus. *Resonance Raman Spectra of Carbon Nanotubes by Cross-Polarized Light*. Physical Review Letters **90**, 10, 107403 (2003). URL `http://link.aps.org/doi/10.1103/PhysRevLett.90.107403`. 14

[Jør06] H. I. Jørgensen, K. Grove-Rasmussen, J. R. Hauptmann, and P. E. Lindelof. *Single wall carbon nanotube double quantum dot*. Applied Physics Letters **89**, 23, 232113 (2006). URL `http://dx.doi.org/10.1063/1.2402887`. 85, 86

[Jor10] A. Jorio, G. Dresselhaus, and M. Dresselhaus. *Carbon Nanotubes: Advanced Topics in the Synthesis, Structure, Properties and Applications*. Topics in Applied Physics. Springer (2010). ISBN 9783642091957. URL http://www.springer.com/materials/nanotechnology/book/978-3-540-72864-1. 89

[Joy10] H. J. Joyce, J. Wong-Leung, Q. Gao, H. H. Tan, and C. Jagadish. *Phase Perfection in Zinc Blende and Wurtzite III/V Nanowires Using Basic Growth Parameters*. Nano Letters **10**, 3, 908 (2010). URL http://dx.doi.org/10.1021/nl903688v. 46

[Kam09] E. Kampert, F. F. B. J. Janssen, D. W. Boukhvalov, J. C. Russcher, J. M. M. Smits, R. de Gelder, B. de Bruin, P. C. M. Christianen, U. Zeitler, M. I. Katsnelson, J. C. Maan, and A. E. Rowan. *Ligand-Controlled Magnetic Interactions in Mn4 Clusters*. Inorganic Chemistry **48**, 24, 11903 (2009). ISSN 0020-1669. URL http://dx.doi.org/10.1021/ic901930w. 90, 91, 100, 126

[Kas04] D. Kashchiev. *Multicomponent nucleation: Thermodynamically consistent description of the nucleation work*. The Journal of Chemical Physics **120**, 8, 3749 (2004). URL http://dx.doi.org/10.1063/1.1643711. 26

[Kat99] H. Kataura, Y. Kumazawa, Y. Maniwa, I. Umezu, S. Suzuki, Y. Ohtsuka, and Y. Achiba. *Optical properties of single-wall carbon nanotubes*. Synthetic Metals **103**, 1–3, 2555 (1999). ISSN 0379-6779. URL http://dx.doi.org/10.1016/S0379-6779(98)00278-1. 11

[Kia98] C.-H. Kiang, M. Endo, P. M. Ajayan, G. Dresselhaus, and M. S. Dresselhaus. *Size Effects in Carbon Nanotubes*. Physical Review Letters **81**, 1869 (1998). URL http://dx.doi.org/10.1103/PhysRevLett.81.1869. 7

[Kim98] G. T. Kim, E. S. Choi, D. C. Kim, D. S. Suh, Y. W. Park, K. Liu, G. Duesberg, and S. Roth. *Magnetoresistance of an entangled single-wall carbon-nanotube network*. Physical Review B: Condensed Matter and Materials Physics **58**, 24, 16064 (1998). URL http://link.aps.org/doi/10.1103/PhysRevB.58.16064. 115, 116

[Kim01] G. Kim, S. Jhang, J. Park, Y. Park, and S. Roth. *Non-ohmic current–voltage characteristics in single-wall carbon nanotube network*. Synthetic Metals **117**, 1–3, 123 (2001). ISSN 0379-6779. URL http://www.sciencedirect.com/science/article/pii/S0379677900005518. 116

[Kim05] T. Kim, J.-M. Zuo, E. A. Olson, and I. Petrov. *Imaging suspended carbon nanotubes in field-effect transistors configured with microfabricated slits for transmission electron microscopy*. Applied Physics Letters **87**, 17, 173108 (2005). URL http://dx.doi.org/10.1063/1.2115070. 44

[Kis04] A. Kis, G. Csanyi, J.-P. Salvetat, T.-N. Lee, E. Couteau, A. J. Kulik, W. Benoit, J. Brugger, and L. Forro. *Reinforcement of single-walled carbon nanotube bundles*



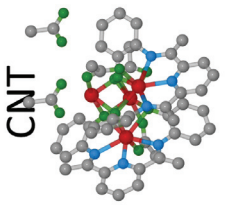

*by intertube bridging*. Nature Materials **3**, 3, 153 (2004). ISSN 1476-1122. URL http://dx.doi.org/10.1038/nmat1076. 112

[Kis08] C. Kisielowski, B. Freitag, M. Bischoff, H. van Lin, S. Lazar, G. Knippels, P. Tiemeijer, M. van der Stam, S. von Harrach, M. Stekelenburg, M. Haider, S. Uhlemann, H. Müller, P. Hartel, B. Kabius, D. Miller, I. Petrov, E. Olson, T. Donchev, E. Kenik, A. Lupini, J. Bentley, S. Pennycook, I. Anderson, A. Minor, A. Schmid, T. Duden, V. Radmilovic, Q. Ramasse, M. Watanabe, R. Erni, E. Stach, P. Denes, and U. Dahmen. *Detection of Single Atoms and Buried Defects in Three Dimensions by Aberration-Corrected Electron Microscope with 0.5-Å Information Limit*. Microscopy and Microanalysis **14**, 05, 469 (2008). URL http://dx.doi.org/10.1017/S1431927608080902. 23

[Kno32] M. Knoll and E. Ruska. *Das Elektronenmikroskop*. Zeitschrift für Physik **78**, 318 (1932). URL http://ernstruska.digilibrary.de/bibliographie/q006/q006.pdf. 23

[Kog92] M. Koguchi, H. Kakibayashi, M. Yazawa, K. Hiruma, and T. Katsuyama. *Crystal Structure Change of GaAs and InAs Whiskers from Zinc-Blende to Wurtzite Type*. Japanese Journal of Applied Physics **31**, Part 1, No. 7, 2061 (1992). URL http://dx.doi.org/10.1143/JJAP.31.2061. 16

[Kon98] J. Kong, H. T. Soh, A. M. Cassell, C. F. Quate, and H. Dai. *Synthesis of individual single-walled carbon nanotubes on patterned silicon wafers*. Nature **395**, 6705, 878 (1998). ISSN 0028-0836. URL http://dx.doi.org/10.1038/27632. 44, 82

[Kon01] J. Kong, E. Yenilmez, T. W. Tombler, W. Kim, H. Dai, R. B. Laughlin, L. Liu, C. S. Jayanthi, and S. Y. Wu. *Quantum Interference and Ballistic Transmission in Nanotube Electron Waveguides*. Physical Review Letters **87**, 106801 (2001). URL http://dx.doi.org/10.1103/PhysRevLett.87.106801. 28

[Kou01] L. P. Kouwenhoven, D. G. Austing, and S. Tarucha. *Few-electron quantum dots*. Reports on Progress in Physics **64**, 701 (2001). URL http://dx.doi.org/10.1088/0034-4885/64/6/201. 34, 35, 36

[Kre10] A. V. Kretinin, R. Popovitz-Biro, D. Mahalu, and H. Shtrikman. *Multimode Fabry-Pérot Conductance Oscillations in Suspended Stacking-Faults-Free InAs Nanowires*. Nano Letters **10**, 9, 3439 (2010). ISSN 1530-6984. URL http://dx.doi.org/10.1021/nl101522j. 17, 26, 124

[Kri07] C. Kristukat. *peak-o-mat. A multi purpose fitting programm written in python. Version 1.1.1*. Sourceforge (2007). URL http://sourceforge.net/projects/lorentz/files/. 22, 125

[Kro85] H. W. Kroto, J. R. Heath, S. C. O'Brien, R. F. Curl, and R. E. Smalley. *C60: Buckminsterfullerene*. Nature **318**, 6042, 162 (1985). URL http://dx.doi.org/10.1038/318162a0. 1

[Krü07] A. Krüger. *Kohlenstoff-Nanoröhren*. In *Neue Kohlenstoffmaterialien*, pp. 125–286. Teubner (2007). ISBN 978-3-8351-9098-6. 10.1007/978-3-8351-9098-6_3, URL http://dx.doi.org/10.1007/978-3-8351-9098-6_3. 6, 9

[Kum94] K. Kumakura, K. Nakakoshi, M. Kishida, J. Motohisa, T. Fukui, and H. Hasegawa. *Dynamics of selective metalorganic vapor phase epitaxy growth for GaAs/AlGaAs micro-pyramids*. Journal of Crystal Growth **145**, 308 (1994). ISSN 0022-0248. URL http://dx.doi.org/10.1016/0022-0248(94)91068-5. 45

[Lam50] R. Lambeir, A. Van Itterbeek, and G. Van Den Berg. *Measurements on the electrical resistivity of thin iron films at. Liquid helium temperatures*. Physica **16**, 11–12, 907 (1950). ISSN 0031-8914. URL http://www.sciencedirect.com/science/article/pii/003189145090098X. 34

[Lam69] J. Lambe and R. C. Jaklevic. *Charge-Quantization Studies Using a Tunnel Capacitor*. Physical Review Letters **22**, 25, 1371 (1969). URL http://link.aps.org/doi/10.1103/PhysRevLett.22.1371. 34

[Lan57] R. Landauer. *Spatial variation of currents and fields due to localized scatterers in metallic conduction*. IBM Journal of Research and Development **1**, 1, 223 (1957). URL http://dx.doi.org/10.1147/rd.13.0223. 28

[Lan87] R. Landauer. *Electrical transport in open and closed systems*. Zeitschrift für Physik B Condensed Matter **68**, 2, 217 (1987). URL http://dx.doi.org/10.1007/BF01304229. 28

[Lan96] L. Langer, V. Bayot, E. Grivei, J.-P. Issi, J. P. Heremans, C. H. Olk, L. Stockman, C. Van Haesendonck, and Y. Bruynseraede. *Quantum Transport in a Multiwalled Carbon Nanotube*. Physical Review Letters **76**, 479 (1996). URL http://dx.doi.org/10.1103/PhysRevLett.76.479. 30, 31

[Lan12] G. P. Lansbergen. *Nanoelectronics: Transistors arrive at the atomic limit*. Nature Nanotechnology **7**, 4, 209 (2012). ISSN 1748-3387. URL http://dx.doi.org/10.1038/nnano.2012.23. 1, 43

[Las09] B. Lassagne, Y. Tarakanov, J. Kinaret, D. Garcia-Sanchez, and A. Bachtold. *Coupling Mechanics to Charge Transport in Carbon Nanotube Mechanical Resonators*. Science **325**, 5944, 1107 (2009). URL http://www.sciencemag.org/content/325/5944/1107.abstract. 39

[Le98] H. Q. Le, C. H. Lin, and S. S. Pei. *Low-loss high-efficiency and high-power diode-pumped mid-infrared GaInSb/InAs quantum well lasers*. Applied Physics Letters **72**, 26, 3434 (1998). URL http://dx.doi.org/10.1063/1.121657. 16



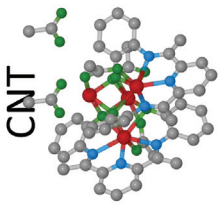

[Lee85] P. A. Lee and A. D. Stone. *Universal Conductance Fluctuations in Metals*. Physical Review Letters **55**, 15, 1622 (1985). URL http://dx.doi.org/10.1103/PhysRevLett.55.1622. 26, 29, 31

[Lee86] P. A. Lee. *Universal conductance fluctuations in disordered metals*. Physica A: Statistical Mechanics and its Applications **140**, 1-2, 169 (1986). ISSN 0378-4371. URL http://dx.doi.org/10.1016/0378-4371(86)90217-7. 31

[Lee87] P. A. Lee, A. D. Stone, and H. Fukuyama. *Universal conductance fluctuations in metals: Effects of finite temperature, interactions, and magnetic field*. Physical Review B: Condensed Matter and Materials Physics **35**, 1039 (1987). URL http://dx.doi.org/10.1103/PhysRevB.35.1039. 61, 62

[Len06] M. Lentzen. *Progress in aberration-corrected high-resolution transmission electron microscopy using hardware aberration correction*. Microscopy and Microanalysis **12**, 03, 191 (2006). URL http://dx.doi.org/10.1017/S1431927606060326. 24

[Len07] M. Lentzen. *Abberation-corrected high-resolution transmission electron microscopy*. In K. Urban (ed.), *38th IFF Spring School: Probing the Nanoworld - Microscopies, Scattering and Spectroscopies of the Solid State*, chapter C1. Forschungszentrum Jülich, Zentralbibliothek (2007). URL http://d-nb.info/983539421. 23, 24

[LeR04] B. J. LeRoy, S. G. Lemay, J. Kong, and C. Dekker. *Electrical generation and absorption of phonons in carbon nanotubes*. Nature **432**, 7015, 371 (2004). ISSN 0028-0836. URL http://dx.doi.org/10.1038/nature03046. 39

[Let09] R. Leturcq, C. Stampfer, K. Inderbitzin, L. Durrer, C. Hierold, E. Mariani, M. G. Schultz, F. von Oppen, and K. Ensslin. *Franck-Condon blockade in suspended carbon nanotube quantum dots*. Nature Physics **5**, 5, 327 (2009). ISSN 1745-2473. URL http://dx.doi.org/10.1038/nphys1234. 39

[Lev96] M. E. Levinsteĭn, S. Rumyantsev, and M. Shur. *Si, Ge, C (Diamond), GaAs, GaP, GaSb, InAs, InP, InSb*. In M. E. Levinsteĭn, S. Rumyantsev, and M. Shur (eds.), *Handbook Series on Semiconductor Parameters*, volume 1. World Scientific Pub Co., London (1996). 16

[Lev11] D. Levshov, T. X. Than, R. Arenal, V. N. Popov, R. Parret, M. Paillet, V. Jourdain, A. A. Zahab, T. Michel, Y. I. Yuzyuk, and J.-L. Sauvajol. *Experimental Evidence of a Mechanical Coupling between Layers in an Individual Double-Walled Carbon Nanotube*. Nano Letters **11**, 11, 4800 (2011). ISSN 1530-6984. URL http://dx.doi.org/10.1021/nl2026234. 14

[Li06] Y. Li, F. Qian, J. Xiang, and C. M. Lieber. *Nanowire electronic and optoelectronic devices*. Materials Today **9**, 18 (2006). URL http://dx.doi.org/10.1016/S1369-7021(06)71650-9. 2, 57

[Li11a] L.-X. Li and F. Li. *The effect of carbonyl, carboxyl and hydroxyl groups on the capacitance of carbon nanotubes.* New Carbon Materials **26**, 3, 224 (2011). ISSN 1872-5805. URL http://dx.doi.org/10.1016/S1872-5805(11)60078-4. 16, 108

[Li11b] Z.-A. Li, C. Moller, V. Migunov, M. Spasova, M. Farle, A. Lysov, C. Gutsche, I. Regolin, W. Prost, F.-J. Tegude, and P. Ercius. *Planar-defect characteristics and cross-sections of* ⟨001⟩*,* ⟨111⟩*, and* ⟨112⟩ *InAs nanowires.* Journal of Applied Physics **109**, 11, 114320 (2011). URL http://dx.doi.org/10.1063/1.3592186. 16

[Lic08] H. Lichte and M. Lehmann. *Electron holography–basics and applications.* Reports on Progress in Physics **71**, 1, 016102 (2008). URL http://stacks.iop.org/0034-4885/71/i=1/a=016102. 67, 124

[Lie03] G. Lientschnig. *Single-electron and molecular devices.* Ph.D. thesis, Technische Universiteit Delft (2003). URL http://repository.tudelft.nl/assets/uuid:8162b114-b6d6-4d0d-b325-4c3321763e38/as_lientschnig_20031124.pdf. 85

[Lin02] J. J. Lin and J. P. Bird. *Recent experimental studies of electron dephasing in metal and semiconductor mesoscopic structures.* Journal of Physics: Condensed Matter **14**, 18, R501 (2002). URL http://stacks.iop.org/0953-8984/14/i=18/a=201. 29, 63

[Liu01] K. Liu, P. Avouris, R. Martel, and W. K. Hsu. *Electrical transport in doped multiwalled carbon nanotubes.* Physical Review B: Condensed Matter and Materials Physics **63**, 161404 (2001). URL http://dx.doi.org/10.1103/PhysRevB.63.161404. 29

[Los98] D. Loss and D. P. DiVincenzo. *Quantum computation with quantum dots.* Physical Review A: Atomic, Molecular, and Optical Physics **57**, 1, 120 (1998). URL http://link.aps.org/doi/10.1103/PhysRevA.57.120. 1, 34

[Lou01] S. Louie. *Electronic Properties, Junctions, and Defects of Carbon Nanotubes.* In M. Dresselhaus, G. Dresselhaus, and P. Avouris (eds.), *Carbon Nanotubes*, volume 80 of *Topics in Applied Physics*, pp. 113–145. Springer Berlin / Heidelberg (2001). ISBN 978-3-540-41086-7. URL http://dx.doi.org/10.1007/3-540-39947-X_6. 9

[Lüt08] H. Lüth. *Quantenphysik in der Nanowelt: Schrödingers Katze bei den Zwergen.* Springer (2008). ISBN 9783540710424. URL http://d-nb.info/989845753. 17, 18

[Mak09] H. Maki, T. Mizuno, S. Suzuki, T. Sato, and Y. Kobayashi. *Multi-Back-Gate Control of Carbon Nanotube Double-Quantum Dot.* Japanese Journal of Applied



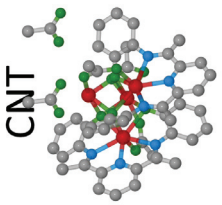

Physics **48**, 4, 04C201 (2009). URL http://dx.doi.org/10.1143/JJAP.48.04C201. 85

[Man08] M. Mannini, P. Sainctavit, R. Sessoli, C. Cartier dit Moulin, F. Pineider, M.-A. Arrio, A. Cornia, and D. Gatteschi. *XAS and XMCD Investigation of $Mn_{12}$ Monolayers on Gold*. Chemistry – A European Journal **14**, 25, 7530 (2008). ISSN 1521-3765. URL http://dx.doi.org/10.1002/chem.200800693. 89

[Mar03] C. R. Martin and P. Kohli. *The emerging field of nanotube biotechnology*. Nature Reviews. Drug Discovery **2**, 1, 29 (2003). ISSN 1474-1776. URL http://dx.doi.org/10.1038/nrd988. 2

[Mau04] J. Maultzsch, S. Reich, and C. Thomsen. *Double-resonant Raman scattering in graphite: Interference effects, selection rules, and phonon dispersion*. Physical Review B: Condensed Matter and Materials Physics **70**, 15, 155403 (2004). URL http://link.aps.org/doi/10.1103/PhysRevB.70.155403. 12

[Mau05] J. Maultzsch, H. Telg, S. Reich, and C. Thomsen. *Radial breathing mode of single-walled carbon nanotubes: Optical transition energies and chiral-index assignment*. Physical Review B: Condensed Matter and Materials Physics **72**, 205438 (2005). URL http://dx.doi.org/10.1103/PhysRevB.72.205438. 11, 55

[Med11] V. Meded, A. Bagrets, K. Fink, R. Chandrasekar, M. Ruben, F. Evers, A. Bernand-Mantel, J. S. Seldenthuis, A. Beukman, and H. S. J. van der Zant. *Electrical control over the Fe(II) spin crossover in a single molecule: Theory and experiment*. Physical Review B: Condensed Matter and Materials Physics **83**, 24, 245415 (2011). URL http://link.aps.org/doi/10.1103/PhysRevB.83.245415. 76, 119, 122

[Mey12] C. Meyer, C. Besson, R. Frielinghaus, A.-K. Saelhoff, H. Flötotto, L. Houben, P. Kögerler, and C. M. Schneider. *Covalent functionalization of carbon nanotubes with tetramanganese complexes*. physica status solidi (b) **249**, 12, 2412 (2012). ISSN 1521-3951. URL http://dx.doi.org/10.1002/pssb.201200135. 90, 91, 92, 100, 102, 127

[Mic09] T. Michel, M. Paillet, D. Nakabayashi, M. Picher, V. Jourdain, J. C. Meyer, A. A. Zahab, and J.-L. Sauvajol. *Indexing of individual single-walled carbon nanotubes from Raman spectroscopy*. Physical Review B: Condensed Matter and Materials Physics **80**, 24, 245416 (2009). URL http://link.aps.org/doi/10.1103/PhysRevB.80.245416. 14

[Mik03] C. Miko, M. Milas, J. W. Seo, E. Couteau, N. Barisic, R. Gaal, and L. Forro. *Effect of electron irradiation on the electrical properties of fibers of aligned single-walled carbon nanotubes*. Applied Physics Letters **83**, 22, 4622 (2003). URL http://dx.doi.org/10.1063/1.1631060. 112

[Mol79] W. W. Molzen, A. N. Broers, J. J. Cuomo, J. M. E. Harper, and R. B. Laibowitz. *Materials and techniques used in nanostructure fabrication.* Journal of Vacuum Science and Technology **16**, 2, 269 (1979). URL http://dx.doi.org/10.1116/1.569924. 47

[Moo65] G. E. Moore. *Cramming more components onto integrated circuits.* Electronics Magazine **38**, 8, 4 (1965). URL http://download.intel.com/museum/Moores_Law/Articles-Press_Releases/Gordon_Moore_1965_Article.pdf. 1

[Moo07] S. Moon, W. Song, J. S. Lee, N. Kim, J. Kim, S.-G. Lee, and M.-S. Choi. *Eightfold Shell Filling in a Double-Wall Carbon Nanotube Quantum Dot.* Physical Review Letters **99**, 17, 176804 (2007). URL http://link.aps.org/doi/10.1103/PhysRevLett.99.176804. 38, 69, 82

[Mot69] N. F. Mott. *Conduction in non-crystalline materials.* Philosophical Magazine **19**, 160, 835 (1969). ISSN 0031-8086. URL http://dx.doi.org/10.1080/14786436908216338. 115

[Mot79] N. Mott and E. Davis. *Electronic Processes in Non-Crystalline Materials.* Oxford University Press (1979). URL http://tocs.ulb.tu-darmstadt.de/81908415.pdf. 115, 116

[Mou12] V. Mourik, K. Zuo, S. M. Frolov, S. R. Plissard, E. P. A. M. Bakkers, and L. P. Kouwenhoven. *Signatures of Majorana Fermions in Hybrid Superconductor-Semiconductor Nanowire Devices.* Science **336**, 6084, 1003 (2012). URL http://dx.doi.org/10.1126/science.1222360. 1, 57

[Muo10] M. Muoth, T. Helbling, L. Durrer, S.-W. Lee, C. Roman, and C. Hierold. *Hysteresis-free operation of suspended carbon nanotube transistors.* Nature Nanotechnology **5**, 8, 589 (2010). ISSN 1748-3387. URL http://dx.doi.org/10.1038/nnano.2010.129. 39, 44

[Mur94] M. Murayama and T. Nakayama. *Chemical trend of band offsets at wurtzite/zinc-blende heterocrystalline semiconductor interfaces.* Physical Review B: Condensed Matter and Materials Physics **49**, 4710 (1994). URL http://dx.doi.org/10.1103/PhysRevB.49.4710. 17

[Mur00] C. B. Murray, C. R. Kagan, and M. G. Bawendi. *Synthesis and characterization of monodisperse nanocrystals and close-packed nanocrystal assemblies.* Annual Review of Materials Science **30**, 1, 545 (2000). ISSN 0084-6600. URL http://dx.doi.org/10.1146/annurev.matsci.30.1.545. 34

[Nee64] P. Neelakantan. *Raman spectrum of acetonitrile.* Proceedings of the Indian Academy of Sciences - Section A **60**, 6, 422 (1064). URL http://eprints.iisc.ernet.in/27986/. 108



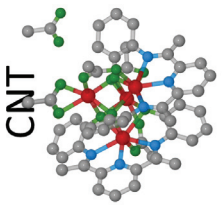

[Nog91] M. Noguchi, K. Hirakawa, and T. Ikoma. *Intrinsic electron accumulation layers on reconstructed clean InAs(100) surfaces*. Physical Review Letters **66**, 2243 (1991). URL http://dx.doi.org/10.1103/PhysRevLett.66.2243. 57

[Nos12] E. Nossol and A. J. Gorgatti Zarbin. *Transparent films from carbon nanotubes/Prussian blue nanocomposites: preparation, characterization, and application as electrochemical sensors*. Journal of Materials Chemistry **22**, 1824 (2012). URL http://dx.doi.org/10.1039/C1JM14225A. 52

[Nov04] K. S. Novoselov, A. K. Geim, S. V. Morozov, D. Jiang, Y. Zhang, S. V. Dubonos, I. V. Grigorieva, and A. A. Firsov. *Electric Field Effect in Atomically Thin Carbon Films*. Science **306**, 5696, 666 (2004). URL http://www.sciencemag.org/content/306/5696/666.abstract. 1, 8

[NP10] S. Nadj-Perge, S. M. Frolov, E. P. A. M. Bakkers, and L. P. Kouwenhoven. *Spin-orbit qubit in a semiconductor nanowire*. Nature **468**, 7327, 1084 (2010). ISSN 0028-0836. URL http://dx.doi.org/10.1038/nature09682. 16

[Nyg01] J. Nygård and D. H. Cobden. *Quantum dots in suspended single-wall carbon nanotubes*. Applied Physics Letters **79**, 25, 4216 (2001). URL http://dx.doi.org/10.1063/1.1428117. 39

[Nyq28] H. Nyquist. *Thermal Agitation of Electric Charge in Conductors*. Physical Review **32**, 110 (1928). URL http://dx.doi.org/10.1103/PhysRev.32.110. 29

[Obe06] D. Obergfell, J. C. Meyer, M. Haluska, A. N. Khlobystov, S. Yang, L. Fan, D. Liu, and S. Roth. *Transport and TEM on dysprosium metallofullerene peapods*. physica status solidi (b) **243**, 13, 3430 (2006). ISSN 1521-3951. URL http://dx.doi.org/10.1002/pssb.200669117. 44

[O'C04] M. J. O'Connell, S. Sivaram, and S. K. Doorn. *Near-infrared resonance Raman excitation profile studies of single-walled carbon nanotube intertube interactions: A direct comparison of bundled and individually dispersed HiPco nanotubes*. Physical Review B: Condensed Matter and Materials Physics **69**, 235415 (2004). URL http://link.aps.org/doi/10.1103/PhysRevB.69.235415. 12

[OC05] M. Oron-Carl, F. Hennrich, M. M. Kappes, H. v. Löhneysen, and R. Krupke. *On the Electron–Phonon Coupling of Individual Single-Walled Carbon Nanotubes*. Nano Letters **5**, 9, 1761 (2005). ISSN 1530-6984. URL http://dx.doi.org/10.1021/nl051107t. 14, 43, 53

[Odo98] T. W. Odom, J.-L. Huang, P. Kim, and C. M. Lieber. *Atomic structure and electronic properties of single-walled carbon nanotubes*. Nature **391**, 6662, 62 (1998). ISSN 0028-0836. URL http://dx.doi.org/10.1038/34145. 43

[Odo00] T. W. Odom, J.-L. Huang, P. Kim, and C. M. Lieber. *Structure and Electronic Properties of Carbon Nanotubes*. The Journal of Physical Chemistry B **104**, 13, 2794 (2000). URL http://dx.doi.org/10.1021/jp993592k. 6

[Ohn04] Y. Ohno, S. Kishimoto, T. Mizutani, T. Okazaki, and H. Shinohara. *Chirality assignment of individual single-walled carbon nanotubes in carbon nanotube field-effect transistors by micro-photocurrent spectroscopy.* Applied Physics Letters **84**, 8, 1368 (2004). URL `http://dx.doi.org/10.1063/1.1650554`. 10

[Oka01] S. Okada, S. Saito, and A. Oshiyama. *Energetics and Electronic Structures of Encapsulated $C_{60}$ in a Carbon Nanotube.* Physical Review Letters **86**, 3835 (2001). URL `http://dx.doi.org/10.1103/PhysRevLett.86.3835`. 89

[Ols96] L. O. Olsson, C. B. M. Andersson, M. C. Håkansson, J. Kanski, L. Ilver, and U. O. Karlsson. *Charge Accumulation at InAs Surfaces.* Physical Review Letters **76**, 3626 (1996). URL `http://dx.doi.org/10.1103/PhysRevLett.76.3626`. 17

[Onn11] H. K. Onnes. *The Superconductivity of Mercury.* Communications from the Physical Laboratory at the University of Leiden **12**, 120 (1911). 26

[Ons31] L. Onsager. *Reciprocal Relations in Irreversible Processes. II.* Physical Review **38**, 12, 2265 (1931). URL `http://dx.doi.org/10.1103/PhysRev.38.2265`. 60

[Ota04] T. Ota, K. Ono, M. Stopa, T. Hatano, S. Tarucha, H. Z. Song, Y. Nakata, T. Miyazawa, T. Ohshima, and N. Yokoyama. *Single-Dot Spectroscopy via Elastic Single-Electron Tunneling through a Pair of Coupled Quantum Dots.* Physical Review Letters **93**, 6, 066801 (2004). URL `http://link.aps.org/doi/10.1103/PhysRevLett.93.066801`. 85, 86

[Pai06] M. Paillet, T. Michel, J. C. Meyer, V. N. Popov, L. Henrard, S. Roth, and J.-L. Sauvajol. *Raman Active Phonons of Identified Semiconducting Single-Walled Carbon Nanotubes.* Physical Review Letters **96**, 25, 257401 (2006). URL `http://link.aps.org/doi/10.1103/PhysRevLett.96.257401`. 14

[Pal01] F. Pallikari, G. Chondrokoukis, M. Rebelakis, and Y. Kotsalas. *Raman spectroscopy: A technique for estimating extent of polymerization in PMMA.* Materials Research Innovations **4**, 89 (2001). ISSN 1432-8917. URL `http://dx.doi.org/10.1007/s100190000076`. 53

[Pan04] H. Pan, Y. P. Feng, and J. Y. Lin. *Ab initio study of OH-functionalized single-wall carbon nanotubes.* Physical Review B: Condensed Matter and Materials Physics **70**, 24, 245425 (2004). URL `http://link.aps.org/doi/10.1103/PhysRevB.70.245425`. 112

[Par00] H. Park, J. Park, A. K. L. Lim, E. H. Anderson, A. P. Alivisatos, and P. L. McEuen. *Nanomechanical oscillations in a single-$C_{60}$ transistor.* Nature **407**, 6800, 57 (2000). ISSN 0028-0836. URL `http://dx.doi.org/10.1038/35024031`. 34



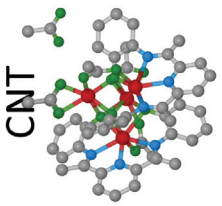

[Par02] J. Park, A. N. Pasupathy, J. I. Goldsmith, C. Chang, Y. Yaish, J. R. Petta, M. Rinkoski, J. P. Sethna, H. D. Abruna, P. L. McEuen, and D. C. Ralph. *Coulomb blockade and the Kondo effect in single-atom transistors*. Nature **417**, 6890, 722 (2002). ISSN 0028-0836. URL http://dx.doi.org/10.1038/nature00791. 34

[Par06] J. S. Park, Y. Oyama, R. Saito, W. Izumida, J. Jiang, K. Sato, C. Fantini, A. Jorio, G. Dresselhaus, and M. S. Dresselhaus. *Raman resonance window of single-wall carbon nanotubes*. Physical Review B: Condensed Matter and Materials Physics **74**, 165414 (2006). URL http://dx.doi.org/10.1103/PhysRevB.74.165414. 55

[Pet01] J. R. Petta and D. C. Ralph. *Studies of Spin-Orbit Scattering in Noble-Metal Nanoparticles Using Energy-Level Tunneling Spectroscopy*. Physical Review Letters **87**, 26, 266801 (2001). URL http://link.aps.org/doi/10.1103/PhysRevLett.87.266801. 34

[Pis07] S. Piscanec, M. Lazzeri, J. Robertson, A. C. Ferrari, and F. Mauri. *Optical phonons in carbon nanotubes: Kohn anomalies, Peierls distortions, and dynamic effects*. Physical Review B: Condensed Matter and Materials Physics **75**, 035427 (2007). URL http://dx.doi.org/10.1103/PhysRevB.75.035427. 14, 54

[Pon08] L. A. Ponomarenko, F. Schedin, M. I. Katsnelson, R. Yang, E. W. Hill, K. S. Novoselov, and A. K. Geim. *Chaotic dirac billiard in graphene quantum dots*. Science **320**, 5874, 356 (2008). ISSN 0036-8075. URL http://dx.doi.org/10.1126/science.1154663. 34

[Pop04] V. N. Popov and L. Henrard. *Comparative study of the optical properties of single-walled carbon nanotubes within orthogonal and nonorthogonal tight-binding models*. Physical Review B: Condensed Matter and Materials Physics **70**, 115407 (2004). URL http://dx.doi.org/10.1103/PhysRevB.70.115407. 11, 54, 55, 103

[Pre09] E. Pretsch, P. Bühlmann, and M. Badertscher. *Structure Determination of Organic Compounds: Tables of Spectral Data*. SpringerLink: Springer e-Books. Springer (2009). ISBN 9783540938095. URL http://d-nb.info/992498538. 100

[Qua07] C. H. L. Quay, J. Cumings, S. J. Gamble, R. d. Picciotto, H. Kataura, and D. Goldhaber-Gordon. *Magnetic field dependence of the spin-1/2 and spin-1 Kondo effects in a quantum dot*. Physical Review B: Condensed Matter and Materials Physics **76**, 24, 245311 (2007). URL http://link.aps.org/doi/10.1103/PhysRevB.76.245311. 69

[Que02] W. Que. *Luttinger parameter g for metallic carbon nanotubes and related systems*. Physical Review B: Condensed Matter and Materials Physics **66**, 193405 (2002). URL http://dx.doi.org/10.1103/PhysRevB.66.193405. 43

[Rad52] L. V. Radushkevich and V. M. Lukyanovich. О Структуре Углерода, Образующегося При Термическом Разложении Окиси Углерода На Железном Контакте *(About the structure of carbon formed at thermal deposition of carbon monoxide on contact with iron)*. Журнал физической химии (Soviet Journal of Physical Chemistry) **26**, 88 (1952). URL `http://nanotube.msu.edu/HSS/2006/4/2006-4.pdf`. 44

[Rai93] M. E. Raikh and G. F. Wessels. *Single-scattering-path approach to the negative magnetoresistance in the variable-range-hopping regime for two-dimensional electron systems*. Physical Review B: Condensed Matter and Materials Physics **47**, 23, 15609 (1993). URL `http://link.aps.org/doi/10.1103/PhysRevB.47.15609`. 117

[Ral95] D. C. Ralph, C. T. Black, and M. Tinkham. *Spectroscopic Measurements of Discrete Electronic States in Single Metal Particles*. Physical Review Letters **74**, 16, 3241 (1995). URL `http://link.aps.org/doi/10.1103/PhysRevLett.74.3241`. 34

[Ram28] C. V. Raman. *A Change of Wave-length in Light Scattering*. Nature **121**, 619 (1928). URL `http://www.nature.com/nature/journal/v121/n3051/pdf/121619b0.pdf`. 12

[Ray71] J. W. S. . B. Rayleigh. *LVIII. On the scattering of light by small particles*. Philosophical Magazine Series 4 **41**, 275, 447 (1871). ISSN 1941-5982. URL `http://dx.doi.org/10.1080/14786447108640507`. 10

[Rec10] F. Reckermann, J. Splettstoesser, and M. R. Wegewijs. *Interaction-Induced Adiabatic Nonlinear Transport*. Physical Review Letters **104**, 22, 226803 (2010). URL `http://link.aps.org/doi/10.1103/PhysRevLett.104.226803`. 40

[Ree97] M. A. Reed, C. Zhou, C. J. Muller, T. P. Burgin, and J. M. Tour. *Conductance of a Molecular Junction*. Science **278**, 5336, 252 (1997). URL `http://www.sciencemag.org/content/278/5336/252`. 34

[Rei95] L. Reimer. *Energy-filtering transmission electron microscopy*. Springer (1995). URL `http://d-nb.info/943410363`. 25

[Rei02] S. Reich, J. Maultzsch, C. Thomsen, and P. Ordejón. *Tight-binding description of graphene*. Physical Review B: Condensed Matter and Materials Physics **66**, 035412 (2002). URL `http://dx.doi.org/10.1103/PhysRevB.66.035412`. 8, 11

[Rei04] S. Reich, C. Thomsen, and J. Maultzsch. *Carbon nanotubes: basic concepts and physical properties*. Wiley-VCH (2004). 6, 8, 9, 11

[Rei08] S. Reich, C. Thomsen, and J. Maultzsch. *Carbon Nanotubes*. John Wiley & Sons (2008). ISBN 9783527618057. URL `http://dx.doi.org/10.1002/9783527618040`. 89



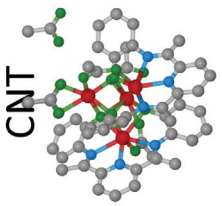

[Ric08] T. Richter, C. BloÌˆmers, H. LuÌˆth, R. Calarco, M. Indlekofer, M. Marso, and T. SchaÌˆpers. *Flux Quantization Effects in InN Nanowires*. Nano Letters **8**, 9, 2834 (2008). URL http://dx.doi.org/10.1021/nl8014389. 18

[Ruz92] I. M. Ruzin, V. Chandrasekhar, E. I. Levin, and L. I. Glazman. *Stochastic Coulomb blockade in a double-dot system*. Physical Review B: Condensed Matter and Materials Physics **45**, 23, 13469 (1992). URL http://link.aps.org/doi/10.1103/PhysRevB.45.13469. 74, 83

[Sae12] A.-K. Saelhoff. *Charakterisierung von funktionalisierten Kohlenstoffnanoröhren*. Diploma thesis, Rheinisch-Westfälische Technische Hochschule Aachen (2012). 90, 91, 100, 102

[Sai93] Y. Saito, T. Yoshikawa, S. Bandow, M. Tomita, and T. Hayashi. *Interlayer spacings in carbon nanotubes*. Physical Review B: Condensed Matter and Materials Physics **48**, 1907 (1993). URL http://dx.doi.org/10.1103/PhysRevB.48.1907. 52, 82

[Sai00] R. Saito, G. Dresselhaus, and M. S. Dresselhaus. *Trigonal warping effect of carbon nanotubes*. Physical Review B: Condensed Matter and Materials Physics **61**, 2981 (2000). URL http://dx.doi.org/10.1103/PhysRevB.61.2981. 7

[Sal08] M. Salvato, M. Cirillo, M. Lucci, S. Orlanducci, I. Ottaviani, M. L. Terranova, and F. Toschi. *Charge Transport and Tunneling in Single-Walled Carbon Nanotube Bundles*. Physical Review Letters **101**, 24, 246804 (2008). URL http://link.aps.org/doi/10.1103/PhysRevLett.101.246804. 116

[Sam04] L. Samuelson, C. Thelander, M. Björk, M. Borgström, K. Deppert, K. Dick, A. Hansen, T. Mårtensson, N. Panev, A. Persson, W. Seifert, N. Sköld, M. Larsson, and L. Wallenberg. *Semiconductor nanowires for 0D and 1D physics and applications*. Physica E: Low-dimensional Systems and Nanostructures **25**, $2-3$, 313 (2004). ISSN 1386-9477. URL http://dx.doi.org/10.1016/j.physe.2004.06.030. 57

[Sap05] S. Sapmaz, P. Jarillo-Herrero, J. Kong, C. Dekker, L. P. Kouwenhoven, and H. S. J. van der Zant. *Electronic excitation spectrum of metallic carbon nanotubes*. Physical Review B: Condensed Matter and Materials Physics **71**, 15, 153402 (2005). URL http://link.aps.org/doi/10.1103/PhysRevB.71.153402. 38

[Sap06] S. Sapmaz, P. Jarillo-Herrero, Y. M. Blanter, C. Dekker, and H. S. J. van der Zant. *Tunneling in Suspended Carbon Nanotubes Assisted by Longitudinal Phonons*. Physical Review Letters **96**, 2, 026801 (2006). URL http://link.aps.org/doi/10.1103/PhysRevLett.96.026801. 39

[Sch36] O. Scherzer. *Über einige Fehler von Elektronenlinsen.* Zeitschrift für Physik A Hadrons and Nuclei **101**, 593 (1936). ISSN 0939-7922. URL http://dx.doi.org/10.1007/BF01349606. 24

[Sch47] O. Scherzer. *Sphärische und chromatische Korrektur von Elektronenlinsen.* Optik **2**, 114 (1947). URL http://www.ensmp.fr/aflb/AFLB-295/aflb295m199.pdf. 24

[Sch01] T. Schäpers. *Superconductor/Semiconductor Junctions*, volume 174 of *Springer Tracts in Modern Physics*. Springer Berlin / Heidelberg (2001). URL http://dx.doi.org/10.1007/3-540-45525-6. 26

[Sch04] T. Schäpers. *Transport in Nanostructures.* Lecture notes, Rheinisch-Westfälische Technische Hochschule Aachen (2004). 27

[Sch10] M. D. Schroer and J. R. Petta. *Correlating the Nanostructure and Electronic Properties of InAs Nanowires.* Nano Letters **10**, 5, 1618 (2010). URL http://dx.doi.org/10.1021/nl904053j. 16, 34, 57, 58, 63, 124

[Sch12] M. Schuck. *Herstellung und Charakterisierung von Halbleiternanodrahtproben für Transportmessungen und Elektronenmikroskopie.* Diploma thesis, Rheinisch-Westfälische Technische Hochschule Aachen (2012). 62

[Sco12] Scopus. *Search query for "nano"* (2012). 1

[Sel11] J. S. Seldenthuis. *Electrical and mechanical effects in single-molecule junctions.* Ph.D. thesis, Technische Universiteit Delft (2011). URL http://www.scm.com/Doc/Seldenthuis2011.pdf. 72, 76, 77, 78, 79

[Shi08] H. Shiozawa, T. Pichler, A. Grüneis, R. Pfeiffer, H. Kuzmany, Z. Liu, K. Suenaga, and H. Kataura. *A Catalytic Reaction Inside a Single-Walled Carbon Nanotube.* Advanced Materials **20**, 8, 1443 (2008). ISSN 1521-4095. URL http://dx.doi.org/10.1002/adma.200701466. 89

[Sho07] I. Shorubalko, A. Pfund, R. Leturcq, M. T. Borgström, F. Gramm, E. Müller, E. Gini, and K. Ensslin. *Tunable few-electron quantum dots in InAs nanowires.* Nanotechnology **18**, 4, 044014 (2007). URL http://stacks.iop.org/0957-4484/18/i=4/a=044014. 57, 65

[Sla10] K. Sladek, A. Penz, K. Weis, S. Wirths, C. Volk, S. Alagha, M. Akabori, S. Lenk, M. Luysberg, H. Lüth, H. Hardtdegen, T. Schäpers, and D. Grützmacher. *Influence of Silicon Doping on the SA-MOVPE of InAs Nanowires.* MRS Proceedings **1258**, 2 (2010). URL http://dx.doi.org/10.1557/PROC-1258-P02-05. 45

[Sla12] K. Sladek, A. Winden, S. Wirths, K. Weis, C. Blömers, n. Gül, T. Grap, S. Lenk, M. von der Ahe, T. E. Weirich, H. Hardtdegen, M. I. Lepsa, A. Lysov, Z.-A. Li, W. Prost, F.-J. Tegude, H. Lüth, T. Schäpers, and D. Grützmacher. *Comparison*



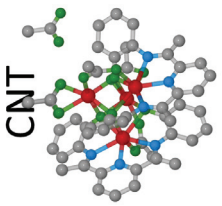

*of InAs nanowire conductivity: influence of growth method and structure*. physica status solidi (c) **9**, 2, 230 (2012). ISSN 1610-1642. URL http://dx.doi.org/10.1002/pssc.201100282. 45, 46

[Slo12] M. Slot. *Raman spectroscopy and electronic transport measurements on carbon nanotube networks: influence of oxidation and functionalization with $Mn_4$ complexes*. Bachelor thesis, Rheinisch-Westfälische Technische Hochschule Aachen (2012). 90, 100, 113

[Smi89] K. Smit, L. Koenders, and W. Monch. *Adsorption of chlorine and oxygen on cleaved InAs(110) surfaces: Raman spectroscopy, photoemission spectroscopy, and Kelvin probe measurements*. In *Journal of Vacuum Science & Technology B*, volume 7 of *4*, pp. 888–893. AVS (1989). URL http://dx.doi.org/10.1116/1.584619. 17

[Smi98] B. W. Smith, M. Monthioux, and D. E. Luzzi. *Encapsulated $C_{60}$ in carbon nanotubes*. Nature **396**, 6709, 323 (1998). ISSN 0028-0836. URL http://dx.doi.org/10.1038/24521. 89

[Smi01] B. W. Smith and D. E. Luzzi. *Electron irradiation effects in single wall carbon nanotubes*. Journal of Applied Physics **90**, 7, 3509 (2001). URL http://dx.doi.org/10.1063/1.1383020. 26

[Soc04] G. Socrates. *Infrared and Raman Characteristic Group Frequencies: Tables and Charts*. John Wiley & Sons (2004). ISBN 9780470093078. URL http://books.google.de/books?id=LDoAAjMnwEIC. 100

[Spu08] C. Spudat, C. Meyer, and C. M. Schneider. *Oxidation induced shifts of Raman modes of carbon nanotubes*. physica status solidi (b) **245**, 10, 2205 (2008). ISSN 1521-3951. URL http://dx.doi.org/10.1002/pssb.200879627. 16, 98

[Spu09] C. Spudat, C. Meyer, K. Goss, and C. M. Schneider. *Peapod synthesis depending on the number of nanotube sidewalls*. physica status solidi (b) **246**, 11-12, 2498 (2009). ISSN 1521-3951. URL http://dx.doi.org/10.1002/pssb.200982323. 16, 44, 89, 92, 93, 113

[Spu10a] C. Spudat. *Correlation between Raman spectroscopy and electron microscopy on individual carbon nanotubes and peapods*. Ph.D. thesis, Universität Duisburg – Essen (2010). URL http://dmssrv.zb.kfa-juelich.de/w2p2/tmp/34C957C5-8B36-4925-BF17-1AEC00D884A2/Information_11.pdf. 22, 23, 26, 82, 93

[Spu10b] C. Spudat, M. Müller, L. Houben, J. Maultzsch, K. Goß, C. Thomsen, C. M. Schneider, and C. Meyer. *Observation of Breathing-like Modes in an Individual Multiwalled Carbon Nanotube*. Nano Letters **10**, 11, 4470 (2010). URL http://dx.doi.org/10.1021/nl102305a. 14, 99

[Sta87] P. Stadelmann. *EMS - a software package for electron diffraction analysis and HREM image simulation in materials science*. Ultramicroscopy **21**, 2, 131 (1987). ISSN 0304-3991. URL http://dx.doi.org/10.1016/0304-3991(87)90080-5. 24

[Sta08] C. Stampfer, E. Schurtenberger, F. Molitor, J. Guettinger, T. Ihn, and K. Ensslin. *Tunable graphene single electron transistor*. Nano Letters **8**, 8, 2378 (2008). ISSN 1530-6984. URL http://dx.doi.org/10.1021/nl801225h. 34

[Ste09a] A. Steele, G. Gotz, , and L. Kouwenhoven. *Tunable few-electron double quantum dots and Klein tunnelling in ultraclean carbon nanotubes*. Nature Nanotechnology **4**, 6, 363 (2009). ISSN 1748-3387. URL http://dx.doi.org/10.1038/nnano.2009.71. 39

[Ste09b] G. A. Steele, A. K. Hüttel, B. Witkamp, M. Poot, H. B. Meerwaldt, L. P. Kouwenhoven, and H. S. J. van der Zant. *Strong Coupling Between Single-Electron Tunneling and Nanomechanical Motion*. Science **325**, 5944, 1103 (2009). URL http://www.sciencemag.org/content/325/5944/1103.abstract. 39

[Sto85] A. D. Stone. *Magnetoresistance fluctuations in mesoscopic wires and rings*. Physical Review Letters **54**, 2692 (1985). URL http://dx.doi.org/10.1103/PhysRevLett.54.2692. 26, 29, 33

[Str03] M. S. Strano, C. A. Dyke, M. L. Usrey, P. W. Barone, M. J. Allen, H. Shan, C. Kittrell, R. H. Hauge, J. M. Tour, and R. E. Smalley. *Electronic Structure Control of Single-Walled Carbon Nanotube Functionalization*. Science **301**, 5639, 1519 (2003). URL http://www.sciencemag.org/content/301/5639/1519.abstract. 89

[Tan97] S. J. Tans, M. H. Devoret, H. Dai, A. Thess, R. E. Smalley, L. J. Geerligs, and C. Dekker. *Individual single-wall carbon nanotubes as quantum wires*. Nature **386**, 6624, 474 (1997). URL http://dx.doi.org/10.1038/386474a0. 38

[Tan01] P. Tan, C. Hu, J. Dong, W. Shen, and B. Zhang. *Polarization properties, high-order Raman spectra, and frequency asymmetry between Stokes and anti-Stokes scattering of Raman modes in a graphite whisker*. Physical Review B: Condensed Matter and Materials Physics **64**, 214301 (2001). URL http://dx.doi.org/10.1103/PhysRevB.64.214301. 52

[Tar96] S. Tarucha, D. G. Austing, T. Honda, R. J. van der Hage, and L. P. Kouwenhoven. *Shell Filling and Spin Effects in a Few Electron Quantum Dot*. Physical Review Letters **77**, 17, 3613 (1996). URL http://link.aps.org/doi/10.1103/PhysRevLett.77.3613. 34

[Tel04] H. Telg, J. Maultzsch, S. Reich, F. Hennrich, and C. Thomsen. *Chirality Distribution and Transition Energies of Carbon Nanotubes*. Physical Review Letters **93**,



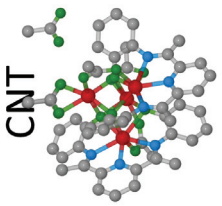

17, 177401 (2004). URL http://link.aps.org/doi/10.1103/PhysRevLett.93.177401. 12

[Tel05] H. Telg, J. Maultzsch, S. Reich, and C. Thomsen. *Chirality dependence of the high-energy Raman modes in carbon nanotubes*. AIP Conference Proceedings **786**, 1, 162 (2005). URL http://dx.doi.org/10.1063/1.2103843. 14

[Tel09] H. Telg. *Raman studies on individual nanotubes and nanotube ensembles – vibrational properties and scattering efficiencies*. Ph.D. thesis, TU Berlin (2009). URL http://opus.kobv.de/tuberlin/volltexte/2009/2474/pdf/telg_hagen.pdf. 12, 13, 14, 102

[The96] A. Thess, R. Lee, P. Nikolaev, H. Dai, P. Petit, J. Robert, C. Xu, Y. H. Lee, S. G. Kim, A. G. Rinzler, D. T. Colbert, G. E. Scuseria, D. Tománek, J. E. Fischer, and R. E. Smalley. *Crystalline Ropes of Metallic Carbon Nanotubes*. Science **273**, 5274, 483 (1996). URL http://dx.doi.org/10.1126/science.273.5274.483. 44

[The98] P. Thevenaz, U. Ruttimann, and M. Unser. *A pyramid approach to subpixel registration based on intensity*. Image Processing, IEEE Transactions on **7**, 1, 27 (1998). ISSN 1057-7149. URL http://bigwww.epfl.ch/publications/thevenaz9801.html. 72

[The11] C. Thelander, P. Caroff, S. Plissard, A. W. Dey, and K. A. Dick. *Effects of Crystal Phase Mixing on the Electrical Properties of InAs Nanowires*. Nano Letters **11**, 6, 2424 (2011). URL http://dx.doi.org/10.1021/nl2008339. 63

[Tho07] C. Thomsen and S. Reich. *Raman Scattering in Carbon Nanotubes*. In M. Cardona and R. Merlin (eds.), *Light Scattering in Solid IX*, volume 108 of *Topics in Applied Physics*, pp. 115–234. Springer Berlin / Heidelberg (2007). ISBN 978-3-540-34435-3. URL http://www.springerlink.com/content/46512485081267ur/. 11, 13, 15

[Tho09] A. Thompson and D. Vaughan. *X-Ray Data Booklet*. Center for X-ray Optics and Advanced Light Source, Lawrence Berkeley National Laboratory, USA (2009). URL http://xdb.lbl.gov/. 93

[Thu07] A. Thust. *Focal-Series reconstruction in HR-TEM: Fundamentals and Applications*. In K. Urban (ed.), *38*$^{\text{th}}$ *IFF Spring School: Probing the Nanoworld -– Microscopies, Scattering and Spectroscopies of the Solid State*, chapter C1. Forschungszentrum Jülich GmbH Zentralbibliothek, Verlag (2007). URL http://d-nb.info/983539421. 24

[Tin75] M. Tinkham. *Introduction to superconductivity*. McGraw-Hill, New York : (1975). ISBN 0070648778. 26

[Tra09] B. Trauzettel and D. Loss. *Nanotubes: Carbon surprises again.* Nature Physics **5**, 5, 317 (2009). ISSN 1745-2473. URL http://dx.doi.org/10.1038/nphys1266. 2

[Tsa94] S. C. Tsang, Y. K. Chen, P. J. F. Harris, and M. L. H. Green. *A simple chemical method of opening and filling carbon nanotubes.* Nature **372**, 6502, 159 (1994). URL http://dx.doi.org/10.1038/372159a0. 16

[Tsu70] D. C. Tsui. *Observation of Surface Bound State and Two-Dimensional Energy Band by Electron Tunneling.* Physical Review Letters **24**, 303 (1970). URL http://dx.doi.org/10.1103/PhysRevLett.24.303. 57

[Tu09] X. Tu, S. Manohar, A. Jagota, and M. Zheng. *DNA sequence motifs for structure-specific recognition and separation of carbon nanotubes.* Nature **460**, 7252, 250 (2009). ISSN 0028-0836. URL http://dx.doi.org/10.1038/nature08116. 44

[Umb84] C. P. Umbach, S. Washburn, R. B. Laibowitz, and R. A. Webb. *Magnetoresistance of small, quasi-one-dimensional, normal-metal rings and lines.* Physical Review B: Condensed Matter and Materials Physics **30**, 4048 (1984). URL http://dx.doi.org/10.1103/PhysRevB.30.4048. 29, 30, 47

[Urb09] K. W. Urban, C.-L. Jia, L. Houben, M. Lentzen, S.-B. Mi, and K. Tillmann. *Negative spherical aberration ultrahigh-resolution imaging in corrected transmission electron microscopy.* Philosophical Transactions of the Royal Society A: Mathematical, Physical and Engineering Sciences **367**, 1903, 3735 (2009). URL http://dx.doi.org/10.1098/rsta.2009.0134. 24

[Urd11] M. Urdampilleta, S. Klyatskaya, J.-P. Cleuziou, M. Ruben, and W. Wernsdorfer. *Supramolecular spin valves.* Nature Materials **10**, 7, 502 (2011). ISSN 1476-1122. URL http://dx.doi.org/10.1038/nmat3050. 89

[Use10] A. Usenko and J. Senawiratne. *Silicon Nitride Surface Conversion into Oxide to Enable Hydrophilic Bonding.* ECS Transactions **33**, 4, 475 (2010). URL http://dx.doi.org/10.1149/1.3483538. 47

[Utk06] P. Utko, J. Nygard, M. Monthioux, and L. Noé. *Sub-Kelvin transport spectroscopy of fullerene peapod quantum dots.* Applied Physics Letters **89**, 23, 233118 (2006). URL http://dx.doi.org/10.1063/1.2403909. 43

[Vav05] J. Vavro, J. M. Kikkawa, and J. E. Fischer. *Metal-insulator transition in doped single-wall carbon nanotubes.* Physical Review B: Condensed Matter and Materials Physics **71**, 15, 155410 (2005). URL http://link.aps.org/doi/10.1103/PhysRevB.71.155410. 117, 118

[Vie00] C. Vieu, F. Carcenac, A. Pépin, Y. Chen, M. Mejias, A. Lebib, L. Manin-Ferlazzo, L. Couraud, and H. Launois. *Electron beam lithography: resolution limits and applications.* Applied Surface Science **164**, 1, 111 (2000). ISSN 0169-4332. URL http://dx.doi.org/10.1016/S0169-4332(00)00352-4. 47



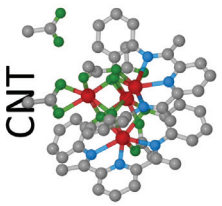

[Wal47] P. R. Wallace. *The Band Theory of Graphite*. Physical Review **71**, 622 (1947). URL http://dx.doi.org/10.1103/PhysRev.71.622. 8

[Wal12] J. Wallentin, M. Ek, L. R. Wallenberg, L. Samuelson, and M. T. Borgström. *Electron Trapping in InP Nanowire FETs with Stacking Faults*. Nano Letters **12**, 1, 151 (2012). URL http://dx.doi.org/10.1021/nl203213d. 63

[Wan95] Z. Wang. *Elastic and inelastic scattering in electron diffraction and imaging*. Plenum Press (1995). URL http://www.springer.com/life+sciences/book/978-0-306-44929-1. 24

[Wan06] C. Wang, G. Zhou, J. Wu, B.-L. Gu, and W. Duan. *Effects of vacancy-carboxyl pair functionalization on electronic properties of carbon nanotubes*. Applied Physics Letters **89**, 17, 173130 (2006). URL http://dx.doi.org/10.1063/1.2364844. 113

[Wan08] S. Wang and M. Grifoni. *Transport properties of double-walled carbon nanotube quantum dots*. Physical Review B: Condensed Matter and Materials Physics **77**, 8, 085431 (2008). URL http://link.aps.org/doi/10.1103/PhysRevB.77.085431. 38, 39, 69, 82

[Was86] S. Washburn and R. A. Webb. *Aharonov-Bohm effect in normal metal quantum coherence and transport*. Advances in Physics **35**, 4, 375 (1986). URL http://dx.doi.org/10.1080/00018738600101921. 30

[Wei09] W. Wei, X.-Y. Bao, C. Soci, Y. Ding, Z.-L. Wang, and D. Wang. *Direct Heteroepitaxy of Vertical InAs Nanowires on Si Substrates for Broad Band Photovoltaics and Photodetection*. Nano Letters **9**, 8, 2926 (2009). URL http://dx.doi.org/10.1021/nl901270n. 2

[Wei13] K. Weis. *Zum Elektronentransport in InAs-Nanodrähten*. Ph.D. thesis, Rheinisch-Westfälische Technische Hochschule Aachen (2013). 45, 46, 57, 63

[Wes11] B. Westenfelder, J. C. Meyer, J. Biskupek, G. Algara-Siller, L. G. Lechner, J. Kusterer, U. Kaiser, C. E. K. III, E. Kohn, and F. Scholz. *Graphene-based sample supports for in situ high-resolution TEM electrical investigations*. Journal of Physics D: Applied Physics **44**, 5, 055502 (2011). URL http://stacks.iop.org/0022-3727/44/i=5/a=055502. 44

[Whi98] C. T. White and T. N. Todorov. *Carbon nanotubes as long ballistic conductors*. Nature **393**, 6682, 240 (1998). ISSN 0028-0836. URL http://dx.doi.org/10.1038/30420. 28

[Wil96] D. Williams and C. Carter. *Transmission Electron Microscopy: Imaging*. Bd. 1. Plenum Press (1996). 23

[Wil98] J. W. G. Wilder, L. C. Venema, A. G. Rinzler, R. E. Smalley, and C. Dekker. *Electronic structure of atomically resolved carbon nanotubes*. Nature **391**, 6662, 59 (1998). ISSN 0028-0836. URL http://dx.doi.org/10.1038/34139. 10

[Wir11] S. Wirths, K. Weis, A. Winden, K. Sladek, C. Volk, S. Alagha, T. E. Weirich, M. von der Ahe, H. Hardtdegen, H. Lüth, N. Demarina, D. Grützmacher, and T. Schäpers. *Effect of Si-doping on InAs nanowire transport and morphology*. Journal of Applied Physics **110**, 5, 053709 (2011). URL http://dx.doi.org/10.1063/1.3631026. 28, 45, 46, 57

[Wu07] Y. Wu, J. Maultzsch, E. Knoesel, B. Chandra, M. Huang, M. Y. Sfeir, L. E. Brus, J. Hone, and T. F. Heinz. *Variable Electron-Phonon Coupling in Isolated Metallic Carbon Nanotubes Observed by Raman Scattering*. Physical Review Letters **99**, 2, 027402 (2007). URL http://link.aps.org/doi/10.1103/PhysRevLett.99.027402. 14

[Yan10a] K. Yanagi, H. Udoguchi, S. Sagitani, Y. Oshima, T. Takenobu, H. Kataura, T. Ishida, K. Matsuda, and Y. Maniwa. *Transport Mechanisms in Metallic and Semiconducting Single-Wall Carbon Nanotube Networks*. ACS Nano **4**, 7, 4027 (2010). ISSN 1936-0851. URL http://dx.doi.org/10.1021/nn101177n. 116

[Yan10b] P. Yang, R. Yan, and M. Fardy. *Semiconductor Nanowire: What's Next?* Nano Letters **10**, 5, 1529 (2010). URL http://dx.doi.org/10.1021/nl100665r. 57

[Yan12] P.-Y. Yang, L. Y. Wang, Y.-W. Hsu, and J.-J. Lin. *Universal conductance fluctuations in indium tin oxide nanowires*. Physical Review B: Condensed Matter and Materials Physics **85**, 085423 (2012). URL http://dx.doi.org/10.1103/PhysRevB.85.085423. 31, 60, 61

[Yeh92] C.-Y. Yeh, Z. W. Lu, S. Froyen, and A. Zunger. *Zinc-blende–wurtzite polytypism in semiconductors*. Physical Review B: Condensed Matter and Materials Physics **46**, 16, 10086 (1992). URL http://link.aps.org/doi/10.1103/PhysRevB.46.10086. 16

[Yos09] H. Yoshida, T. Shimizu, T. Uchiyama, H. Kohno, Y. Homma, and S. Takeda. *Atomic-Scale Analysis on the Role of Molybdenum in Iron-Catalyzed Carbon Nanotube Growth*. Nano Letters **9**, 11, 3810 (2009). URL http://dx.doi.org/10.1021/nl9019903. 44

[Zan99] A. Zannoni. *On the Quantization of the Monoatomic Ideal Gas*. ArXiv:cond-mat **9912229**, 1 (1999). URL http://arxiv.org/abs/cond-mat/9912229. 27

[Zan07] Z. Zanolli, F. Fuchs, J. Furthmüller, U. von Barth, and F. Bechstedt. *Model GW band structure of* InAs *and* GaAs *in the wurtzite phase*. Physical Review B: Condensed Matter and Materials Physics **75**, 245121 (2007). URL http://dx.doi.org/10.1103/PhysRevB.75.245121. 17



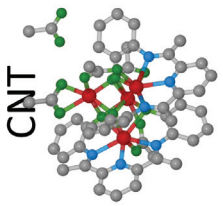

[Zha92] X.-C. Zhang and D. H. Auston. *Optoelectronic measurement of semiconductor surfaces and interfaces with femtosecond optics*. Journal of Applied Physics **71**, 1, 326 (1992). URL http://dx.doi.org/10.1063/1.350710. 16

[Zha03] J. Zhang, H. Zou, Q. Qing, Y. Yang, Q. Li, Z. Liu, X. Guo, and Z. Du. *Effect of Chemical Oxidation on the Structure of Single-Walled Carbon Nanotubes*. Journal of Physical Chemistry B **107**, 16, 3712 (2003). ISSN 1520-6106. URL http://dx.doi.org/10.1021/jp027500u. 112, 113

[Zha08] H. Zhang, N. Du, P. Wu, B. Chen, and D. Yang. *Functionalization of carbon nanotubes with magnetic nanoparticles: general nonaqueous synthesis and magnetic properties*. Nanotechnology **19**, 31, 315604 (2008). URL http://stacks.iop.org/0957-4484/19/i=31/a=315604. 98

## List of Figures





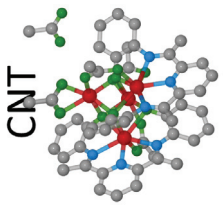

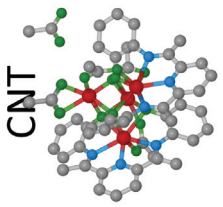

## List of Tables





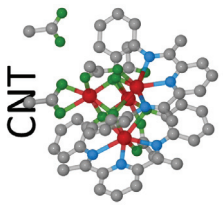

## List of Own Publications

### Articles

- Phase-coherence and symmetry in four-terminal magneto-transport measurements on InN nanowires
  **Robert Frielinghaus,** Sergio Estévez Hernández, Raffaella Calarco, and Thomas Schäpers
  *Applied Physics Letters* **94**, 252107 (2009)

- Josephson supercurrent in Nb/InN-nanowire/Nb junctions
  **Robert Frielinghaus,** Igor E. Batov, Martin Weides, Hermann Kohlstedt, Raffaella Calarco, and Thomas Schäpers
  *Applied Physics Letters* **96**, 132504 (2010)

- Comprehensive characterization of an individual carbon nanotube transport device
  **Robert Frielinghaus**, Karin Goß, Stefan Trellenkamp, Lothar Houben, Claus M. Schneider, and Carola Meyer
  *physica status solidi (b)* **248**, 2660 (2011)

- Manipulating InAs nanowires with submicrometer precision
  Kilian Flöhr, Markus Liebmann, Kamil Sladek, H. Yusuf Günel, **Robert Frielinghaus**, Fabian Haas, Carola Meyer, Hilde Hardtdegen, Thomas Schäpers, Detlev Grützmacher, and Markus Morgenstern
  *Review of Scientific Instruments* **82**, 113705 (2011)

- Monitoring structural influences on quantum transport in InAs nanowires
  **Robert Frielinghaus**, Kilian Flöhr, Kamil Sladek, Thomas E. Weirich, Stefan Trellenkamp, Hilde Hardtdegen, Thomas Schäpers, Claus M. Schneider, and Carola Meyer
  *Applied Physics Letters* **101**, 062104 (2012)

- Covalent functionalization of carbon nanotubes with tetramanganese complexes
  Carola Meyer, Claire Besson, **Robert Frielinghaus**, Anna-Katharina Saelhoff, Henrik Flötotto, Lothar Houben, Paul Kögerler, and Claus M. Schneider
  *physica status solidi (b)*, **249**, 2412 (2012)



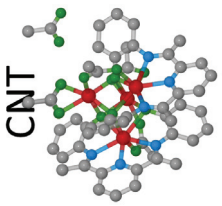

## Conference contributions

- Phase-coherent transport in InN nanowires
  Thomas Schäpers, Sergio Estévez Hernández, Gunnar Petersen, **Robert Frielinghaus,** Christian Blömers, Thomas Richter, Raffaella Calarco, Hans Lüth, Michel Marso und K. Michael Indlekofer
  413. Wilhelm und Else-Heraeus-Seminar, Bad Honnef (30.09.2008)

- Semiconductor nanowires as building blocks for quantum devices
  Thomas Schäpers, Sergio Estévez Hernández, Gunnar Petersen, **Robert Frielinghaus,** Shima Alagha, Christian Blömers, Thomas Richter, Raffaella Calarco Hans Lüth, Michel Marso und K. Michael Indlekofer
  Frühjahrstagung der Deutschen Physikalischen Gesellschaft, Sektion kondensierte Materie, in Dresden (25.03.2009)

- Gate-controlled conductance fluctuations in InN nanowires
  Sergio Estévez Hernández, Gunnar Petersen, **Robert Frielinghaus,** Ralph Meijers, Raffaella Calarco, Thomas Schäpers, and Detlev Grützmacher
  Frühjahrstagung der Deutschen Physikalischen Gesellschaft, Sektion kondensierte Materie, in Dresden (26.03.2009)

- Correlating different characterization methods on individual carbon nanotubes
  **Robert Frielinghaus,** Karin Goß, Christian Spudat, Lothar Houben, Caitlin Morgan, Stefan Trellenkamp, Matthias Müller, Janina Maultzsch, Christian Thomsen, Claus M. Schneider, and Carola Meyer
  Nanoelectronics Days 2010 in Aachen (04.10.2010)

- Correlating different characterization methods on individual carbon nanotubes
  **Robert Frielinghaus,** Karin Goß, Christian Spudat, Lothar Houben, Matthias Müller, Christian Thomsen, Stefan Trellenkamp, Carola Meyer, and Claus M. Schneider
  International Workshop on Electronic Properties of Novel Materials in Kirchberg, Austria (28.02.2011)

- Structural influences on electronic transport in nanostructures
  **Robert Frielinghaus,** Kamil Sladek, Kilian Flöhr, Lothar Houben, Stefan Trellenkamp, Thomas E. Weirich, Hilde Hardtdegen, Thomas Schäpers, Claus M. Schneider, and Carola Meyer
  $17^{\text{th}}$ International Winterschool on New Developments in Solid State Physics in Mauterndorf, Austria (14.02.2012)

- Functionalization of carbon nanotubes with $\{Mn_4\}$ polymetallic complexes
  Carola Meyer, **Robert Frielinghaus,** Anna-Katharina Saelhoff, Claire Besson, Lothar Houben, Paul Kögerler und Claus M. Schneider
  International Workshop on Electronic Properties of Novel Materials in Kirchberg, Austria (06.03.2012)

- Correlating the crystal structure and quantum transport of individual InAs nanowires
  M. Schuck, Christian Blömers, **Robert Frielinghaus,** Thorsten Rieger, Stefan Trellenkamp, Carola Meyer, Mihail I. Lepsa, Detlev Grützmacher, and Thomas Schäpers
  Frühjahrstagung der Deutschen Physikalischen Gesellschaft, Sektion kondensierte Materie, in Berlin (27.03.2012)

- $\{Mn_4\}$–clusters covalently bonded to carbon nanotubes
  Carola Meyer, **Robert Frielinghaus,** Anna-Katharina Saelhoff, Claire Besson, Henrik Flötotto, Lothar Houben, Paul Kögerler, and Claus M. Schneider
  Frühjahrstagung der Deutschen Physikalischen Gesellschaft, Sektion kondensierte Materie, in Berlin (27.03.2012)

- Manipulating and contacting single InAs Nanowires at GaAs edges
  Kilian Flöhr, H. Yusuf Günel, Kamil Sladek, **Robert Frielinghaus,** Hilde Hardtdegen, Carola Meyer, Markus Liebmann, Thomas Schäpers, and Markus Morgenstern
  Frühjahrstagung der Deutschen Physikalischen Gesellschaft, Sektion kondensierte Materie, in Berlin (27.03.2012)

- Functionalization of carbon nanotubes with $\{Mn_4\}$–clusters
  Anna-Katharina Saelhoff, **Robert Frielinghaus,** Claire Besson, Henrik Flötotto, Lothar Houben, Paul Kögerler, Claus M. Schneider, and Carola Meyer
  Frühjahrstagung der Deutschen Physikalischen Gesellschaft, Sektion kondensierte Materie, in Berlin (29.03.2012)

- Structural influences on electronic transport in nanostructures
  **Robert Frielinghaus,** Kamil Sladek, Kilian Flöhr, Lothar Houben, Stefan Trellenkamp, Thomas E. Weirich, Markus Morgenstern, Hilde Hardtdegen, Thomas Schäpers, Claus M. Schneider, and Carola Meyer
  Nature Conference Frontiers in Electronic Materials in Aachen (18.06.2012)
  *Appeared in* J. Heber, D. Schlom, Y. Tokura, R. Waser, and M. Wuttig (eds.): *Frontiers in electronic materials*, Weinheim: Wiley-VCH-Verlag (2012)

- Preparing InAs nanowires for functionalized STM tips
  Kilian Flöhr, H. Yusuf Günel, Kamil Sladek, **Robert Frielinghaus,** Hilde Hardtdegen, Markus Liebmann, Thomas Schäpers, Markus Morgenstern
  Nature Conference Frontiers in Electronic Materials in Aachen (19.06.2012)
  *Appeared in* J. Heber, D. Schlom, Y. Tokura, R. Waser, and M. Wuttig (eds.): *Frontiers in electronic materials*, Weinheim: Wiley-VCH-Verlag (2012)

- Functionalization and characterization of individual carbon nanotubes and transport devices
  Carola Meyer, **Robert Frielinghaus,** Anna-Katharina Saelhoff, Claire Besson, Henrik Flötotto, Lothar Houben, Paul Kögerler, Claus M. Schneider
  International Conference on Nanoscience + Technology in Paris, France (24.07.2012)



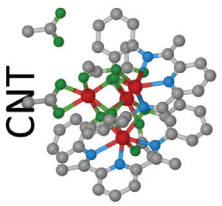

- Functionalization of carbon nanotubes with tetramanganese complexes
  Carola Meyer, **Robert Frielinghaus,** Anna-Katharina Saelhoff, Claire Besson, Lothar Houben, Paul Kögerler, Claus M. Schneider
  2012 Fall Meeting of the European Materials Research Society in Warsaw, Poland, (17.09.2012)

- Tip-enhanced Raman spectroscopy of functionalized carbon nanotubes with $\{Mn_4\}$–complexes
  Emanuele Poliani, Asmus Vierck, **Robert Frielinghaus,** Anna-Katharina Saelhoff, Carola Meyer, Janina Maultzsch
  International Conference on Enhances Spectroscopy on Porquerolles Island, France (04.10.2012)

## Talks

- Phase-coherent transport in indium nitride nanowires – Analysis by four-terminal measurements
  Frühjahrstagung der Deutschen Physikalischen Gesellschaft, Sektion kondensierte Materie, in Dresden (24.03.2009)

- Correlation of transport, Raman and TEM measurements on functionalized carbon nanotubes
  Spin Transport and Coherence. Ph.D. school of the Deutsche Forschungsgemeinschaft, Forschergruppe 912 (08.04.2010)

- Quantum transport in indium nitride nanowires and carbon nanotubes
  Seminar talk at the department of Physics of the University of Nairobi, Kenya (18.01.2011)

- Correlating different characterization methods on individual carbon nanotubes
  Frühjahrstagung der Deutschen Physikalischen Gesellschaft, Sektion kondensierte Materie, in Dresden (18.03.2011)

- Correlating different characterization methods on individual carbon nanotubes
  Spin Transport and Coherence. Ph.D. school of the Deutsche Forschungsgemeinschaft, Forschergruppe 912 (06.04.2011)

- Structural influences on quantum transport in nanowires
  Spin physics of topological insulators, graphene, spin chains and nanowires. Project meeting of the Deutsche Forschungsgemeinschaft, Forschergruppe 912 (17.02.2012)

- Structural influences on quantum transport in InAs nanowires
  Frühjahrstagung der Deutschen Physikalischen Gesellschaft, Sektion kondensierte Materie, in Dresden (28.03.2012)



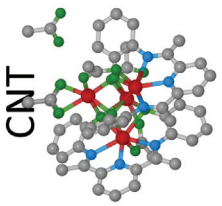

## Curriculum Vitae

| | |
|---|---|
| **Personal Data** | |
| | Robert Dietrich Frielinghaus<br>Born 08.05.1984 in Bochum<br>German |
| **Education** | |
| 09/1994 – 06/2003 | Hildegardis-Schule Bochum |
| 06/2003 | Abitur |
| 10/2004 – 03/2009 | Rheinisch-Westfälische Technische Hochschule Aachen |
| 03/2009 | Diploma in physics, Supervisor: Prof. Dr. Thomas Schäpers<br>Institut für Bio- und Nanosysteme, Forschungszentrum Jülich |
| 10/2006 – 07/2007 | École Polytechnique Fédérale de Lausanne |
| 08/2009 – 12/2009 | University of Nairobi |
| Since 01/2010 | Universität Duisburg–Essen<br>Ph.D. in physics, Supervisor: Prof. Dr. Claus M. Schneider<br>Peter Grünberg Institut, Forschungszentrum Jülich |
| **Work Experience** | |
| 05/2009 – 08/2009 | Kammrath & Weiss GmbH<br>Internship on electron microscopy accessories |
| Since 01/2010 | Forschungszentrum Jülich GmbH<br>Research assistant |
| Since 10/2010 | Forschungszentrum Jülich GmbH<br>Tour guide |



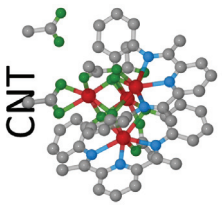

## Erklärung

Jülich, den 22. März 2013

Hiermit erkläre ich, die vorliegende Arbeit selbstständig und ohne fremde Hilfe verfasst zu haben. Ferner habe ich nur die angegebenen Quellen und Hilfsmittel benutzt. Die dem Sinn oder Wortlaut nach entnommenen Textpassagen oder Abbildungen habe ich in jedem Einzelfall kenntlich gemacht. Dieser Dissertation geht weder ein erfolgloser Promotionsversuch voraus, noch wurde sie in einem weiteren Promotionsverfahren eingereicht. Abgesehen von den angegebenen und beiliegenden Publikationen sind die Ergebnisse dieser Monographie unveröffentlicht. Diese Dissertation, die den Doktorgrad „Dr. rer. nat.“ anstrebt, wurde von Prof. Dr. Claus M. Schneider betreut.

Robert Frielinghaus



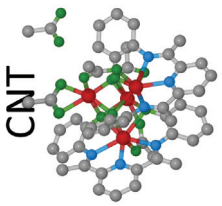

## Nomenclature

The following table gives a comprehensive list of all used symbols and abbreviations. Some quantities are indicated with a non-SI unit if this the common usage.

Vectorial symbols are indicated by an arrow. Their modulus is denoted if it is omitted. Operators are marked by a ˆ sign.

Also the sketches share a common colour coding as far as possible. Electrons are always red while positive charges are blue. The samples are green. Elements are coded gray for carbon, blue for nitrogen, green for oxygen and red for manganese.

| | |
|---|---|
| $(n, m)$ | Carbon nanotube chiral indices |
| $\alpha_D$ | Drain lever arm ... V/V |
| $\alpha_G$ | Gate lever arm (Gate voltage to energy conversion) ... eV/V |
| $\alpha_S$ | Source lever arm ... V/V |
| $\beta$ | Prefactor for UCF amplitude, cf. eq. (III.13) |
| $\delta_G$ | Universal conductance fluctuations ... $e^2/h$ |
| $\epsilon_0$ | Dielectric constant of the vacuum ... $\mathrm{F} \cdot \mathrm{m}^{-1}$ |
| $\epsilon_r$ | Relative dielectric constant ... $\epsilon_0$ |
| $\Gamma$ | Half width at half maximum |
| $\gamma$ | Proportionality constant relating $l_\varphi$ and $B_C$, cf. eq. (III.17) |
| gcd | Greatest common divisor |
| $\hat{H}$ | Hamiltonian ... eV |
| $\hbar$ | Reduced Planck's constant $\hbar := h/(2\pi)$ ... Js |
| $\lambda_F$ | Fermi wavelength ... nm |
| $\lambda_L$ | Raman laser wavelength ... nm |
| $\mathcal{D}$ | Diffusion constant ... $\mathrm{cm}^2/\mathrm{s}$ |
| $\mu$ | Charge carrier mobility ... $\mathrm{cm}^2/(\mathrm{Vs})$ |
| $\mu_i$ | Chemical potential ... eV |
| $\nu$ | CNT Family index mod $(n - m, 3) \Rightarrow \nu \in [0, 1, 2]$ |
| $\nu'$ | CNT branch number $2n + m$ |



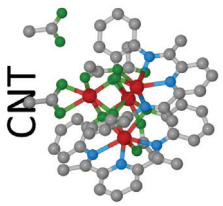

| | |
|---|---|
| $\omega$ | Raman shift ... $\mathrm{cm}^{-1}$ |
| $\Phi$ | Magnetic flux $\Phi := \vec{B} \cdot \vec{A}$ ... $h/e$ |
| $\Phi_0$ | Flux quantum $\Phi_0 = h/e$ |
| $\sigma$ | Conductivity ... S/m |
| $\sigma_{\delta_G}$ | Root mean square of the UCFs ... $e^2/h$ |
| $\tau$ | Lifetime ... s |
| $\theta$ | Carbon nanotube chiral angle ... $^\circ$ |
| $\tilde{D}$ | $D$ mode with additional features from acetonitrile |
| $\underline{\underline{\sigma}}$ | Pauli spin matrix |
| $\Gamma$ | Crystallographic point of highest symmetry |
| $\vec{a}_1, \vec{a}_2$ | Graphene base vectors ... Å |
| $\vec{B}$ | Magnetic field ... T |
| $\vec{c}_h$ | Carbon nanotube chiral (circumference) vector ... nm |
| $\vec{k}$ | Wave vector ... $\mathrm{cm}^{-1}$ |
| $\vec{q}$ | Phonon wave vector ... $\mathrm{cm}^{-1}$ |
| $\vec{r}$ | Position vector ... nm |
| $\vec{\tau}$ | Carbon nanotube translational vector ... nm |
| $\vec{\kappa}$ | Wave vector around $K$ or $K'$: $\vec{\kappa} = \vec{k} - K$ ... $\mathrm{cm}^{-1}$ |
| $\mathcal{A}, \mathcal{B}$ | Graphene crystal sublattices |
| $a_{CC}$ | C-C atom distance (graphene) ... Å |
| $B_C$ | Correlation field ... T |
| $C$ | Capacity ... F |
| $C_S$ | Spherical aberrations ... $\mu$m |
| $D$ | Diameter *or* CNT defect Raman mode ... nm |
| $d$ | Dimensionality of the system ($d \in [1, 2, 3]$) |
| $E$ | Energy ... eV |
| $e$ | Electron charge |
| $e^-$ | Electron (red) |
| $E_C$ | Quantum dot charging energy ... eV |
| $E_F$ | Fermi energy ... eV |
| $E_G$ | Bandgap ... eV |
| $E_L$ | Laser energy ... eV |
| $E_{\mathrm{Add}}$ | Addition energy |
| $E_{\mathrm{ph}}$ | Phonon energy, with ph=(RBM,$D$, $G^{\pm}$...) ... eV |
| $E_{ii}^{M/S}$ | (Optical) transition energy for metallic (semiconducting) CNTs ... eV |
| $E_{ST}$ | Interaction energy between transfer and spectator dot ... eV |
| $G$ | Conductance ... $\mho$ |

| | |
|---|---|
| $G^{\pm}$ | CNT high-energy Raman modes |
| $G_0$ | Conductance quantum $G_0 = e^2/h$ |
| $h$ | Hybridization parameter |
| $h$ | Planck's constant ... Js |
| $I$ | Source-drain current ... nA |
| $I_R$ | Raman scattering intensity |
| $I_S$ | EELS intensity |
| $I_X$ | EDX intensity |
| $K, K'$ | Crystallographic points |
| $k_B$ | Boltzmann constant ... J/K |
| $k_F$ | Fermi wave vector ... 1/m |
| $l$ | A length ... nm |
| $l_e$ | Elastic mean free path ... nm |
| $l_T$ | Thermal length ... nm |
| $M$ | Magnetization ... emu/g |
| $m^*$ | Effective mass ... $m_e$ |
| $m_e$ | Electron mass ... kg |
| $N$ | An integer ($N \in \mathbb{N}$) |
| $n$ | Charge carrier density ... $\mathrm{cm}^{-3}$ |
| $n_S$ | Surface charge carrier density ... $\mathrm{cm}^{-2}$ |
| $T$ | Temperature ... K |
| $t$ | Time ... s |
| $v_F$ | Fermi velocity ... m/s |
| $v_F$ | Fermi velocity ... m/s |
| $V_B$ | Source-Drain or bias voltage ... mV |
| $z$ | Dimension along the nanostructure's axis |
| $Z_f$ | Defocus ... nm |
| 2DEG | Two-dimensional electron gas |
| $\mathcal{C}$ | Contrast transfer function |
| AFM | Atomic force microscopy |
| BF | Bright field |
| CNT | Carbon nanotube |
| DOS | Density of States ... $\mathrm{eV}^{-1}$ |
| e-beam | Electron beam lithography |
| EDX | Energy-dispersive X-Ray spectroscopy |
| EELS | Electron energy loss spectroscopy |
| FEG | Field emission gun |



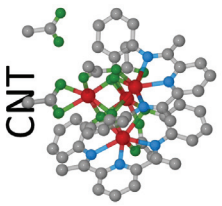

| | |
|---|---|
| FWHM | Full width at half maximum |
| HAADF | High-angle annular dark-field |
| HEM | High-energy mode ($G^{\pm}$) |
| HRTEM | High-resolution transmission electron microscopy |
| HSQ | Hydrogen silsesquioxane |
| MBE | Molecular beam epitaxy |
| NW | Nanowire |
| PMMA | Polymethylmethacrylate |
| RBM | Radial breathing mode |
| SA-MOVPE | Selective-area metalorganic vapour phase epitaxy |
| SEM | Scanning electron microscopy |
| sHEM | Super high-energy mode |
| SQUID | Superconducting quantum interference device |
| STEM | Scanning transmission electron microscopy |
| STM | Scanning tunnelling microscopy |
| TEM | Transmission electron microscopy |
| TGA | Thermogravimetric analysis |
| TMIn | Trimethylindium |
| UCF | Universal conductance fluctuations |
| VRH | Variable range hopping |

# Index





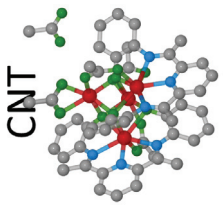

Band / Volume 47
**STM beyond vacuum tunnelling: Scanning Tunnelling Hydrogen Microscopy as a route to ultra-high resolution**
C. Weiss (2012), II, 165 pp.
ISBN: 978-3-89336-813-6

Band / Volume 48
**High Temperature Radio-Frequency Superconducting Quantum Interference Device System for Detection of Magnetic Nanoparticles**
A. Pretzell (2012), 122 pp.
ISBN: 978-3-89336-814-3

Band / Volume 49
**Study of Molecule-Metal Interfaces by Means of the Normal Incidence X-ray Standing Wave Technique**
G. Mercurio (2012), XXII, 361 pp.
ISBN: 978-3-89336-816-7

Band / Volume 50
**5th Georgian-German School and Workshop in Basic Science**
**Tbilisi, Georgia/August 6 – 10, 2012. Batumi, Georgia/August 13 – 17, 2012**.
Org. Committee: E. Abrosimova, A. Bakuridze, A. Kacharava, A. Kvitashvili, A. Prangishvili, H. Ströher (2012); CD-ROM
ISBN: 978-3-89336-818-1

Band / Volume 51
**Exploring the electronic properties of novel spintronic materials by photoelectron spectroscopy**
A. Herdt (2012), ii, 126 pp.
ISBN: 978-3-89336-831-0

Band / Volume 52
**Quantum Information Processing**
Lecture Notes of the 44$^{th}$ IFF Spring School 2013
February 25 – March 8, 2013 Jülich, Germany
D. DiVincenzo (Ed.) ca. 1000 pp.
ISBN: 978-3-89336-833-4

Band / Volume 53
**Real-Space Finite-Difference PAW Method for Large-Scale Applications on Massively Parallel Computers**
P.F. Baumeister (2012), vi, 212 pp.
ISBN: 978-3-89336-836-5

Band / Volume 54
**Einfluss unkonventioneller Medien auf die Selektivität ThDP-abhängiger Enzyme**
T. Gerhards (2013), XIV, 199 pp.
ISBN: 978-3-89336-846-4

Band / Volume 55
**Aufbau einer Vierspitzen-Rastertunnelmikroskop/Rasterelektronenmikroskop-Kombination und Leitfähigkeitsmessungen an Silizid Nanodrähten**
E. Zubkov (2013), 150 pp.
ISBN: 978-3-89336-848-8

Band / Volume 56
**Interplay between magnetic and dielectric phenomena at transition metal oxide interfaces**
D. Schumacher (2013), IV, 128 pp.
ISBN: 978-3-89336-855-6

Band / Volume 57
**Single $NdPc_2$ Molecules on Surfaces: Adsorption, Interaction, and Molecular Magnetism**
S. Fahrendorf (2013), viii, 100 pp.
ISBN: 978-3-89336-856-3

Band / Volume 58
**Heyd-Scuseria-Ernzerhof Screened-Exchange Hybrid Functional for Complex Materials: All-Electron Implementation and Application**
M. Schlipf (2013), XV, 170 pp.
ISBN: 978-3-89336-857-0

Band / Volume 59
**Orbital-dependent exchange-correlation functionals in density-functional theory realized by the FLAPW method**
M. Betzinger (2013), vi, 173 pp.
ISBN: 978-3-89336-858-7

Band / Volume 60
**Structural influences on electrical transport in nanostructures**
R. D. Frielinghaus (2013), viii, 190 pp.
ISBN: 978-3-89336-867-9

Weitere ***Schriften des Verlags im Forschungszentrum Jülich*** unter
http://wwwzb1.fz-juelich.de/verlagextern1/index.asp

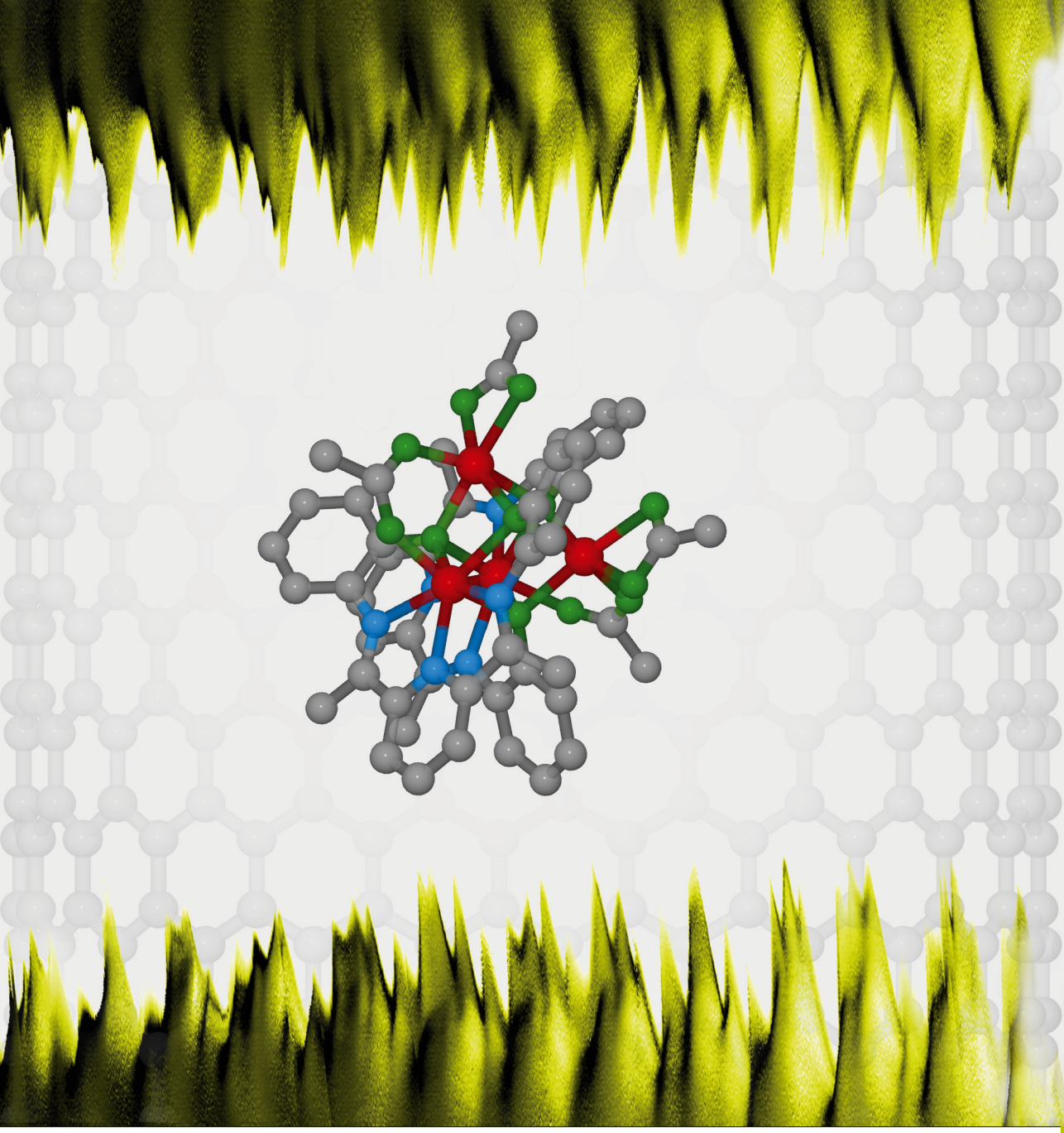

Schlüsseltechnologien / Key Technologies
Band / Volume 60
ISBN 978-3-89336-867-9

JÜLICH
FORSCHUNGSZENTRUM